ABSTRACT

Title of dissertation: **A LARGE EDDY SIMULATION STUDY OF THE EFFECTS OF WIND AND SLOPE ON THE STRUCTURE OF A TURBULENT LINE FIRE**

Salman Verma, Doctor of Philosophy, 2019

Dissertation directed by: Professor Arnaud Trouvé
Department of Mechanical Engineering

Due to a complex coupling between a large number of physical and chemical processes that happen over a wide range of length and time scales, our current fundamental understanding of wildland fire spread is limited. Wildland fire spread is affected by many parameters, but two of the most important parameters are wind and slope both of which tilt the flame and plume and bring them closer to the unburnt fuel, which, among other things, increases the convective heat transfer and hence the spread rate. The primary objective of this work is to enhance our fundamental understanding of the effects of wind and slope on the structure of a turbulent, buoyant line fire.

To meet the aforementioned objective we perform well-resolved Large Eddy Simulations (LES) of a simplified configuration corresponding to a turbulent, buoyant, methane-fueled, stationary, line fire and subjected to wind or slope. Simulations are performed with an LES solver developed by FM Global and called FireFOAM which is based on the OpenFOAM CFD library.

For the cases with wind, the transition from the buoyancy-dominated (in which the flame and plume are mostly detached from the downwind surface and have a tilted vertical shape; entrainment is two-sided; downwind surfaces experience convective cooling) to wind-dominated (in which the flame and plume are attached to the downwind surface; entrainment is one-sided; downwind surfaces experience convective heating) regime happens when the Byram's convection number N_C is ≈ 1. The flame and plume attachment lengths (defined as the x-wall-distance downwind of the burner within the flame and plume regions, respectively) are found to fluctuate significantly in time.

For the cases with slope the transition from the detached regime (equivalent to the buoyancy-dominated regime) to the attached regime (equivalent to the wind-dominated regime) is found to happen between slopes of 16 and 32 degrees. Upslope of the flame zone, the velocity tangent to the surface is found to change from a relatively small negative value (≈ -0.3 m/s) to a relatively large positive value ($\approx$ 2.5 m/s), when the slope is increased from 16 to 32 degrees. The flame attachment length (defined as the tangential-wall-distance upslope of the burner within the flame region) is again found to fluctuate significantly in time.

An integral model, capable of describing the effects of cross-wind on the structure of a turbulent, buoyant line fire, is also developed in this work. The model, after some simplifications, suggests that the plume tilt angle is controlled by the Byram's convection number N_C and the entrainment coefficients α and β. Detailed comparisons are made between the model and LES and show that the model performs well for the cases belonging to the buoyancy-dominated regime ($N_C \gtrsim 1$)

but fails to describe the cases belonging to the wind-dominated regime ($N_C \lesssim 1$) because of the absence of a wall attachment sub-model.

A LARGE EDDY SIMULATION STUDY OF THE EFFECTS OF WIND AND SLOPE ON THE STRUCTURE OF A TURBULENT LINE FIRE

by

Salman Verma

Dissertation submitted to the Faculty of the Graduate School of the
University of Maryland, College Park in partial fulfillment
of the requirements for the degree of
Doctor of Philosophy
2019

Advisory Committee:
Professor Arnaud Trouvé, Chair/Advisor
Professor Johan Larsson
Professor Amir Riaz
Professor Michael Gollner
Professor Elaine Oran, Dean's Representative

Acknowledgments

First, I would like to thank my advisor Dr. Arnaud Trouvé. I came to Dr. Trouvé's group more than half a decade ago; a fairly long time scale, so there have been many ups and downs; in my case the latter have been orders of magnitude more than the former; so without his high level of patience this would definitely not have worked. There are many other things that are also very important (e.g., attention to detail, ample computational resources) but patience is the high-order bit.

I would also like to thank Dr. Michael Gollner for his patience with me on the wildland fire project over the last half a decade or so. The joint meetings with Dr. Gollner's group have been an important part of my journey at UMD. Also the experimental support we have received from his group has been very generous.

Thanks also to Dr. André Marshall who has played a VERY important role in my journey at UMD. Again very high level of patience; in addition he has been very supportive and kind to me over the last half a decade.

Further thanks to Dr. Amir Riaz for being on the committee. The only pure CFD course I have taken in my life is from Dr. Riaz, which has definitely improved the quality of the present work. Thanks to Dr. Johan Larsson for being on the committee as well. During my initial days at UMD there was a time when my life revolved around some of Dr. Larsson's papers, and I learnt a lot from them. Thanks also to Dr. Elaine Oran for being on the committee. In addition to being one of the biggest names in the CFD world, she is unbelievably nice. I am not sure that I

need to say much more because we all know her. I am glad that Drs. Riaz, Larsson and Oran are on the committee. I also want to thank Drs. Larsson and Oran for their patience, support and comments during the proposal stage.

I also want to thank Drs. Christopher Cadou, Joseph Ruf (NASA Marshall), Mark Finney (US Forest Service) and Yi Wang (FM Global). Without their support and patience nothing would have worked.

Special thanks to Dr. Randall McDermott (NIST) for his support and guidance over the years. I do not think that I need to talk too much about Dr. McDermott, all of us at UMD love him. I would just make one comment here, about the "Advanced Fire Modeling" class (which involved quite a lot of CFD) that he co-taught with Dr. Trouve: it is one of the best class I have ever taken and has played a critical role in my research.

Thanks also to Dr. James White (FM Global) for providing the experimental data for the validation task (presented in Chapter 3); he is an "A" player and I am not sure if I need to say anything else.

Additional thanks to the (former/present) graduate/visiting students of the Mechanical, Aerospace and Fire Protection Engineering Departments: Lin Jiang, Wei Tang, Cong Zhang, Xiaoyue Pi, Xingyu Ren, Andrew Voegele, Sergio Vargas-Cordoba, Ajay Vikram Singh, Colin Miller, Rui Xu, Shiyun Wu, Minh Le, Colin Adamson, Chandan Kittur, Yan Ding, Sriram Hariharan, Dushyant, Vivien Lecoustre, Evan Sluder, Paul Anderson, Pietro Maisto, Eric Link and Talia. They are all a critical part of my journey at UMD.

Finally, thanks to the staff of the Mechanical and Fire Protection Engineering

Departments; specifically, Christine O'Brien, Kerri Poppler James and Marta Manzano. Thanks also to the International Students & Scholar Services (ISSS) staff; in particular, Bijoya Chakraborty (for her help and patience). I also want to thank Dianne Barrett from the Registrar's office for her help and patience.

This work is financially supported by the Missoula Fire Sciences Laboratory, Rocky Mountain Research Station, USDA Forest Service (with Dr. Mark Finney as the program manager) and by FM Global (with Dr. Yi Wang as the program manager). This work used the University of Maryland supercomputing resources (http://hpcc.umd.edu). This work also used the eXtreme Science and Engineering Discovery Environment (XSEDE) [1], which is supported by National Science Foundation grant number ACI-1548562; the resource used in this work is Comet at the San Diego Supercomputer Center (SDSC) through allocation TG-CTS140046.

Table of Contents

Nomenclature

Acronyms

CFD	- Computational Fluid Dynamics
DNS	- Direct Numerical Simulation/s
LES	- Large Eddy Simulation/s
WRLES	- Well-Resolved Large Eddy Simulation/s
RANS	- Reynolds Averaged Navier-Stokes
NVD	- Normalized Variable Diagram
CBC	- Convection Boundedness Criterion
SIMPLE	- Semi-Implicit Method for Pressure-Linked Equations
PISO	- Pressure-Implicit with Splitting of Operators
HRR	- Heat Release Rate
EDC	- Eddy Dissipation Concept
WALE	- Wall-Adapting Local Eddy-viscosity
TKE	- Turbulent Kinetic Energy
UMD	- University of Maryland
RTE	- Radiative Transfer Equation
PDFs	- Probability Density Functions
GER	- Global Equivalence Ratio

Symbols

x	- streamwise direction/distance
y	- spanwise direction/distance
z	- vertical direction/distance
x_i	- coordinate in index notation
t	- time
i	- index
u_i	- velocity component in index notation
g_i	- gravity component in index notation
p	- pressure
T	- temperature
R_u	- universal gas constant
$R = R_u/MW_{air}$	- specific gas constant
MW	- molecular weight
U_∞	- freestream or wind velocity
T_∞	- freestream temperature
h_s	- sensible enthalpy
Y	- mass fraction
D	- molecular diffusivity
$u_\tau = \sqrt{\tau_w/\rho_w}$	- friction velocity
$x^+ = (u_\tau x)/\nu_w$	- streamwise wall unit
$y^+ = (u_\tau y)/\nu_w$	- spanwise wall unit

$z^+ = (u_\tau z)/\nu_w$	- vertical wall unit
g	- gravity acceleration scalar value
c_p	- specific heat at constant pressure
$\mathrm{Le} = \alpha/D$	- Lewis number
$\mathrm{Pr} = \nu/\alpha$	- Prandtl number
$\mathrm{Sc} = \nu/D$	- Schmidt number
I	- fireline intensity (HRR per unit spanwise length)
s	- distance along the flame/plume centerline
b	- flame/plume half width
u_p	- flame/plume centerline velocity
T_p	- flame/plume temperature
u_e	- entrainment velocity
$\dot{m}'_p = \rho_p(2b)u_p$	- mass flow rate per unit spanwise length
Y_F	- mass fraction of fuel
Y_{O_2}	- mass fraction of oxygen
$Y_{O_2,\infty}$	- mass fraction of oxygen in ambient air
Z	- mixture fraction
r_s	- stoichiometric oxygen to fuel mass ratio
x_c	- x-coordinate of the flame/plume centerline
z_c	- z-coordinate of the flame/plume centerline
μ	- dynamic viscosity
ρ	- density
ρ_∞	- ambient air density
ρ_p	- flame/plume density
$\nu = \mu/\rho$	- kinematic viscosity
β	- coefficient of thermal expansion
τ_w	- wall shear stress
κ	- thermal conductivity of air
α	- thermal diffusivity
$\overline{\dot{\omega}'''_{h_s}}$	- source term in the enthalpy transport equation
$\overline{\dot{\omega}'''_{Y_k}}$	- source terms in the species transport equations
Δx	- streamwise grid spacing
Δy	- spanwise grid spacing
Δz	- vertical grid spacing
Δz_w	- distance between the wall and center of first cell layer
$\Delta x^+ = (u_\tau \Delta x)/\nu_w$	- streamwise grid spacing in wall units
$\Delta y^+ = (u_\tau \Delta y)/\nu_w$	- spanwise grid spacing in wall units
$\Delta z^+ = (u_\tau \Delta z)/\nu_w$	- vertical grid spacing in wall units
$\Delta z_w^+ = (u_\tau \Delta z_w)/\nu_w$	- vertical grid spacing at the wall in wall units
ΔH	- heat of combustion
δ_f	- local vertical flame extension
θ	- angle from the horizontal
χ_{rad}	- radiative loss fraction
$\dot{\Omega}''_F$	- fuel mass reaction rate integrated across f(p)lume width

ΔH_{O_2}	- combustion heat release per unit mass of oxygen

Subscripts

w	- wall
∞	- freestream
p	- flame/plume
T	- thermal or temperature based
SGS	- Sub-Grid Scale
k	- species k

1: Introduction

Wildland fires can cause significant economic losses (e.g., because of suppression efforts and damage to property) and result in loss of life; and among other things, they can also affect people's health (through increased pollution) and their aftereffects can include flooding, erosion, debris flows and landslides. Unfortunately, the effects of wildland fires are expected to increase in the coming decades due to the changing climate [2, 3] and the ever increasing population.

Despite decades of research our current fundamental understanding of wildland fire spread is limited [4] because it involves a complex coupling between a large number of physical and chemical processes that happen over a wide range of length and time scales. Because of this the operational models [5] that are being used at present (e.g., FARSITE [6]), by fire managers for making predictions, often have limited accuracy. Accordingly, there is a need to enhance our fundamental understanding of wildland fire spread, which can subsequently help in improving the operational models and thus our ability to manage wildland fires in the future.

There are three major factors that influence wildland fire spread: fuel (fine or heavy, arrangement and continuity, fuel moisture etc.), topography (flat or sloped, aspect etc.) and weather (wind, temperature, relative humidity, precipitation etc.); see Figure 1.1. The present work is concerned with the effects of two key parameters, wind and slope, that can affect wildland fire spread substantially [7–9]. In this study

Figure 1.1: The fire behaviour triangle. Figure reproduced from [10].

the effects of wind and slope are studied separately i.e., either wind is considered or slope is considered, cases where both of them are present simultaneously are not studied. One of the primary reasons why wildland fire spread rate changes significantly because of changes in wind and/or slope is the resulting change in flame and plume geometry (which is what the present study is focused on): as wind and/or slope increases the flame and plume are pushed downstream (see e.g., Figures 1.2 and 1.3), closer to the fresh fuel (if any), which among other things, increases the convective heat transfer to the fresh fuel and hence the spread rate. The flame is considered to be the region with hot gases where combustion reactions and heat release are taking place whereas the plume is considered to be the region where the gas temperature is higher than ambient but there is no reaction.

The effects of wind on the flame and plume geometry have been studied theoretically, numerically and experimentally over the past several decades. Note that, theoretical work in this document refers to work that involves integral models (e.g., [13–16]) which in the end also require numerical solutions of their equations;

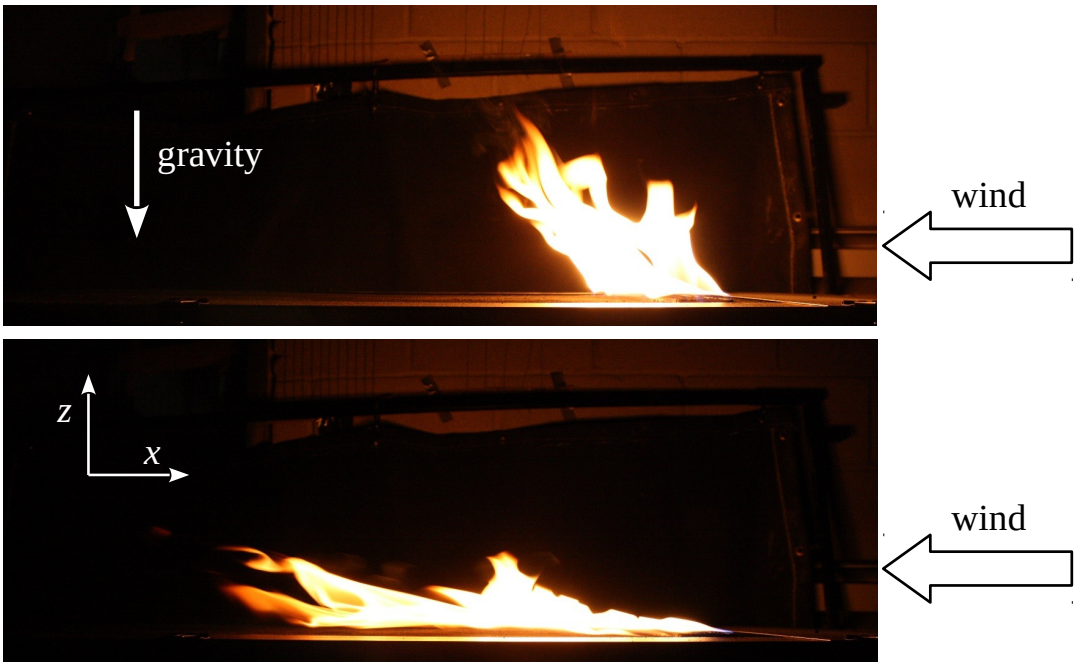

Figure 1.2: Line fire with cross-wind, side-view. In the top image buoyancy is dominant (hence the flame is mostly detached from the downstream surface), whereas in the bottom image cross-wind dominates the flow physics (hence the flame is mostly attached to the downstream surface). Figure adapted from [11].

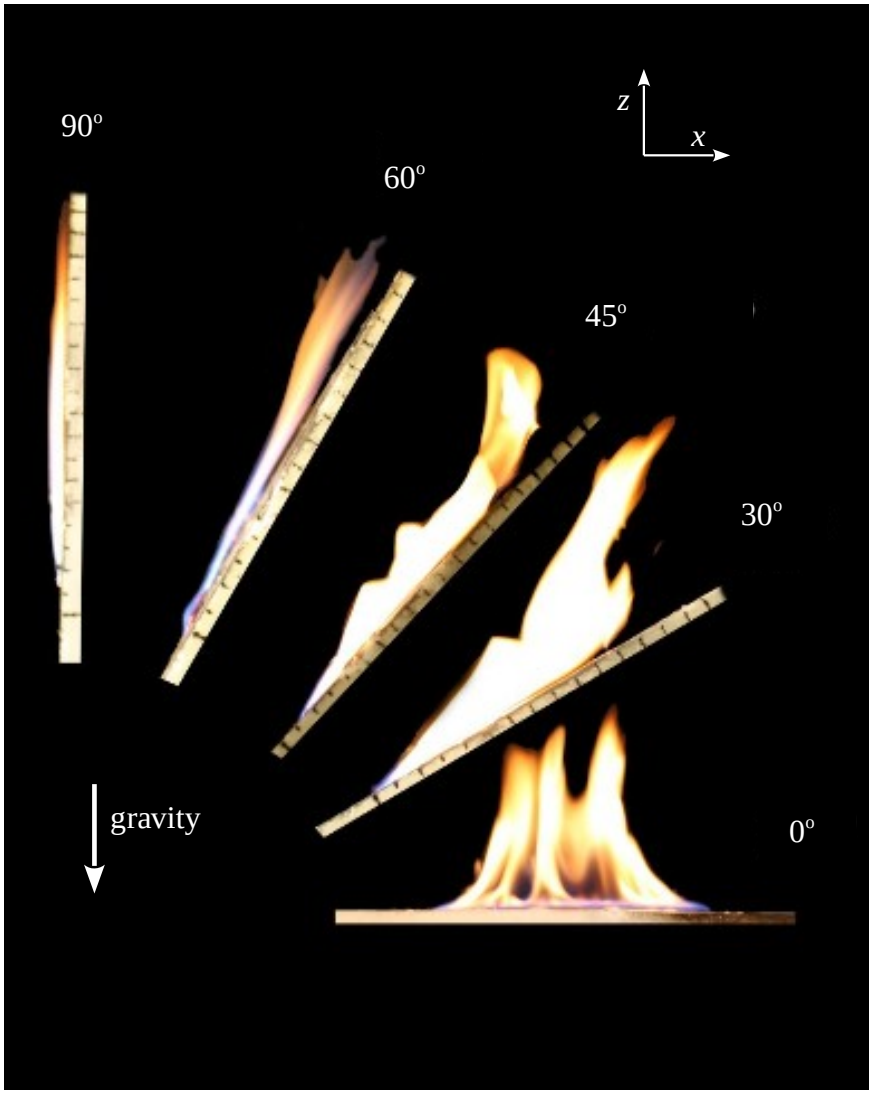

Figure 1.3: Effect of slope on the flame geometry. As the angle between the bottom surface and the horizontal plane increases a larger portion of the flame becomes attached to the downstream or upslope surface. Figure adapted from [12].

and numerical work in this document refers to CFD based work (e.g., [17–20]).

Before discussing some of the relevant work on the effects of cross wind on flame and/or plume geometry it is worth mentioning that the quantities of interest in these studies are flame/plume attachment length, height, length and tilt angle (see Figure 1.4 for a visualization of these quantities). Note that attachment length is sometimes called "flame drag" in the fire literature [21]. Most of the studies are concerned with time averaged values of these quantities but recently the dynamics has also started receiving some attention (see e.g., [22]). There is also a significant amount of interest in the transition from a buoyancy-dominated regime (in which the flame and plume are mostly detached from the downstream surface and have a tilted vertical shape; entrainment is two-sided; unburnt fuel experiences convective cooling; see the top picture in Figure 1.2) to a wind-dominated regime (in which the flame and plume are attached to the downstream surface; entrainment is one-sided; unburnt fuel experiences convective heating; see the bottom picture in Figure 1.2). This transition is generally considered to be controlled by Byram's convection number $N_C = (2Ig)/(\rho_\infty c_{p,\infty} T_\infty U_\infty^3)$ [23, 24]. See the nomenclature for the definition of notations.

As far as theoretical work is concerned; Hoult et al. [13] appear to be the first to have created a fairly complete theoretical or integral model for predicting the geometry of a turbulent plume in the presence of cross wind. Key assumptions made in this study are: the effects of turbulence in the cross-wind are not important; the wind direction is uniform; the profiles of different variables are self-similar and have a top-hat form; the shape of the plume is circular; entrainment

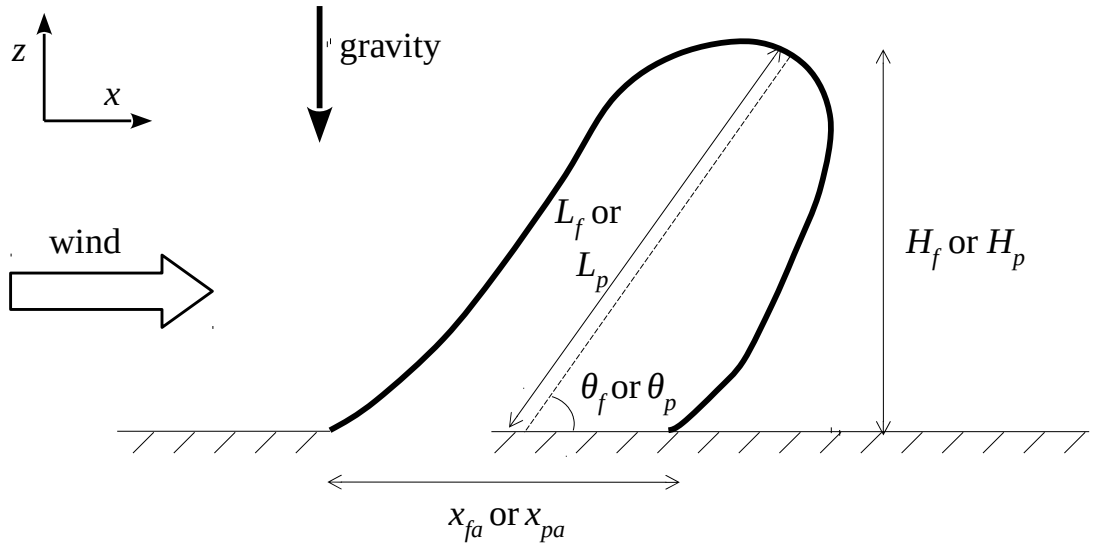

Figure 1.4: Geometrical parameters of a line flame or plume in cross-wind. Here, x_{fa}, H_f, L_f and θ_f (x_{pa}, H_p, L_p and θ_p) refer to flame (plume) attachment length, height, length and tilt angle, respectively.

rate is proportional to the difference between the plume velocity and the ambient velocity both in the direction parallel and perpendicular to the plume centerline, $u_e = \alpha|u_p - U_\infty \cos(\theta)| + \beta|U_\infty \sin(\theta)|$. Here, u_e is the entrainment velocity, u_p is the plume centerline velocity, θ is the angle that the plume centerline makes with the horizontal and α and β are entrainment coefficients. The model consists of six coupled ordinary differential equations ODEs (for mass, momentum in the direction parallel to the plume centerline, momentum in the direction perpendicular to the plume centerline, energy, x and z locations of the plume centerline) which are to be integrated along the plume centerline. Laboratory scale tests are conducted to determine α and β, which are found to be universal constants. The plume height predicted by the theory is found to be within 15% of the observed plume height

(which is about the uncertainty in the observations considered in this study). Some issues with this model are: this model invokes the Boussinesq approximation and can not handle large differences in density between the plume and the surrounding air, the model is not capable of describing combustion and radiation, and it is designed for circular plumes, as mentioned above.

Escudier [14] extended the integral model created by Hoult et al. [13], by removing the Boussinesq approximation and including the effects of combustion and radiation. To account for large density differences the author followed the idea by Ricou and Spalding [25] and scaled the entrainment velocity expression of Hoult et al. by $(\rho/\rho_\infty)^{1/2}$ and wrote it as $u_e = (\alpha|u_p - U_\infty \cos(\theta)| + \beta|U_\infty \sin(\theta)|)(\rho/\rho_\infty)^{1/2}$. Two reaction rate models are considered in this study and both of them produced similar results. One of the models is from Nielsen and Tao [26], which assumes that both reaction and mixing rates inside the plume are infinitely fast; this model has no model "constant". For radiation it is assumed that the heat loss from the edges of the plume to the environment is the dominant effect. Escudier's integral model has four equations (for the species; fuel, O_2, CO_2 and H_2O) in addition to the six equations in the Hoult et al. model. Plume trajectories, temperature profiles etc. predicted by the integral model for different cross-flow velocities are presented and discussed. Major issues with this study are: the model is again designed for circular plumes, the fuel jets considered in this study are momentum dominated (specifically in the flame zone) and are not relevant to fires which are buoyancy dominated, and the model is not validated in any way in this study.

Albini [15] developed an integral model for predicting the effect of wind on

the structure or geometry of a turbulent buoyant line fire. The entrainment idea exploited by Hoult et al. [13], Escudier [14] and many others is replaced by accretion in this model, which is assumed to be proportional to the cross-wind velocity, $u_e = \eta U_\infty$ (η is the entrainment coefficient). The reaction is considered to be mixing-controlled with the rate being proportional to the mean rate of strain. Radiation is neglected in this model. The model consists of four ODEs (for mass, x-momentum, z-momentum and fuel mass fraction) which are to be integrated along the vertical z-direction. Sample calculations for uniform cross-wind speed are performed and they suggest, among other things, that the flame tilt angle is nearly constant throughout the flame zone. This observation is then used to come up with an approximate expression for the flame tilt angle which suggests that the tangent of the tilt angle is proportional to the inverse of the square root of the Froude number based on flame height, $\tan(\theta) \propto (Fr = U_\infty^2/gH_f)^{-1/2}$, with the constant of proportionality dependent only on the choice of the flame tip temperature (a value of 500 K is used in this study for which the constant of proportionality is 3/2). Note that the tilt angle is measured from the vertical direction in [15] but it is measured from the horizontal plane in the present study. Flame height predicted by the model is found to be controlled by the product of the Froude number (based on the burner length or the burner dimension in the wind direction, D) and the ratio of the cross-wind velocity to the fuel injection velocity (w_0), $U_\infty^3/(gDw_0)$. Flame height variations are $\pm 30\%$ which if neglected suggest that the flame entrains around ten times the stoichiometric amount of air. The flame length reaches a minimum value with U_∞, which happens at $\theta \approx 35$ degrees. The minimum flame length is found to be $\propto I^{2/3}$.

The predicted mean flame height, tilt angle and length are found to be in reasonable agreement with the experimental data gathered by burning pine needle beds in a wind tunnel. Some of the issues with this study are: the model developed in this study is applicable only in the flame zone, by design this model will fail for lower wind velocities (this can be clearly seen in a recent paper by Nelson et al. [23]), limited amount of experimental data is used for model validation, an untested model is used for relating the fuel consumption rate with the rate of production of combustible volatiles and an unjustified assumption of 70% of wind being accreted in the flame is used.

Mercer and Weber [16] developed an integral model for describing, exclusively, the plume zone of wind-blown line fires. This model is heavily inspired by the Hoult et al. [13] model discussed above, the major difference being that this model is designed for line plumes. Being a plume zone model, this model requires the initial width, velocity and temperature of the plume above the flame zone; which can be either determined from experiments or from flame zone models like the one developed by Albini [15], discussed above. The model consists of six ODEs (for mass, momentum in the direction parallel to the plume centerline, momentum in the direction perpendicular to the plume centerline, energy, x and z locations of the plume centerline) which are to be integrated along the plume centerline. The equations are solved for different but uniform U_∞ values. The calculations clearly show that, away from the source, the plume trajectory is a straight line ($z \propto x$) or the plume angle is constant. Drawbacks of this study are: the model is only applicable away from the flame zone and no validation of the model is provided.

Putnam [27] experimentally studied the geometry of wind-blown line fires (which were created with a series of point sources). Fuel used in this study is natural gas. Photographs are used for quantifying the flame geometry. The flame height in this study is found to vary as $H_f/H_{f,0} = (1 + 4\mathrm{Fr}_0)^{-1/2}$ and the tangent of the flame tilt angle is found to be $\propto \mathrm{Fr}_0^{-1/2}$. Here, $\mathrm{Fr}_0 = (U_\infty^2/gH_{f,0})$ is the Froude number based on the flame height in the absence of wind, $H_{f,0}$. Note that $H_{f,0} \propto (I/(\rho_\infty c_{p,\infty} T_\infty \sqrt{g}))^{2/3}$, so $\mathrm{Fr}_0 \propto N_C^{-2/3}$ which suggests that $\tan(\theta) \propto N_C^{1/3}$. One of the issues with this study is that the line fire is created from point sources and does not represent an ideal line fire scenario.

Nelson et al. [23] recently used experimental data (22 wind aided pine litter fires in a laboratory and 32 field fires in southern rough and litter-grass fuels), theoretical models (including the one from Albini [15]) and regression techniques to come up with expressions for flame tilt angle and flame height. The two regimes (buoyancy- and wind-dominated), discussed above, are seen in most of the data: buoyancy-dominated for $N_C > 10$ and wind-dominated for $N_C < 10$. The tangent of the flame tilt angle is found to be $\propto N_C^{1/2}$ (if entrainment is assumed to be proportional to U_∞, following Albini [15]) and $\propto N_C^{1/3}$ (if entrainment is assumed to be proportional to the buoyant velocity $w_B = U_\infty N_C^{1/3}$) for $N_C < 10$. But for $N_C > 10$ the tangent of the tilt angle is $\propto N_C^{2/3}$. For field fires the tangent of the flame tilt angle is independent of N_C for all values of N_C. The flame height is found to be $\propto I^{2/3}$ with the constant of proportionality different for $N_C > 10$ and $N_C < 10$ for the laboratory fires.

Tang et al. [11] recently studied the structure of wind blown line fires pro-

duced using stationary gas burners. The authors observed the two flame regimes: buoyancy-dominated (for lower wind speeds) and wind-dominated (for higher wind speeds). As far as flame geometry is concerned the focus in this study was placed on the flame attachment length instead of flame height, length and tilt angle. The flame attachment length is found to be linearly correlated with the location where $\mathrm{Ri}_x = \mathrm{Gr}_x/\mathrm{Re}_x^2 = g\beta(T_f - T_\infty)x/U_\infty^2$ reaches a value of unity; $x_{fa}/D_H = 1.55 + 0.5(x_{\mathrm{Ri}_x=1}/D_H)$. Here, x is measured from the leading edge of a metal plate placed before the burner, β is the coefficient of thermal expansion, T_f is the flame temperature and D_H is the hydraulic diameter. In a subsequent study Tang et al. [22] studied the dynamics of wind blown line fires, again using stationary gas burners. With increasing wind velocity flames are found to extend further downstream from the mean flame position. The variance of the flame attachment length is found to be strongly correlated with $\mathrm{Fr}_{D_H}^{2/3}/Q^*$. Here, $\mathrm{Fr}_{D_H} = U_\infty^2/gD_H$ is the Froude number based on the hydraulic diameter of the gas burner, $Q^* = \dot{Q}/(\rho_\infty c_{p,\infty} T_\infty \sqrt{g} D_H^{2.5})$ is the non-dimensional heat release rate and $\dot{Q}$ is the heat release rate of the fire. One of the issues with these two studies is that the flames are small and not fully turbulent.

Porterie et al. [17] seem to be the first to apply classical CFD to a wind-blown buoyant plume. Some sample solutions with different ambient wind velocity profiles are presented in this study. The temperature distributions predicted by the model are in reasonable agreement with those predicted by the integral model of Mercer and Weber [16], discussed above. Velocity vectors are also presented which show reversed flow downstream of the plume. The model used in this study is not capable

of describing the flame zone; in addition, the effects of turbulence are completely ignored in the model. This model was later enhanced, by e.g., including the effects of turbulence through the RNG k-ϵ model and those of combustion through the EDC model [28]; and was used to study a wind-blown turbulent buoyant diffusion flame by the same group [18]. The authors saw the two flame regimes in their simulations: buoyancy-dominated (for lower values of U_∞) and wind-dominated (for larger values of U_∞). In the former regime large oscillations e.g., of the flame height are seen because of the puffing instabilities; whereas in the latter regime the flame is much more stable. Because of the RANS framework the model is only capable of describing mean flow fluctuations, fluctuations due to turbulence are not captured.

In a subsequent study from the same group [19], propagation of wind-blown line fires through fuel beds, corresponding to the experiments by Mendes-Lopez et al. [29], was studied using RANS simulations. Simulations with three wind velocities (1, 2, and 3 m/s) are performed. Again as the wind speed is increased the situation transitions from being buoyancy-dominated to wind-dominated. The predicted flame geometry (in terms of flame height, length and tilt angle) agrees satisfactorily with the experiment [29] for the 1 m/s case. For the 2 m/s case the simulations underpredict the flame height, length and tilt angle; it is argued that this is because of the 2D nature of the simulations in this study, which leads to over-attachment of the flame [30]. The 3 m/s case, in addition to the over attachment issue, never reached a quasi-steady state in the simulations. In addition to comparisons with the corresponding experiments [29] the authors also compared the predicted flame height, length and tilt angle for the three cases with the correlations available in

the literature. For the 1 m/s case the simulations overpredicted the angle and for the other two cases the angle was underpredicted. The flame height and length were underpredicted for all three cases when compared to the correlations. Again it was argued that this is due to the over-attachment in the simulations due their 2D nature.

Nmira et al. [20] used RANS simulations to study the geometry of stationary vegetation based line fires. Predicted values of flame height, length and tilt angle are in agreement with the data available in the literature. Results suggest that the flame length and height normalized with the flame depth D, scale with $\mathrm{Fr}_D = U_\infty^2/gD$ and the dimensionless heat release rate. Predicted streamlines are almost straight in the flame and plume zones suggesting that a far field analysis might be enough for determining the flame tilt angle. Such an analysis leads to the conclusion that the flame tilt angle should scale with Froude number based on the characteristic length scale of the plume $\mathrm{Fr}_{L_c} = U_\infty^2/gL_c$, where $L_c = (I/\rho_\infty c_{p,\infty} T_\infty \sqrt{g})^{2/3}$ which suggests that $\mathrm{Fr}_{L_c} \propto N_C^{-2/3}$. In terms of N_C this study suggests that the tangent of the flame tilt angle is $\propto N_C^{0.71(2/3)}$. The correlations proposed in this study are supported by both laboratory-scale and field scale experiments.

From the literature survey it appears that the effects of slope, on the flame and plume geometry, have received significantly less attention than the effects of wind. It also seems that most of attention in this scenario is given to the transition from the detached regime (in which the flame and plume are mostly detached from the downstream surface and are almost vertical in shape; entrainment is two-sided; unburnt fuel experiences convective cooling; see the 0 degrees case in Figure 1.3) to

the attached regime (in which the flame and plume are attached to the downstream surface; entrainment is one-sided; unburnt fuel experiences convective heating; see the cases with inclination ≥ 45 degrees in Figure 1.3). Again most of the times the flame and plume geometry is analyzed in the mean sense and no heed is paid to the dynamics.

Theoretical work for this configuration is almost non-existent, probably because the change in flame and plume geometry in this configuration happens because of an imbalance in entrainment on the two sides of the flame/plume, due to the inclination of the bottom surface, which may not be straightforward to include in a 1D integral model framework. As far as experimental and numerical studies are concerned the effect of slope on a fire attracted significant amount of attention (albeit the configuration in most of these studies contains side walls) because of the King's Cross fire in 1987 which spread rapidly and killed 31 people and injured several more. Subsequent investigations [31–33] revealed that if the inclination angle is above a certain critical value then the flame and/or plume get(s) attached to the downstream surface and the rate of spread increases dramatically. Note that the flame/plume attachment phenomenon is called "trench effect" in the papers related to this event. Roughly a decade ago the wildland fire community also started paying attention to the transition from a detached regime to an attached regime [34, 35].

Wu et al. [36] used a schlieren system to analyze the effects of slope on the geometry of a line fire produced using a stationary gas burner. They found that the plume attachment length increases sharply when the slope is increased beyond 24 degrees (which is the critical angle). Critical angle is found not to change sig-

nificantly with heat release rate of the fire and also with the downstream surface conditions (adiabatic or isothermal). However, the flames considered in this study are small, 1 to 3 kW, and are not turbulent.

Morandini et al. [37] recently performed experiments on a porous bed of excelsior in a large-scale facility with two slopes (0 and 30 degrees) and three fuel loads. They used PIV, recorded video images and measured heat flux and temperature. In the 0 degrees case: the plume is quasi-vertical, characterized by equal entrainment from both sides of the flame, which leads to convective cooling of the fuel ahead of the fire. In the 30 degrees case: the plume is tilted towards the downstream surface, entrainment on the burnt side was found to increase significantly, in addition the flow on the unburnt side was found to be in the same direction as the fire direction and detached at a certain characteristic distance from the fire. The periodical bursts of flame were also identified as a mechanism by which convective heating occurred, far downstream of the flame, and increased the spread rate in the 30 degrees slope case.

The numerical study by Woodburn and Drysdale [38] included 2D RANS simulations of a fire on an inclined plane, which is a configuration that is quite relevant to the present study. The primary objective behind these 2D simulations was to find out the critical inclination angle above which the flame and plume remain completely attached to the downstream surface. The predicted critical angle was 10 degrees which seemed correct based on some of the experiments reported in [39], that were close to this 2D configuration.

Overall, the literature survey suggests that there is at present no theoretical

or integral model that can describe the effects of wind on both the flame and plume geometries of a turbulent buoyant line fire. This study aims to fill that gap. A theoretical framework is needed because e.g., with the help of some assumptions it can provide considerable insights into the scaling of some of the geometrical parameters [13, 14], specifically the tilt angle (Figure 1.4). And expressions provided by such a theoretical model are expected to be more versatile than the expressions that have appeared in the literature over the past several decades (some of which were discussed above).

The literature survey also suggests that the past experimental studies typically use a limited range of diagnostics, primarily video imaging and temperature measurements, while past numerical (or CFD) studies typically use a lower-order approach, RANS simulations, that does not resolve the relevant turbulent flow and flame scales. Thus, an understanding of the effects of wind and slope on the dynamics of the flame and plume geometries of a turbulent buoyant line fire is lacking. Filling this gap is one of the goals of this study. For doing so we perform well- and wall-resolved LES of turbulent, buoyant, methane-fueled, stationary line flames in the presence of cross-wind and slope. In addition to shedding light on flame and plume geometry dynamics, these simulations provide extensive data for validation and calibration of the integral model discussed above.

En route to accomplishing the aforementioned goals (related to the wildland fire spread problem) we have also attempted to fill in the following gaps in the fire and CFD (more precisely, OpenFOAM) literatures. First, higher order validation of LES for fire simulations, using a co-flow stabilized turbulent buoyant line fire. The

point is that while several successful LES based validation studies have been reported in the fire literature, see e.g., [40–43] for pool fire based investigations, in most such studies, comparisons are limited to first and second order moments or sometimes even to first order moments [40, 43], which are insufficient for proper validation of an approach like LES. Additionally, the investigated flames are in some cases not fully turbulent and are not practically relevant. Finally, most studies feature coarse LES simulations [41] and hence have room for improvement.

Second, a better understanding of the convection schemes available in the OpenFOAM library. Despite OpenFOAM's large user base and its object oriented open-source nature, understanding its various elements (e.g., solvers, boundary conditions and numerical schemes) is far from trivial probably because many of its parts are developed on the fly and never documented (e.g., the extra undocumented term in OpenFOAM's PISO algorithm [44]) and also because of the huge size of the code. Accordingly, over the past several years many researchers have worked on the description and assessment of the different elements of OpenFOAM, see e.g., [45, 46]; work of this kind has attracted a lot of attention. During the course of this study it became clear that there is a need for a better description and assessment of some of the most popular convection schemes in OpenFOAM.

1.1 Thesis outline

This thesis is organized as follows. In Chapter 2 the numerical aspects are discussed. First, a brief description of the governing equations is provided, then a description and assessment of some of the most popular convection schemes in

OpenFOAM is presented, followed by the description and assessment of time integration schemes. After that the turbulence models invoked in the present study are discussed briefly. The combustion model is presented first and then the radiation model.

In Chapter 3 a higher order validation of our numerical methodology is presented. Well resolved LES of a co-flow stabilized, methane-fueled, turbulent, buoyant, line fire (in the absence of cross-wind or slope effects) are considered in this chapter. In addition to comparisons of mean vertical velocity profiles with the correlations in the literature and comparisons of mean and *rms* temperature profiles with experimental data; integral time scales and temperature Probability Density Functions (PDFs) are also compared with those measured in the measurements.

Chapter 4 considers the effects of cross wind on the flame and plume geometry of a turbulent buoyant line fire. Well- and wall-resolved LES of a turbulent, buoyant, methane-fueled, stationary, line flame are presented in this chapter. In addition to the mean flame and plume geometry, the flame dynamics are also studied. An integral model that is applicable both in the flame and plume zones of a turbulent, buoyant, line fire in cross-wind is also presented. Finally, detailed comparisons between the integral model and LES are made.

Chapter 5 discusses the effects of slope on the geometry of a turbulent buoyant line fire. Well- and wall-resolved LES of a turbulent, buoyant, methane-fueled, stationary, line flame are considered in this chapter. In addition to the mean flame and plume geometry, the flame dynamics are also studied.

Finally, in Chapter 6 the present study is summarized and future work is

discussed.

2: FireFOAM (OpenFOAM)

All the simulations in the present study are performed using FireFOAM [47], which is based on the OpenFOAM CFD library [48]. OpenFOAM has attracted a lot of attention in the past decade (both from the academia and the industry) due, primarily, to the following main features:

- Open access to its source code.
- Ease of extensibility due to object oriented C++ [49]; which is of paramount importance, especially in a research environment as new models, solvers, and boundary-conditions can be implemented fairly easily.
- Availability of a number of advanced models for describing multi-physics flow problems (e.g., models for describing turbulence, combustion, heat transfer, multiple phases).
- Ability to handle polyhedral meshes; which makes it fairly straightforward to transition from simulations of canonical/academic problems to simulations of practical devices/problems.
- Good scalability up to 1000s of processors.
- Absence of licensing cost (a major factor for the industry).
- Wide range of ready-made pre- and post-processing utilities.

FireFOAM is an LES based fire dynamics solver that uses Favre-filtered compressible Navier-Stokes equations [50] (see Section 2.1) and provides additional models for the treatment of turbulent reactive flows [51], solid fuel pyrolysis [52], soot radiation [53] and transport of liquid water sprays and surface wetting [54].

Next, the governing equations relevant to FireFOAM (and LES) are presented. Then some of the convection schemes available in OpenFOAM are described and assessed. The OpenFOAM temporal schemes are also detailed and evaluated. Turbulence models invoked in this study are then discussed, followed by a description of the combustion model used in the present work. Finally, the radiation model leveraged in the present study is described.

2.1 Governing equations

Favre-filtered mass, momentum, sensible enthalpy and species equations [50], solved by FireFOAM, are written below:

Mass:

$$\frac{\partial \overline{\rho}}{\partial t} + \frac{\partial (\overline{\rho}\widetilde{u}_j)}{\partial x_j} = 0 \tag{2.1}$$

Momentum:

$$\frac{\partial (\overline{\rho}\widetilde{u}_i)}{\partial t} + \frac{\partial (\overline{\rho}\widetilde{u}_i\widetilde{u}_j)}{\partial x_j} = -\frac{\partial \overline{p}}{\partial x_i} + \frac{\partial}{\partial x_j}\left(\overline{\rho}(\nu + \nu_{SGS})\left(\frac{\partial \widetilde{u}_i}{\partial x_j} + \frac{\partial \widetilde{u}_j}{\partial x_i} - \frac{2}{3}\frac{\partial \widetilde{u}_k}{\partial x_k}\delta_{ij}\right)\right) + \overline{\rho} g_i \tag{2.2}$$

Sensible enthalpy:

$$\frac{\partial \left(\overline{\rho}\widetilde{h}_s\right)}{\partial t} + \frac{\partial (\overline{\rho}\widetilde{u}_j\widetilde{h}_s)}{\partial x_j} = \frac{\mathrm{D}\overline{p}}{\mathrm{D}t} + \frac{\partial}{\partial x_j}\left(\overline{\rho}\left(\alpha + \frac{\nu_{SGS}}{\mathrm{Pr}_{SGS}}\right)\frac{\partial \widetilde{h}_s}{\partial x_j}\right) + \overline{\dot{\omega}_{h_s}^{'''}} - \overline{\dot{q}_r^{'''}} \tag{2.3}$$

Species mass fraction:

$$\frac{\partial\left(\overline{\rho}\widetilde{Y}_k\right)}{\partial t}+\frac{\partial(\overline{\rho}\widetilde{u}_j\widetilde{Y}_k)}{\partial x_j}=\frac{\partial}{\partial x_j}\left(\overline{\rho}\left(D_{Y_k}+\frac{\nu_{SGS}}{\mathrm{Sc}_{SGS}}\right)\frac{\partial\widetilde{Y}_k}{\partial x_j}\right)+\overline{\dot{\omega}'''_{Y_k}} \tag{2.4}$$

where $\tilde{}$ is the Favre filter operator and δ_{ij} refers to the Kronecker delta symbol. The filtered chemical source terms, $\overline{\dot{\omega}'''_{Y_k}}$, and the volumetric heat release rate (HRR), $\overline{\dot{\omega}'''_{h_s}}$, require closure modeling. In this study, an Eddy dissipation Concept (EDC) model (Section 2.5) is used to estimate the chemical source terms, $\overline{\dot{\omega}'''_{Y_k}}$, and the volumetric heat release rate (HRR), $\overline{\dot{\omega}'''_{h_s}}$. The radiation source term, $\overline{\dot{q}'''_r}$, will be described in the radiation section (2.6). The Lewis number is defined as:

$$\mathrm{Le}_k=\frac{\alpha}{D_{Y_k}}=\frac{\text{thermal diffusivity}}{\text{mass diffusivity of species } k} \tag{2.5}$$

We assume $\mathrm{Le}_k=1$.

A combination of the PISO and SIMPLE solution algorithms, referred to as PIMPLE in the OpenFOAM framework, is used for handling pressure velocity coupling. Additional information about the iteration procedure can be found in [55].

We now focus our attention on the description and assessment of some of the convection schemes in OpenFOAM.

2.2 Convection schemes

One of the more important aspects in the numerical procedure for solving the equations presented in Section 2.1 is the discretization of the convective term (the second term on the left hand side of Equations 2.2 to 2.4).

Discretization of the convective term has already been discussed extensively in the literature. Some of the schemes that were developed, but never reported,

by the developers of OpenFOAM, have also been described (albeit briefly) in the literature in recent years (see e.g., [56–58]). Nevertheless, some of the convection schemes available in OpenFOAM are discussed in the following because during the course of this study:

- Implementation of one of the most thoroughly described and frequently used schemes in OpenFOAM (the Gamma scheme [59]) was found to be bugged.
- A couple of widely used schemes in the context of OpenFOAM (limitedLinear and linearUpwind schemes) were found to be incorrectly described in the OpenFOAM documentation [58].
- It was found that the description of one of the schemes in OpenFOAM (i.e., filteredLinear2) that has been used for the past several years in the author's present group [43, 60, 61] has been far from satisfactory so far (see e.g., [62]).

In the cell-centred, finite-volume (or OpenFOAM) framework [46] the problem of discretization of the convective term $(\partial(u_j\phi)/\partial x_j)$ in the transport equation for a scalar ϕ boils down to finding the value of ϕ at the face (ϕ_f) using information available in the neighboring cells. On uniform meshes; most of the relevant schemes that are up to second order accurate, require only the values of ϕ; in the upwind (C), downwind (D) and far-upwind (U) cells (see Figure 2.1 for an illustration of the arrangement of cells with respect to the face under consideration).

One convenient framework for analyzing convection schemes, in situations represented by Figure 2.1, is the Normalized Variable Diagram (NVD) framework

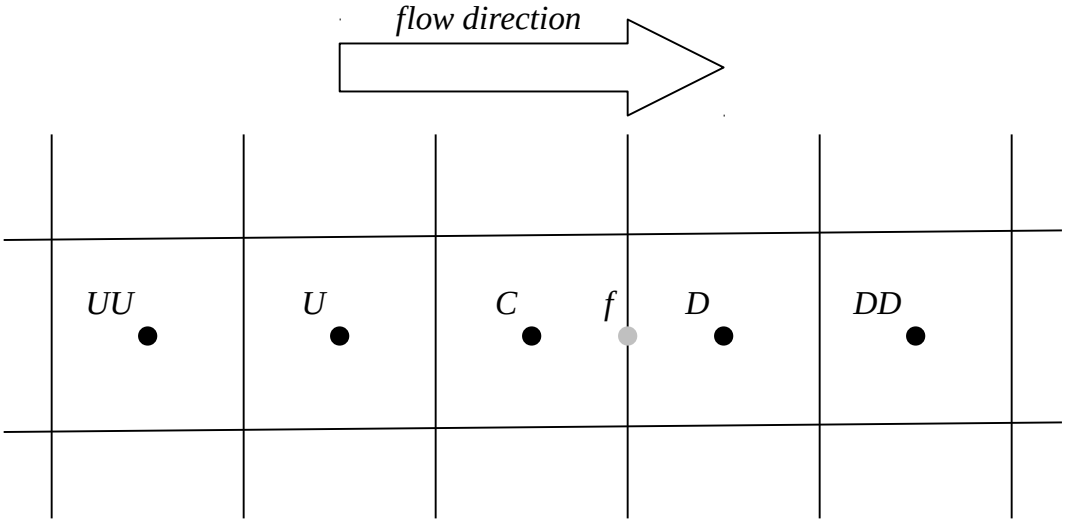

Figure 2.1: A schematic showing a face f and the neighboring cells, on a uniform mesh, used in constructing convection schemes. Most of the schemes in OpenFOAM can be represented with local information at the upwind (C), downwind (D) and far-upwind cells (U).

[46, 63, 64]; in which the variable ϕ is normalized as follows:

$$\widetilde{\phi} = \frac{\phi - \phi_U}{\phi_D - \phi_U} \tag{2.6}$$

With this normalization, any scheme that needs only the values of ϕ in cells C, D and U for evaluating ϕ_f can be written in the following manner:

$$\widetilde{\phi}_f = f(\widetilde{\phi}_C) \tag{2.7}$$

with

$$\widetilde{\phi}_C = \frac{\phi_C - \phi_U}{\phi_D - \phi_U} \tag{2.8}$$

and

$$\widetilde{\phi}_f = \frac{\phi_f - \phi_U}{\phi_D - \phi_U} \tag{2.9}$$

As a consequence, all such schemes can be straightforwardly described by plotting $\widetilde{\phi}_f$ as a function of $\widetilde{\phi}_C$ (with the ensuing plot being called the NVD diagram). The region on an NVD diagram which corresponds to bounded behaviour, and called the Convection Boundedness Criterion (CBC), is well-known [46, 59, 64]; which makes it easy to see which scheme possesses boundedness and which one does not (the CBC is presented in Figure 2.2, see [46] for details on the CBC). Accordingly, the NVD framework will be used in the following, whenever possible.

Discussion of all the schemes in OpenFOAM is beyond the scope of the present study. Only five schemes are presented (*linearUpwind*, *LUST*, *Gamma*, *limitedLinear* and *filteredLinear2*): some because they are commonly invoked and some because of their relevance to the author's present group.

We will start with the *linearUpwind* scheme, followed by the Linear-Upwind Stabilised Transport (*LUST*) scheme. Then the *Gamma* scheme will be discussed

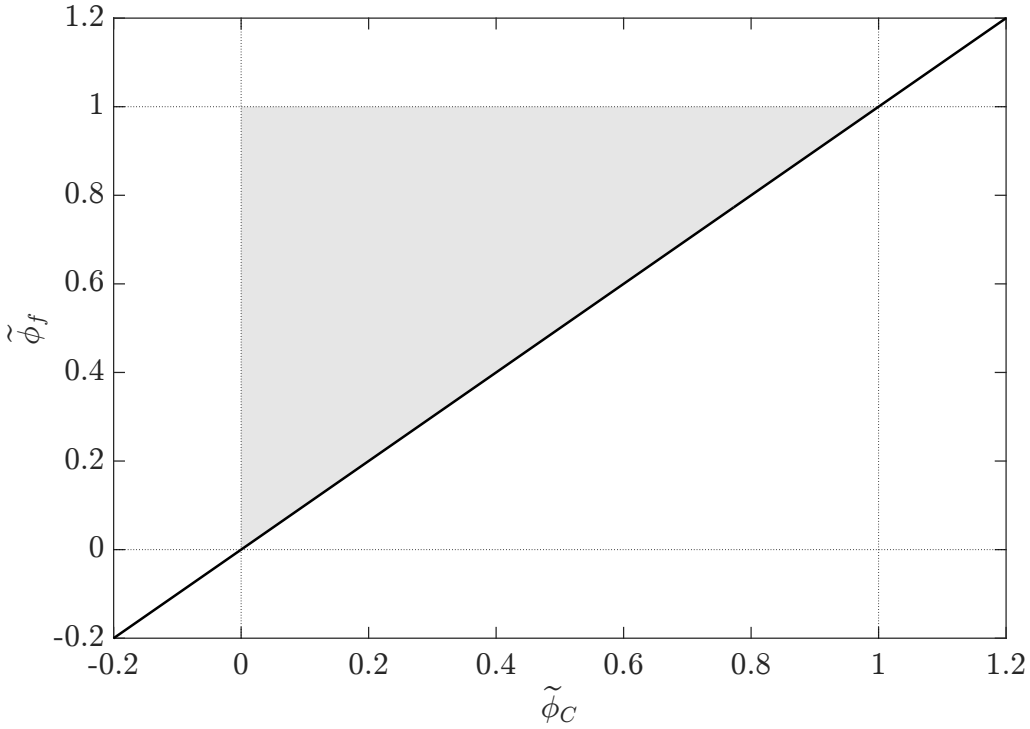

Figure 2.2: The Convection Boundedness Criterion (CBC), colored with grey, on the NVD diagram. It includes the line ($\widetilde{\phi}_f = \widetilde{\phi}_C$).

after which the *limitedLinear* scheme will be delineated. Finally, the *filteredLinear2* scheme will be presented.

2.2.1 *linearUpwind scheme*

The *linearUpwind* scheme implemented in OpenFOAM operates as follows:

$$\phi_f = \phi_C + \mathbf{r} \cdot (\nabla\phi)_C \tag{2.10}$$

where $\mathbf{r}$ denotes the vector connecting the center of the upwind cell C with the center of the face f (where the value of ϕ is being evaluated) and $(\nabla\phi)_C$ is the gradient of ϕ at the center of the upwind cell C.

For a uniform grid and "central difference" approximation of $(\nabla\phi)_C$; Equation 2.10 becomes:

$$\phi_f = \phi_C + \frac{1}{4}\phi_D - \frac{1}{4}\phi_U \tag{2.11}$$

which after normalization [63, 64] can be expressed as:

$$\widetilde{\phi}_f = \widetilde{\phi}_C + \frac{1}{4} \tag{2.12}$$

Equations 2.11 and 2.12 clarify that the OpenFOAM *linearUpwind* scheme (when combined with central differencing for evaluation of the gradient) corresponds to the FROMM scheme [46] and not to the Second Order Upwind (SOU) scheme, as has been (incorrectly) alluded to in the OpenFOAM Documentation [58]. It is worth mentioning, however, that for "backward difference" approximation of the gradient (which is rarely, if ever, used to the best of the present author's knowledge) the *linearUpwind* scheme indeed reduces to the SOU scheme (Equations 2.13 and 2.14).

$$\phi_f = \frac{3}{2}\phi_C - \frac{1}{2}\phi_U \tag{2.13}$$

$$\widetilde{\phi}_f = \frac{3}{2}\widetilde{\phi}_C \tag{2.14}$$

The *linearUpwind* scheme (Equation 2.12) is presented on the NVD diagram in Figure 2.3, along with the SOU scheme (Equation 2.14). As is well-known these schemes do not satisfy the CBC. Since the *linearUpwind* scheme is closer to the *linear* scheme (or the central difference scheme) as compared to the SOU scheme, it is expected to be less dissipative than the SOU scheme.

We will now turn to the discussion of the $LUST$ scheme.

2.2.2 Linear-Upwind Stabilised Transport (LUST) scheme

The Linear-Upwind Stabilised Transport ($LUST$) scheme is simply a blend of the *linear* (or central difference) and *linearUpwind* (or FROMM) schemes. The version available in OpenFOAM has a hard-coded 75 (25) percent contribution from the former (latter); which is recommended in [65]. Accordingly, this scheme is given as:

$$\phi_f = 0.75(f_x\phi_C + (1 - f_x)\phi_D) + 0.25(\phi_C + \mathbf{r} \cdot (\nabla\phi)_C) \tag{2.15}$$

where f_x represents the mesh non-uniformity in the direction of the vector $\mathbf{r}$. For uniform grids (for which $f_x = 1/2$) and "central difference" approximation of $(\nabla\phi)_C$, Equation 2.15 becomes:

$$\phi_f = \frac{10}{16}\phi_C + \frac{7}{16}\phi_D - \frac{1}{16}\phi_U \tag{2.16}$$

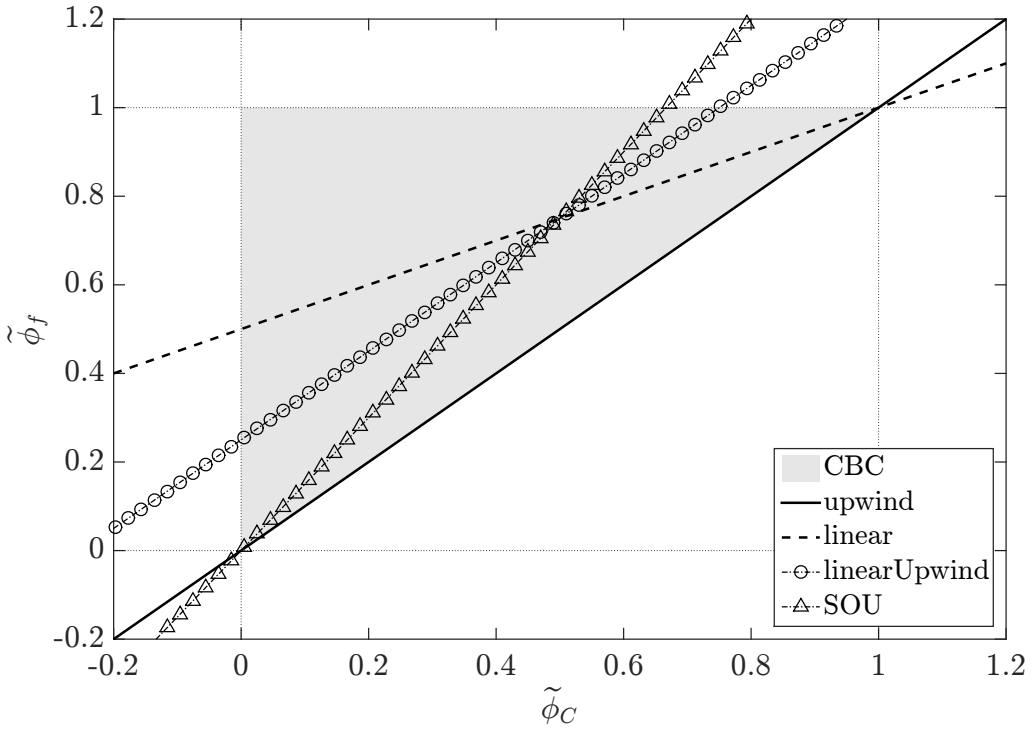

Figure 2.3: The *linearUpwind* scheme, along with the Second Order Upwind (SOU) scheme, on the NVD diagram. For reference the *upwind* and *linear* schemes are also presented. The light grey region is the Convection Boundedness Criterion (CBC), which includes the upwind line ($\widetilde{\phi}_f = \widetilde{\phi}_C$).

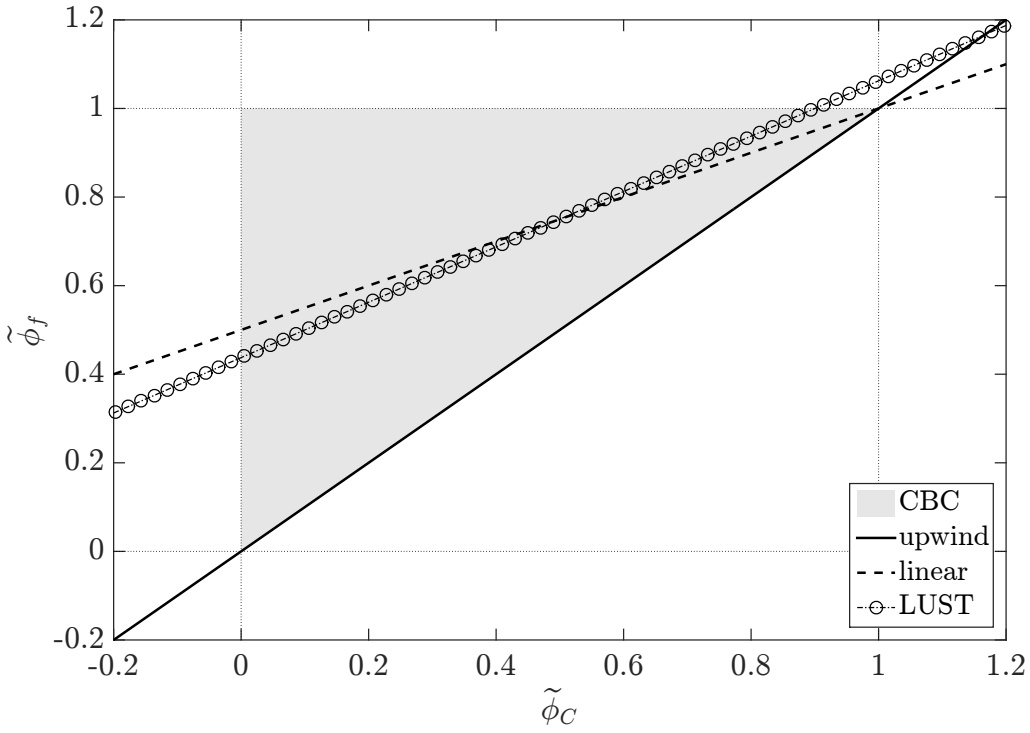

Figure 2.4: The Linear-Upwind Stabilised Transport ($LUST$) scheme on the NVD diagram. For reference the *upwind* and *linear* schemes are also presented. The light grey region is the Convection Boundedness Criterion (CBC), which includes the upwind line ($\widetilde{\phi}_f = \widetilde{\phi}_C$).

which after normalization gives:

$$\widetilde{\phi}_f = \frac{10}{16}\widetilde{\phi}_C + \frac{7}{16} \tag{2.17}$$

This scheme is presented on the NVD diagram in Figure 2.4: as expected, it does not satisfy CBC; and is quite close to the *linear* scheme.

In the context of OpenFOAM, the $LUST$ scheme has been used quite successfully by various independent groups [57, 65–67] for performing LES.

Next, we will consider the *Gamma* scheme.

2.2.3 *Gamma scheme*

The *Gamma* scheme [59], which by design satisfies the CBC, is one of the more popular schemes in the OpenFOAM library. It blends the *upwind* and *linear* schemes, and works as follows:

$$\phi_f = \begin{cases} (1-\gamma(1-f_x))\phi_C + \gamma(1-f_x)\phi_D & 0 < \widetilde{\phi}_C < \dfrac{k}{2} \\ f_x\phi_C + (1-f_x)\phi_D & \dfrac{k}{2} \leq \widetilde{\phi}_C < 1 \\ \phi_C & \text{elsewhere} \end{cases} \tag{2.18}$$

where $\gamma = (2\widetilde{\phi}_C/k)$ is the blending factor and k is a factor specified by the user (to be discussed later). In Equation 2.18, $\widetilde{\phi}_C$ is evaluated using the following expression, which is valid for complex meshes (see [59] for details).

$$\widetilde{\phi}_C = 1 - \frac{\phi_D - \phi_C}{2(\nabla\phi)_C \cdot \mathbf{d}} \tag{2.19}$$

with $\mathbf{d}$ denoting the vector connecting the center of the upwind cell C with the center of the downwind cell D.

When uniform grids are considered, Equation 2.18 reduces to the following form:

$$\phi_f = \begin{cases} (1-\dfrac{\gamma}{2})\phi_C + \dfrac{\gamma}{2}\phi_D & 0 < \widetilde{\phi}_C < \dfrac{k}{2} \\ \dfrac{1}{2}\phi_C + \dfrac{1}{2}\phi_D & \dfrac{k}{2} \leq \widetilde{\phi}_C < 1 \\ \phi_C & \text{elsewhere} \end{cases} \tag{2.20}$$

Finally, after approximating $(\nabla\phi)_C$ (in Equation 2.19) through central differencing, substituting the resulting expression for γ, and normalization, we find the following

form for the Gamma scheme:

$$\widetilde{\phi}_f = \begin{cases} -\dfrac{\widetilde{\phi}_C^2}{k} + \left(1 + \dfrac{1}{k}\right)\widetilde{\phi}_C & 0 < \widetilde{\phi}_C < \dfrac{k}{2} \\ \dfrac{1}{2}\widetilde{\phi}_C + \dfrac{1}{2} & \dfrac{k}{2} \leq \widetilde{\phi}_C < 1 \\ \widetilde{\phi}_C & \text{elsewhere} \end{cases} \tag{2.21}$$

The user specified factor k, which can only take values between 0 and 1, controls the transition between *upwind* and *linear* schemes: lower values of k correspond to a faster transition, with $k = 0$ leading to the bounded linear (or central difference) scheme [46]. The effect of k is illustrated in Figure 2.5, which presents the *Gamma* scheme (Equation 2.21) on the NVD diagram for $k = 1$ and 0.2.

Note that the factor k used here is twice the factor β_m ($k = 2\beta_m$) used in [59]. Furthermore, in [59] the user is recommended not to use $\beta_m < 0.1$ (or $k < 0.2$) because doing so was found to introduce the "switching" instability due to an abrupt transition from the *upwind* scheme to the *linear* scheme. As will be discussed later, we experienced the same unstable behaviour.

Based on the present author's inspection of the code it seems that the implementation of this scheme in OpenFOAM is bugged and the implemented version works as follows (in terms of normalized variables):

$$\widetilde{\phi}_f = \begin{cases} -\dfrac{\widetilde{\phi}_C^2}{k} + \left(1 + \dfrac{1}{k}\right)\widetilde{\phi}_C & 0 < \widetilde{\phi}_C < \dfrac{k}{2} \\ \dfrac{1}{2}\widetilde{\phi}_C + \dfrac{1}{2} & \dfrac{k}{2} \leq \widetilde{\phi}_C \\ \widetilde{\phi}_C & \text{elsewhere} \end{cases} \tag{2.22}$$

Figure 2.6 presents Equations 2.21 and 2.22, for $k = 0.2$, on the NVD diagram. Clearly, the implemented version does not satisfy the CBC (because $\widetilde{\phi}_f \neq \widetilde{\phi}_C$ for

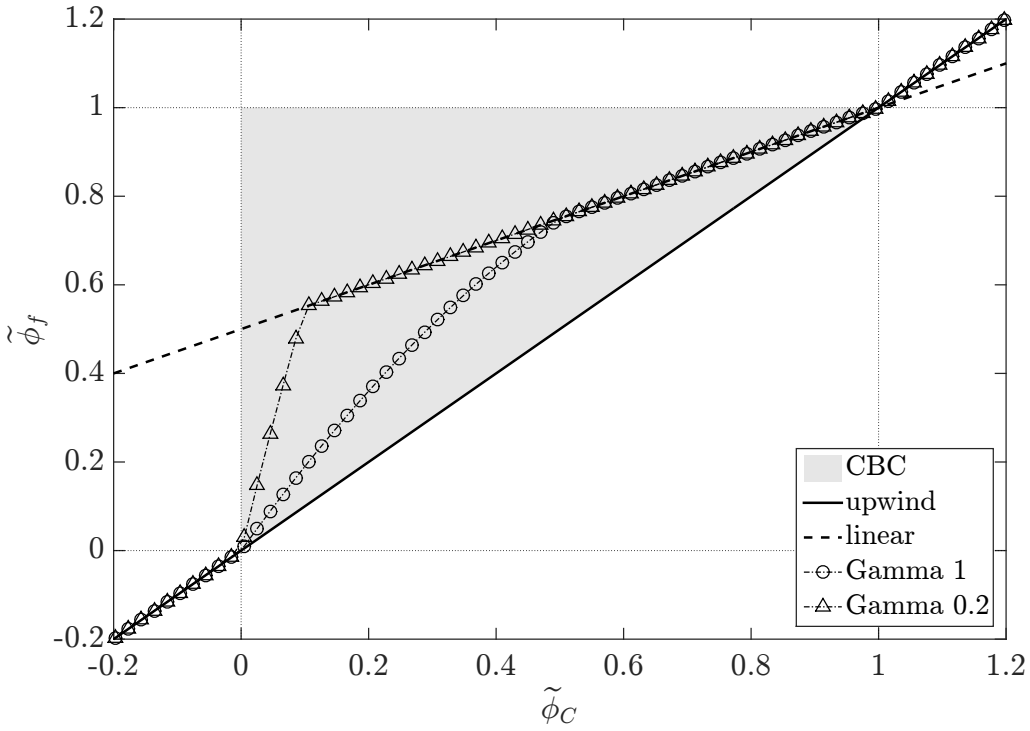

Figure 2.5: The *Gamma* scheme on the NVD diagram for $k = 1$ and 0.2. For reference the *upwind* and *linear* schemes are also presented. The light grey region is the Convection Boundedness Criterion (CBC), which includes the upwind line ($\widetilde{\phi}_f = \widetilde{\phi}_C$).

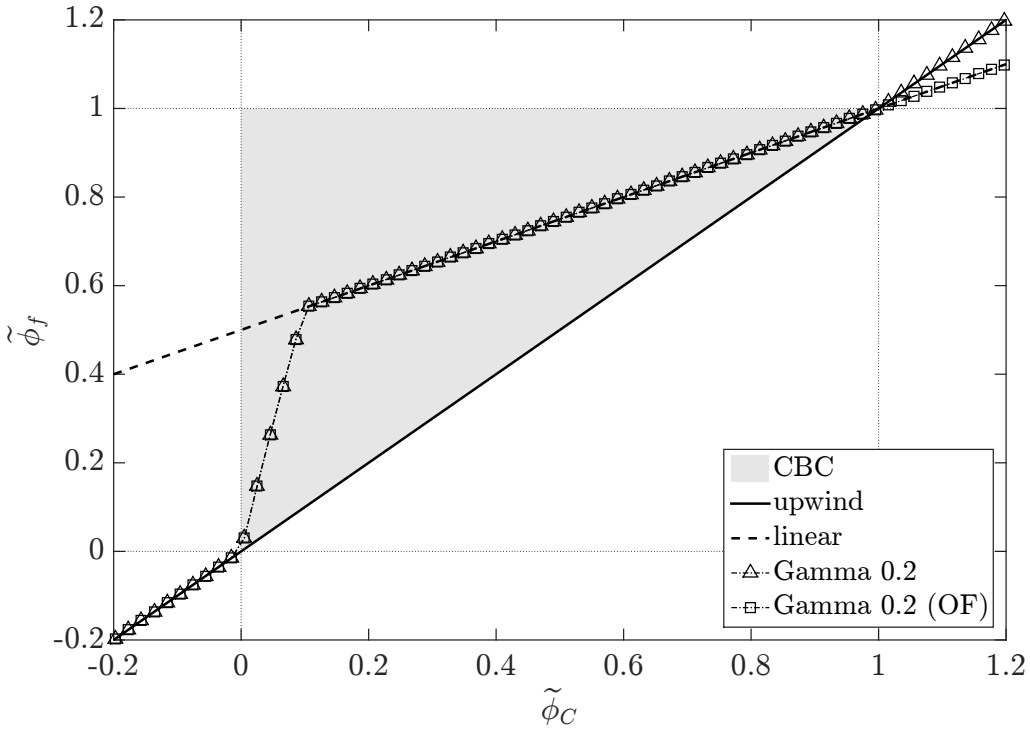

Figure 2.6: The two versions of the *Gamma* scheme (first, proposed in [59] and second, implemented in OpenFOAM) on the NVD diagram for $k = 0.2$. Note the difference between the two schemes for $\widetilde{\phi}_C > 1$. For reference the *upwind* and *linear* schemes are also presented. The light grey region is the Convection Boundedness Criterion (CBC), which includes the upwind line ($\widetilde{\phi}_f = \widetilde{\phi}_C$).

$\widetilde{\phi}_C > 1$), which could be the reason behind some of the dispersion related issues reported in the literature with this scheme in OpenFOAM (see e.g., [68, 69]).

In the next section we will discuss the *limitedLinear* scheme.

2.2.4 *limitedLinear scheme*

The *limitedLinear* scheme is another very popular scheme in the context of OpenFOAM, which is again a blend of the *upwind* and *linear* schemes, and satisfies

the CBC by design. It works as follows:

$$\phi_f = \begin{cases} (1 - \frac{2r}{k}(1 - f_x))\phi_C + \frac{2r}{k}(1 - f_x)\phi_D & 0 < r < \frac{k}{2} \\ f_x\phi_C + (1 - f_x)\phi_D & \frac{k}{2} \leq r \\ \phi_C & \text{elsewhere} \end{cases} \tag{2.23}$$

where r is expressed as:

$$r = \frac{2(\nabla\phi)_C \cdot \mathbf{d}}{\phi_D - \phi_C} - 1 \tag{2.24}$$

The factor k will be discussed later. For uniform grids Equation 2.23 takes the following form:

$$\phi_f = \begin{cases} (1 - \frac{r}{k})\phi_C + \frac{r}{k}\phi_D & 0 < r < \frac{k}{2} \\ \frac{1}{2}\phi_C + \frac{1}{2}\phi_D & \frac{k}{2} \leq r \\ \phi_C & \text{elsewhere} \end{cases} \tag{2.25}$$

After invoking a "central difference" approximation for $(\nabla\phi)_C$ and normalization, Equation 2.23 becomes:

$$\widetilde{\phi}_f = \begin{cases} \left(1 + \frac{1}{k}\right)\widetilde{\phi}_C & 0 < \widetilde{\phi}_C < \frac{k}{2+k} \\ \frac{1}{2}\widetilde{\phi}_C + \frac{1}{2} & \frac{k}{2+k} \leq \widetilde{\phi}_C < 1 \\ \widetilde{\phi}_C & \text{elsewhere} \end{cases} \tag{2.26}$$

Similar to the *Gamma* scheme, the factor k in this scheme is specified by the user and controls the transition from the upwind scheme to the linear scheme; with lower values leading to a faster transition and $k = 0$ leading to the bounded linear (or central difference) scheme. Again k can only take values between 0 and 1 in

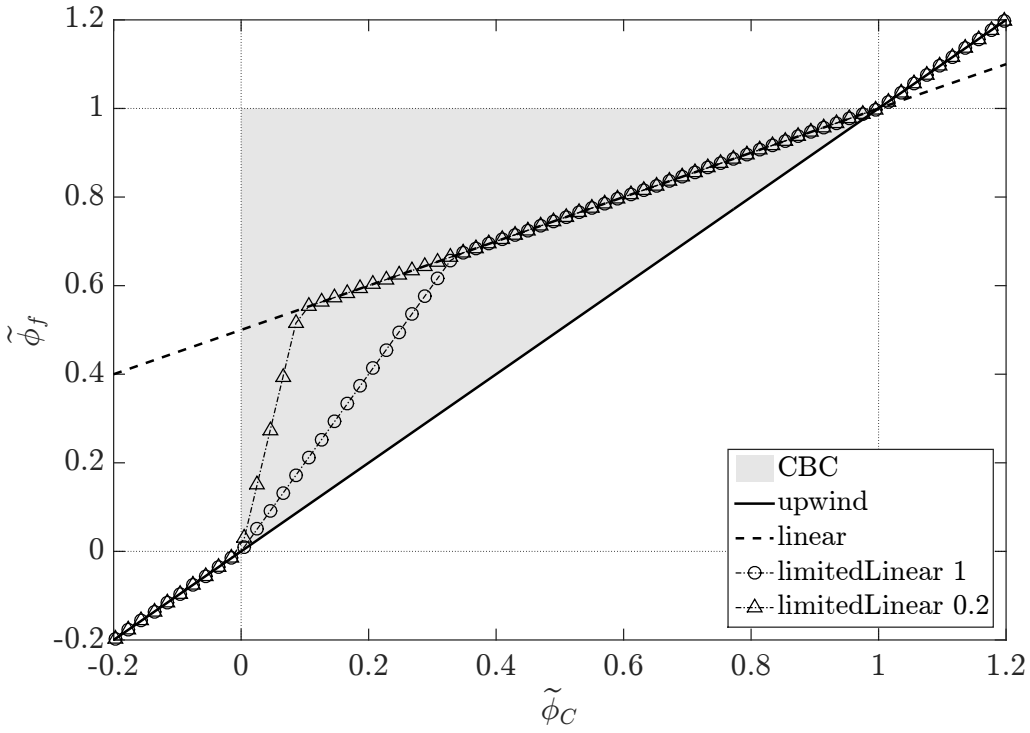

Figure 2.7: The *limitedLinear* scheme on the NVD diagram for $k = 1$ and 0.2. For reference the *upwind* and *linear* schemes are also presented. The light grey region is the Convection Boundedness Criterion (CBC), which includes the upwind line ($\widetilde{\phi}_f = \widetilde{\phi}_C$).

OpenFOAM. The effect of k for this scheme is illustrated in Figure 2.7, which presents it (Equation 2.26) on the NVD diagram for $k = 1$ and 0.2.

In Figure 2.8 this scheme is again presented on the NVD diagram with $k = 1$; but this figure also includes the curve used to represent this scheme in the OpenFOAM Documentation [58]. As can be seen, this scheme is incorrectly described on the NVD diagram in the OpenFOAM Documentation [58].

Finally, this scheme is compared with the *Gamma* scheme. Figures 2.9 and 2.10 present the *limitedLinear* and *Gamma* schemes on the NVD diagram for $k = 1$ and

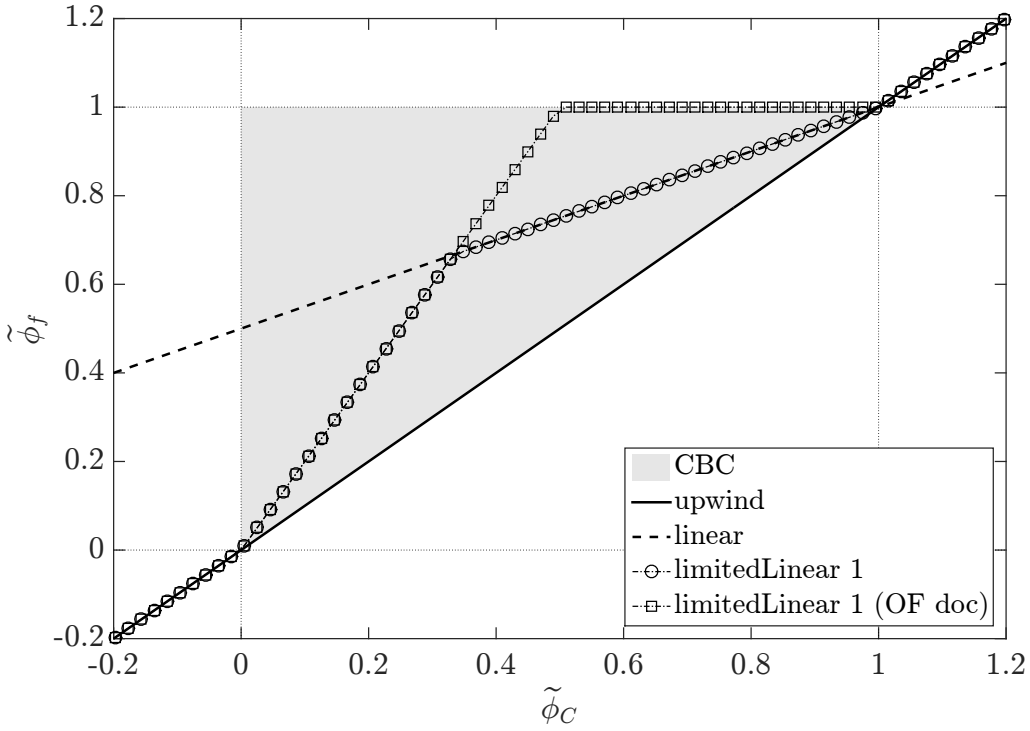

Figure 2.8: The *limitedLinear* scheme on the NVD diagram for $k = 1$. Two versions of this scheme are presented: one based on inspection of the code and the other from the OpenFOAM Documentation [58]. For reference the *upwind* and *linear* schemes are also presented. The light grey region is the Convection Boundedness Criterion (CBC), which includes the upwind line ($\widetilde{\phi}_f = \widetilde{\phi}_C$).

0.2, respectively. Note that in these figures the correct version of the *Gamma* scheme (called hereafter *dbGamma*) is shown and not the bugged one from OpenFOAM. From Figure 2.9 it is clear that, for $k = 1$, if stability is desired then the *Gamma* scheme would be a better choice; because of a smoother transition from *upwind* to *linear* scheme. For $k = 0.2$ (Figure 2.10) these two schemes are practically identical. So, if the *Gamma* scheme can lead to the "switching" instability for $k < 0.2$ (as found in [59]) then the *limitedLinear* scheme is expected to show the same behaviour and should not be used with $k < 0.2$. It is worth mentioning here that the author's present group has been using the *limitedLinear* scheme with $k = 0.1$ for the past several years [43, 61]. Consequently, the effect of the factor k on the performance of this scheme will be checked later by simulating a representative test case.

We will now move on to discussing the final convection scheme i.e., the *filteredLinear2* scheme.

2.2.5 *filteredLinear2 scheme*

The *filteredLinear2* scheme is not commonly used and to the best of the present author's knowledge has never been satisfactorily described anywhere. Based on the inspection of the code, it can be written as:

$$\phi_f = \begin{cases} (1 - r(1 - f_x))\phi_C + r(1 - f_x)\phi_D & 0 < r < 1 \\ f_x\phi_C + (1 - f_x)\phi_D & 1 \leq r \\ \phi_C & \text{elsewhere} \end{cases} \tag{2.27}$$

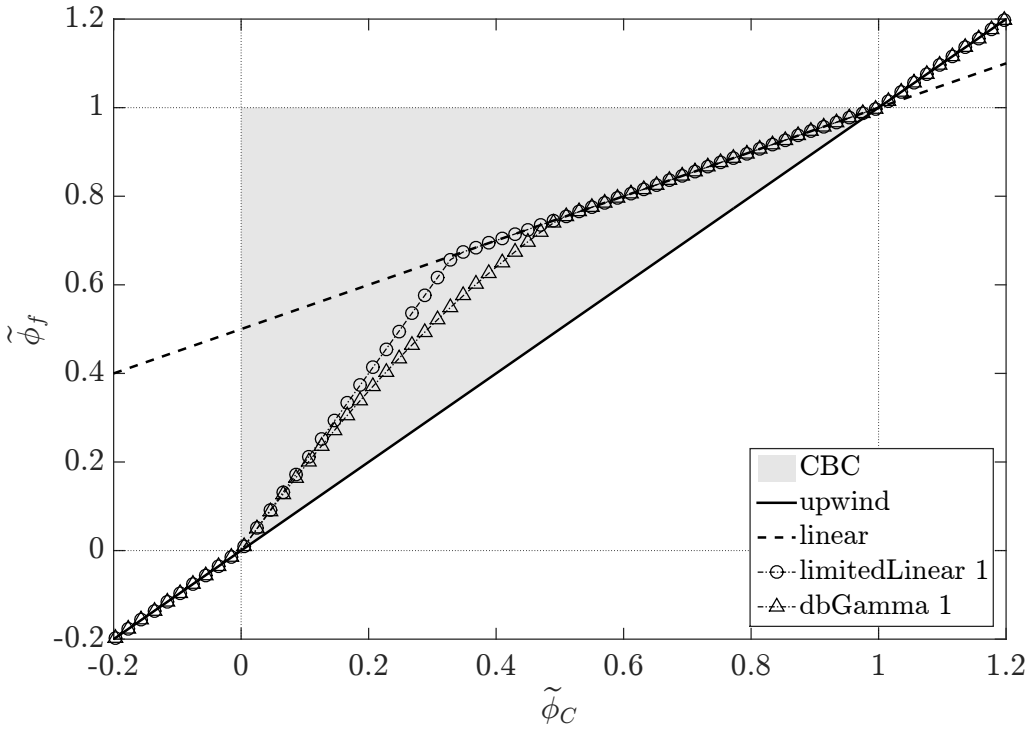

Figure 2.9: The *limitedLinear* and *Gamma* schemes on the NVD diagram for $k = 1$. For reference the *upwind* and *linear* schemes are also presented. The light grey region is the Convection Boundedness Criterion (CBC), which includes the upwind line ($\widetilde{\phi}_f = \widetilde{\phi}_C$).

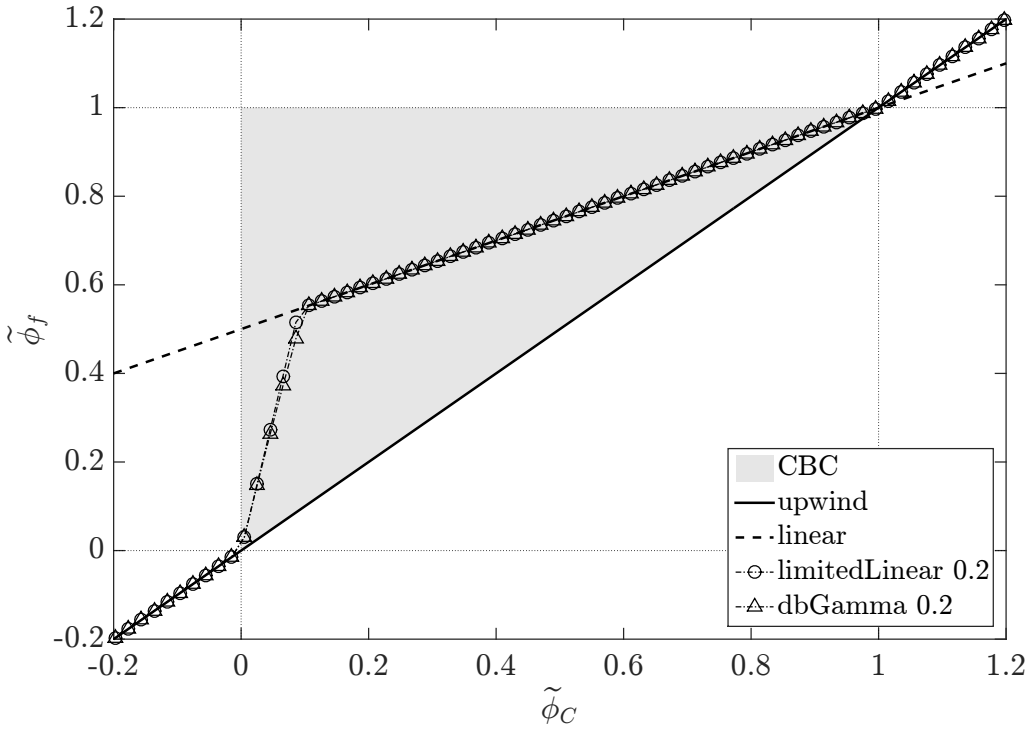

Figure 2.10: The *limitedLinear* and *Gamma* schemes on the NVD diagram for $k = 0.2$. For reference the *upwind* and *linear* schemes are also presented. The light grey region is the Convection Boundedness Criterion (CBC), which includes the upwind line ($\widetilde{\phi}_f = \widetilde{\phi}_C$).

where r is expressed as:

$$r = 1+l-k\left(\frac{\min(\max((\phi_D-\phi_C)-2\mathbf{d}\cdot(\nabla\phi)_C,0),\max((\phi_D-\phi_C)-2\mathbf{d}\cdot(\nabla\phi)_D,0))}{\max(|\phi_D-\phi_C|,\max(|2\mathbf{d}\cdot(\nabla\phi)_C|,|2\mathbf{d}\cdot(\nabla\phi)_D|))}\right) \tag{2.28}$$

if $(\phi_D - \phi_C) > 0$ and as:

$$r = 1+l-k\left(\frac{\min(\max(2\mathbf{d}\cdot(\nabla\phi)_C-(\phi_D-\phi_C),0),\max(2\mathbf{d}\cdot(\nabla\phi)_D-(\phi_D-\phi_C),0))}{\max(|\phi_D-\phi_C|,\max(|2\mathbf{d}\cdot(\nabla\phi)_C|,|2\mathbf{d}\cdot(\nabla\phi)_D|))}\right) \tag{2.29}$$

if $(\phi_D - \phi_C) \leq 0$. The factors k and l are controlled by the user and take values between 0 and 1; and will be discussed further in the following. This scheme is invoked as follows in the OpenFOAM framework: *filteredLinear2* k l, with the specification of k preceding that of l.

For uniform grids and "central difference" approximation of $(\nabla\phi)_C$ and $(\nabla\phi)_D$; the *filteredLinear2* scheme becomes:

$$\phi_f = \begin{cases} (1-\frac{r}{2})\phi_C + \frac{r}{2}\phi_D & 0 < r < 1 \\ \frac{1}{2}\phi_C + \frac{1}{2}\phi_D & 1 \leq r \\ \phi_C & \text{elsewhere} \end{cases} \tag{2.30}$$

with r reducing to the following form:

$$r = 1 + l - k\left(\frac{\min(\max(\phi_U-\phi_C,0),\max(\phi_D-\phi_{DD},0))}{\max(|\phi_D-\phi_C|,\max(|\phi_D-\phi_U|,|\phi_{DD}-\phi_C|))}\right) \tag{2.31}$$

for $(\phi_D - \phi_C) > 0$ and to:

$$r = 1 + l - k\left(\frac{\min(\max(\phi_C-\phi_U,0),\max(\phi_{DD}-\phi_D,0))}{\max(|\phi_D-\phi_C|,\max(|\phi_D-\phi_U|,|\phi_{DD}-\phi_C|))}\right) \tag{2.32}$$

for $(\phi_D - \phi_C) \leq 0$. Since this scheme requires the value of ϕ not only at cells

C, D and U but also at cell DD, it can not be completely represented on an NVD diagram. Notwithstanding, the following comments can be made about this scheme:

- This scheme is also clearly a blend of the *upwind* and *linear* schemes, like the *Gamma* and *limitedLinear* schemes.
- The factor k scales the amount of overall upwinding that is applied based on the differences in ϕ in the neighboring cells; with an increase in k from 0 to 1 leading to higher amount of upwinding, overall.
- Specifying $k = 0$ reduces this scheme to a *linear* scheme, regardless of the value of the factor l.
- As the factor l is increased from 0 to 1 the amount of overall upwinding is reduced independent of the state of the flow.

No attempt is made to further understand this scheme because the simulations of a representative test case (discussed next) clearly show that this scheme is handicapped by severe dispersion issues.

2.2.6 Assessment of different schemes

In this section we will evaluate the performance of different convection schemes discussed in the previous section, along with the classical *upwind* and *linear* schemes, using a representative test case. We will also study the effects of the scheme's parameters (k and or l) wherever applicable.

We follow [70] and consider a 2D test case in which a prescribed profile of a scalar ϕ is advected, in the absence of diffusion, by a velocity field that corresponds

to solid-body-rotation. The adopted variation of ϕ is, however, different from those used in [70] and consists of three disparate profiles selected in [63]: a step, a $\sin^2$ wave and a semi-ellipse.

The numerical configuration for the test case is illustrated in Figure 2.11. The computational domain is 400-cm-long in the x-direction, 200-cm-wide in the y-direction. In the x-direction the domain starts at $x = -200$ cm and extends up to $x = 200$ cm; and in the y-direction it starts (ends) at $y = 0$ (200) cm.

The velocity field used in this case is given as:

$$(u_x, u_y) = (y, -x) \tag{2.33}$$

which corresponds to a clockwise solid-body-rotation, around the origin $(x, y) = (0, 0)$, with an angular velocity of 1 rad/s. The vectors in Figure 2.11 present the velocity field given by Equation 2.33.

The domain is initialized with $\phi = 0$. The profile of ϕ imposed at the inlet ($y = 0$ and $x < 0$) is

$$\phi(x) = \begin{cases} 1 & \text{for } x <= -150 \\ \sin^2\left[\dfrac{\pi(x+110)}{20}\right] & \text{for } -110 \leq x \leq -90 \\ \sqrt{1 - \left(\dfrac{x+50}{10}\right)^2} & \text{for } -60 \leq x \leq -40 \\ 0 & \text{elsewhere} \end{cases} \tag{2.34}$$

which, as mentioned above, contains a step, a $\sin^2$ wave and a semi-ellipse; arranged from left to right in the x-direction. Equation 2.34 is plotted in Figure 2.12. The value of ϕ is set to 1 at the left ($x = -200$ cm), top ($y = 200$ cm) and right ($x = 200$

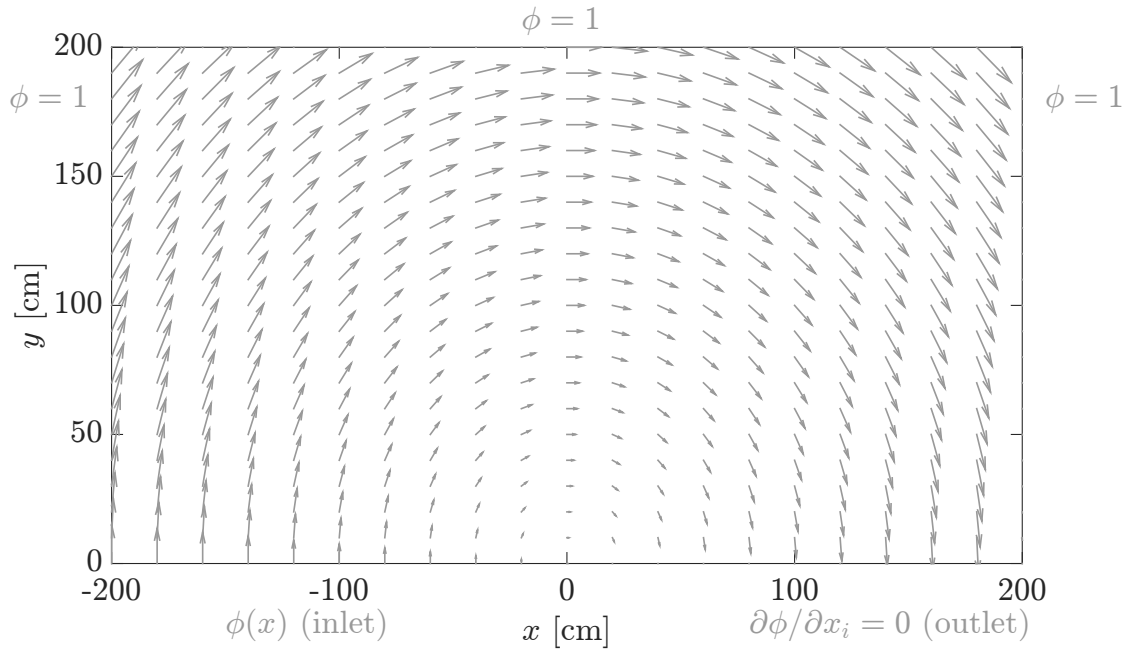

Figure 2.11: The numerical configuration for the solid-body-rotation case for evaluating the performance of different convection schemes in OpenFOAM.

cm) boundaries. At the outlet boundary ($y = 0$ and $x > 0$) a zero-gradient boundary condition is applied for ϕ ($\partial\phi/\partial x_i = 0$).

The mesh consists of 400 (200) cells in the x- (y-) direction, yielding $\Delta x = \Delta y = 1$ cm. This resolution corresponds to 20 cells across the $\sin^2$ wave and the semi-ellipse at the inlet.

FireFOAM was adapted to solve this case in the steady state framework in the SIMPLE mode:

$$\frac{\partial(u_j\phi)}{\partial x_j} = 0 \tag{2.35}$$

In order to avoid the concomitant convergence issues, relaxation had to be used. In OpenFOAM one has a choice between relaxing either the variable or the equation. We relaxed the latter with a factor of 0.8. Simulations were considered converged

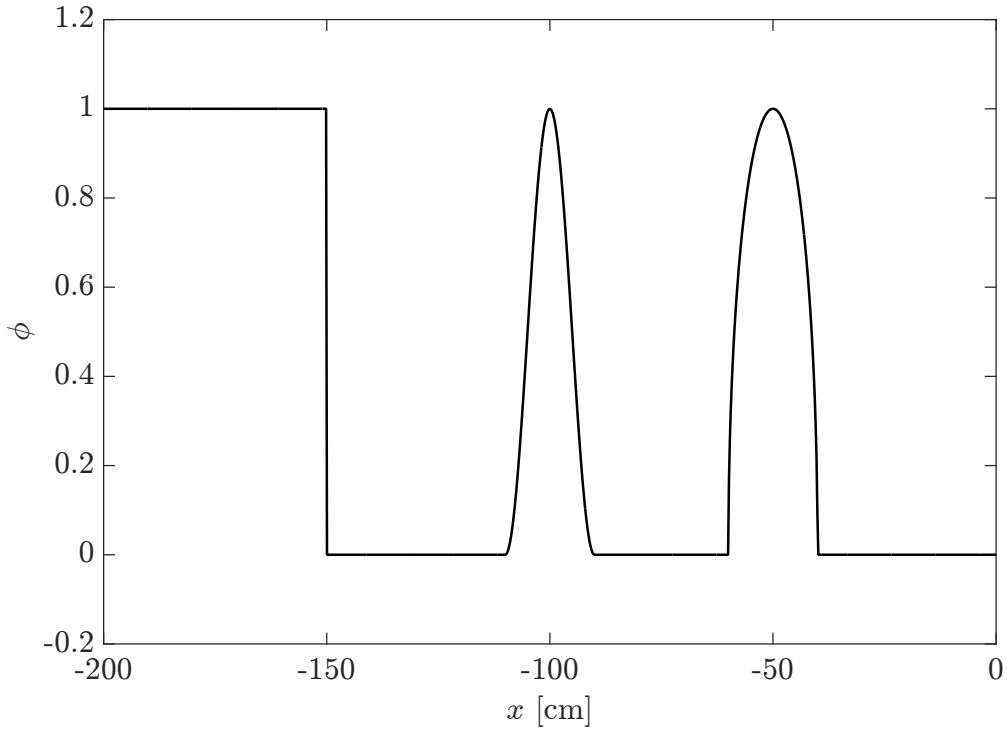

Figure 2.12: Profile of the scalar ϕ imposed at the inlet in the solid-body-rotation case for evaluating the performance of different convection schemes. The profile consists of a step, a $\sin^2$ wave and a semi-ellipse; see Equation 2.34.

when OpenFOAM's "Intial residual" became smaller than 1e-05; and every iteration within the simulations was considered converged when OpenFOAM's "Final residual" became less than 1e-09. The Preconditioned Bi-Conjugate Gradient (PBiCG) linear-solver was used along with the Diagonal-based Incomplete LU (DILU) preconditioner for solving the system.

The exact solution for this test is given by Equation 2.34, with $r = \sqrt{x^2 + y^2}$ replacing x; because in the absence of diffusion the profile imposed at the inlet should remain unchanged while undergoing solid-body-rotation and should reach the outlet as is.

Figures 2.13 to 2.26 present results for the *upwind*, *linear*, *linearUpwind grad(U)*, *LUST grad(U)*, *dbGamma 1*, *Gamma 1*, *dbGamma 0.2*, *dbGamma 0.1*, *limitedLinear 1*, *limitedLinear 0.2*, *limitedLinear 0.1*, *filteredLinear2 1 0.05*, *filteredLinear2 0.1 0.05*, and *filteredLinear2 1 1* schemes, respectively. The top panels in these figures contain the steady-state contours of ϕ and the bottom panels present ϕ, plotted as a function of r, at the inlet and outlet boundary faces and inside all the computational cells.

For a quantitative performance assessment, of the different choices for the convection scheme listed above, Table 2.1 provides the following quantities:

- The L_1-norm error; $\epsilon = (\sum_{n=1}^{N_{cells}} |\phi_n - \phi_{exact}|)/N_{cells}$
- A measure of unboundedness (or the amount of overshoots and undershoots) in the solution; $OU = \sum_{n=1}^{N_{cells}} (\max(\phi_n - 1, 0) + \max(-\phi_n, 0))$
- Number of iterations required to bring OpenFOAM's "Initial residual" below

1e-05; N_{it}

- Average number of steps required during each iteration to make OpenFOAM's "Final residual" smaller than 1e-09; n_{st}

- The convergence speed measured by the reciprocal of the product of N_{it} and n_{st}, $(N_{it} \times n_{st})^{-1}$. The higher the value of $(N_{it} \times n_{st})^{-1}$ the faster the convergence.

The results shown in Figures 2.13 to 2.26 and in Table 2.1 are summarized below:

- As expected the *upwind* scheme is too diffusive and smears the shapes of the three profiles significantly, after only half a rotation (Figure 2.13). It has the largest error ϵ; which renders it unusable despite being bounded and having the best convergence speed.

- As also expected, the solution given by the *linear* scheme is plagued by dispersion and boundedness issues (Figure 2.14). In addition the linear scheme has a significantly worse convergence speed as compared to the upwind scheme.

- The *linearUpwind grad(U)* scheme has a significantly smaller error, when compared to both the *upwind* and *linear* schemes, but it is unbounded as one may expect (Figure 2.15). Its convergence speed is as good as the upwind scheme.

- Overall, the *LUST grad(U)* scheme is more accurate than the *linearUpwind grad(U)* scheme; but the latter outperforms the former in terms of boundedness and convergence speed.

- When the *dbGamma* scheme is invoked with the factor k set to 1, the solution overall is not as accurate as those given by the *linearUpwind grad(U)* and *LUST grad(U)* schemes. This is probably due to the inability of *dbGamma* to maintain the peak of the $\sin^2$ wave; a well-known issue, known as "clipping" in the literature [59]. But *dbGamma* with $k = 1$ is bounded and has a convergence speed that is nearly as good as the *LUST grad(U)* scheme. For this test the performance of *dbGamma* is almost identical to that of *Gamma*. When *dbGamma* is used with $k = 0.2$, its accuracy lies between that of *linearUpwind grad(U)* and *LUST grad(U)*; the solution is also bounded. However, the simulation with $k = 0.2$ never converges; in other words, OpenFOAM's "Initial residual" for this scheme never drops below 1e-05. Further discussion of the convergence issue is beyond the scope of the present work, but it should be noted that this is a well-known issue with NVD-type schemes [59]. Finally, when *dbGamma* is used with $k = 0.1$, the solution is slightly less accurate than that given by *dbGamma* with $k = 0.2$; in addition, the solution is unbounded. This behaviour is probably due to the onset of the so-called "switching" instability [59].

- For $k = 1$ the *limitedLinear* scheme produces a slightly more accurate solution than *dbGamma*, probably because of a faster switch to the linear scheme (Figure 2.9). On the other hand, the convergence speed for *dbGamma* is better (although not significantly) than that of *limitedLinear*. For $k = 0.2$ and 0.1 the performance of *limitedLinear* is practically identical to that of *dbGamma*,

which may have been expected due to their similarity on the NVD diagram for smaller values of k (Figure 2.10).

- The overall performance of the *filteredLinear2* scheme, for different combinations of the factors k and l, is quite similar to the *linear* scheme and hence this scheme should be avoided. Setting $k = 1$ and prescribing a value close to 0 for l definitely improves its behaviour, but not enough to make it usable.

Overall, the *limitedLinear 1* scheme has the best performance in this test; considering accuracy, boundedness and convergence speed. One should have in mind that the convergence behaviour heavily depends up on the selected tolerance value (as mentioned above we use 1e-05 for determining convergence). And currently it is unclear what level of tolerance is enough. Accordingly, schemes at this stage can not be disregarded solely based on their convergence behaviour. So, if convergence speed is ignored then both *limitedLinear 0.2* and *dbGamma 0.2* have the best performance. Note that this conclusion is independent of grid resolution; see Tables 2.2 and 2.3, which present results from a coarser ($\Delta x = \Delta y = 2$ cm) and finer ($\Delta x = \Delta y = 0.5$ cm) grid, respectively.

Before going further, it is worth mentioning that the solid-body-rotation test was performed after finishing the simulations reported in Chapters 3 to 5. Simulations reported in those chapters use the *filteredLinear2* scheme (with $k = 0.1$ and $l = 0.05$) for the convection terms in the momentum equations (and use the *limitedLinear* scheme with $k = 0.1$ for the convection terms in the scalar equations, see below), because the same choices were made in one of the recent studies

in our group [43]. Specifically, the V version of the *filteredLinear2* scheme, called *filteredLinear2V*, is used in the simulations in those chapters. The V version of different schemes in OpenFOAM are specifically designed for the convective terms in the momentum equations: they are more dissipative than the baseline schemes, see [58,71]. As mentioned above, the *limitedLinear* scheme (with $k = 0.1$) is used for the convective terms in the scalar transport equations. For mass fraction transport equations the 01 version of this scheme, called *limitedLinear01*, is used. The 01 version of different schemes bounds the values of the scalar between 0 and 1; see [58]. In the future, we will choose convection schemes based on their performance in representative test cases like the one used in this section.

We now turn to the description and assessment of the temporal schemes available in the OpenFOAM library.

2.3 Temporal schemes

In this section we will describe and assess the time integration schemes available in OpenFOAM. We will also study the effects of CFL and the parameter *nOuterCorrectors* (to be described briefly later) on the solution.

Since the time integration schemes in OpenFOAM have already been detailed in the literature (see e.g., [46]); we will restrict ourselves to their brief description. OpenFOAM provides three temporal schemes; named *Euler*, *backward* and *CrankNicolson*. *Euler* is the classical backward Euler scheme and is given as:

$$\frac{\partial \phi}{\partial t} \approx \frac{\phi^t - \phi^{t-\Delta t}}{\Delta t} \tag{2.36}$$

The rest of the terms (convection, source, etc.) are evaluated at time t which requires

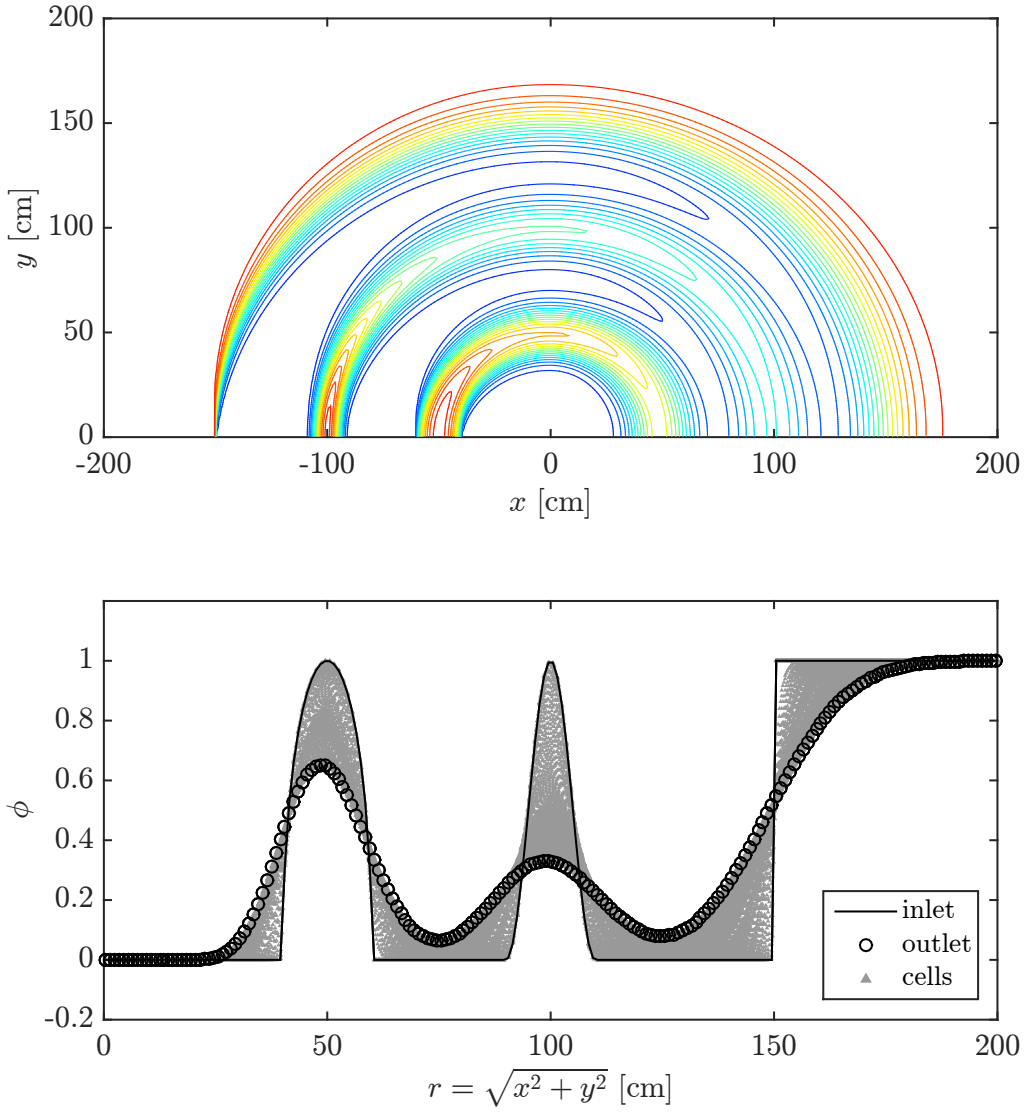

Figure 2.13: Results for the *upwind* scheme; steady state contour of ϕ (top) and variation of ϕ plotted against r at faces on the inlet and outlet boundaries and in all the cells inside the domain (bottom). In the contour, dark blue (red) corresponds to $\phi = -0.2$ (1.2). For an ideal convection scheme the profile imposed at the inlet would remain unchanged while undergoing solid-body-rotation and hence, the black and grey symbols would overlap the black solid line, which represents the exact solution.

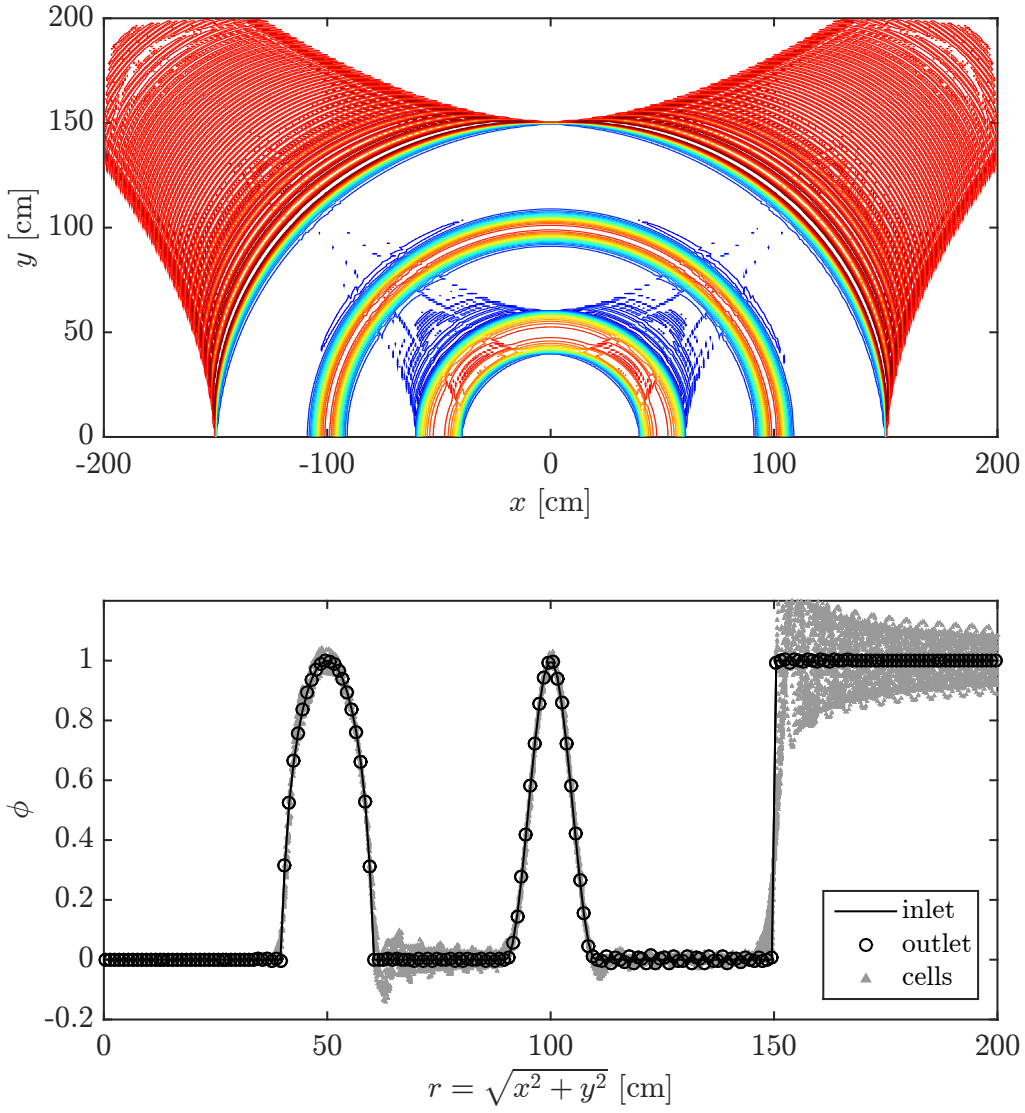

Figure 2.14: Results for the *linear* scheme. See Figure 2.13 caption for additional details.

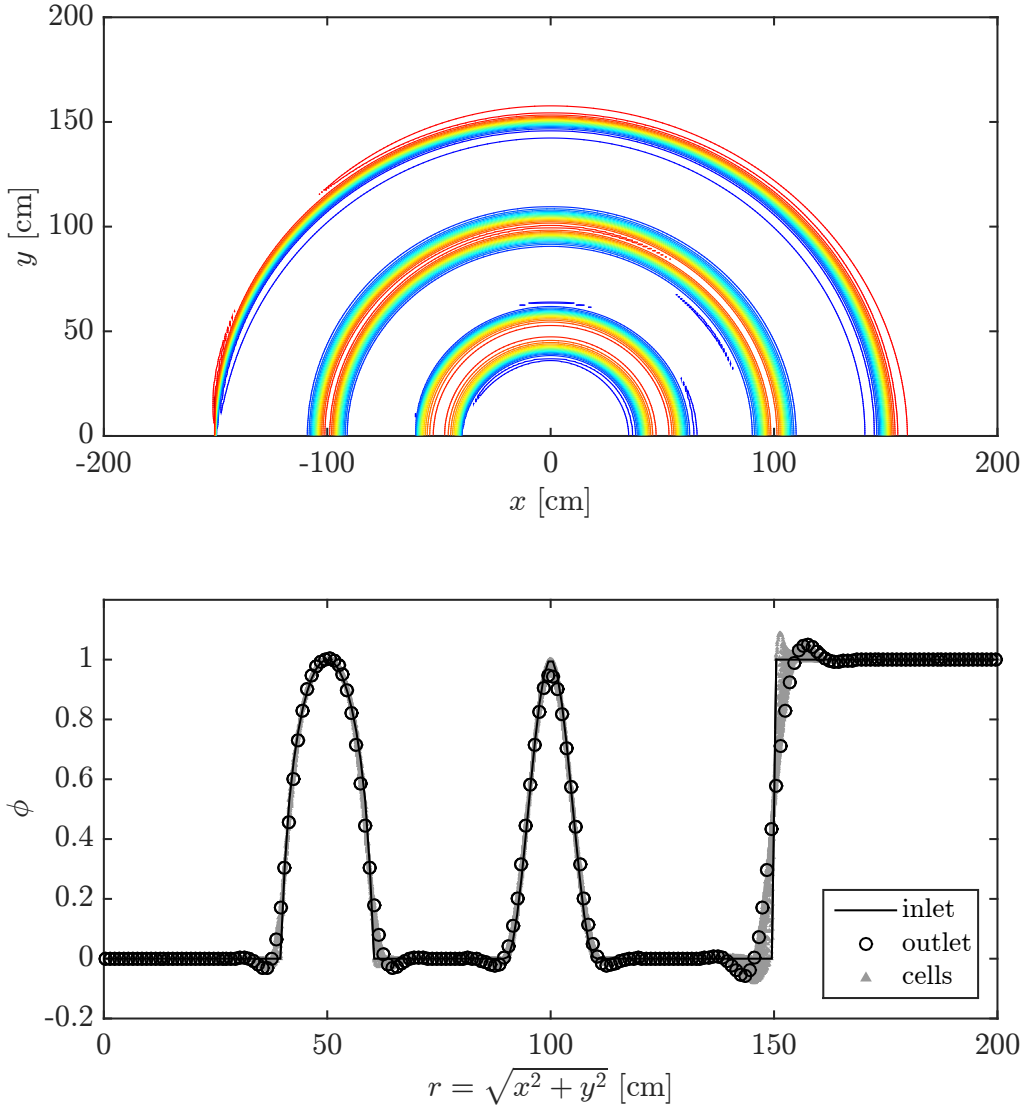

Figure 2.15: Results for the *linearUpwind grad(U)* scheme. See Figure 2.13 caption for additional details.

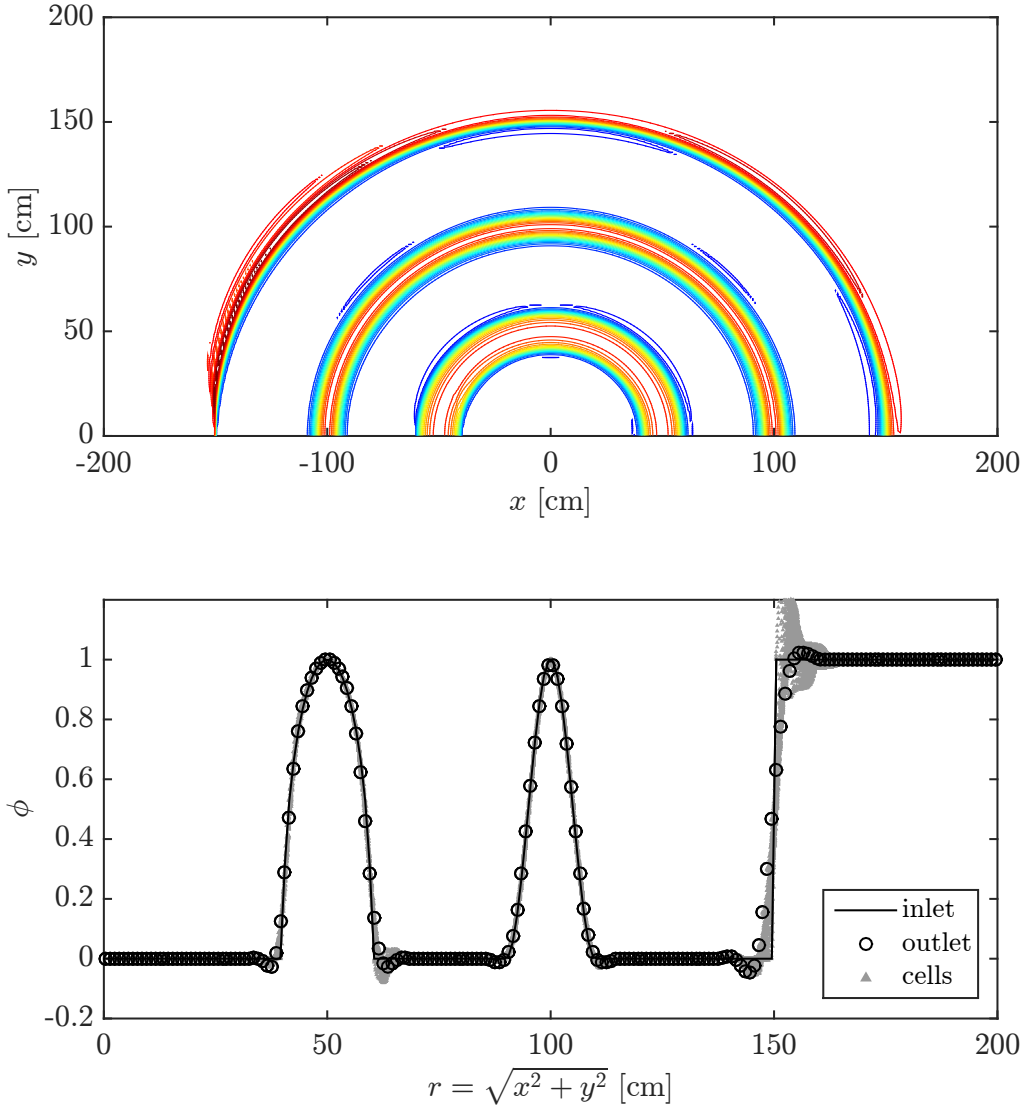

Figure 2.16: Results for the *LUST grad(U)* scheme. See Figure 2.13 caption for additional details.

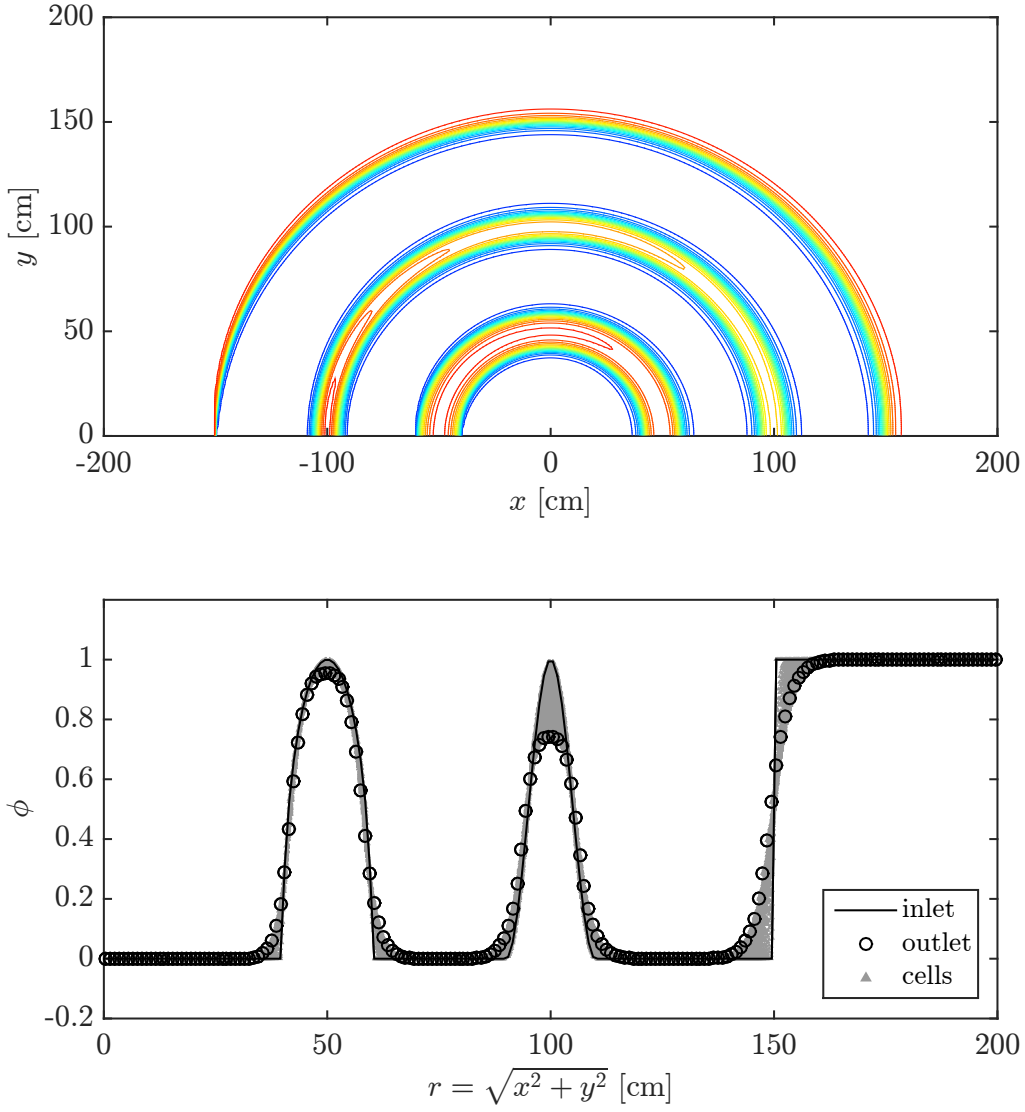

Figure 2.17: Results for the *dbGamma 1* scheme. See Figure 2.13 caption for additional details.

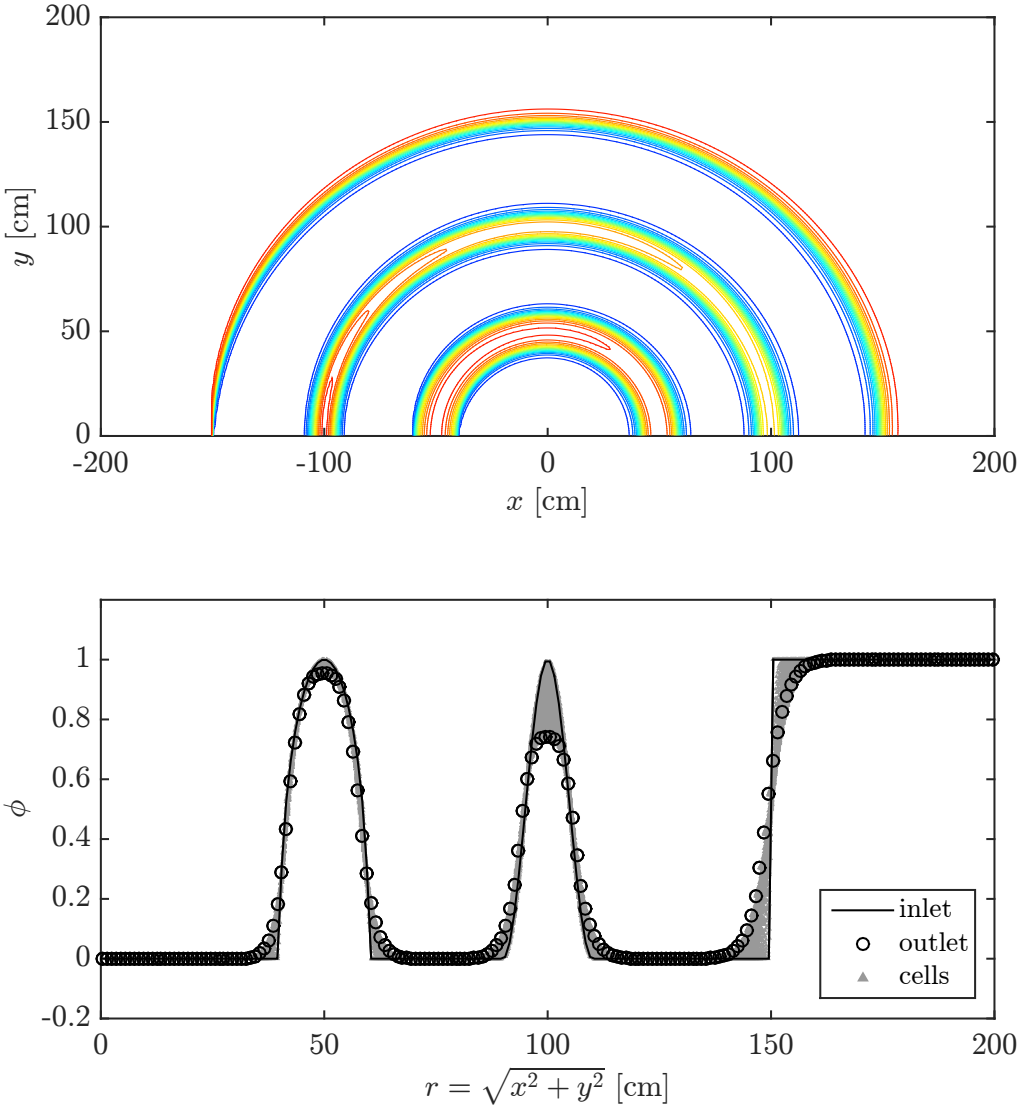

Figure 2.18: Results for the *Gamma 1* scheme. See Figure 2.13 caption for additional details.

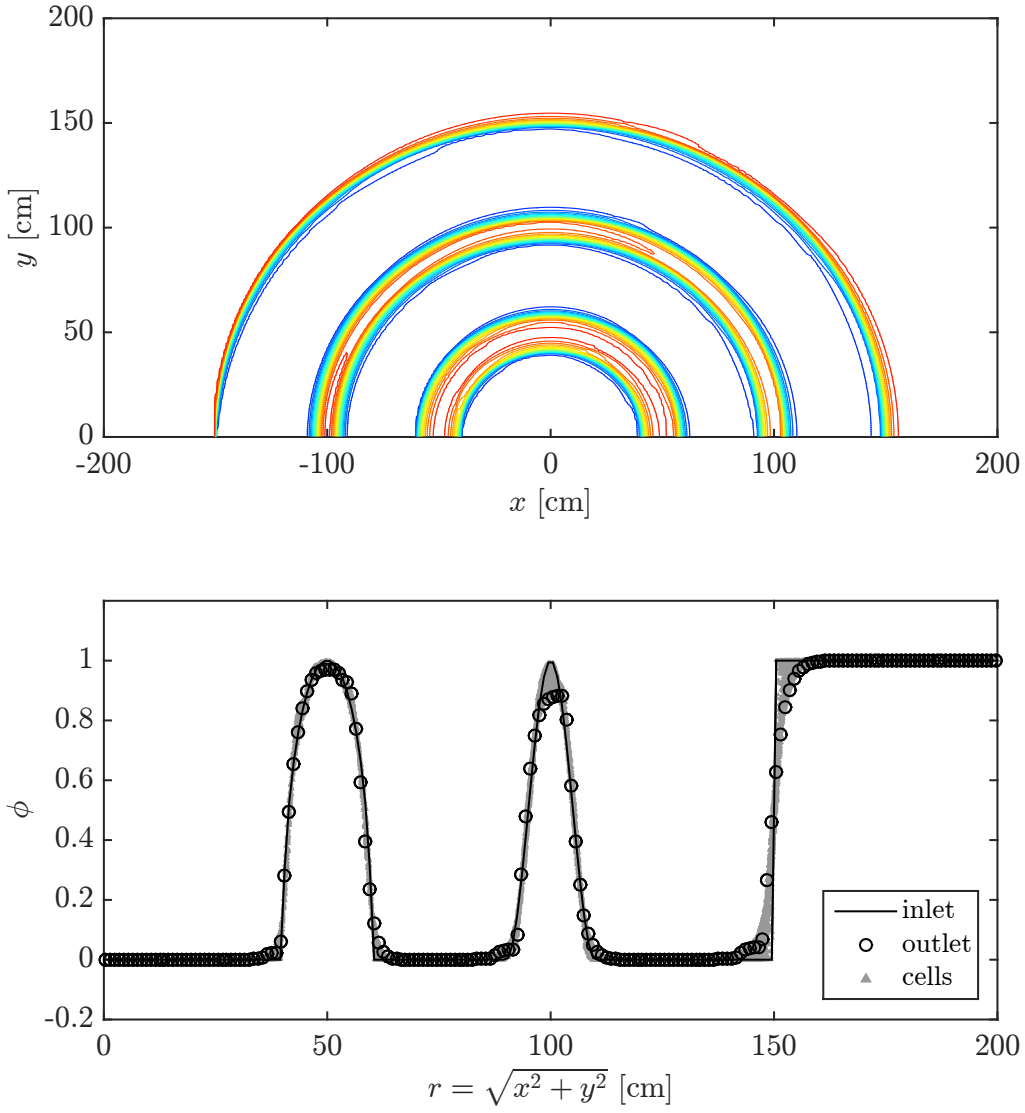

Figure 2.19: Results for the *dbGamma 0.2* scheme. See Figure 2.13 caption for additional details.

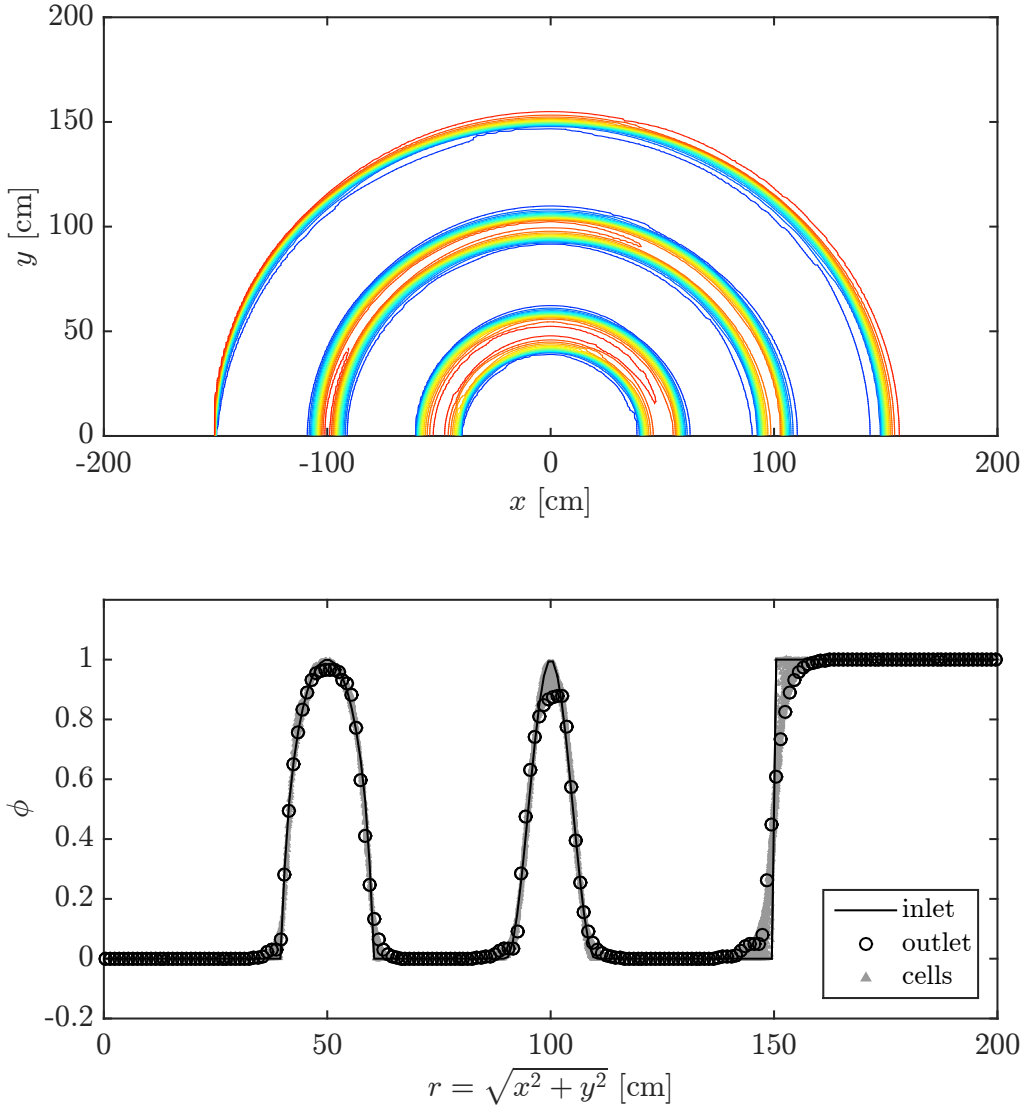

Figure 2.20: Results for the *dbGamma 0.1* scheme. See Figure 2.13 caption for additional details.

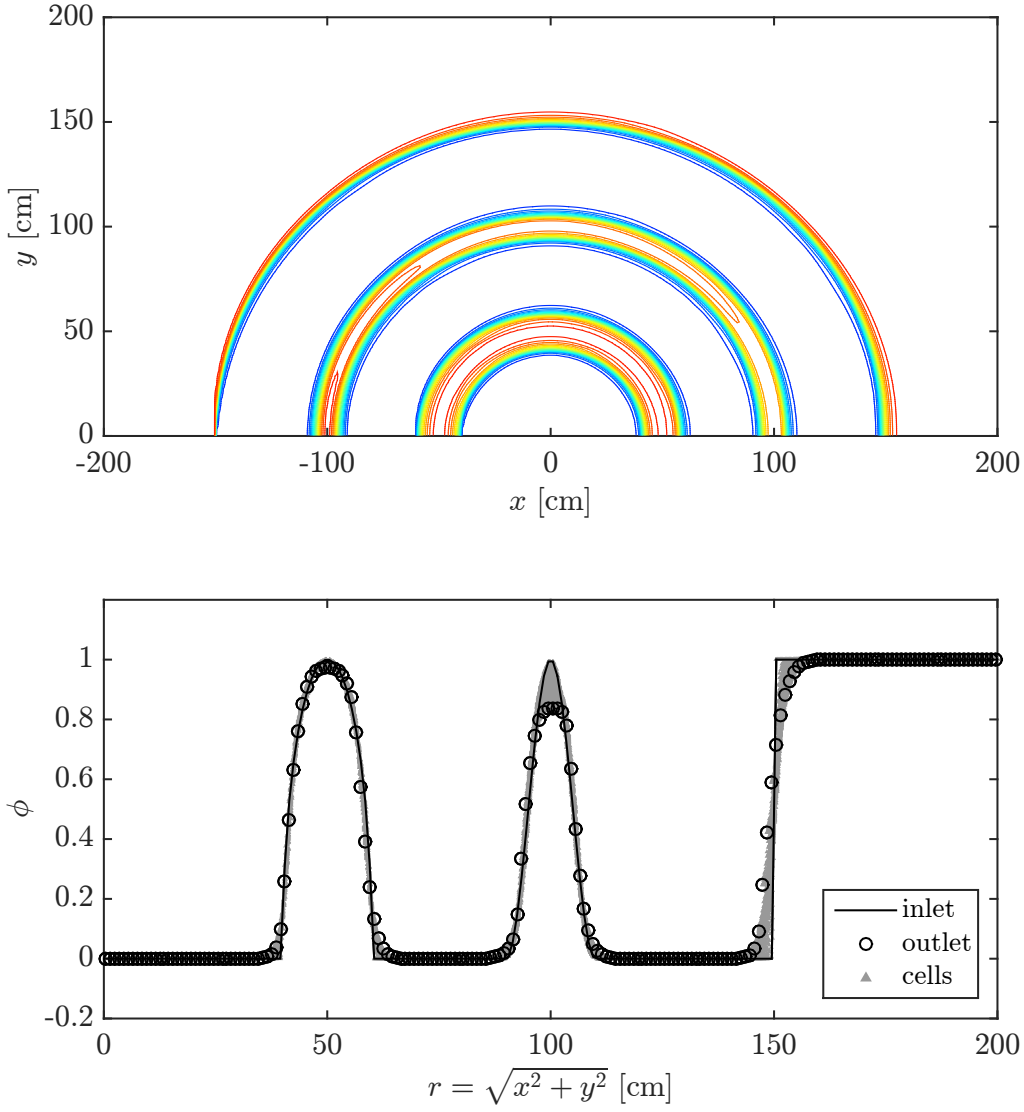

Figure 2.21: Results for the *limitedLinear 1* scheme. See Figure 2.13 caption for additional details.

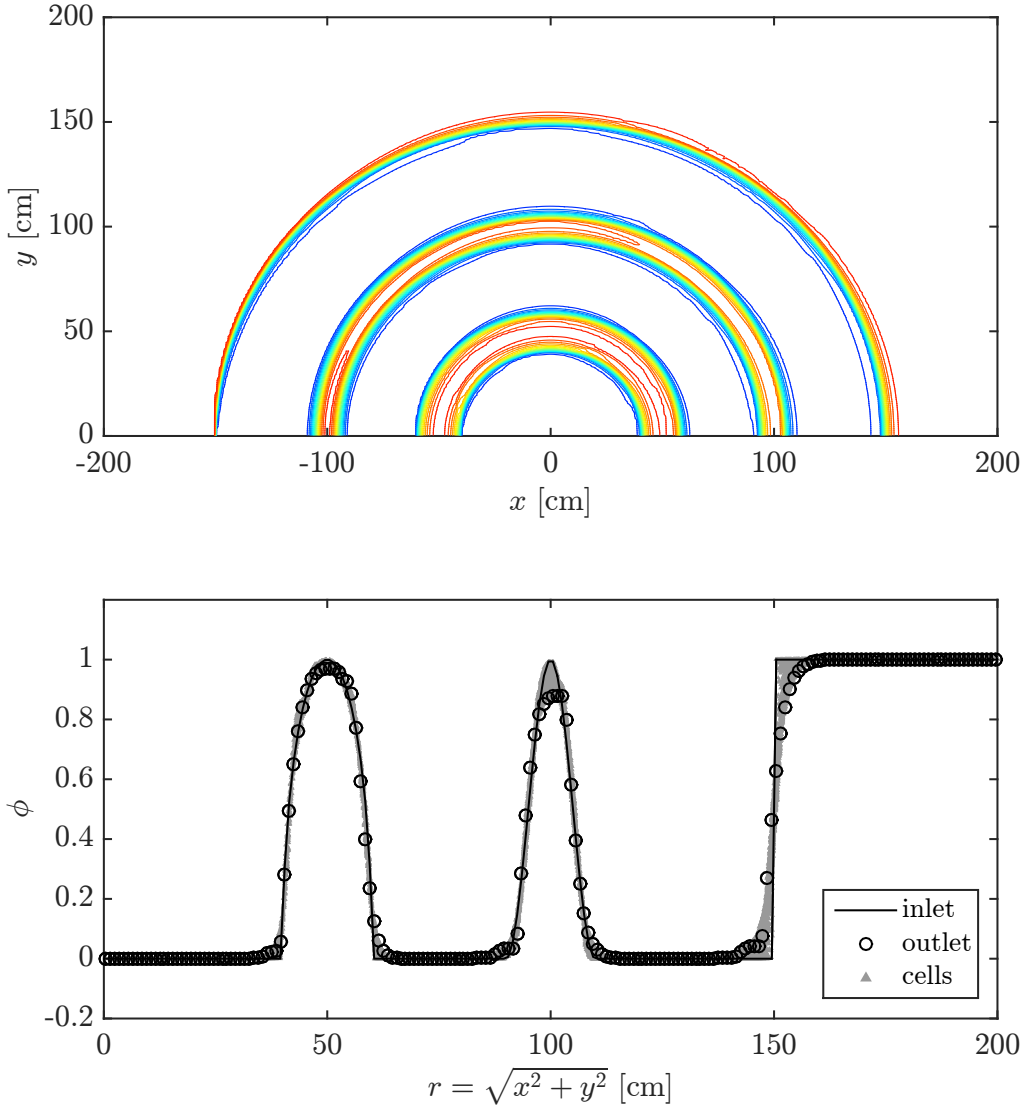

Figure 2.22: Results for the *limitedLinear 0.2* scheme. See Figure 2.13 caption for additional details.

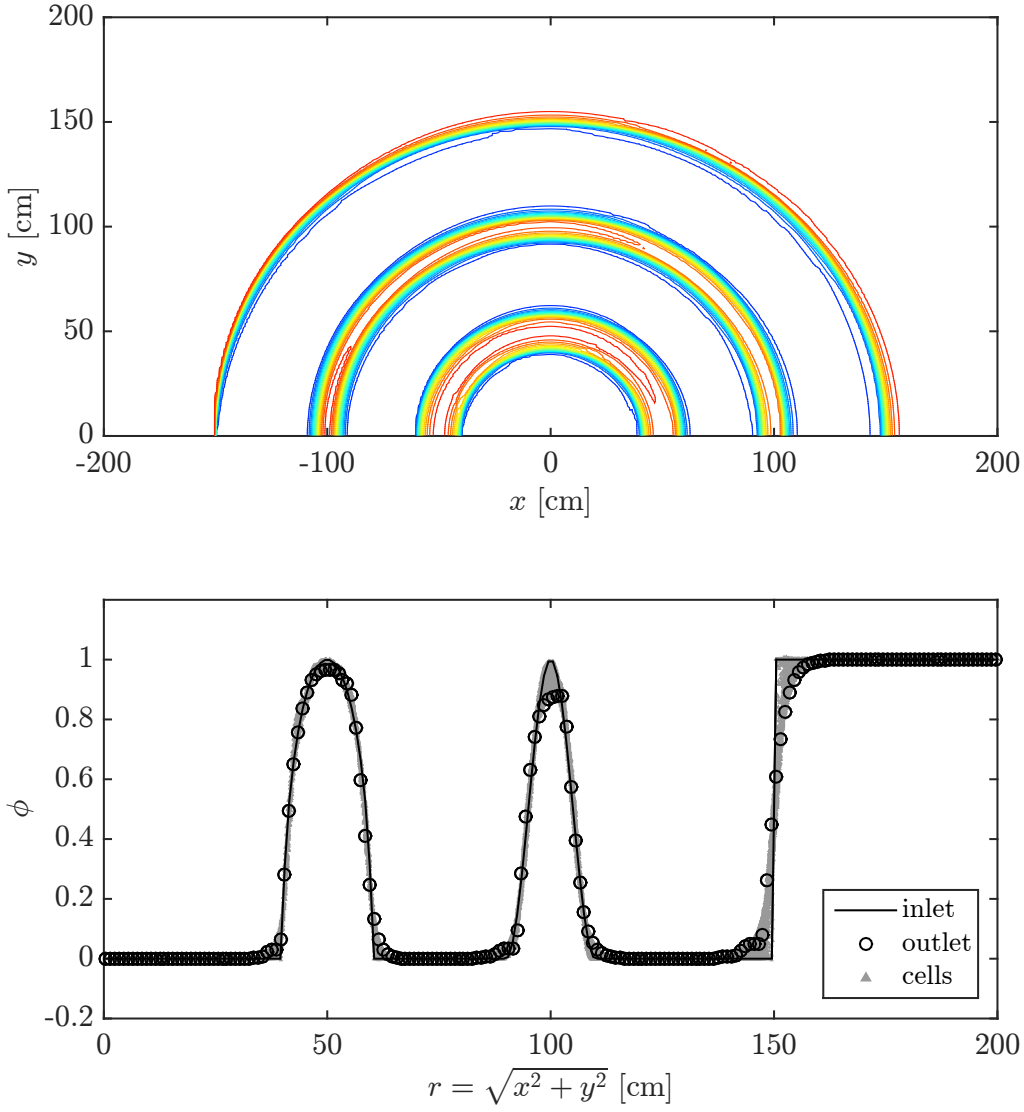

Figure 2.23: Results for the *limitedLinear 0.1* scheme. See Figure 2.13 caption for additional details.

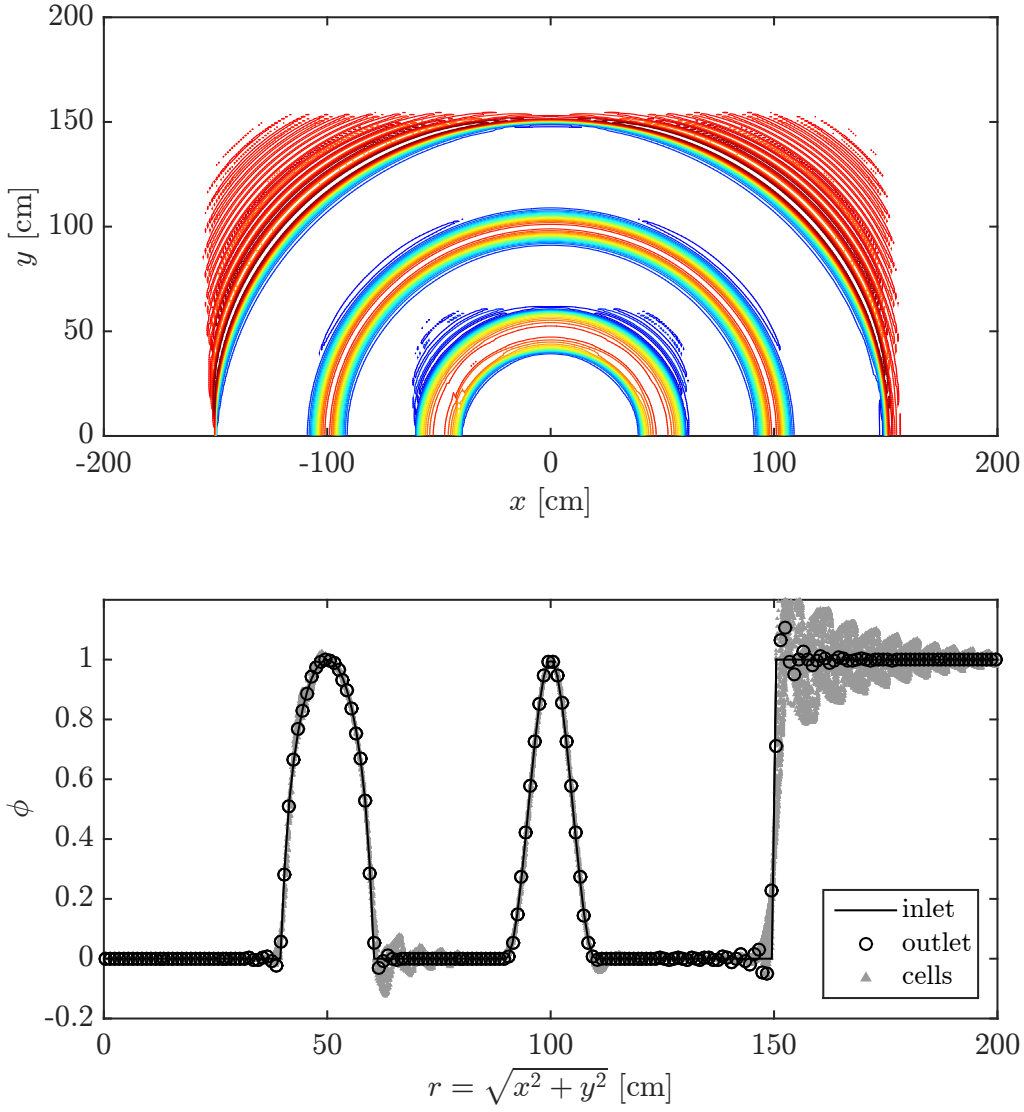

Figure 2.24: Results for the *filteredLinear2 1 0.05* scheme. See Figure 2.13 caption for additional details.

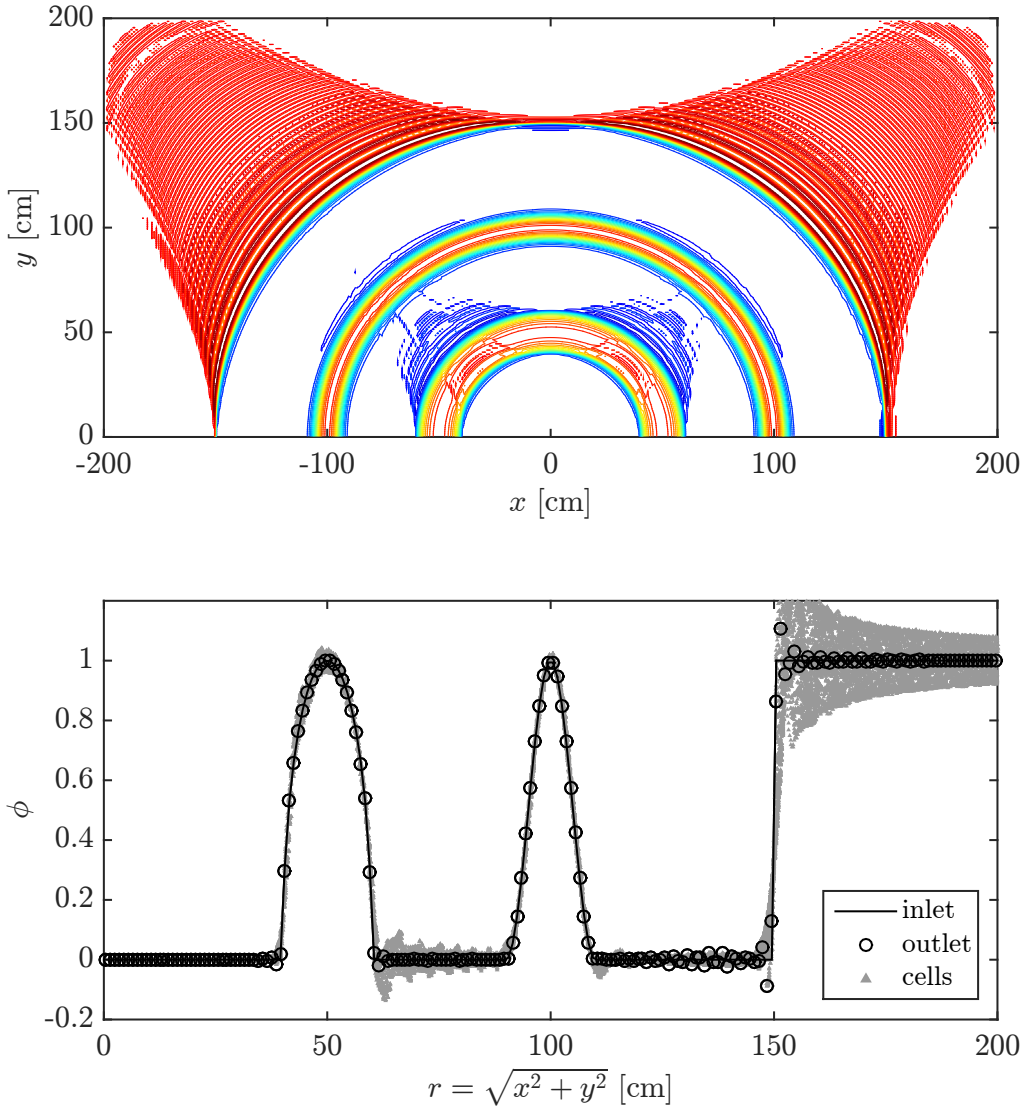

Figure 2.25: Results for the *filteredLinear2 0.1 0.05* scheme. See Figure 2.13 caption for additional details.

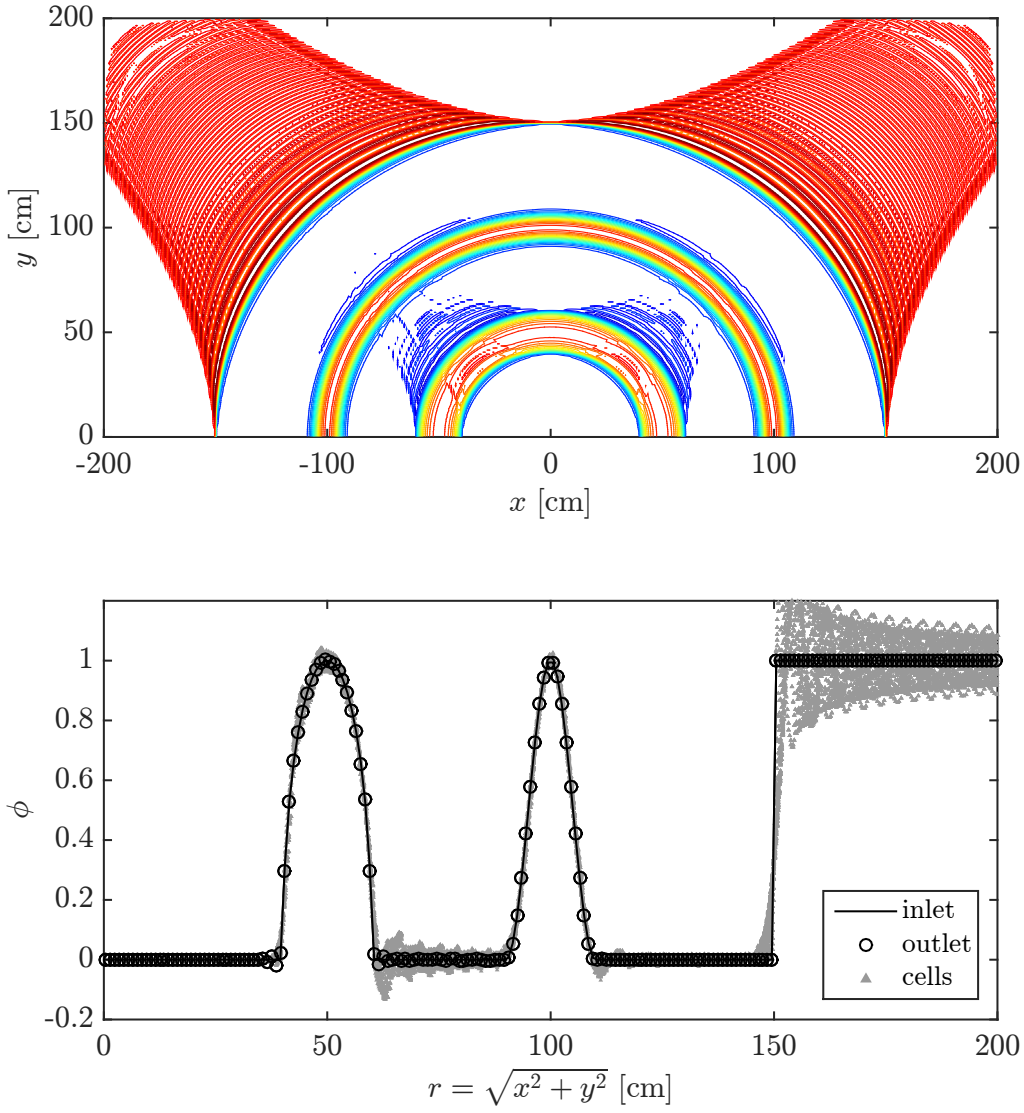

Figure 2.26: Results for the *filteredLinear2 1 1* scheme. See Figure 2.13 caption for additional details.

Table 2.1: Performance comparison of different choices for the convection scheme, using the solid-body-rotation case. The quantity ϵ is the L_1-norm error; $OU = \sum_{n=1}^{N_{cells}}(\max(\phi_n - 1, 0) + \max(-\phi_n, 0))$ is a measure of unboundedness in the solution; N_{it} is the number of iterations required for the simulation to converge; n_{st} represents the average number of steps needed for convergence of every iteration; $(N_{it} \times n_{st})^{-1}$ represents the convergence speed. $N_{it} = 10000$ denotes an unconverged simulation.

scheme	$\epsilon \times 10^2$	OU	N_{it}	n_{st}	$(N_{it} \times n_{st})^{-1} \times 10^5$
upwind	8.3528	0.0	182	14.4	38.2
linear	3.4813	1154.0	2088	6.3	7.6
linearUpwind grad(U)	1.4686	202.6	185	14.3	37.8
LUST grad(U)	1.2082	216.8	632	6.4	24.8
dbGamma 1	2.1223	0.0	742	6.6	20.5
Gamma 1	2.1215	0.0	737	6.6	20.7
dbGamma 0.2	1.3281	0.0	10000	7.1	1.4
dbGamma 0.1	1.3846	0.2	10000	7.2	1.4
limitedLinear 1	1.3939	0.0	753	7.9	16.7
limitedLinear 0.2	1.3411	0.0	10000	7.2	1.4
limitedLinear 0.1	1.3887	0.2	10000	7.3	1.4
filteredLinear2 1 0.05	2.1173	613.2	1196	6.1	13.6
filteredLinear2 0.1 0.05	3.1598	1026.3	1983	6.1	8.3
filteredLinear2 1 1	3.4416	1140.9	2514	6.3	6.3

Table 2.2: Performance comparison of different choices for the convection scheme, using the solid-body-rotation case. This table contains results from a coarser grid with $\Delta x = \Delta y = 2$ cm (note that Table 2.1 contains results from the baseline grid with $\Delta x = \Delta y = 1$ cm). See Table 2.1 caption for additional details.

scheme	$\epsilon \times 10^2$	OU	N_{it}	n_{st}	$(N_{it} \times n_{st})^{-1} \times 10^5$
upwind	11.5126	0.0	104	14.6	65.8
linear	5.1851	413.6	1586	6.6	9.5
linearUpwind grad(U)	3.0234	97.8	108	14.3	64.7
LUST grad(U)	2.3353	104.8	344	7.0	41.4
dbGamma 1	4.1090	0.0	402	6.9	35.9
Gamma 1	4.1073	0.0	402	6.9	36.2
dbGamma 0.2	2.4581	0.0	10000	7.9	1.3
dbGamma 0.1	2.6179	0.1	10000	8.2	1.2
limitedLinear 1	2.8756	0.0	10000	5.3	1.9
limitedLinear 0.2	2.4882	0.0	10000	8.1	1.2
limitedLinear 0.1	2.6281	0.1	10000	8.2	1.2
filteredLinear2 1 0.05	3.4515	239.2	774	7.0	18.5
filteredLinear2 0.1 0.05	4.9048	384.5	1120	6.8	13.1
filteredLinear2 1 1	5.1803	413.3	1543	7.0	9.2

Table 2.3: Performance comparison of different choices for the convection scheme, using the solid-body-rotation case. This table contains results from a finer grid with $\Delta x = \Delta y = 0.5$ cm (note that Table 2.1 contains results from the baseline grid with $\Delta x = \Delta y = 1$ cm). See Table 2.1 caption for additional details.

scheme	$\epsilon \times 10^2$	OU	N_{it}	n_{st}	$(N_{it} \times n_{st})^{-1} \times 10^5$
upwind	5.8575	0.0	334	11.3	26.4
linear	2.4076	3290.5	3658	5.5	5.0
linearUpwind grad(U)	0.7808	437.9	332	11.1	27.2
LUST grad(U)	0.6893	479.2	1207	5.5	15.1
dbGamma 1	1.1433	0.0	1425	6.3	11.2
Gamma 1	1.1464	0.0	1416	6.0	11.7
dbGamma 0.2	0.7324	0.0	10000	6.1	1.6
dbGamma 0.1	0.7790	0.3	10000	6.4	1.6
limitedLinear 1	0.7583	0.0	1448	6.6	10.4
limitedLinear 0.2	0.7416	0.0	10000	6.2	1.6
limitedLinear 0.1	0.7800	0.3	10000	6.4	1.6
filteredLinear2 1 0.05	1.3731	1655.7	1880	5.6	9.5
filteredLinear2 0.1 0.05	2.0870	2784.0	3061	5.5	6.0
filteredLinear2 1 1	2.4040	3292.9	4030	5.7	4.4

the solution of a system of equations. Accordingly, this is an implicit scheme. As is well-known this scheme is bounded but is only first order accurate.

The *backward* scheme in OpenFOAM belongs to the backward differentiation formula (BDF) family of schemes and operates as follows:

$$\frac{\partial \phi}{\partial t} \approx \frac{3\phi^t - 4\phi^{t-\Delta t} + \phi^{t-2\Delta t}}{2\Delta t} \tag{2.37}$$

The rest of the terms (convection, source, etc.) are evaluated at time t. This is a second order implicit scheme but it is unbounded.

Finally, the scheme called *CrankNicolson* in OpenFOAM is a blend between backward Euler and the Crank-Nicolson schemes. The Crank-Nicolson scheme implemented in OpenFOAM is given below:

$$\frac{\partial \phi}{\partial t} \approx \frac{\phi^t - \phi^{t-2\Delta t}}{2\Delta t} \tag{2.38}$$

with the rest of the terms being evaluated at time $(t - \Delta t)$. Clearly, OpenFOAM's Crank-Nicolson scheme appears to be quite different from the classical Crank-Nicolson scheme. Note that this is not an explicit scheme; in OpenFOAM the implementation of this scheme has two steps, one is backward Euler (which is implicit) and the other is forward Euler (which is explicit), see [46]. The blending in OpenFOAM is controlled by the user through a factor (ψ); with $\psi = 1$ giving the pure Crank-Nicolson scheme and $\psi = 0$ giving the backward Euler scheme.

We will now move on to an evaluation of the performance of some relevant choices for the temporal scheme in OpenFOAM. A 1D advection test is used for assessing the performance of the different schemes available in OpenFOAM. We use

a combination of the same three profiles that were used for testing the convection schemes: a step, a $\sin^2$ wave, and a semi-ellipse.

The 1D computational domain is 400-cm-long in the x-direction and starts at $x = -200$ cm. A constant velocity of 1 m/s is imposed on the domain. Initial variation of ϕ is given by Equation 2.34 and a zero-gradient boundary condition is applied for ϕ on the left ($x = -200$ cm) and right ($x = 200$ cm) boundaries. The mesh consists of 400 cells; thus $\Delta x = 1$ cm, which leads to 20 cells across the $\sin^2$ wave and the semi-ellipse.

FireFOAM was adapted to solve the following equation in the PIMPLE mode:

$$\frac{\partial \phi}{\partial t} + u_x \frac{\partial \phi}{\partial x} = 0 \tag{2.39}$$

The convection term is handled using *limitedLinear 1.* No relaxation was used in this case. Every time step is considered converged when OpenFOAM's residual becomes smaller than 1e-09. The Preconditioned Bi-Conjugate Gradient (PBiCG) linear-solver is used along with the Diagonal-based Incomplete LU (DILU) preconditioner for solving the system.

The simulation is ran for a duration of 1.5 s. The exact solution for this test is given by Equation 2.34, with $(x - 150)$ replacing x; because in the absence of diffusion the profile should just translate by 150 cm in the positive x-direction during 1.5 s.

Figures 2.27 to 2.31 present results for *nOuterCorrectors*= 1 with CFL of 0.5, 0.4, 0.3, 0.25 and 0.2, respectively; with the corresponding $\Delta t = (\text{CFL}\Delta x)/u_x =$

CFL/100. The parameter *nOuterCorrectors* will be discussed briefly later. The cell values of the scalar ϕ are plotted as a function of x in these figures; for the following choices for the time integration scheme: *Euler*, *backward*, *CrankNicolson 1*, *CrankNicolson 0.9*, and *CrankNicolson 0.5*. Figures 2.32 and 2.33 provide a quantitative comparison of the schemes by displaying the L_1-norm error (ϵ) and the unboundedness measure (OU), respectively. *Euler*, as expected, is the most dissipative and can not be used for high-fidelity simulations. *CrankNicolson 0.5*, like *Euler*, is bounded for all the CFL numbers tested in this study, but lacks accuracy. *CrankNicolson 0.9* and *CrankNicolson 1* are the best in terms of accuracy but are only bounded for CFL$\leq$0.3. The *backward* scheme has the worst performance in terms of boundedness (it is only bounded for CFL$\leq$0.25) and is either close to *CrankNicolson 0.5* or close to *CrankNicolson 0.9* and *CrankNicolson 1* in terms of accuracy; depending up on CFL.

Similar simulations are performed with *nOuterCorrectors*= 2 and 3 to check this parameter's effect on the performance of different schemes. The parameter *nOuterCorrectors* represents the so-called outer loops in OpenFOAM's PIMPLE algorithm; which are needed to handle the coupling between the governing equations. The outer loop includes all the equations except continuity. At first sight one would expect the results to be independent of the value of *nOuterCorrectors* because this problem requires the solution of only one equation (Equation 2.39), but that is not the case, as elaborated below.

Results for *nOuterCorrectors*= 2 are summarized in Figures 2.34 and 2.35 and for *nOuterCorrectors*= 3 are shown in Figures 2.36 and 2.37. As can be seen in

Figures 2.33, 2.35 and 2.37, boundedness is signifcantly affected when *nOuterCorrectors* is increased from 1 to 2 but a further increase in its value to 3 does not make a big difference. For *nOuterCorrectors*>1 all the choices are bounded except *backward*, which is bounded only for CFL$\leq$0.3. In terms of accuracy, an increase in *nOuterCorrectors* from 1 to 2 has practically no effect on the performance of *Euler* and *CrankNicolson 0.5*; but the performance of the rest of the choices improves for CFL $>$ 0.3 (see Figures 2.32, 2.34 and 2.36). A further increase in *nOuterCorrectors* from 2 to 3 has no practical effect on the accuracy of the different choices. For *nOuterCorrectors*$=2$ and 3, *backward* is as good as *CrankNicolson 0.9* in terms of accuracy; with the performance of *CrankNicolson 1* being better than both of them.

Overall, based on the present results *CrankNicolson* with a factor close to 1 has the best performance, considering both accuracy and boundedness. If boundedness is disregarded then *backward* shows similar performance.

Similar to the convection schemes; the temporal schemes have also been tested after performing the simulations presented in Chapters 3 to 5. In the simulations in those chapters we use the backward scheme with a CFL of 0.5 with 3 *nOuterCorrectors*, because the same choices were made in one of the recent studies in our group [43]. In the future, we will select the temporal scheme based on its performance in benchmark cases like the one considered here.

We now turn to the discussion of turbulence models.

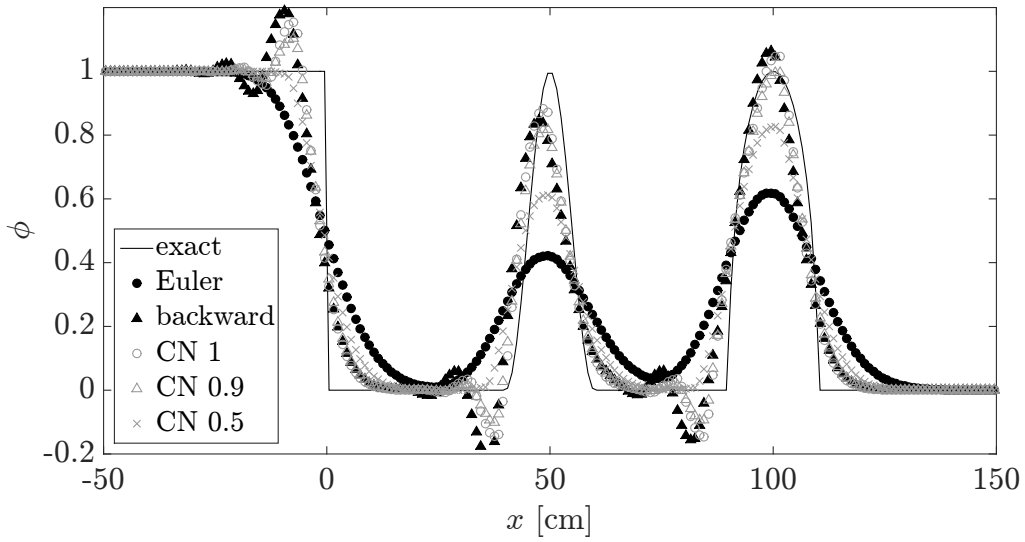

Figure 2.27: Variation of ϕ at $t = 1.5$ s in the 1D advection case with CFL = 0.5. In the legend CN stands for *CrankNicolson*. The parameter *nOuterCorrectors* is set to 1 in these simulations.

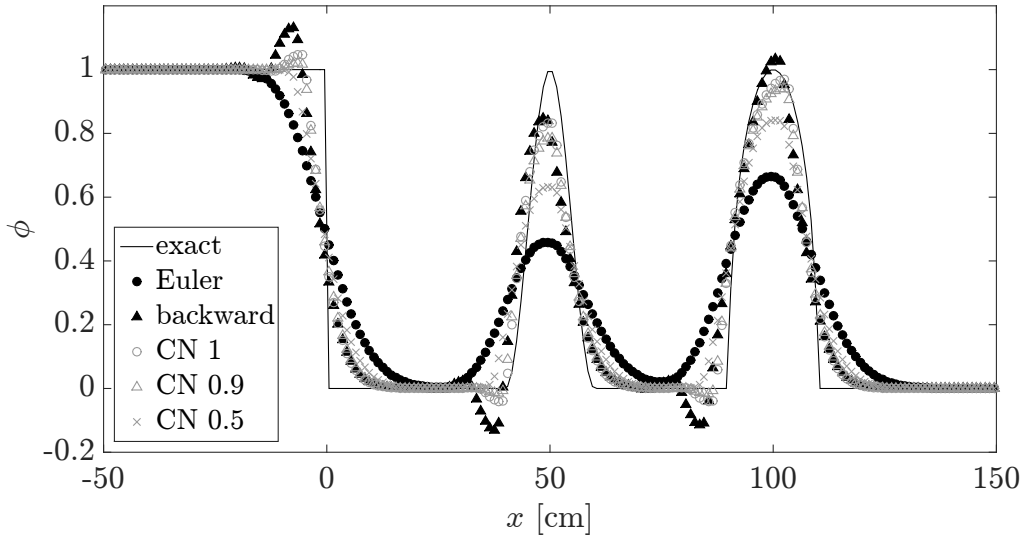

Figure 2.28: Variation of ϕ at $t = 1.5$ s in the 1D advection case with CFL = 0.4. In the legend CN stands for *CrankNicolson*. The parameter *nOuterCorrectors* is set to 1 in these simulations.

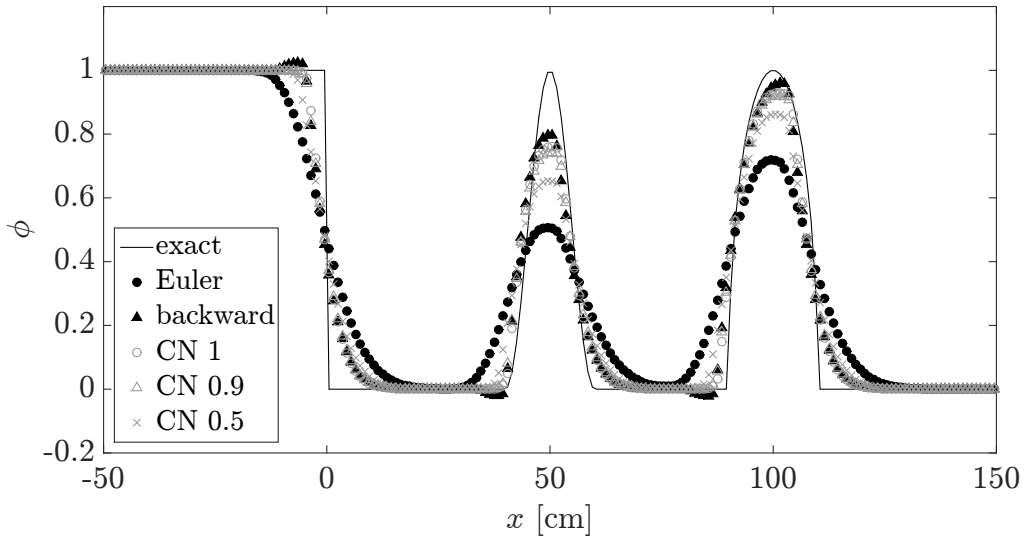

Figure 2.29: Variation of ϕ at $t = 1.5$ s in the 1D advection case with CFL $= 0.3$. In the legend CN stands for *CrankNicolson*. The parameter *nOuterCorrectors* is set to 1 in these simulations.

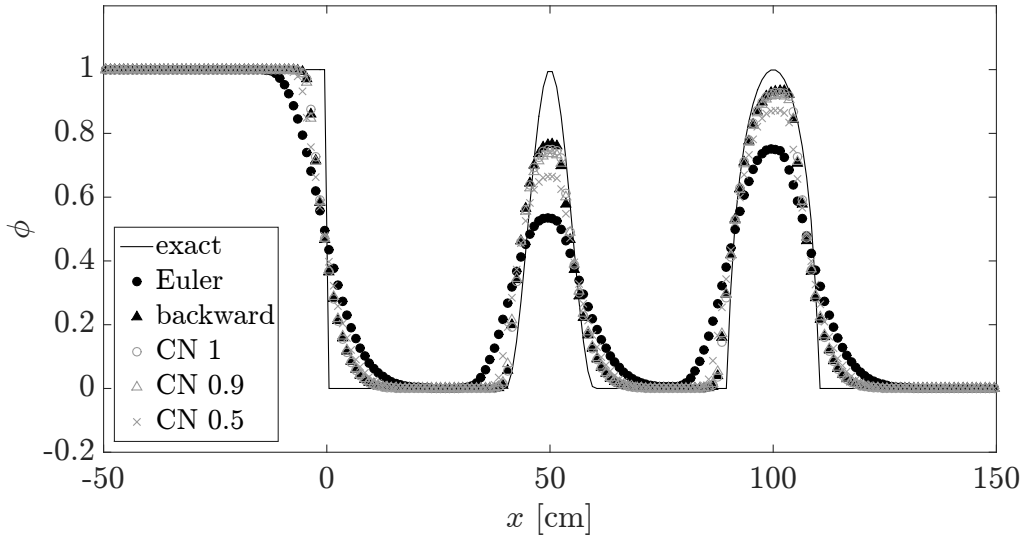

Figure 2.30: Variation of ϕ at $t = 1.5$ s in the 1D advection case with CFL $= 0.25$. In the legend CN stands for *CrankNicolson*. The parameter *nOuterCorrectors* is set to 1 in these simulations.

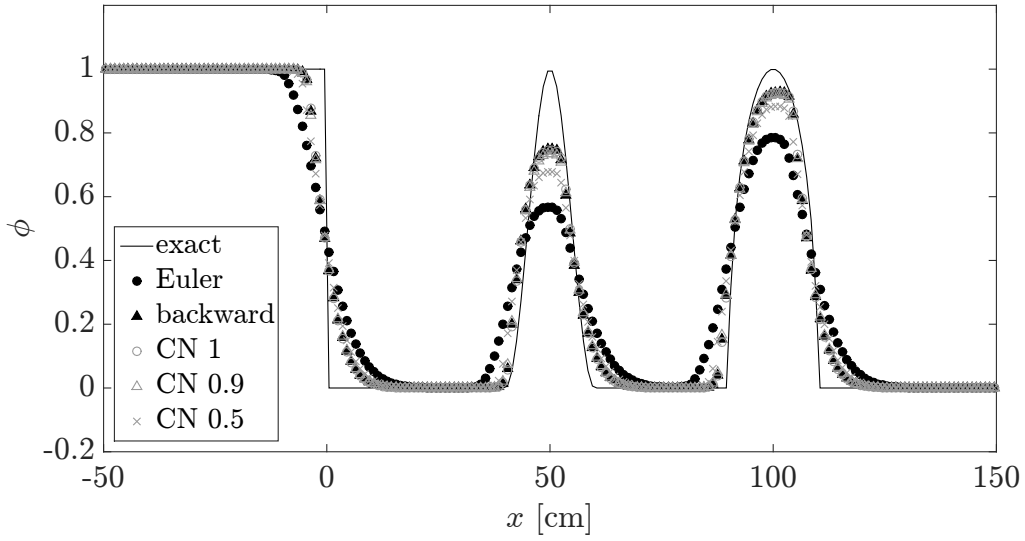

Figure 2.31: Variation of ϕ at $t = 1.5$ s in the 1D advection case with CFL = 0.2. In the legend CN stands for *CrankNicolson*. The parameter *nOuterCorrectors* is set to 1 in these simulations.

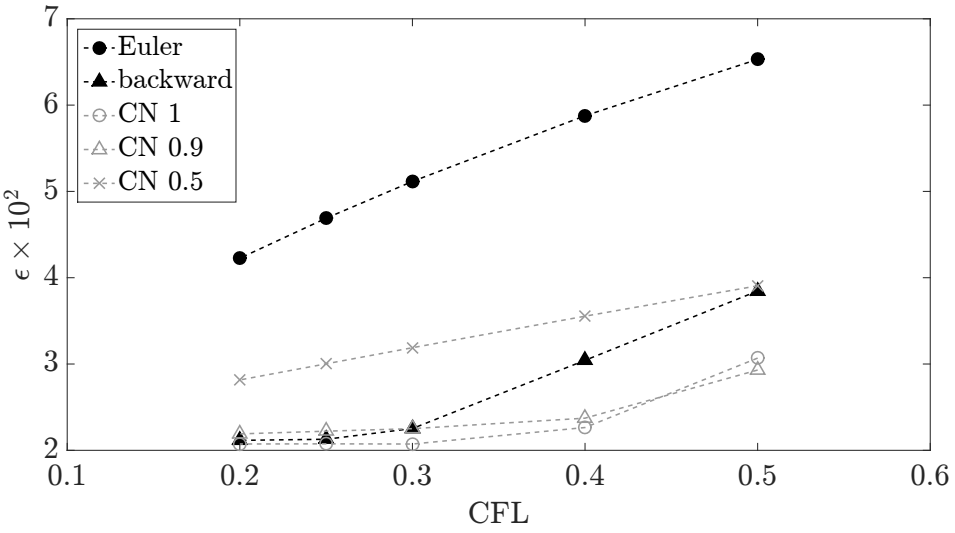

Figure 2.32: The L_1-norm error (ϵ) from the 1D advection case for different choices for the time scheme in OpenFOAM. In the legend CN stands for *CrankNicolson*. The parameter *nOuterCorrectors* is set to 1 in these simulations.

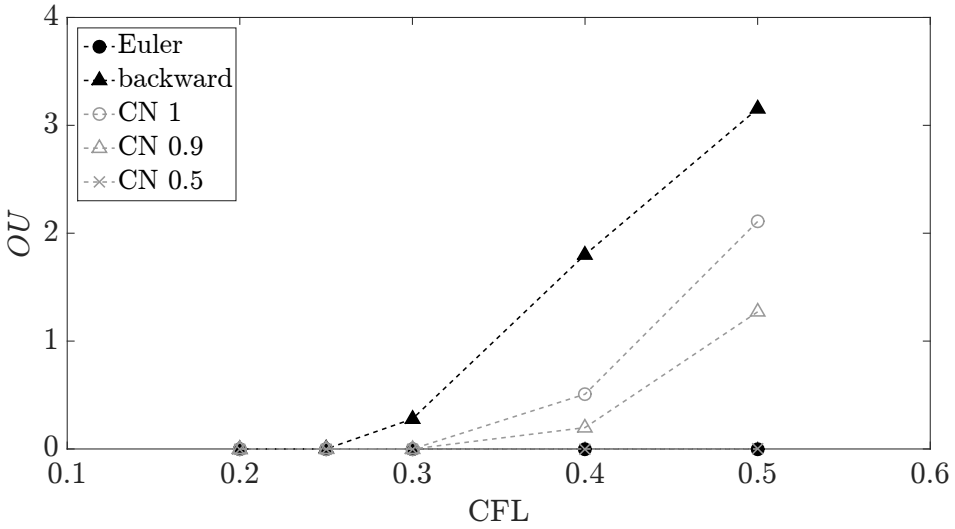

Figure 2.33: Unboundedness indicator, $OU = \sum_{n=1}^{N_{cells}}(\max(\phi_n - 1, 0) + \max(-\phi_n, 0))$, from the 1D advection case for different choices for the time scheme in OpenFOAM. In the legend CN stands for *CrankNicolson*. The parameter *nOuterCorrectors* is set to 1 in these simulations.

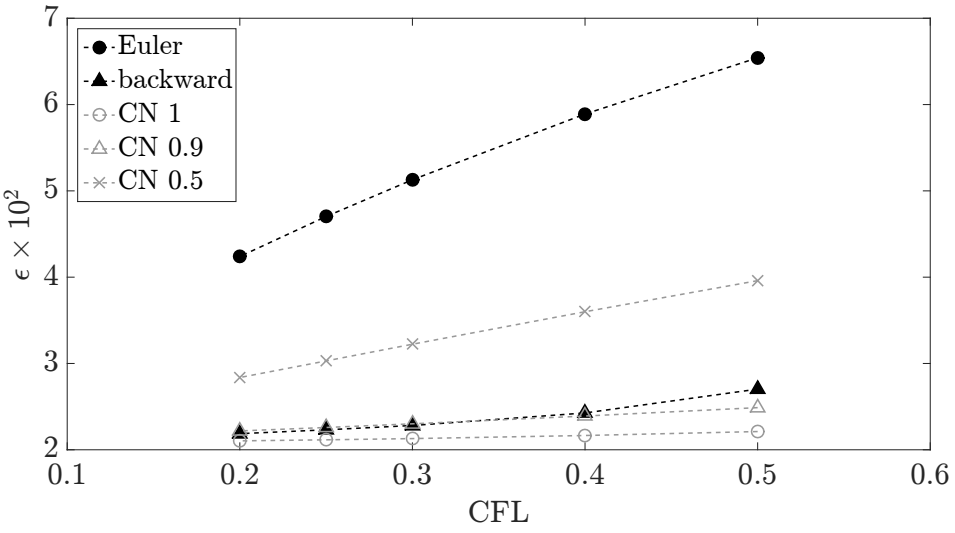

Figure 2.34: The L_1-norm error (ϵ) from the 1D advection case for different choices for the time scheme in OpenFOAM. In the legend CN stands for *CrankNicolson*. The parameter *nOuterCorrectors* is set to 2 in these simulations.

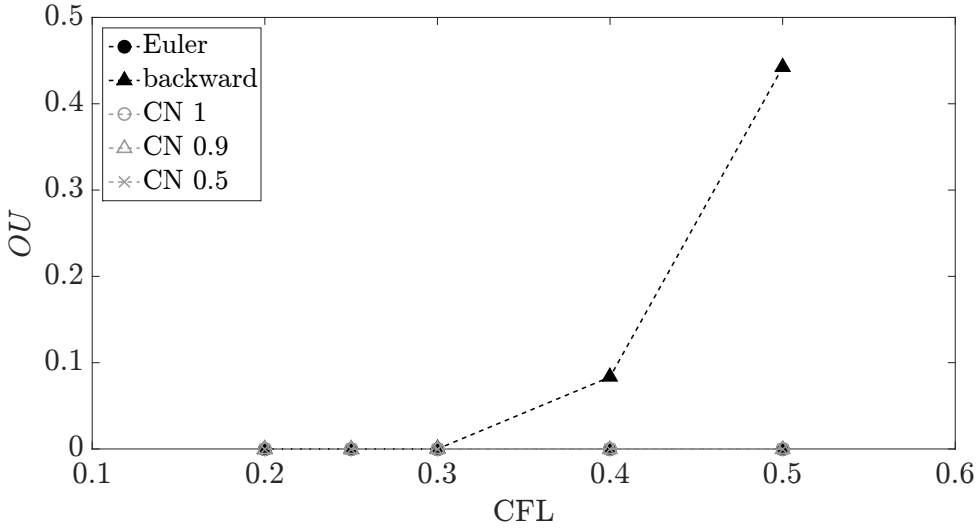

Figure 2.35: Unboundedness indicator, $OU = \sum_{n=1}^{N_{cells}}(\max(\phi_n - 1, 0) + \max(-\phi_n, 0))$, from the 1D advection case for different choices for the time scheme in OpenFOAM. In the legend CN stands for *CrankNicolson*. The parameter *nOuterCorrectors* is set to 2 in these simulations.

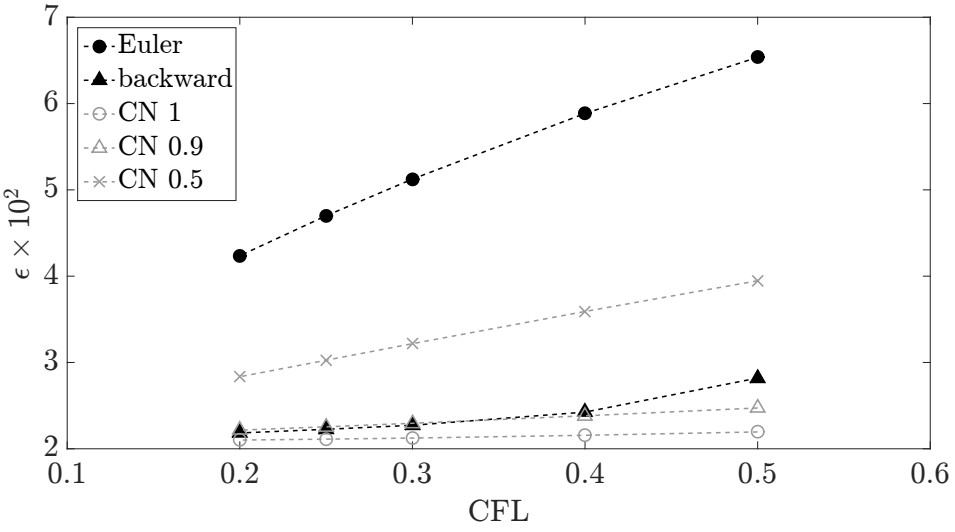

Figure 2.36: The L_1-norm error (ϵ) from the 1D advection case for different choices for the time scheme in OpenFOAM. In the legend CN stands for *CrankNicolson*. The parameter *nOuterCorrectors* is set to 3 in these simulations.

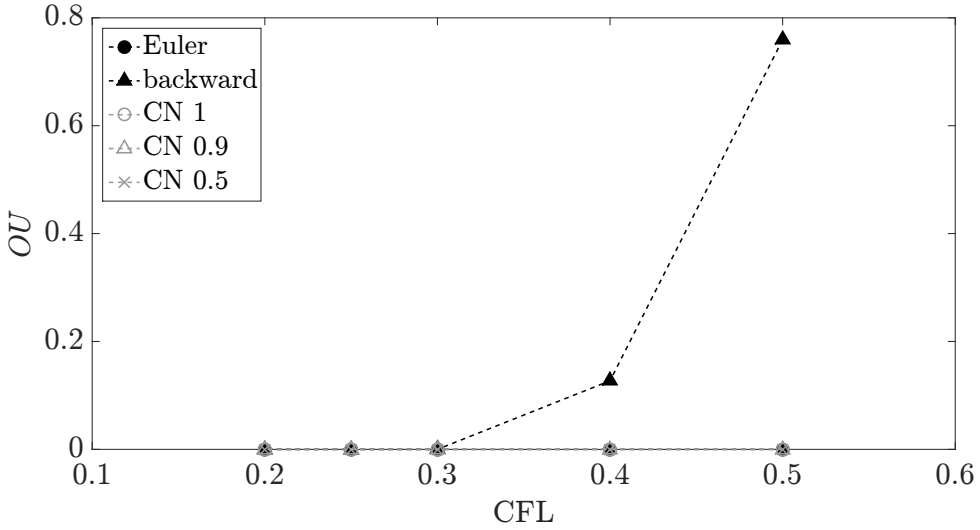

Figure 2.37: Unboundedness indicator, $OU = \sum_{n=1}^{N_{cells}}(\max(\phi_n - 1, 0) + \max(-\phi_n, 0))$, from the 1D advection case for different choices for the time scheme in OpenFOAM. In the legend CN stands for *CrankNicolson*. The parameter *nOuterCorrectors* is set to 3 in these simulations.

2.4 Turbulence models

In the LES framework not all the scales of the flow are resolved; the large scales are resolved by the grid and effects of sub-grid scales on the larger resolved scales are brought in the simulation through a model called turbulence model. In the context of the present study the first job of the turbulence model is to determine the sub-grid scale viscosity ν_{SGS} for Equations 2.2 to 2.4. The coarser the grid resolution the higher the value of ν_{SGS} and hence the greater the importance of the turbulence model. But since the simulations presented in the following are well resolved the choice of the turbulence model is not important from the standpoint of determining ν_{SGS} for Equations 2.2 to 2.4.

However, the turbulence model also provides the mixing time scale used in the combustion model (discussed later); therefore the choice of the turbulence model is still crucial. Each model has its strengths and weaknesses. Two models are used in the present study. For the co-flow stabilized turbulent line fire configuration the one-equation-eddy-viscosity model is exploited; which has been used successfully in the past for the same configuration [43]. For the cases with wind and slope, the WALE model is used as it has been shown to do well in a similar configuration [60]. Both models are described briefly below.

2.4.1 One-equation eddy viscosity model

This model, called *oneEqEddy* model in FireFOAM/OpenFOAM, is based on the solution of a transport equation for the SGS turbulent kinetic energy (TKE)

k_{SGS} [72], which is:

$$\frac{\partial\left(\overline{\rho}k_{SGS}\right)}{\partial t}+\frac{\partial\left(\overline{\rho}k_{SGS}\widetilde{u}_i\right)}{\partial x_i}=\frac{\partial}{\partial x_i}\left(\overline{\rho}\left(\nu+\nu_{SGS}\right)\frac{\partial k_{SGS}}{\partial x_i}\right)+P-\overline{\rho}\varepsilon_{SGS} \tag{2.40}$$

The SGS eddy dissipation rate is expressed as $\varepsilon_{SGS}=C_e k_{SGS}^{3/2}/\Delta$, where the model constant $C_e=1.048$ and where Δ is the filter width, which represents the grid cell size and is defined as $\Delta=(\Delta_x\Delta_y\Delta_z)^{1/3}$. The SGS eddy viscosity is calculated from the SGS kinetic energy as follows:

$$\nu_{SGS}=C_k k_{SGS}^{1/2}\Delta \tag{2.41}$$

where $C_k=0.094$. The production term, P, is written as:

$$-\frac{2}{3}\overline{\rho}\left(k_{SGS}+\nu_{SGS}\frac{\partial\tilde{u}_k}{\partial x_k}\right)\frac{\partial\tilde{u}_i}{\partial x_i}+2\overline{\rho}\nu_{SGS}\tilde{S}_{ij}\tilde{S}_{ij} \tag{2.42}$$

where the first term corresponds to the variation of TKE due to thermal expansion and the second term represents the variations of TKE due to strain rate. The strain rate tensor has been defined here in index notation as:

$$\tilde{S}_{ij}=\frac{1}{2}\left(\frac{\partial\tilde{u}_i}{\partial x_j}+\frac{\partial\tilde{u}_j}{\partial x_i}\right) \tag{2.43}$$

The turbulent mixing time scale, τ_{SGS}, used in the combustion model is defined as follows:

$$\tau_{SGS}=\frac{k_{SGS}}{\varepsilon_{SGS}}=\frac{1}{C_e}\frac{\Delta}{k_{SGS}^{1/2}} \tag{2.44}$$

2.4.2 Wall-Adapting Local Eddy-viscosity (WALE) model

In the WALE model (Nicoud et al. [73]) the SGS viscosity is expressed as:

$$\nu_{sgs}=(C_w\Delta)^2\frac{(S_{ij}^d S_{ij}^d)^{3/2}}{(\tilde{S}_{ij}\tilde{S}_{ij})^{5/2}+(S_{ij}^d S_{ij}^d)^{5/4}} \tag{2.45}$$

where the model constant $C_w = 0.55$. S_{ij}^d is a special tensor defined as:

$$S_{ij}^d = (\tilde{S}_{ik}\tilde{S}_{kj}) + (\tilde{\Omega}_{ik}\tilde{\Omega}_{kj}) - \frac{1}{3}\delta_{ij}(\tilde{S}_{mn}\tilde{S}_{mn} - \tilde{\Omega}_{mn}\tilde{\Omega}_{mn}) \tag{2.46}$$

with δ_{ij} being the Kronecker delta symbol and $\tilde{\Omega}_{ij}$ being the rotation rate tensor which can be written as:

$$\tilde{\Omega}_{ij} = \frac{1}{2}\left(\frac{\partial \tilde{u}_i}{\partial x_j} - \frac{\partial \tilde{u}_j}{\partial x_i}\right) \tag{2.47}$$

The expression for the SGS turbulent mixing time in the WALE model is:

$$\tau_{SGS} = \frac{(C_w\Delta)^2}{\nu_{SGS}} \tag{2.48}$$

2.5 Combustion model

In FireFOAM, combustion is described using a global single-step combustion equation combined with the Eddy Dissipation Concept (EDC) model [28]. EDC is used for modeling a turbulent diffusion flame assuming that the reaction is primarily controlled by turbulent mixing and the fuel mass reaction rate is expressed as:

$$\overline{\dot{\omega}_{Y_{fuel}}'''} = \frac{\overline{\rho}}{\tau_{EDC}}\min\left(\widetilde{Y}_{fuel}, \frac{\widetilde{Y}_{O_2}}{r_s}\right) \tag{2.49}$$

where, $\widetilde{Y}_{fuel}$ and $\widetilde{Y}_{O_2}$ are the filtered fuel and oxygen mass fractions, respectively and r_s the stoichiometric oxygen-to-fuel mass ratio. In the fully-developed turbulent flow regime, the EDC mixing time scale is taken from the turbulence model (Equations 2.44 and 2.48): $\tau_{EDC} = \tau_{sgs}/C_{EDC}$ and $C_{EDC} = 4$ [60]. However, this description assumes turbulent mixing and does not apply to regions where the flow is quasi-laminar. In these regions, fuel-air mixing is controlled by molecular diffusion and we may write: $\tau_{EDC} = C_{diff}\,(\Delta^2/\alpha)$, where C_{diff} is a model coefficient

($C_{diff} = 0.5$) and α is the molecular thermal diffusivity. We finally combine these two expressions and write:

$$\tau_{EDC} = \min\left(\tau_{sgs}/C_{EDC}, C_{diff}\Delta^2/\alpha\right) \tag{2.50}$$

2.6 Radiation model

Thermal radiation is known to be an important heat transfer mechanism in large-scale fires and is often considered as the dominant mechanism in wildfire spread. Because of the wavelength dependence, radiation modeling is non-trivial. There are a number of radiation models with a range of complexity in the literature [74]. These can be classified into two main groups: grey and non-grey models. Grey models assume that radiation does not vary with wavelength. In many combustion problems, an optically thin medium assumption is also made when applying grey gas models. The optically thin limit assumption neglects the self-absorption of the gas, and utilizes the Planck mean absorption coefficient, thereby simplifying the radiation treatment. Non-grey narrow-band and wide-band models that pay heed to the variation of radiative properties with wavelength, are more complex and more costly than grey models, but are more accurate.

In the present study a grey model is used. Furthermore, a non-scattering, non-absorbing, optically-thin medium is assumed and the empirical concept of a user-prescribed global radiative loss fraction χ_{rad} is invoked ($\chi_{rad} = 0.23$ is used in the present work). The final form of the Radiative Transfer Equation (RTE) that

is solved in the present study is:

$$\frac{dI}{ds} = \frac{\chi_{rad}\overline{\dot{\omega}'''_{h_s}}}{4\pi} \tag{2.51}$$

where I is the radiation intensity and s the distance along a particular ray. The radiative power density (*i.e.*, the radiation source term that appears in the enthalpy equation, Equation 2.3) is then obtained as the integral of the right-hand side of Equation 2.51 over angular space:

$$\overline{\dot{q}'''_r} = \int_{4\pi} \left(\frac{\chi_{rad}\overline{\dot{\omega}'''_{h_s}}}{4\pi} \right) d\Omega = \chi_{rad}\overline{\dot{\omega}'''_{h_s}} \tag{2.52}$$

The assumption of an emitting but non-absorbing medium as well as that of a prescribed radiative loss fraction should be viewed as intermediate modeling steps.

3: Structure of a turbulent line fire without wind and slope

3.1 Introduction

In this chapter we focus on the validation of our numerical approach, and simulate a co-flow stabilized, turbulent, buoyant, methane-fueled line fire in the absence of wind and slope [75]. This configuration is chosen because of the availability of high resolution temperature measurements which enable a higher order validation of the numerical methodology. Higher order validation is needed in the present study because not only the mean results but also the grid resolved fluctuations will be analyzed in Chapters 4 and 5 in order to understand the effects of wind and slope on the structure of the same line fire.

This chapter is organized as follows. The experimental configuration is described in the next section followed by the description of the numerical configuration. Then the results are presented and discussed. Finally, some concluding remarks are made.

3.2 Experimental configuration

The experimental configuration considered here was primarily designed for studying fire suppression [76, 77]. It has already been simulated before [43], but

recently more detailed measurements (described below) have been performed for this configuration. Briefly, this configuration corresponds to a co-flow stabilized buoyant, turbulent, methane-fueled diffusion flame [77, 78]. Flames are stabilized above a 5-cm-long by 50-cm-wide slot burner surrounded by a 15-cm-long by 60-cm-wide plate of ceramic fiberboard which itself is surrounded by a 50-cm-long by 75-cm-wide air co-flow (Figure 3.1). The plate adds a horizontal component to the flow motion near the flame base and was introduced in previous work with the intent to promote faster transition to fully turbulent flow conditions [77].

The methane velocity is 6.0 cm/s, corresponding to a mass flow rate of 1.0 g/s, and a nominal total heat release rate of 50 kW. The air co-flow velocity is $\approx$ 25 cm/s, corresponding to a mass flow rate of 85 g/s which is approximately five times the stoichiometric requirement of the methane flow. Note that this flow rate is too low to supply all of the gas entrained by the flame and that while the base of the flame is exclusively exposed to the co-flow, the tip region of the flame is exposed to entrained air from the open ambient. While an undesirable feature, numerical tests suggest that this effect remains limited and that the heat release rate associated with the uncontrolled entrained ambient air corresponds to less than 5% of the total heat release rate of the flame [75].

Previously, 1000 μm bead-diameter K-type thermocouple probes (uncertainty $\pm$2 K; response time $\sim$3 s) were used [43] for measurements, whereas currently 12.7-μm-diameter Type-S (Pt/10%Rh) thermocouples with a sampling rate of 10,000 Hz are being used in the experiment. The time constant of the thermocouples is estimated to be $\approx$1 ms for the conditions encountered in the present configuration.

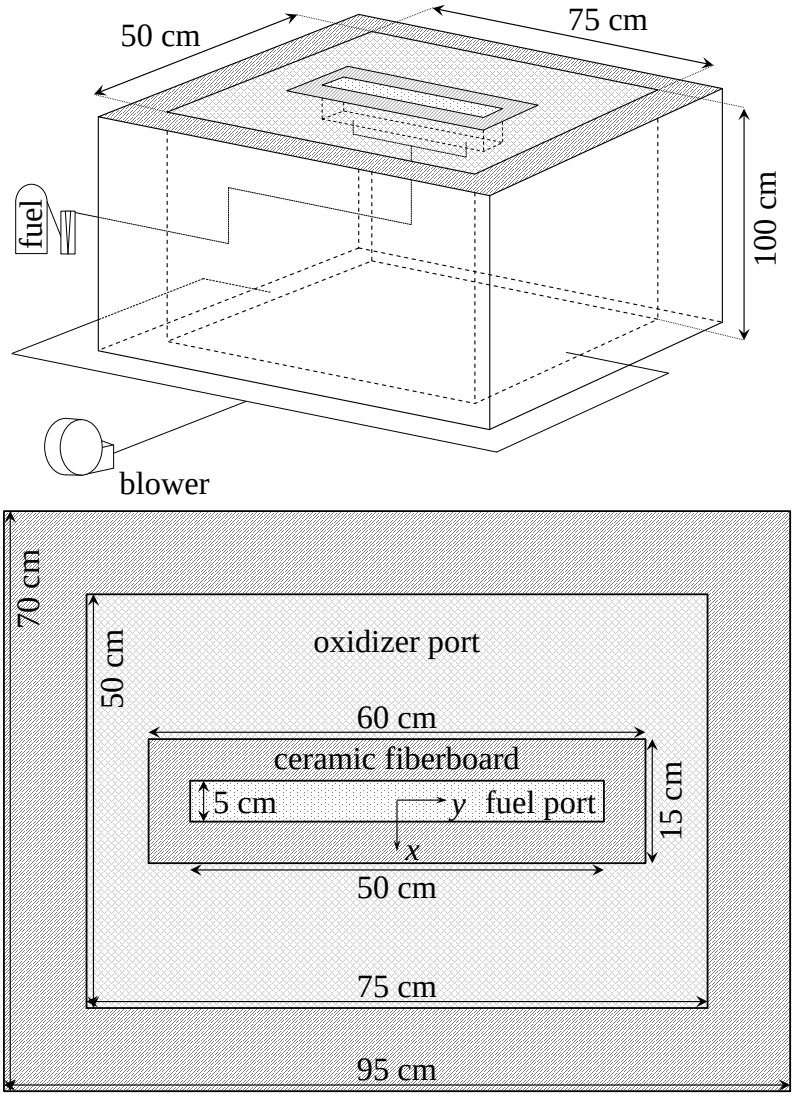

Figure 3.1: Diagram of experimental facility (top) and top-view of burner/co-flow outlet (bottom); reproduced from [77].

The new thermocouples, due to their small bead size and fast response time, can be considered to be measuring the real, time-resolved, gas temperatures. First, such measurements allow direct comparisons between measured and simulated mean and rms temperatures, without the need for any correction for radiative heat losses, as was done earlier [43]; second, they allow the determination of integral time scales which can subsequently be compared with simulation results; and finally, they allow more detailed comparisons beyond mean and rms values of temperature e.g., one can compare temperature probability density functions (PDFs). Overall, the recent experimental data enables a more rigorous validation of our numerical approach.

3.3 Numerical configuration

The numerical configuration is exactly the same as was presented in [43]. The configuration is shown in Figure 3.2, which visualizes the simulated flame at ambient condition. The computational domain is 200-cm-long in the cross-stream x-direction, 85-cm-wide in the spanwise y-direction and 200-cm-high in the vertical z-direction. Boundary conditions for the fuel port (1 g/s methane at 306 K) and oxidizer port (85 g/s air at 299 K) are specified to match the experiment. Note that both convective and diffusive mass fluxes are taken into account at the fuel port, which is important because of the small convective velocity (= 6 cm/s) at the fuel port [42]. The domain volume is initialized with quiescent air at 295 K.

A block-structured grid is used and features three levels of grid resolution (Figure 3.2). The level-one refinement block contains the flame region and features an almost uniform grid with nearly cubic cells of size equal to ≈5 mm. The burner

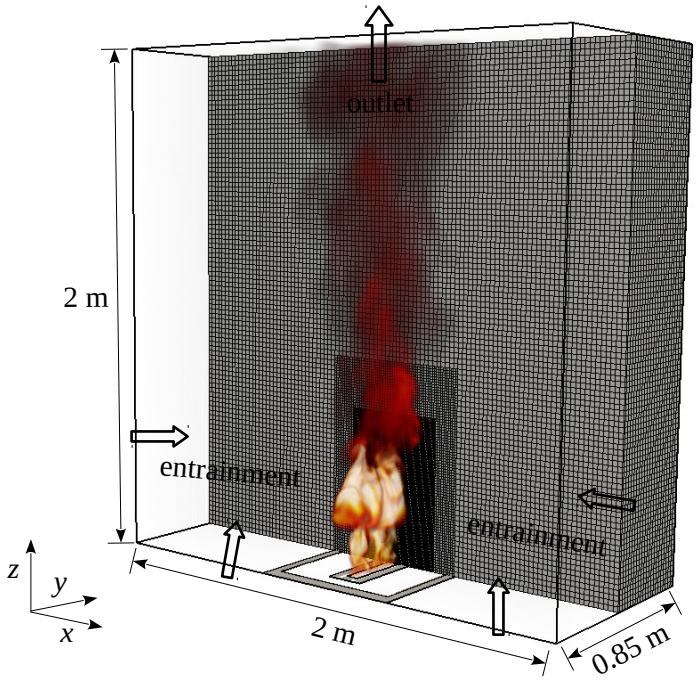

Figure 3.2: Illustration of the FireFOAM numerical configuration; the 50 kW methane diffusion flame is visualized using volume rendering of temperature.

length is resolved with 12 grid cells. The level-one refinement block is 40-cm-long, 60-cm-wide, and 60-cm-high. The level-two refinement block features an almost uniform grid with nearly cubic cells of size equal to ≈10 mm; this block is 60-cm-long, 60-cm-wide, and 80-cm-high. The level-three refinement block contains the far-field air entrainment and upper plume regions and features an almost uniform grid with nearly cubic cells of size equal to ≈20 mm. The total number of cells is 1.76 million.

All simulations are run for a total duration of 30 s. Time-mean statistics for quantities of interest are gathered typically over the final 20 s of each simulation, during a period when the flow field is statistically stationary and initial transients can be disregarded.

Simulations are conducted using 80 processors on the University of Maryland Deepthought2 high performance computing cluster. A typical simulation requires roughly 5000 CPU hours using Intel Ivy Bridge E5-2680v2 2.80 GHz processors.

3.4 Results and discussion

3.4.1 Mean flame height and spatial variations of mean and rms vertical velocity

Figure 3.3 presents the mean flame height both from FireFOAM and experiment. Variations of mean and *rms* vertical velocity w, from FireFOAM, along the burner centerline are also shown in these plots. Mean vertical velocity expected, in the plume zone, from a correlation in the literature, $2.04(gI/(\rho_\infty c_{p,\infty} T_\infty))^{1/3}$, [79] is

also included in the top panel in Figure 3.3. Most of the data in these plots have already been discussed in a previous publication from our group [43] and the new experimental data does not affect this discussion in any way; but it is being briefly discussed here again for completeness.

As can be seen, the mean flame height predicted by FireFOAM (54.4 cm) is in good agreement with that seen in the experiment (50 cm). But as has already been pointed out in [43] the definitions used in the experiment and simulation are different: in the experiment it is based on a 50% intermittency criterion for visible flame emission [77], whereas in the simulation it is based on time-averaging of the maximum elevation of the instantaneous contour of volumetric heat release rate (200 $\mathrm{kW/m^3}$).

The mean vertical velocity $\overline{w}$ profile presented in the top panel in Figure 3.3 is obtained by time- and spanwise-averaging (between $-10 \leq y \leq 10$ cm) the grid-resolved w. As shown, $\overline{w}$ starts from a low value at 0 elevation because of the boundary condition at the burner face and increases fairly rapidly due to buoyancy to a value of ≈ 2.5 m/s at ≈ 50 cm elevation (mean flame height). Beyond 50 cm elevation $\overline{w}$ stays close to 2.5 m/s. The small jumps seen in the $\overline{w}$ profile at 60 and 80 cm elevations are because of the jumps in the grid resolution (see Figure 3.2). In the plume zone (or above the mean flame height) the FireFOAM profile agrees reasonably well with the correlation in the literature $2.04(gI/(\rho_\infty c_{p,\infty} T_\infty))^{1/3}$ [79]. It should be noted that for the coefficient in the correlation (whose value is set to 2.04 here), the values reported in the literature range from 1.66 to 2.13 [79]; this accounts for some of the differences seen between FireFOAM and the correlation.

The vertical velocity fluctuation values, in terms of w_{rms}, reported in Figure 3.3 are obtained by spanwise averaging (between $-10 \leq y \leq 10$ cm) the *rms* of $(w(x,y,z,t) - \overline{w(x,y,z,t)})$, where $w(x,y,z,t)$ denotes the grid-resolved vertical velocity at location (x,y,z) at time t and the overbar symbol denotes time averaging. So the w_{rms} values reported in Figure 3.3 only represent the fluctuations captured on the grid but as has been discussed in [43], the present simulations are well-resolved, thus, most of the turbulent fluctuations are captured on the grid and w_{rms} reported in Figure 3.3 is expected to be very close to the real values of w_{rms} that one would get e.g., from DNS. The w_{rms} profile also starts from a low value at 0 elevation (because of the fixed velocity boundary condition at the burner face); it then increases rapidly to a value of $\approx$ 1 m/s at $\approx$25 cm elevation (the mid flame height) and stays at that level up to $\approx$ 60 cm elevation; then it dips suddenly to a value of $\approx$ 0.9 m/s at 60 cm elevation because of the grid resolution jump and stays almost constant till $\approx$ 80 cm elevation; it then dips further down suddenly to a value of $\approx$ 0.8 m/s at 80 cm elevation because of the second grid resolution jump; then it stays close to $\approx$ 0.8 m/s throughout the rest of the computational domain. The w_{rms} value dips because of grid resolution jumps because with a reduction in grid resolution the fluctuations captured on the grid are expected to decrease. The value of the turbulent intensity is $\approx$ 30% throughout most of the plume zone.

We will now move on to a discussion of the mean and *rms* temperature profiles from FireFOAM simulations and experimental measurements.

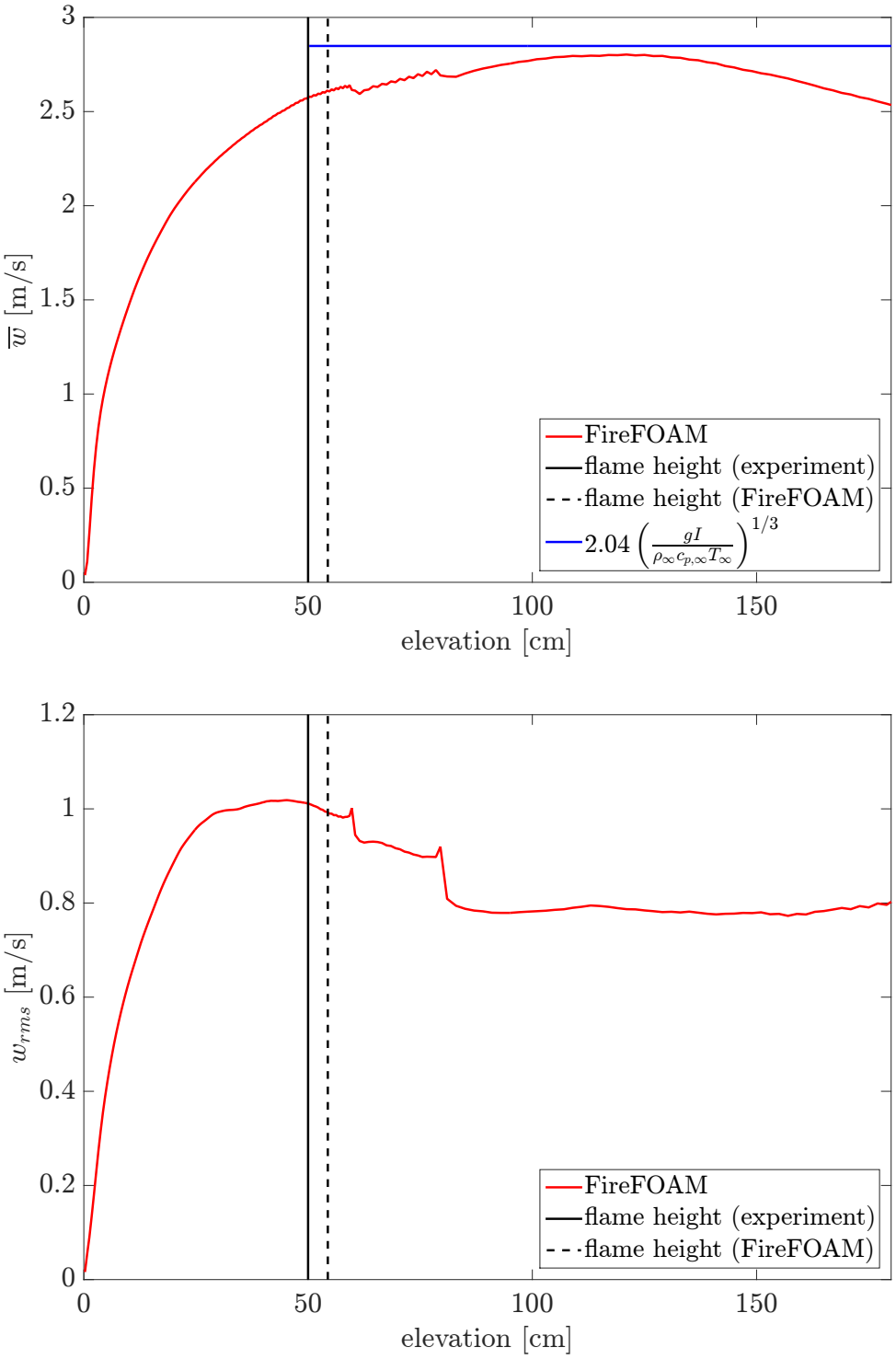

Figure 3.3: Mean (top) and *rms* (bottom) vertical velocity profiles along the burner centerline. The vertical solid (dashed) line represents the mean flame height from experiment (FireFOAM).

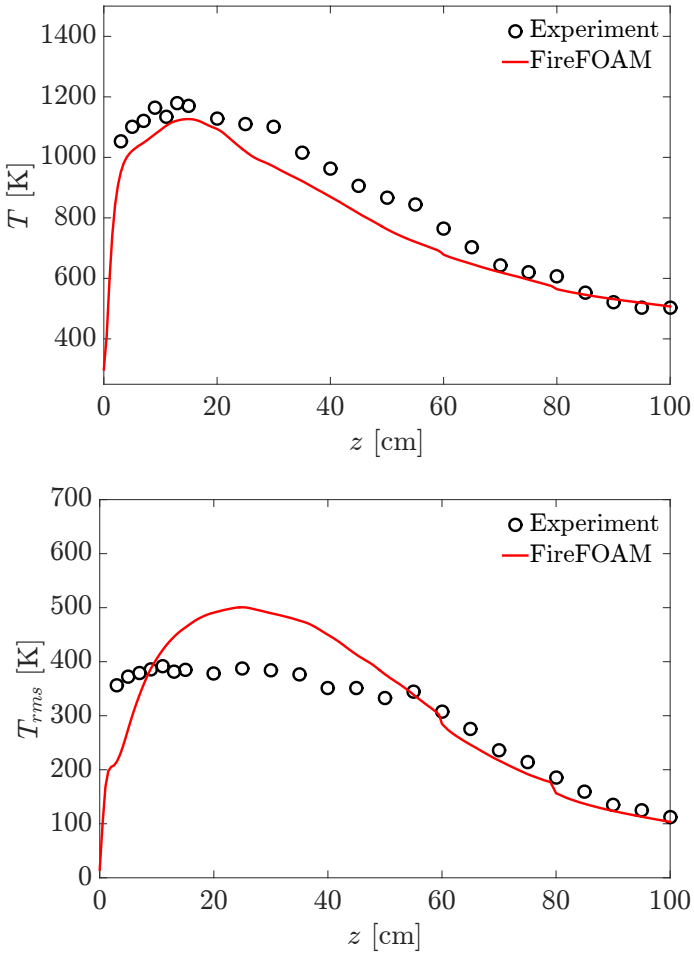

Figure 3.4: Mean and *rms* temperature profiles along the burner centerline. Comparison between experiment and FireFOAM.

3.4.2 Spatial variations of mean and rms temperature

In this section we consider the comparisons between measured and simulated profiles of mean and *rms* temperature along the vertical centerline and along x at two elevations: 25 and 50 cm (Figures 3.4 to 3.6). The mean and *rms* temperature values are obtained using the same methods that were used to extract the mean and *rms* vertical velocity values in the previous section.

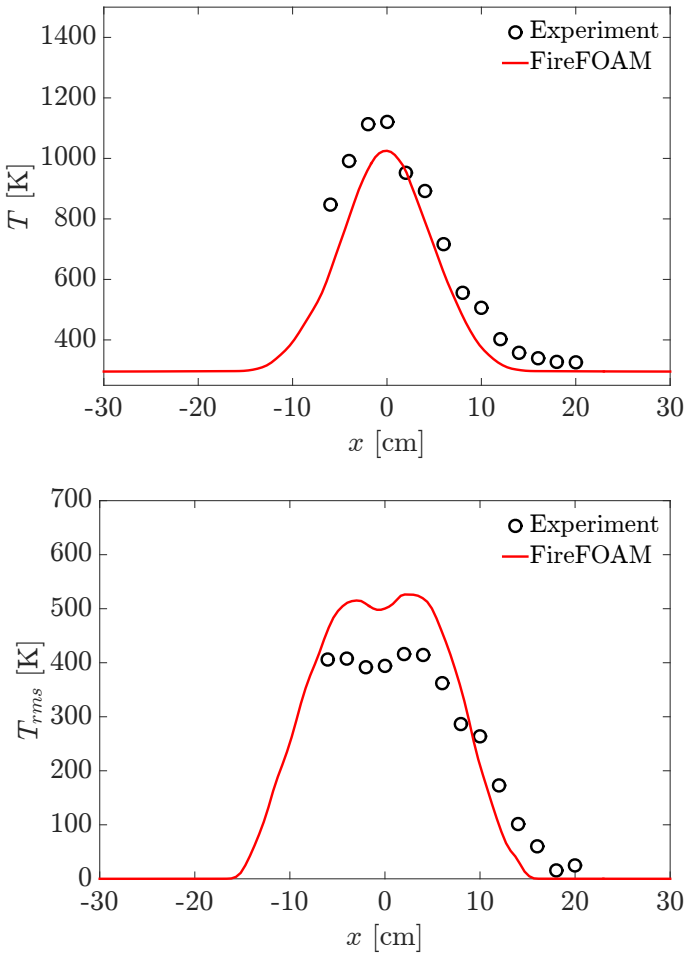

Figure 3.5: Mean and *rms* temperature profiles along x at 25 cm elevation. Comparison between experiment and FireFOAM.

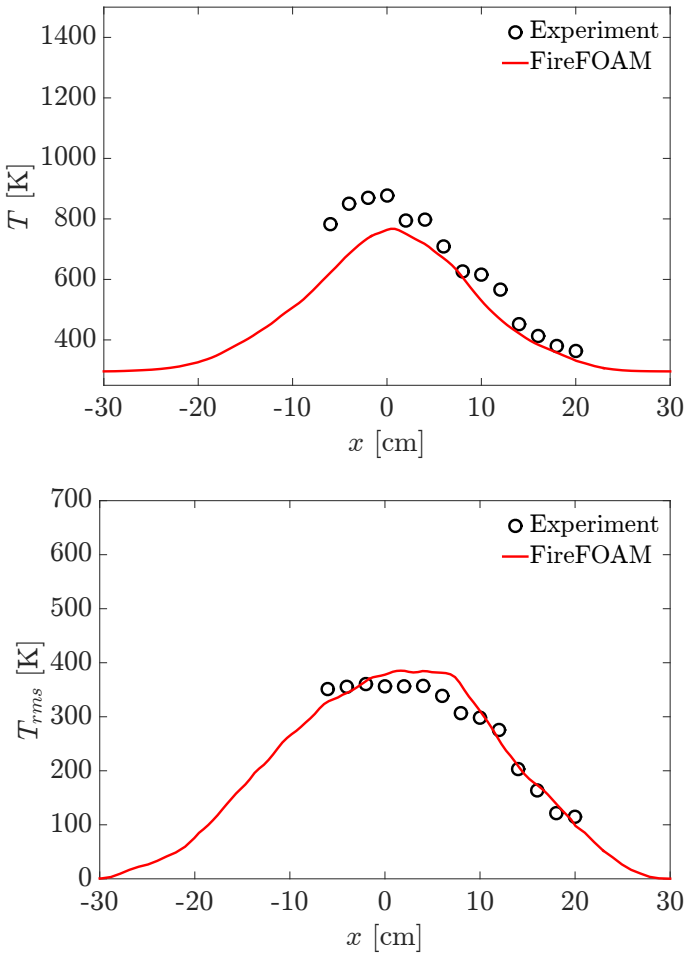

Figure 3.6: Mean and *rms* temperature profiles along x at 50 cm elevation. Comparison between experiment and FireFOAM.

Figure 3.4 shows comparisons along the vertical centerline. The mean temperature in both experiment and FireFOAM simulation increases rapidly with elevation to a value of ≈1200 K at ≈ 15 cm elevation and then decays at a slower rate with a further increase in elevation. Overall, FireFOAM agrees well with the measurements. For T_{rms} the simulated profile follows the same trend, rapidly reaching a value of about 500 K at ≈ 25 cm elevation (mid flame height) and then decaying relatively slowly with elevation afterwards; whereas the measured profile has a plateau that extends up to ≈ 50 cm elevation (flame height) and then decays at a rate similar to the simulated profile. The T_{rms} profile suggests that in FireFOAM, at elevations lower than ≈50 cm, the flow is relatively more turbulent than that in the experiment. Nevertheless, the simulations agree reasonably well with measurements.

As one would expect from Figure 3.4, at 25 cm elevation the mean temperature peak is underpredicted (Figure 3.5 top) and the T_{rms} peak is overpredicted by FireFOAM (Figure 3.5 bottom). The flame width is predicted fairly well at this elevation. The overall agreement between experiment and FireFOAM in Figure 3.5 is reasonably good.

Similarly, the overall agreement between experiments and simulations, for both mean temperature and T_{rms}, is reasonably good at 50 cm elevation as well (Figure 3.6); albeit there is an underprediction in the peak mean temperature.

We now move on to a discussion of the integral length and time scales.

3.4.3 Integral length and time scales

Determination of integral length and time scales in a problem is attractive not only because of validation but also because they e.g., enable assessment of grid resolution and domain size and also provide a quantitative understanding of the flow structure. For determining the integral length and time scales, profiles of the normalized correlation function, $R_{TT}(x, y, z, \Delta x, \Delta y, \Delta z, \Delta t)$, are needed, which can be written as:

$$R_{TT}(x, y, z, \Delta x, \Delta y, \Delta z, \Delta t) = \frac{\overline{T'(x, y, z, t)T'(x + \Delta x, y + \Delta y, z + \Delta z, t + \Delta t)}}{\overline{T'(x, y, z, t)T'(x, y, z, t)}} \tag{3.1}$$

where the overbar symbol denotes time averaging, $T'(x, y, z, t)$ represents the temperature fluctuation at location (x, y, z), at time t and is defined as follows:

$$T'(x, y, z, t) = T(x, y, z, t) - \overline{T(x, y, z, t)} \tag{3.2}$$

with $T(x, y, z, t)$ representing the grid-resolved temperature at location (x, y, z), at time t. $T'(x + \Delta x, y + \Delta y, z + \Delta z, t + \Delta t)$ represents the temperature fluctuation at location $(x + \Delta x, y + \Delta y, z + \Delta z)$, at time $(t + \Delta t)$.

We first evaluate the vertical variation of the integral length scale in the y-direction L_y. Currently no experimental data is available for L_y but it is nevertheless evaluated below for the other reasons discussed above. For quantifying L_y at different elevations we extracted profiles of the normalized correlation function for $x = 0$, $y = 0$, $\Delta x = 0$, $\Delta z = 0$ and $\Delta t = 0$

$$R_{TT}(0, 0, z, 0, \Delta y, 0, 0) = \frac{\overline{T'(0, 0, z, t)T'(0, 0 + \Delta y, z, t)}}{\overline{T'(0, 0, z, t)T'(0, 0, z, t)}} \tag{3.3}$$

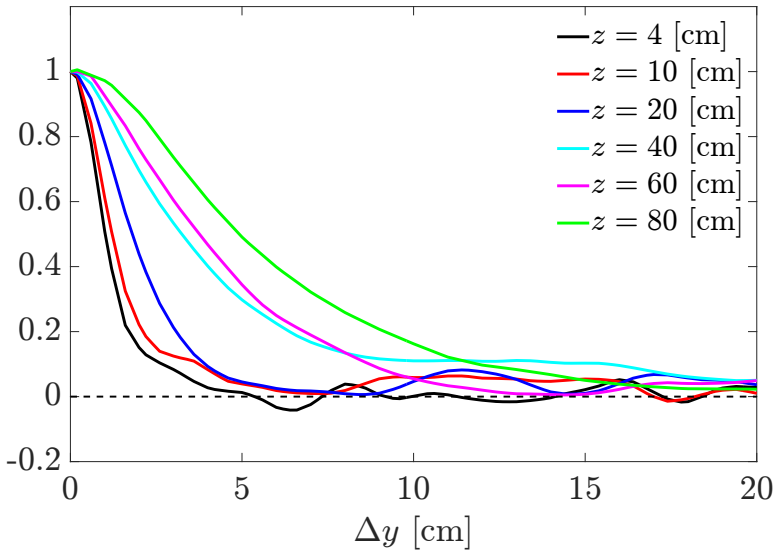

Figure 3.7: Profiles of the normalized correlation function $R_{TT}(0,0,z,0,\Delta y,0,0)$, see Equation 3.3, at different elevations, extracted from FireFOAM.

from FireFOAM (see Figure 3.7), all of which by definition, start from unity and move with different rates towards zero with Δy, where they end up oscillating.

As is well known [80], normalized correlation profiles can be processed in several different ways to extract the integral length (or time) scales. Consequently, five different definitions of the integral length scale are explored (Figure 3.8) and are presented below:

$$L_y = \int_0^{\infty} R_{TT}(0,0,z,0,\Delta y,0,0)d\Delta y \tag{3.4}$$

$$L_y = \int_0^{\Delta y_{(R_{TT}(0,0,z,0,\Delta y,0,0)=1/e)}} R_{TT}(0,0,z,0,\Delta y,0,0)d\Delta y \tag{3.5}$$

$$L_y = \int_0^{\Delta y_{(R_{TT}(0,0,z,0,\Delta y,0,0)=0.2)}} R_{TT}(0,0,z,0,\Delta y,0,0)d\Delta y \tag{3.6}$$

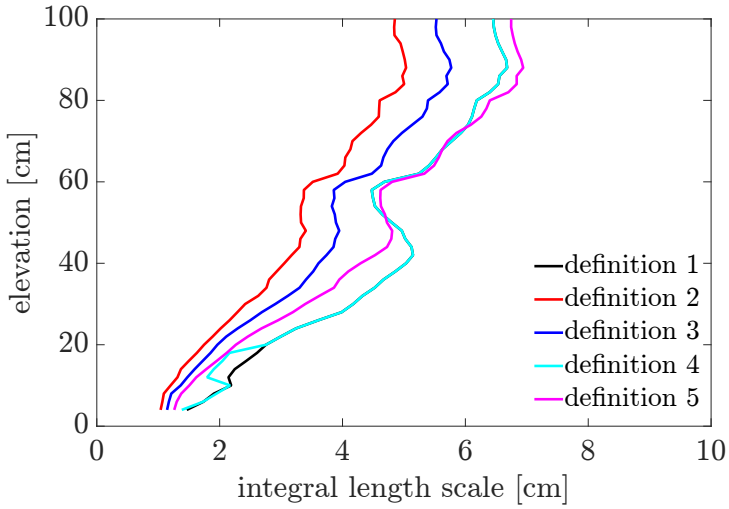

Figure 3.8: Variation of L_y with elevation extracted from FireFOAM. Here L_y is the integral length scale in the y-direction. Definitions 1, 2, 3, 4 and 5 are given in Equations 3.4, 3.5, 3.6, 3.7 and 3.8, respectively.

$$L_y = \int_0^{\Delta y1_{(R_{TT}(0,0,z,0,\Delta y,0,0)=0.0)}} R_{TT}(0,0,z,0,\Delta y,0,0)d\Delta y \tag{3.7}$$

$$R_{TT}(0,0,z,0,\Delta y,0,0)_{(\Delta y=L_y)} = 1/e \tag{3.8}$$

where $\Delta y1_{(R_{TT}(0,0,z,0,\Delta y,0,0)=0.0)}$ refers to the first value of Δy for which the normalized correlation function $R_{TT}(0,0,z,0,\Delta y,0,0)$ becomes 0. Equations 3.4 to 3.8 correspond to definitions one to five in Figure 3.8, respectively.

First, all five definitions provide similar magnitudes and vertical variations of L_y. Second, at the base the length scale is ≈2 cm, which is what Linear Stability Theory (LST) for Rayleigh Taylor Instability (RTI) suggests [81]. Third, the length scale increases with elevation as one would expect considering experimental and computational visualizations (see e.g., Figure 3.11). Finally, the grid resolution

jumps at 60 and 80 cm elevation (Figure 3.2) which should be borne in mind when interpreting these profiles. Definition five ($R_{TT}(0,0,z,0,\Delta y,0,0)_{(\Delta y=L_y)} = 1/e$) is chosen for the present study owing to its simplicity, and hence a similar definition ($R_{TT}(0,0,z,0,0,0,\Delta t)_{(\Delta t=\tau)} = 1/e$) will be applied in the following to extract the integral time scale (ITS), τ. Where $R_{TT}(0,0,z,0,0,0,\Delta t)$ reads:

$$R_{TT}(0,0,z,0,0,0,\Delta t) = \frac{\overline{T'(0,0,z,t)T'(0,0,z,t+\Delta t)}}{\overline{T'(0,0,z,t)T'(0,0,z,t)}} \tag{3.9}$$

Profiles of $R_{TT}(0,0,z,0,0,0,\Delta t)$ at different elevations are presented in Figure 3.9 both from experiment and FireFOAM. Again the profiles by definition start from unity, and decrease with Δt, and fluctuate for large values of Δt. As one would expect from these profiles, the time scales from measurements and simulations compare favorably (Figure 3.10 top). The corresponding vertical length scale L_z comparison is also shown in Figure 3.10 (bottom). For converting integral time scales to vertical integral length scales, the time- and spanwise-averaged vertical velocity profile from FireFOAM is used in the expression, $L_z = \overline{w}\tau$ (where, the overbar symbol denotes time and spanwise averaging, w is the vertical flow velocity). Overall, similar to the horizontal length scale L_y, the vertical length scale L_z also increases with elevation. As one would expect from flame visualization (see e.g., Figure 3.11) L_z is consistently larger than L_y (Figure 3.12).

Next we consider the simulated and measured temperature PDFs.

3.4.4 Temperature Probability Density Functions (PDFs)

Before comparing measured temperature PDFs with temperature PDFs from FireFOAM, the convergence of the PDFs (both measured and simulated) is checked.

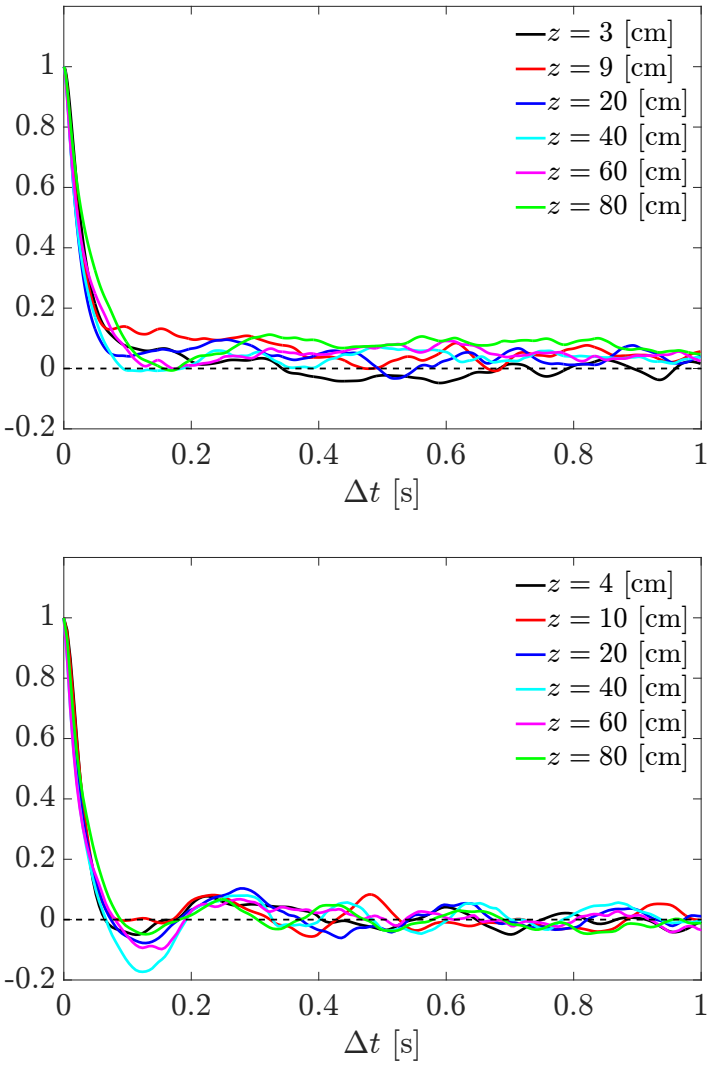

Figure 3.9: Profiles of the normalized correlation function $R_{TT}(0, 0, z, 0, 0, 0, \Delta t)$, see Equation 3.9, at different elevations, extracted from experiment (top) and FireFOAM (bottom).

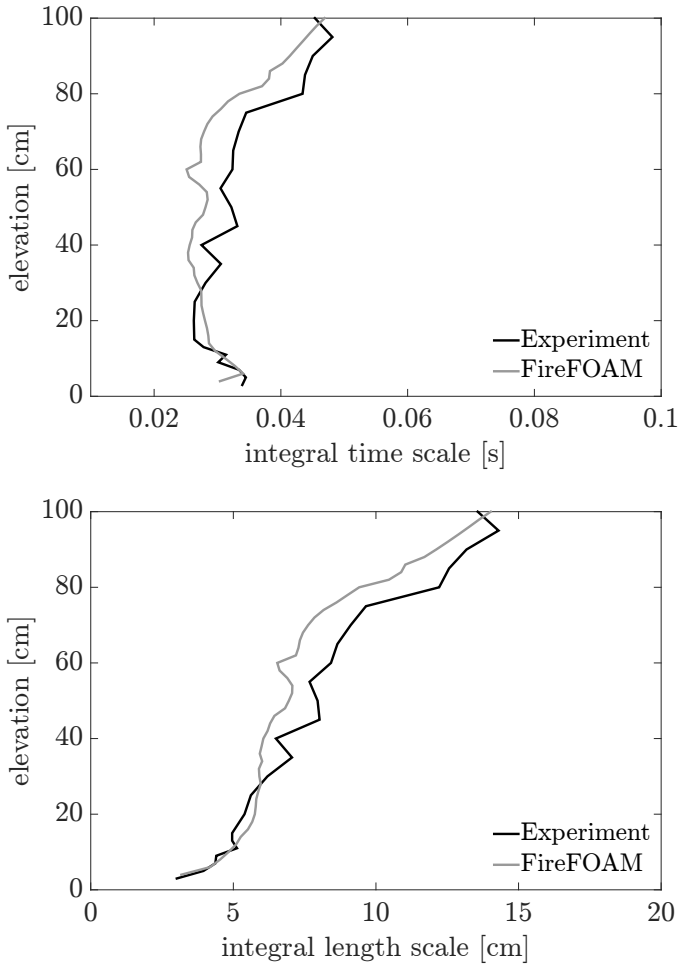

Figure 3.10: Variation of integral time scale (top) and vertical integral length scale L_z (bottom) with elevation. Comparison between experiment and FireFOAM.

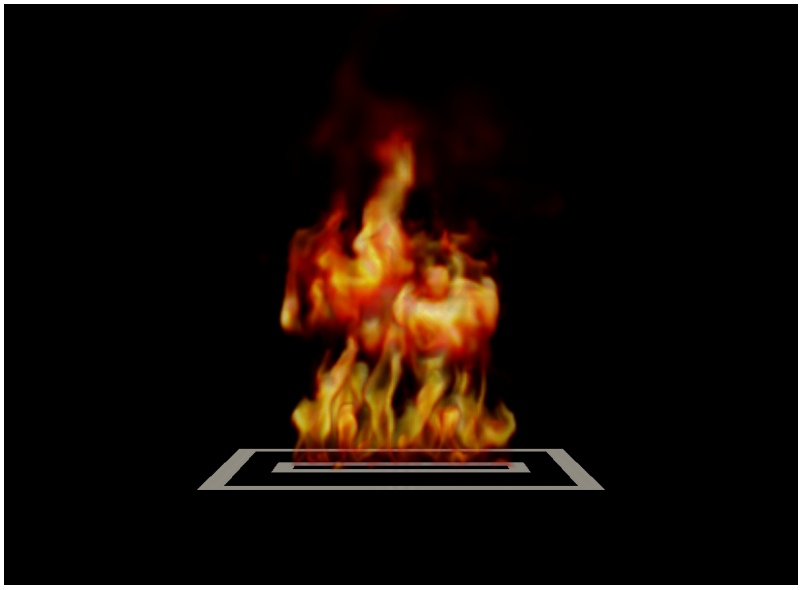

Figure 3.11: Simulated flame structure for the co-flow stabilized, turbulent, buoyant line fire without wind and slope; visualized using volume rendering of temperature.

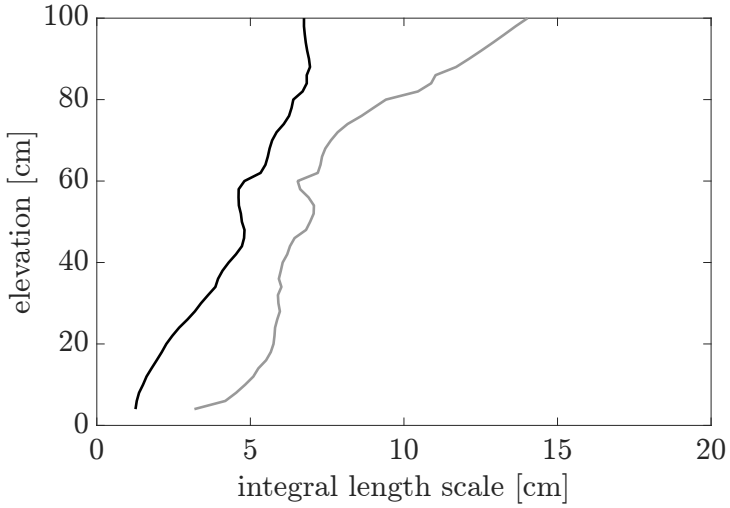

Figure 3.12: Simulated horizontal length scale L_y (black solid line) compared with the simulated vertical length scale L_z (grey solid line) along the burner centerline.

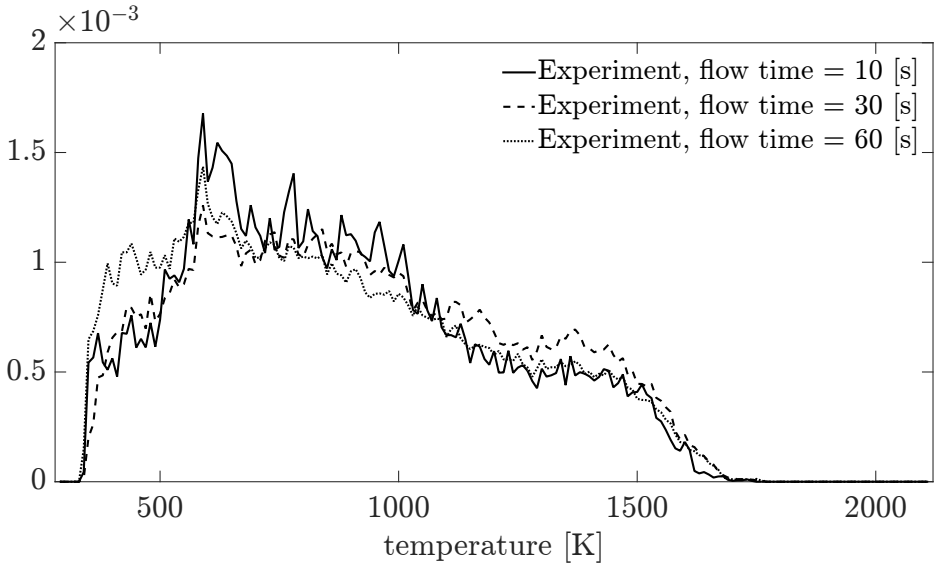

Figure 3.13: Experimental temperature PDF at 50 cm elevation along the centerline. Sensitivity to flow time.

Figure 3.13 shows the sensitivity of a typical experimental temperature PDF (at 50 cm elevation along the burner centerline) to flow time, in which different amounts of experimental data is processed. Clearly the PDF is not fully converged, which is counter intuitive as one would expect the PDF to converge in 60 s, based on the value of the integral time scale at this location, $\approx$ 30 ms (see top panel in Figure 3.10). This issue is currently being investigated by the experimental team.

We now turn to check the convergence of the simulated temperature PDFs. In the simulations, along with sensitivity to flow time, sensitivity to grid resolution is also checked. It is worth mentioning here that all the FireFOAM based PDFs presented in the following are generated using grid-resolved temperature data, and hence, do not represent the real PDFs that one would get e.g., from DNS. Figure 3.14, which contains the temperature PDF from FireFOAM at 50 cm elevation

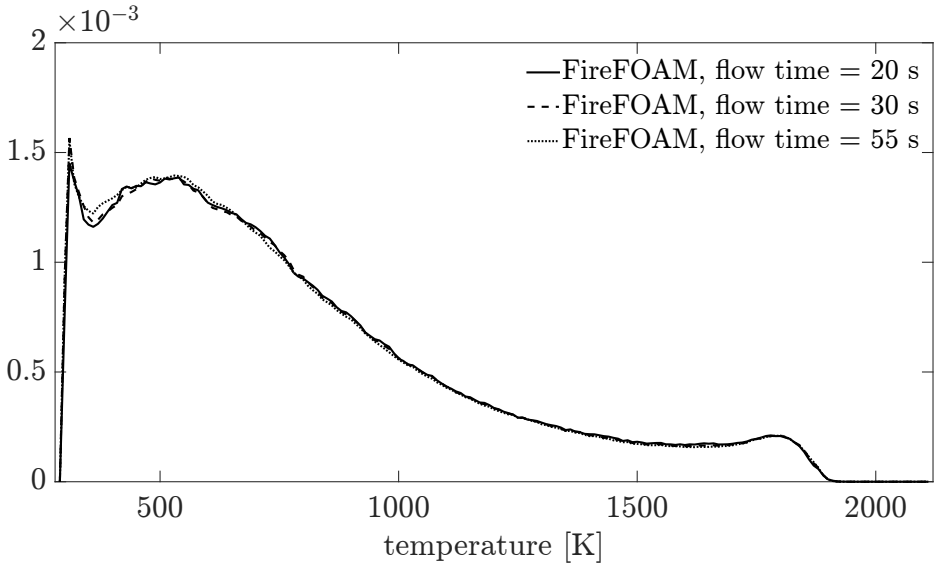

Figure 3.14: Simulated temperature PDF at 50 cm elevation along the centerline. Sensitivity to flow time.

along the burner centerline, indicates that the PDF converges in 20 s. However, it should be noted that for generating the simulated PDF, temperature data from all the grid cells along the span (between $y = -10$ to 10 [cm]) are used which is primarily responsible for the favorable convergence behaviour seen in Figure 3.14. Accordingly, all the simulation-based PDFs in the following will be generated with data corresponding to 20 s of flow time.

The sensitivity of the simulated temperature PDFs (at nine different elevations) to grid resolution is considered in Figure 3.15. At 10 and 20 cm elevations the PDFs are not completely converged with a ≈5 mm grid but at elevations ≥30 cm the ≈5 mm grid appears to be sufficient. This observation seems consistent with the horizontal integral length scale L_y variation shown in Figure 3.12. In Figure 3.12 L_y takes a value close to 2 cm at 10 cm elevation (indicating that the ≈5 mm grid

resolution is coarse at this elevation); whereas it takes a value of about 4 cm at 30 cm elevation (indicating that ≈5 mm grid spacing should be appropriate at this elevation).

In summary, the convergence study suggests that the experimental temperature PDFs are currently not converged in time and the simulated temperature PDFs are not grid converged below approximately $z = 30$ cm; heed will be paid to both these issues in the future.

Nevertheless, it still makes sense to compare the experimental and simulated PDFs. Thus, the experimental and simulated temperature PDFs are compared at nine different elevations along the centerline in Figure 3.16. Both experimental and simulated PDFs are broad and bi-modal at low elevations in the flame region, indicating intermittent occurrence of relatively cold gas due to ambient air entrainment and hot gas due to combustion; whereas the PDFs are narrow and mono-modal at high elevations in the plume region. The simulated PDFs compare favorably above $z \approx 50$ cm. On the other hand, at lower elevations there are discrepancies, for instance, unlike the experimental PDFs, the simulated PDFs indicate the presence of ambient temperatures. This and other discrepancies in the flame zone could be due to several reasons. First, the combustion and radiation models invoked in these simulations are of lower order (see Chapter 2 for details) and are expected to have significant effects on the temperature PDFs in the flame zone. A higher order combustion and radiation modeling framework is currently under development in the author's group [82] and is expected to reduce some of the discrepancies. Second, the numerical schemes used in these simulations do not perform well on representa-

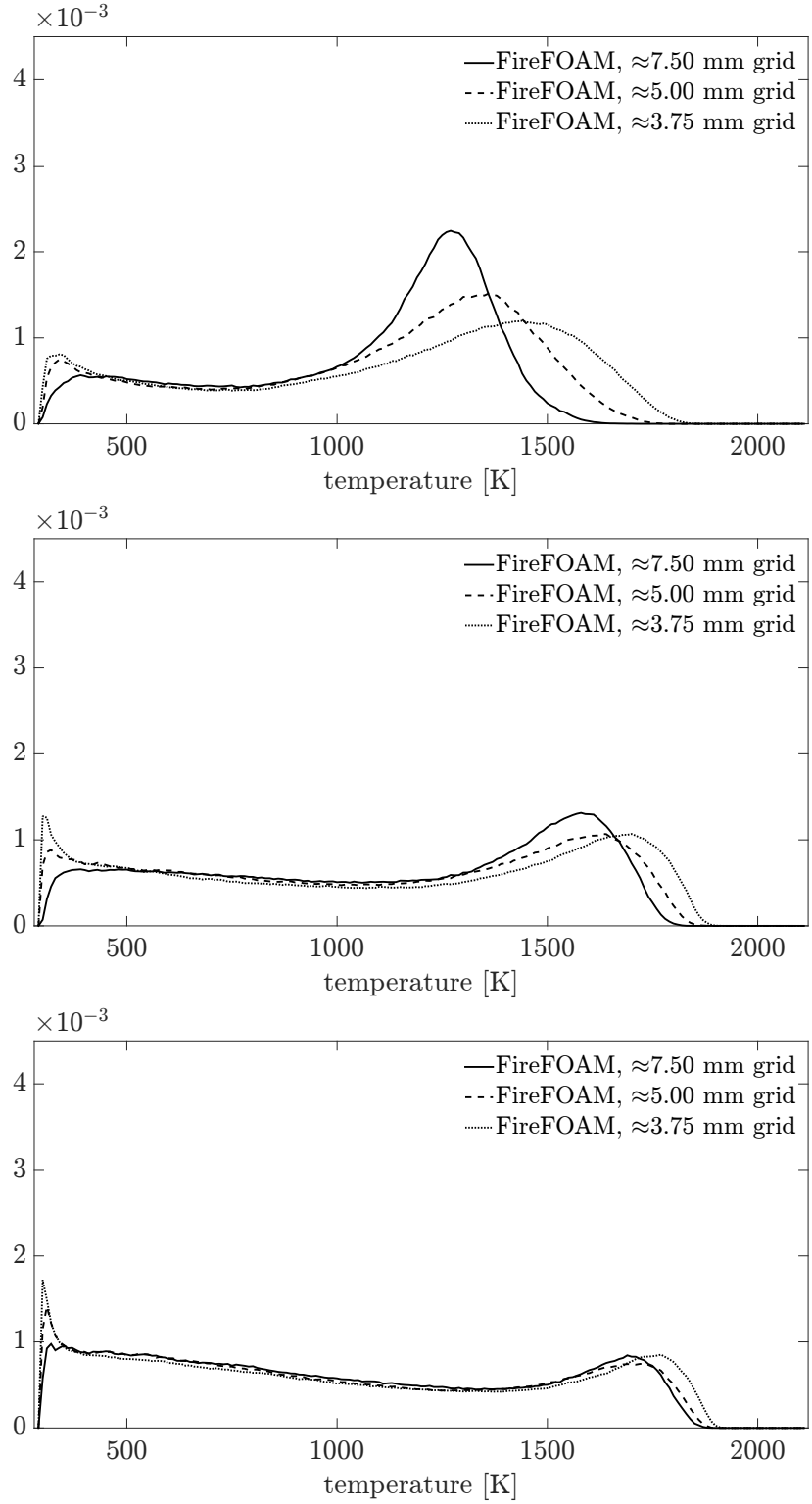

Figure 3.15: Sensitivity of the PDFs, at z = 10, 20, 30, 40, 50, 60, 70, 80 and 90 cm (top to bottom) along the burner centerline, to variations in grid resolution.

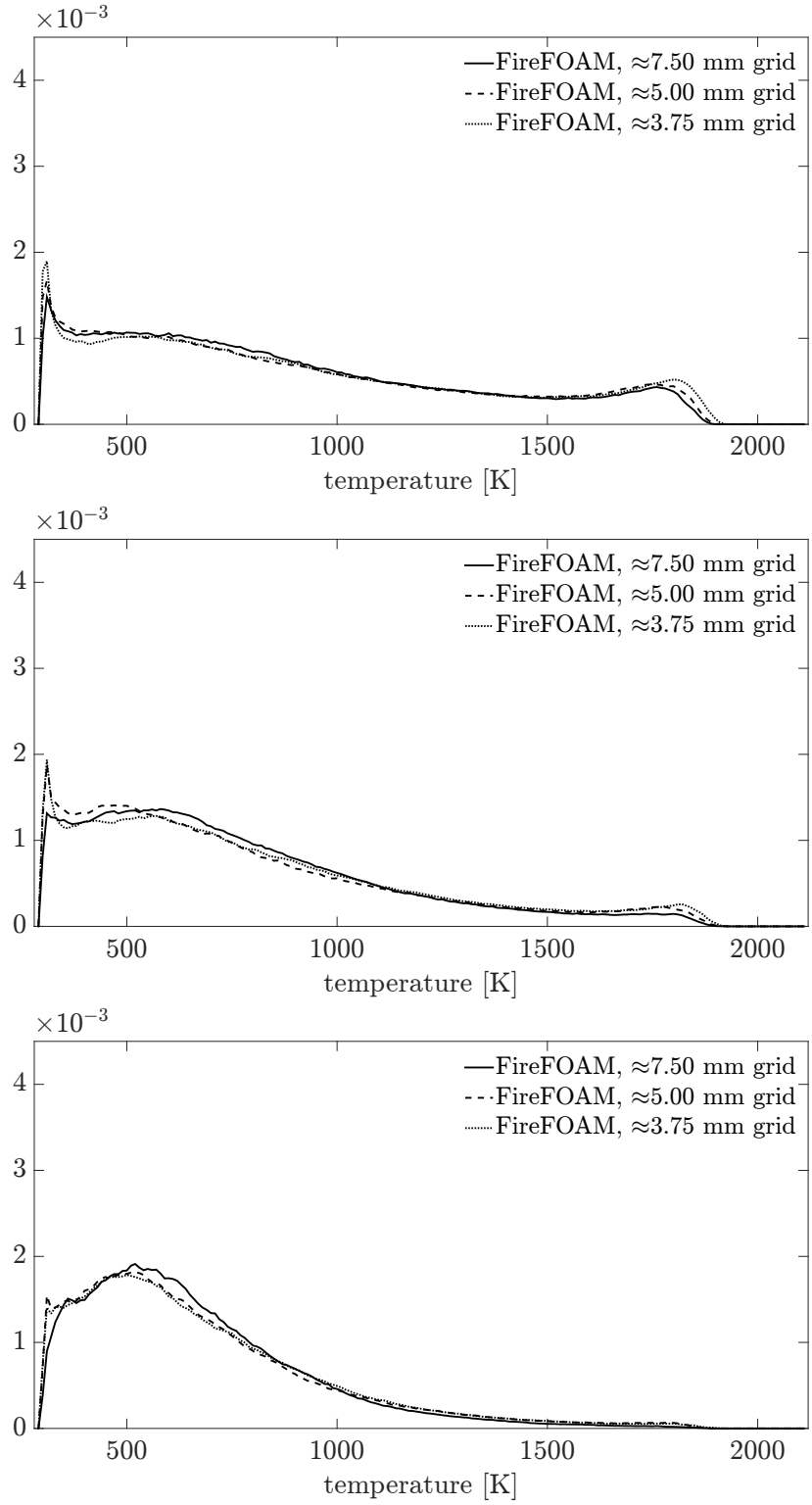

Figure 3.15: Continued.

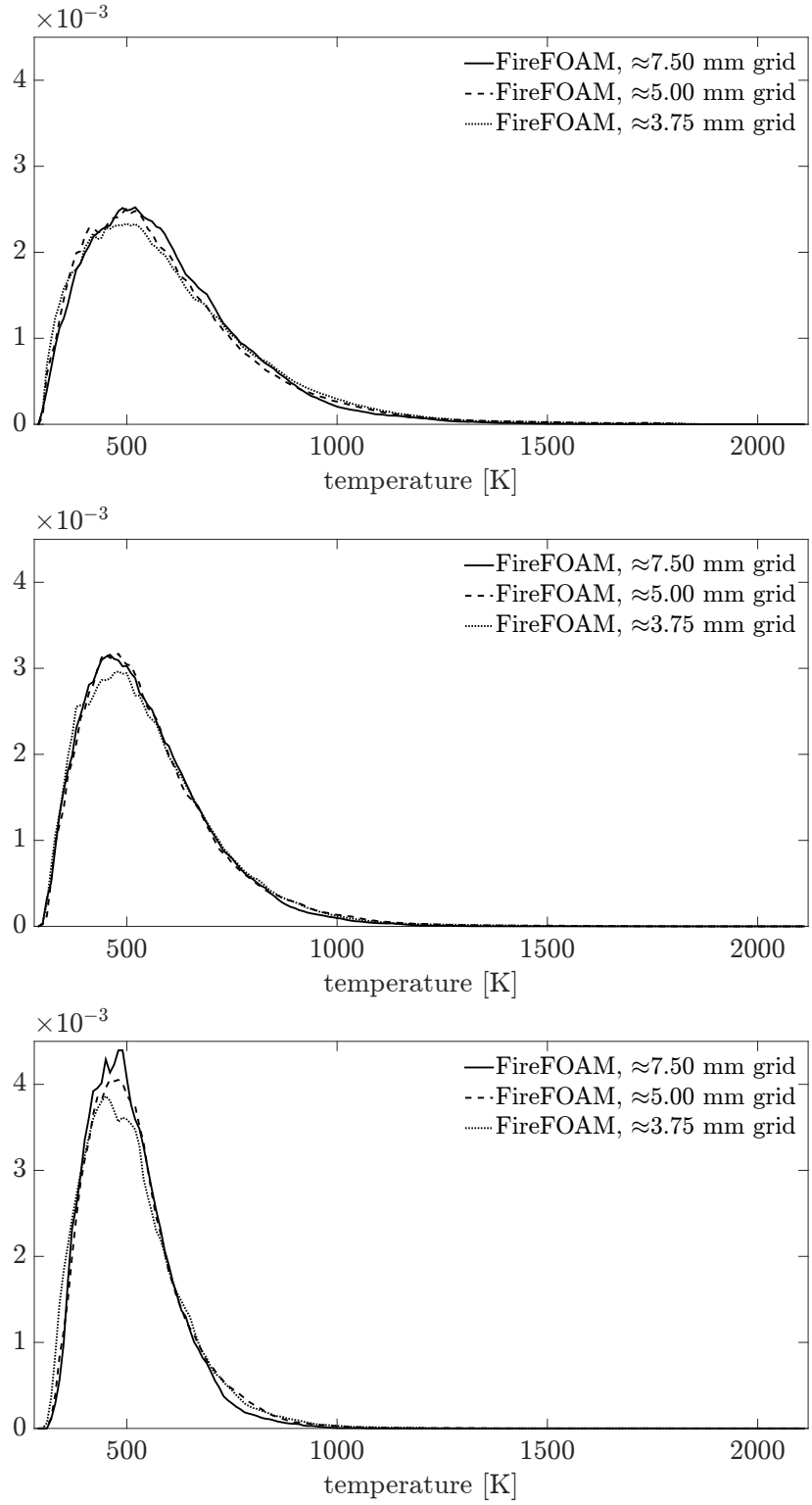

Figure 3.15: Continued.

tive test cases (see Chapter 2 for details) and might be responsible for some of the issues seen in Figure 3.16. In the future the schemes will be selected based on their performance in a comprehensive suite of benchmark cases. Third, the convergence issues discussed above (specifically with the experimental data) might also be behind some of the discrepancies. This is currently being actively investigated by the experimental team at UMD.

3.5 Concluding remarks

We have performed well-resolved simulations of a co-flow stabilized, turbulent, buoyant, methane-fueled line fire in the absence of wind and slope, with the goal of doing a higher order validation of our numerical approach.

The simulated mean and rms temperature profiles compare reasonably well with measurements, with simulations overpredicting turbulent fluctuations in the flame zone. Both horizontal and vertical integral length scales increase with elevation, with the latter being larger than the former (consistent with flame visualizations). The latter length scale agrees well with measurements and the former agrees with Linear Stability Theory (LST) for Rayleigh Taylor Instability (RTI) at the base.

The experimental PDFs are found to be sensitive to measurement duration, whereas the simulated PDFs seem to be sensitive to the grid resolution below approximately half the mean flame height (25 cm). Both experimental and simulated PDFs are broad and bi-modal at low elevations in the flame region, indicating intermittent occurrence of relatively cold gas due to ambient air entrainment and hot gas

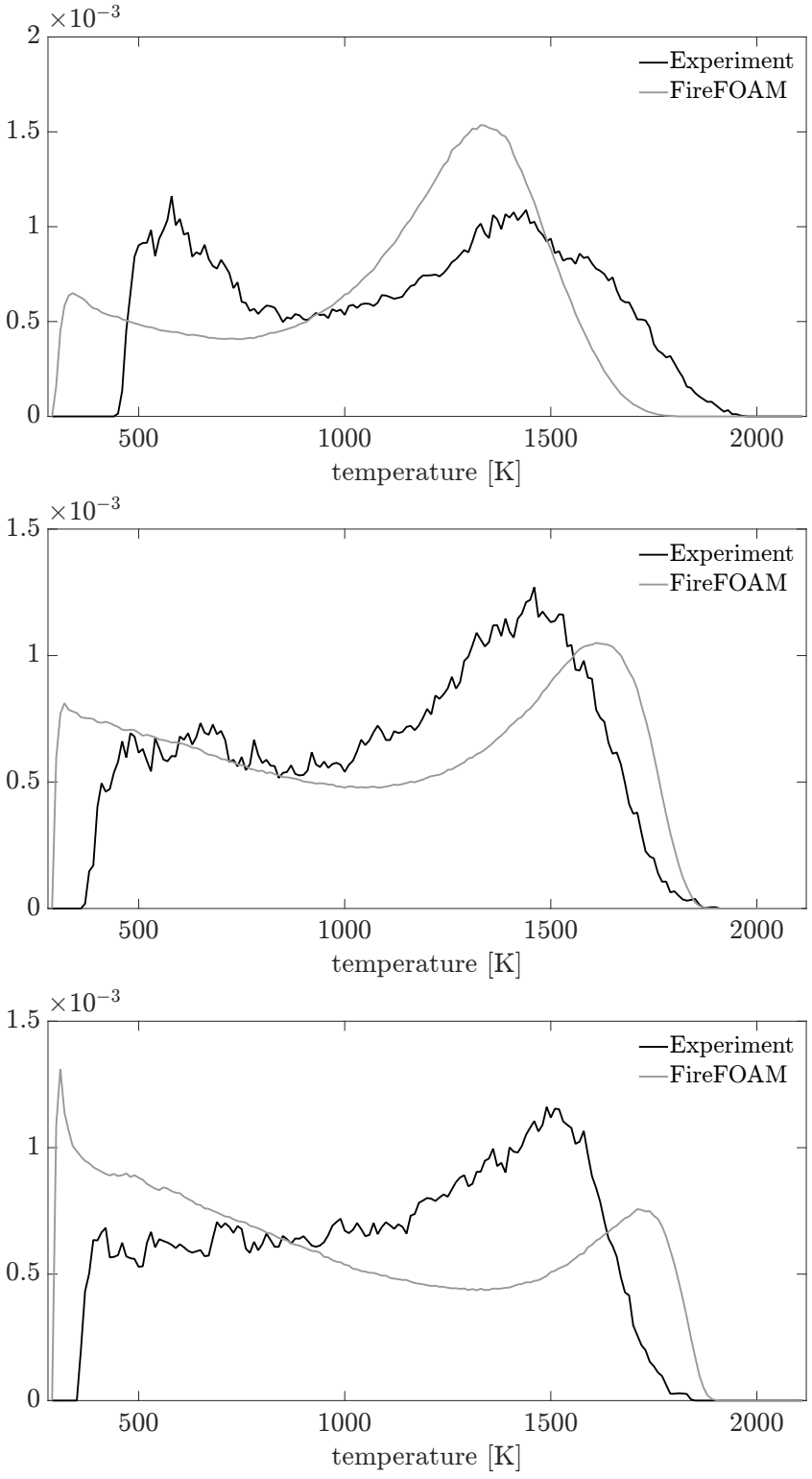

Figure 3.16: Temperature PDFs, at z = 10, 20, 30, 40, 50, 60, 70, 80 and 90 cm (top to bottom) along the burner centerline; comparison between experiment and FireFOAM. Simulated results are from the ≈5 mm grid.

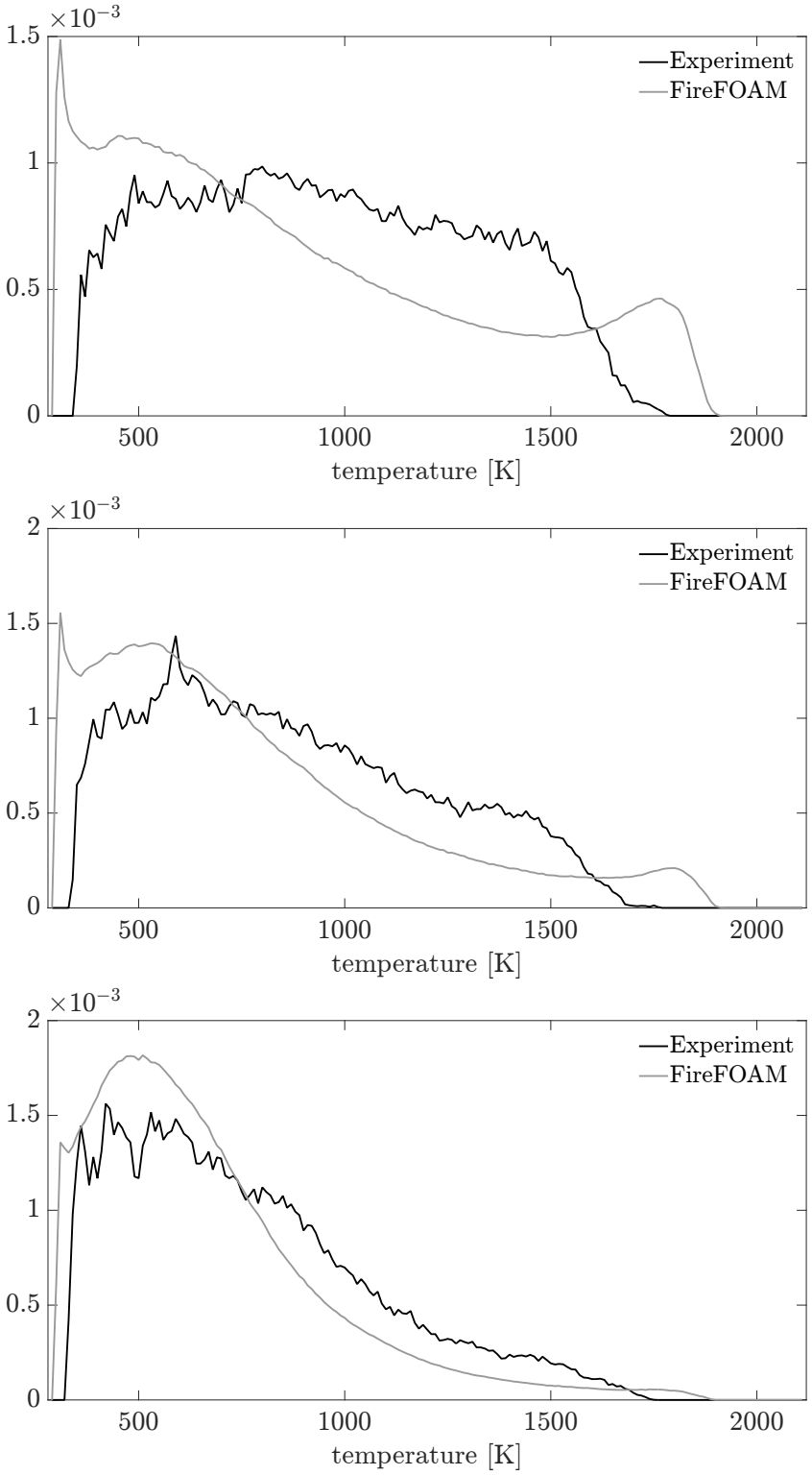

Figure 3.16: Continued.

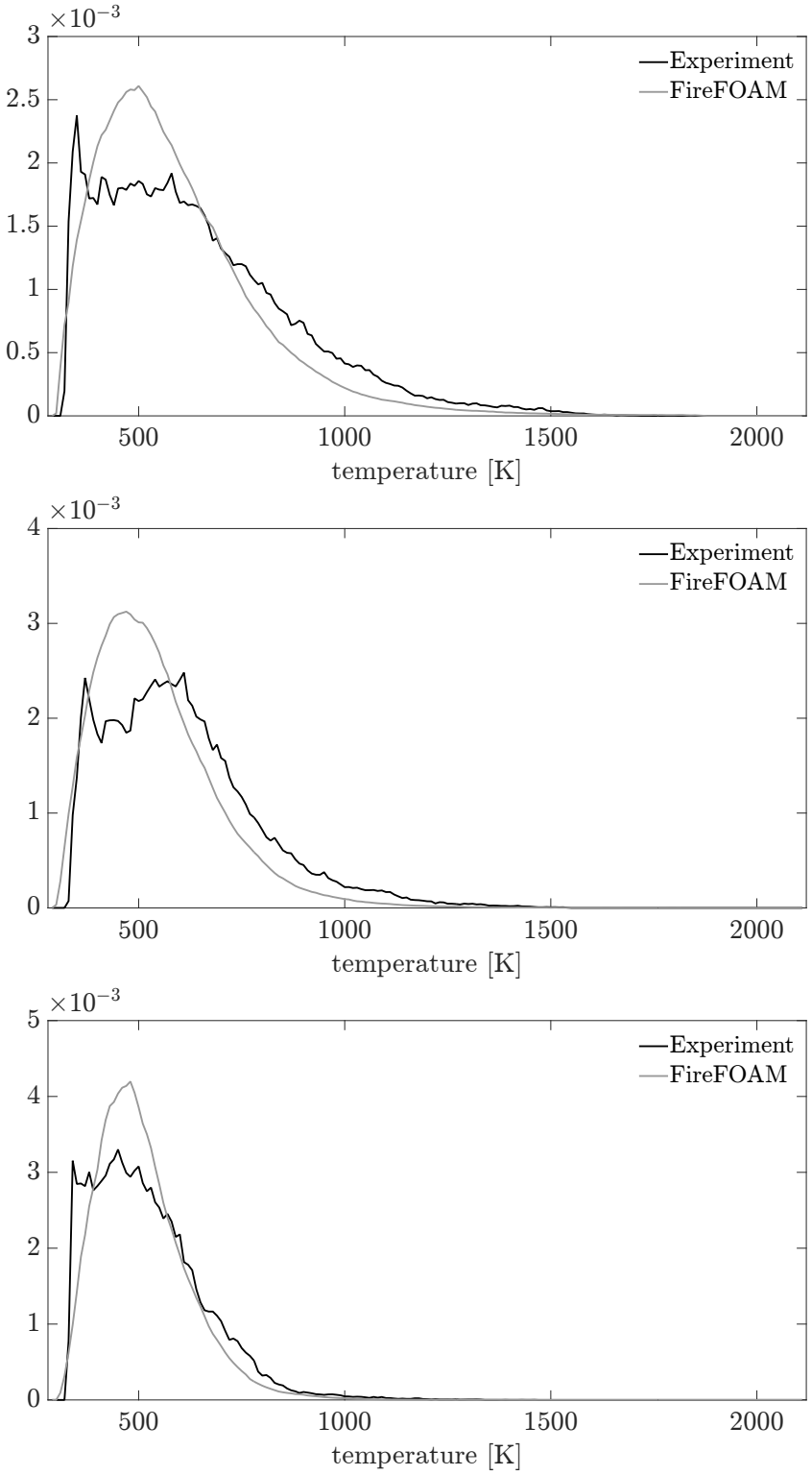

Figure 3.16: Continued.

due to combustion; whereas the PDFs are narrow and mono-modal at high elevations in the plume region. At present, the PDFs from experiments and simulations agree well above the mean flame height, but there are discrepancies below it including the presence of ambient temperatures in simulations which are not seen in the measurements.

Issues that are currently being studied include: lower order of the combustion and radiation models invoked in the present simulations; questionable performance of some of the selected numerical schemes in representative test cases; lack of grid convergence of the simulated temperature PDFs at lower elevations; lack of temporal convergence seen in the experimental temperature PDFs even with a flow time of 60 s.

Despite the issues that require further work, the numerical approach is deemed sufficiently accurate and will be used in the next two chapters to study the structure of this turbulent, buoyant, line fire in the presence of wind and slope.

4: Effects of wind on the structure of a turbulent line fire

4.1 Introduction

In this chapter we will study the effects of cross-wind on the structure of the same turbulent, buoyant, stationary, methane-fueled, line fire that was studied in the last chapter. For doing so couple of changes will (or had to) be made to the configuration discussed in the last chapter: first the co-flow is removed as the flame does not need stabilization in the presence of cross-wind; second, the configuration is made periodic in the spanwise y-direction in order to avoid edge effects, this is done to enable comparisons with the integral model which can only describe an infinitely long line fire.

This chapter is organized as follows. The numerical configuration is presented in the next section, followed by the presentation of the integral model developed in this study. After that the results are presented and discussed. The final section contains some concluding remarks.

4.2 Numerical configuration

The numerical configuration is presented in Figure 4.1. The computational domain is 780-cm-long in the streamwise x-direction, 50-cm-wide in the spanwise

y-direction and 250-cm-high in the vertical z-direction. The line burner face is 5-cm-long in the x-direction and 50-cm-wide in the y-direction; and the spanwise center of its leading edge is placed at the origin $(x, y, z) = (0, 0, 0)$. The burner is flush-mounted on a 50-cm-wide horizontal solid plate that starts at $x = (-20)$ cm and ends at $x = 205$ cm. The cross-flow air is injected through a 50-cm-wide and 50-cm-high wind tunnel whose outlet is located at the inlet boundary of the computational domain, at $x = (-30)$ cm. A 5-mm-long, 50-cm-wide and 5-mm-high trip wire is placed at $x = (-10.5)$ cm in order to perturb the incoming flow and promote laminar-to-turbulent transition.

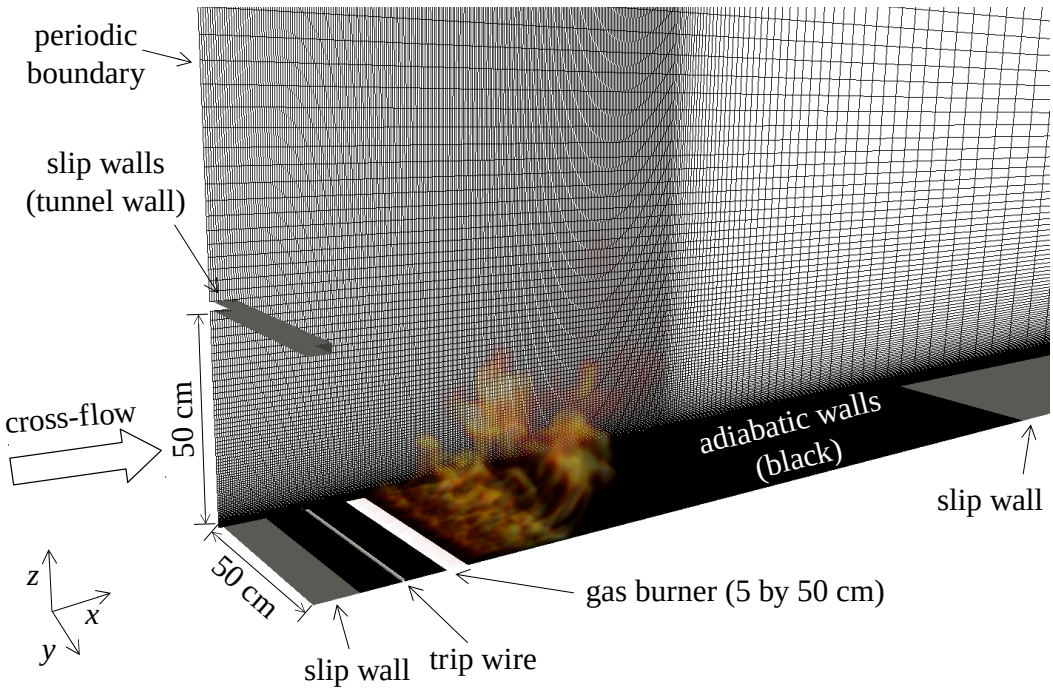

Figure 4.1: Numerical configuration used for studying the effects of cross-wind on a turbulent line fire; the 50 kW methane diffusion flame is visualized using volume rendering of temperature.

The computational grid is a rectangular Cartesian mesh. Grid spacing in the streamwise x-direction is uniform and is equal to 5 mm for $x \leq 100$ cm; beyond that location, the x-grid is stretched with a stretch factor equal to 1.06 (see top panel in Figure 4.2). Grid spacing in the spanwise y-direction is uniform and is equal to 5 mm. This streamwise (spanwise) resolution corresponds to 10 (100) grid cells across the burner length (width). Grid spacing in the vertical z-direction is non-uniform: the z-grid spacing is 1.2 mm at $z = 0$ (i.e, the first cell center is 0.6 mm above the south boundary of the computational domain) and is 20 mm at $z = 50$ cm with a stretching factor of 1.04. For $z \geq 50$ cm, the z-grid is stretched with a stretch factor equal to 1.06 (see bottom panel in Figure 4.2). Appendix A presents an assessment of the chosen vertical grid resolution at the wall, $\Delta z_w = 0.6$ mm. Note that with the present resolution, the trip wire is under-resolved and is described with 1 (4) grid cell(s) in the x- (z-) direction. The total number of cells is 3.5 million.

The methane mass flow rate is prescribed at the burner boundary and the air velocity is fixed at the tunnel outlet. Similar to the simulations in Chapter 3, both convective and diffusive mass fluxes are taken into account at the burner boundary [42]. The horizontal solid plate and the trip wire are both treated as no-slip adiabatic solid walls. The surface located at $z = 0$ between the tunnel outlet and the leading edge of the solid plate is treated as a slip wall. The surface located at $z = 0$ beyond the solid plate, at $x \geq 205$ cm, is also treated as a slip wall. The side boundaries at $y = (-25)$ and 25 cm correspond to periodic conditions. Other boundaries are treated as boundaries with open flow conditions.

In all cases, the methane mass flow rate is linearly increased from 0 to 1 g/s

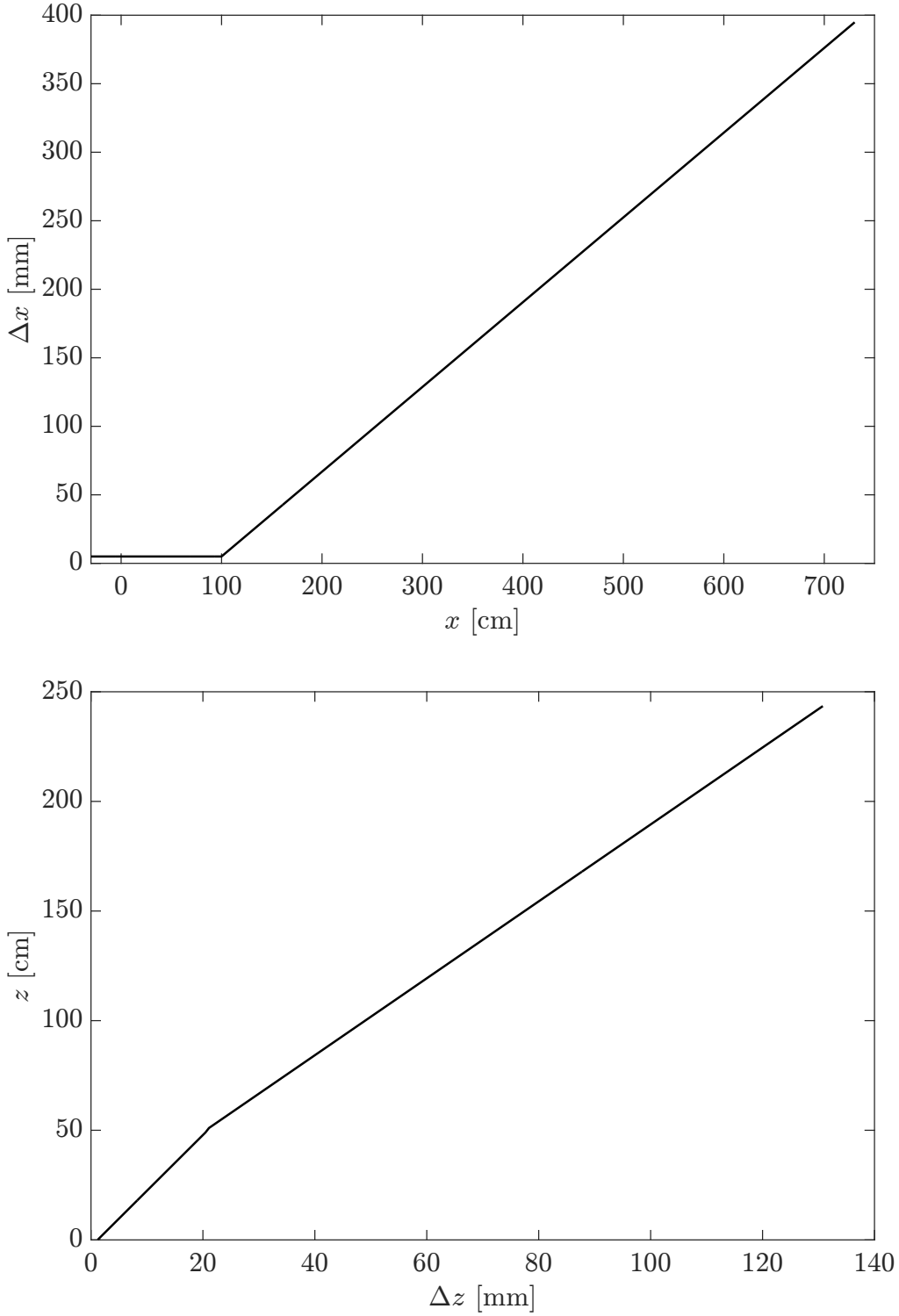

Figure 4.2: Horizontal variation of Δx (top) and vertical variation of Δz (bottom).

during the first five seconds and is then held constant for the remainder of the simulations. This is done to allow the cross-flow to establish itself over the line burner before the fire reaches its nominal value of the heat release rate equal to 50 kW. All simulations are performed for a duration of 30 s. Turbulent statistics are collected for the final 15 s of each simulation, after the flow and flame become statistically stationary and long enough for the statistics to be converged (to improve convergence, statistics are computed using both temporal- and spanwise-averaging). The time step is controlled by a classical Courant-Friedrichs-Lewy (CFL) condition and is approximately equal to 0.35 ms. Each simulation is run using 200 processors on a large-scale Linux cluster with a typical simulation requiring 40,000 CPU-hours.

4.3 Integral model

This section elaborates the integral model (developed in this work) that can describe the structure of both the flame and plume zones of a turbulent, buoyant, line fire subjected to cross-wind. The schematic of the model is presented in Figure 4.3. The assumptions involved are as follows:

- All the quantities are independent of time (steady state).
- The cross-wind is perpendicular to the longer dimension of the fuel source and does not change in space.
- The effects of turbulence in the cross-wind are not important [13].
- Profiles of all the variables are self-similar and have the top-hat form.

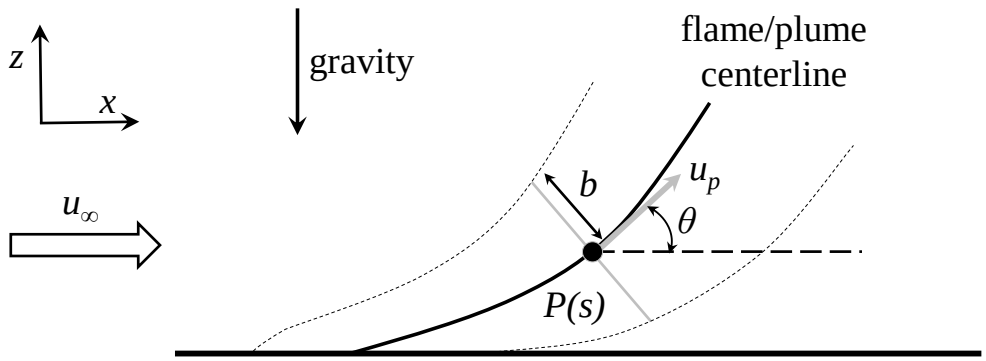

Figure 4.3: Schematic illustration of the integral model developed in the present work.

With the above assumptions the governing equations take the following form:

$$\frac{d}{ds}(\dot{m}'_p) = 2\rho_\infty u_e \tag{4.1}$$

$$\frac{d}{ds}(\dot{m}'_p u_p \sin(\theta)) = (\rho_\infty - \rho_p)(2b)g \tag{4.2}$$

$$\frac{d}{ds}(\dot{m}'_p u_p \cos(\theta)) = \frac{d}{ds}(\dot{m}'_p)u_\infty \tag{4.3}$$

$$\frac{d}{ds}(\dot{m}'_p c_p T_p) = \frac{d}{ds}(\dot{m}'_p)c_{p,\infty}T_\infty + (1-\chi_{rad}) \times \dot{\Omega}''_F(r_s \Delta H_{O_2}) \tag{4.4}$$

$$\frac{d}{ds}(\dot{m}'_p Y_F) = -\dot{\Omega}''_F \tag{4.5}$$

$$\frac{d}{ds}(\dot{m}'_p Y_{O_2}) = \frac{d}{ds}(\dot{m}'_p)Y_{O_2,\infty} - r_s\dot{\Omega}''_F \tag{4.6}$$

$$\frac{d}{ds}(\dot{m}'_p Z) = 0 \tag{4.7}$$

Equations 4.1, 4.2, 4.3, 4.4, 4.5, 4.6 and 4.7 represent conservation of mass, momentum in the vertical z-direction, momentum in the horizontal x-direction, energy, fuel mass, oxygen mass and mixture fraction, respectively; along the flame/plume centerline s. The model includes two additional equations for the flame/plume centerline coordinates:

$$\frac{d}{ds}(x_c) = \cos(\theta) \tag{4.8}$$

$$\frac{d}{ds}(z_c) = \sin(\theta) \tag{4.9}$$

See the nomenclature for the definition of notations. In the above set of equations models for u_e and $\dot{\Omega}''_F$ are required. For the former we follow Escudier [14] and write $u_e = (\alpha|u_p - U_\infty \cos(\theta)| + \beta|U_\infty \sin(\theta)|)(\rho/\rho_\infty)^{1/2}$ (we use $\alpha = 0.16$ and $\beta = 0.5$ [16]) and for the latter we write $\dot{\Omega}''_F = GER(Y_{O_2,\infty}/r_s)2\rho_\infty u_e$ (we use global equivalence ratio, $GER = 0.1$). Equations 4.1 to 4.9 can be numerically solved to get variations of $\dot{m}'_p$, u_p, θ, T_p, Y_F, Y_{O_2}, Z, x_c and z_c with s (before doing so Equations 4.2 and 4.3 first need to be manipulated to get equations for u_p and θ).

4.4 Results and discussion

4.4.1 Instantaneous flame, plume and flow structure

We first consider the instantaneous flame, plume and flow structure seen in our simulations with U_∞ = 0.75, 1, 1.25, 1.5, 2, 3 m/s (the corresponding values of N_C are 10.2, 4.3, 2.2, 1.3, 0.5 and 0.2, respectively; note that the expression for N_C used here is slightly different from the one used in the literature, N_C =

$(1-\chi_{rad})(2Ig)/(\rho_\infty c_{p,\infty} T_\infty U_\infty^3))$. Figures 4.4 to 4.9 present the flame, plume and flow structure in terms of volume rendering of heat release rate per unit volume, volume rendering of temperature and isocontour of Q-criterion colored with grid-resolved streamwise velocity u, for the six cases at $t = 30$ s. To provide a holistic view of the structure at this particular instant, four different views are displayed in these figures: top, side, front-perspective and front.

The two flame regimes discussed in the literature and in Chapter 1 (buoyancy- and wind-dominated) [18] can be clearly seen in Figures 4.4 to 4.9 (specifically panel b which presents the side-view): cases with $U_\infty \leq 1.5$ belong to the former regime and the other two cases belong to the latter regime. The transition from one regime to the other happens close to $N_C = 1$; thus the present simulations support the idea that the transition from one flame regime to the other is controlled by the Byram's convection number N_C [23, 24].

The 0.75 and 1 m/s cases have the puffing instability, see panel b in Figures 4.4 and 4.5. Panel b in Figure 4.4 also suggests that there exist two different regions in the 0.75 m/s case: one where the flame is restricted to a thin region close to the wall and the other where the flame/plume is nearly vertical and the transition (in terms of downstream distance) between the two regions is fairly abrupt. To some extent the two different regions are also present in the 1 m/s case; for the rest of the cases the flame height above the bottom surface appears to evolve at a uniform rate with downstream distance.

Middle plot in panel a in Figures 4.4 to 4.9 indicates that with an increase in wind velocity the maximum temperature seen in the flame also increases (this is

indicated by an increase in the semi-transparent white color in these plots). So, with an increase in cross-wind velocity not only is the flame closer to the downstream surface but it is also hotter, which would lead to a further enhancement of the spread rate in a spreading fire.

Sooner or later, the flame/flow transitions from a laminar to a turbulent state, in all the simulated cases. The laminar-to-turbulent transition for the flame in the 0.75 m/s case begins with two-dimensional waves that spread across the entire span (50 cm) of the computational domain (see panel a in Figure 4.4). For higher wind speeds the flame starts out from the burner in a three-dimensional state. As indicated by the Q-criterion isocontours, the flow contains perturbations well before the beginning of the burner; which are induced either by the perturbation or trip wire placed at $x = -10.5$ cm (for lower wind speeds) or by the interface between the slip wall and the adiabatic bottom surface at $x = -20$ cm (for higher wind speeds). Exactly how much of the initial flame state is controlled by the upstream perturbations is not completely clear, specifically for $U_\infty \geq 1$ m/s. Simulations without the perturbation wire can be used to answer this question, and suggest that the role of the wire is significant. Another pertinent question is how much the upstream perturbations are affected by the presence of the flame. Cold flow simulations can be used to shed light on this aspect. These questions are beyond the scope of the present work.

In all cases the spanwise length scale of the structures, seen close to the burner, is found to increase with streamwise distance, and reaches in the lower velocity cases a value that is of the order of the spanwise domain size. It is worth mentioning here

that the flame structure seen in the present simulations is qualitatively similar to that reported in a recent experimental study [83]; where a configuration similar to the one exploited in the present study was used.

Furthermore, from Figures 4.4 to 4.9 it is clear that all the flames (even those in the wind dominated cases, $U_\infty = 2$ and 3 m/s) are populated by thermals, suggesting that turbulence generation is mostly happening because of buoyancy or unstable thermal stratification (see [84] for some quantitative support for this observation). This is consistent with the results reported in [85].

Figures 4.10 to 4.12 provide a quantitative view of the instantaneous flame, plume and flow structure (for the cases with $U_\infty = 0.75$, 1.5 and 3 m/s), through velocity vectors and temperature isocontours. For clarity the heat release rate per unit volume isocontours are not included in these figures. Most of the features that were discussed above (two flame regimes, puffing instability at low velocity, increase in the spanwise length scale of the structures in the downwind direction etc.) can be seen in these figures as well. In addition one can see in these figures that on station 1 (or $x = 2.5$ cm, which is at the center of the gas burner) the thermal boundary layer thickness (which at this station is expected to be equal to the local flame height) is almost independent of the wind velocity and is ≈ 1 cm. So, contrary to what one might expect *a priori*, the grid spacing in the vertical direction close to the wall needs to be almost equal in the low and high wind cases, for wall-resolved simulations.

In the 0.75 m/s case the cross-flow is deflected upwards and accelerated significantly by the flame/plume (indicated by the increase in the length of the velocity

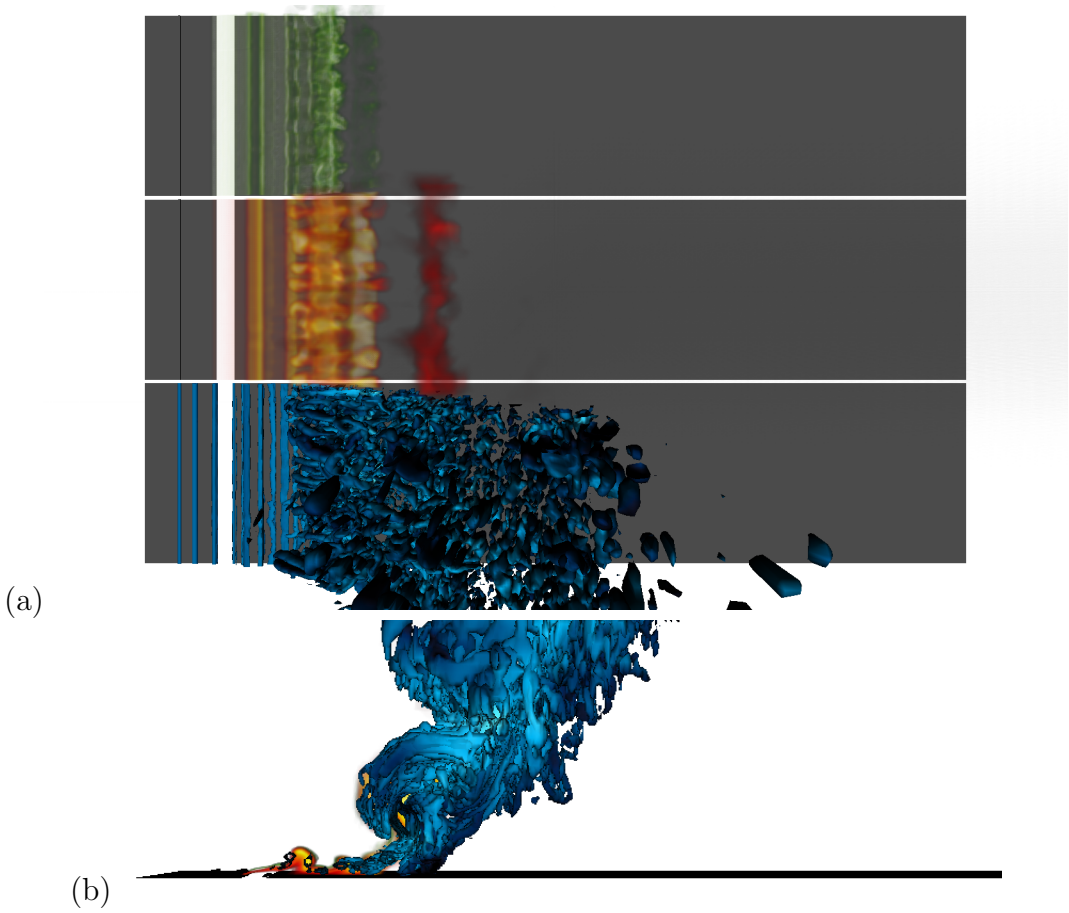

Figure 4.4: Instantaneous flame, plume and flow structure for the $U_\infty = 0.75$ m/s case at $t = 30$ s; illustrated through volume rendering of heat release rate per unit volume (green) and temperature (orange) and isocontour of Q-criterion (500) colored with grid-resolved streamwise velocity u (blue). The color for heat release rate goes from dark green to semi-transparent white via light green, for temperature goes from black to semi-transparent white via orange and for u goes from dark blue to white via cyan using a linear mapping from 0-10 MW/m^3, 500-1800 K and (-0.5)-4 m/s respectively. Panels a, b, c and d correspond to top, side, front-perspective and front views, respectively.

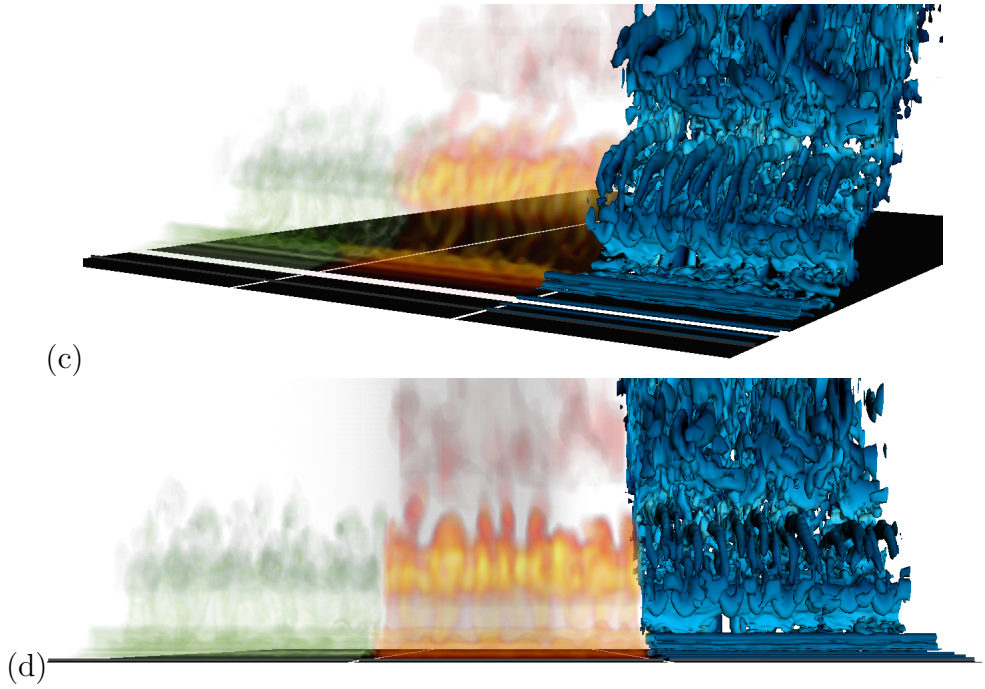

Figure 4.4: Continued.

vectors) and the flame/plume lift-off at $x \approx 30$ cm induces reversed flow on the downwind side leading to two-sided entrainment similar to the flow-field in a pool fire scenario. The 1.5 m/s case is similar to the 0.75 m/s case; but the flow deflection and acceleration are not as strong; also the flame/plume lift-off happens at $x \approx 60$ cm. Again the scenario is similar to a pool fire. For the 3 m/s case, the flow field is hardly affected by the presence of the flame/plume; flow, flame and plume remain attached to the downwind surface in this case; and entrainment is one-sided.

In the next section we will consider the mean flame, plume and flow structure.

4.4.2 Mean flame, plume and flow structure

In the mean sense, we first consider the mean flame shape for a range of cross-flow velocities (Figure 4.13). The mean flame shape in this figure is marked by the 50

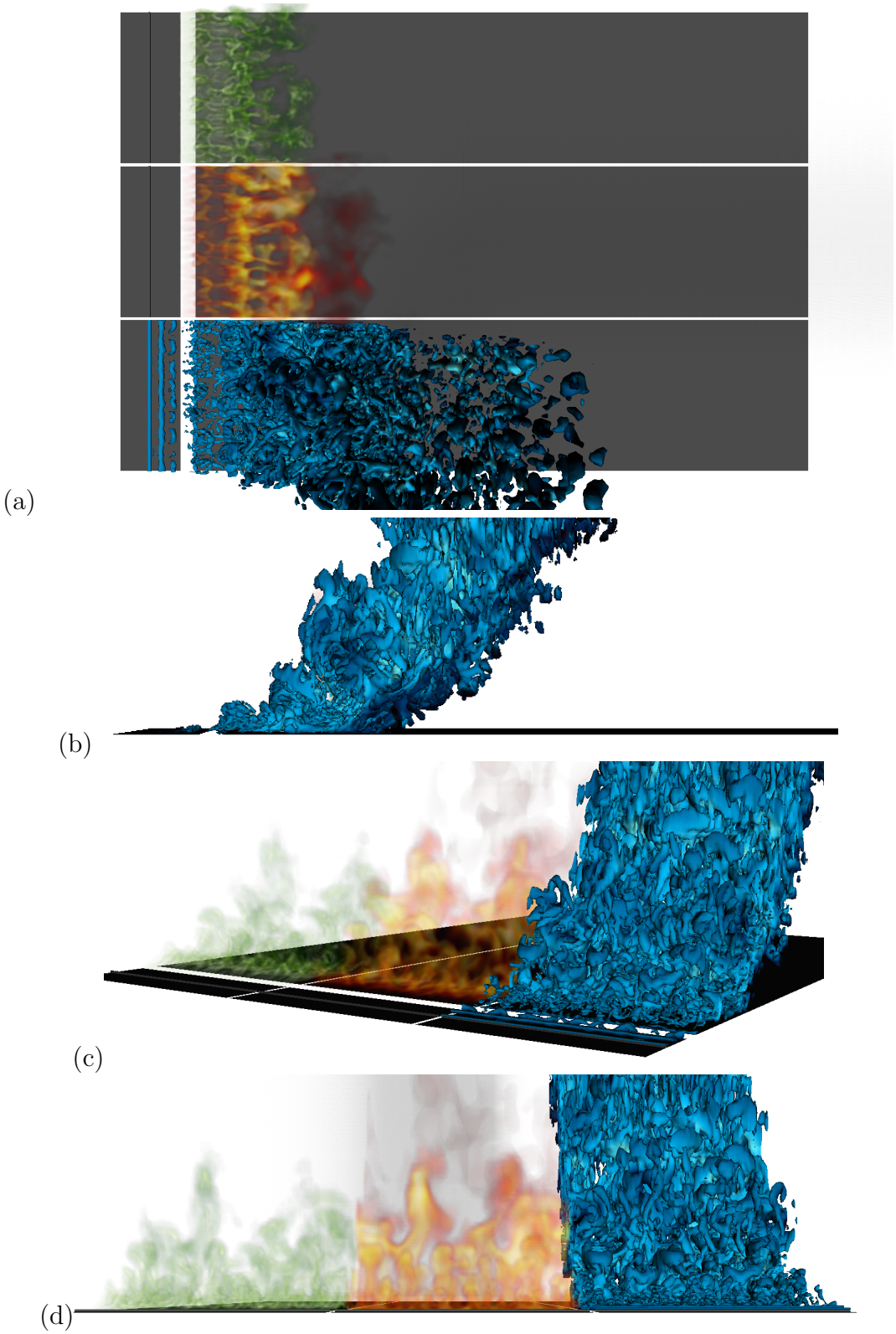

Figure 4.5: Instantaneous flame, plume and flow structure for the $U_\infty = 1$ m/s case at $t = 30$ s. See Figure 4.4 caption for additional details.

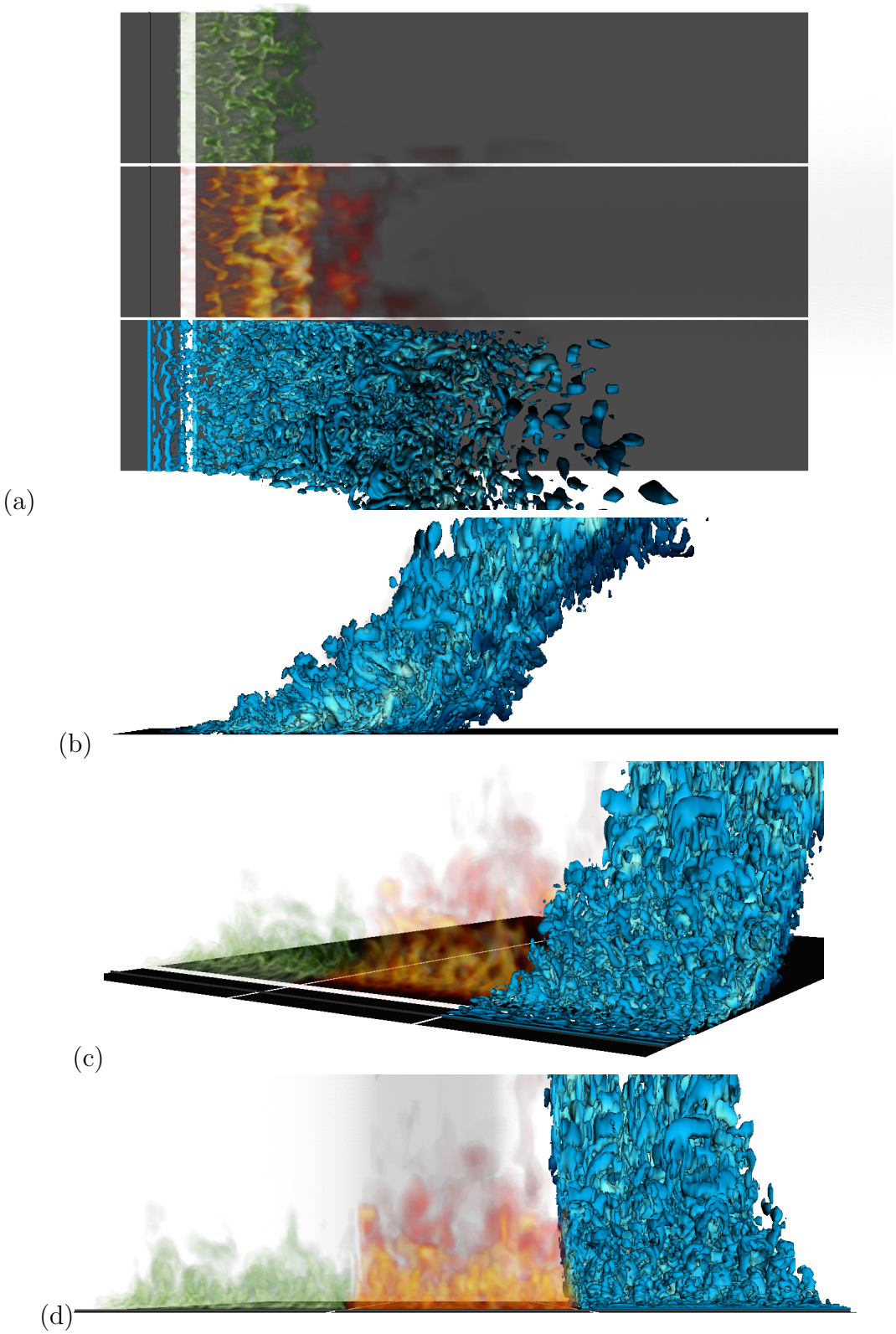

Figure 4.6: Instantaneous flame, plume and flow structure for the $U_\infty = 1.25$ m/s case at $t = 30$ s. See Figure 4.4 caption for additional details.

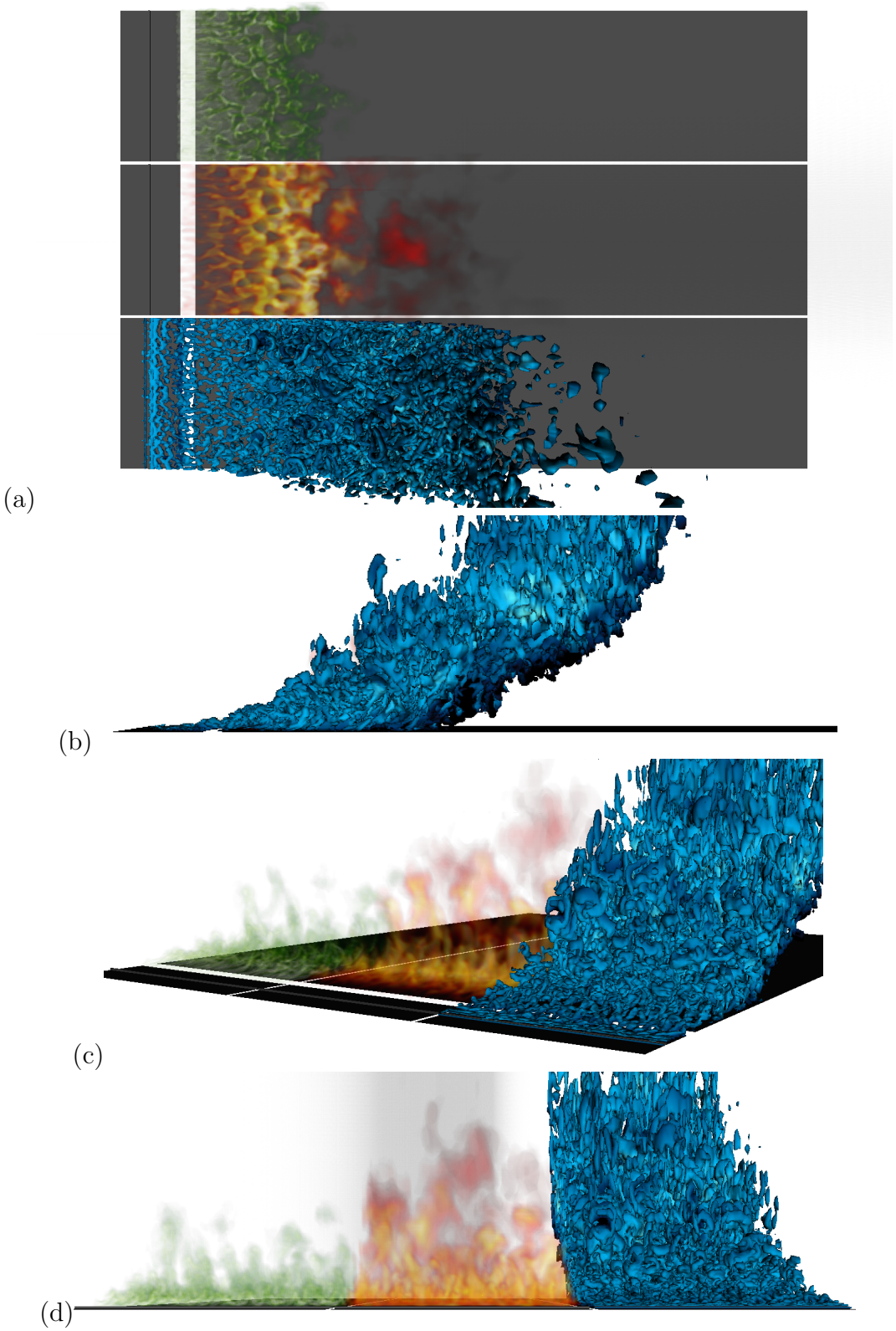

Figure 4.7: Instantaneous flame, plume and flow structure for the $U_\infty = 1.5$ m/s case at $t = 30$ s. See Figure 4.4 caption for additional details.

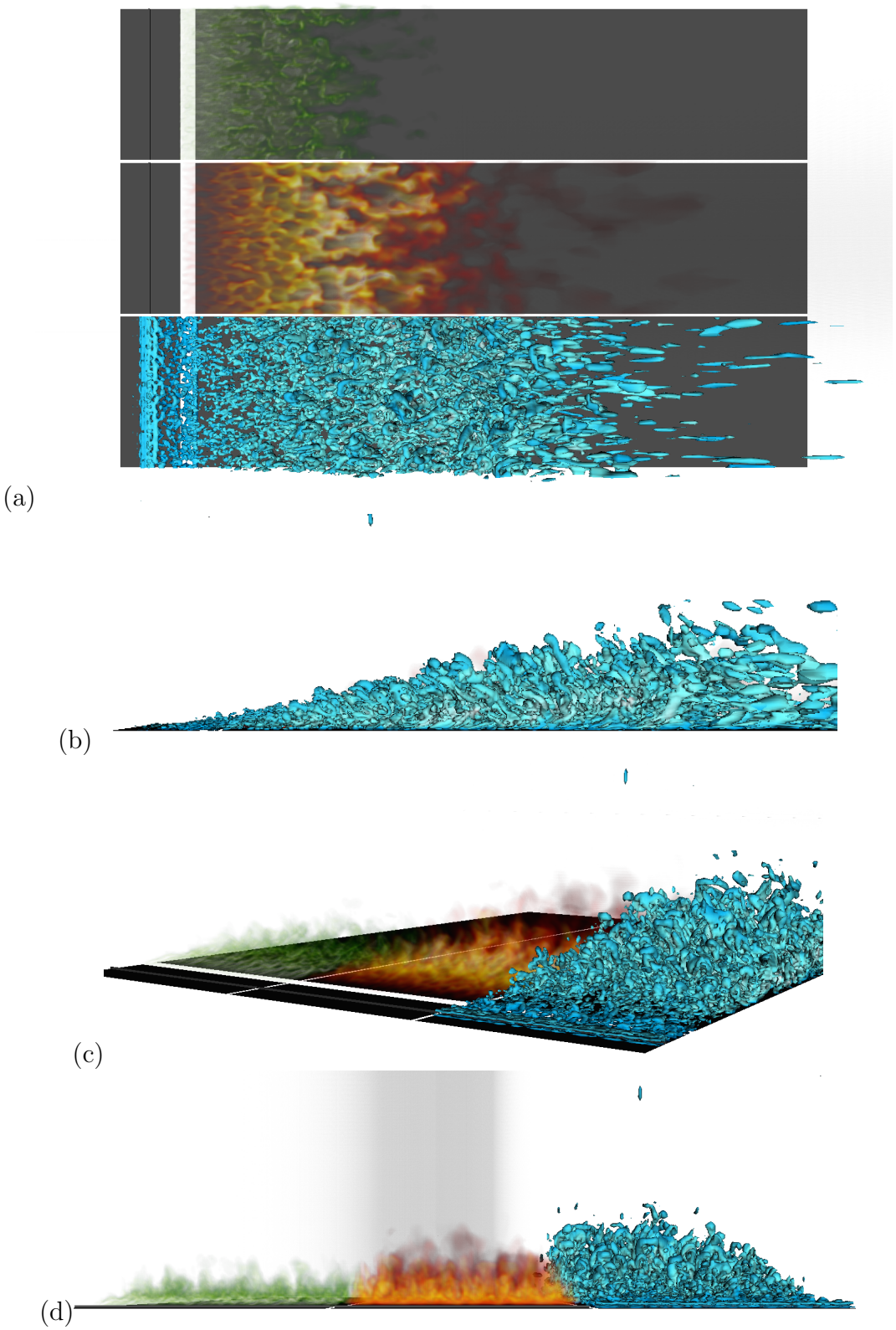

Figure 4.8: Instantaneous flame, plume and flow structure for the $U_\infty = 2$ m/s case at $t = 30$ s. See Figure 4.4 caption for additional details.

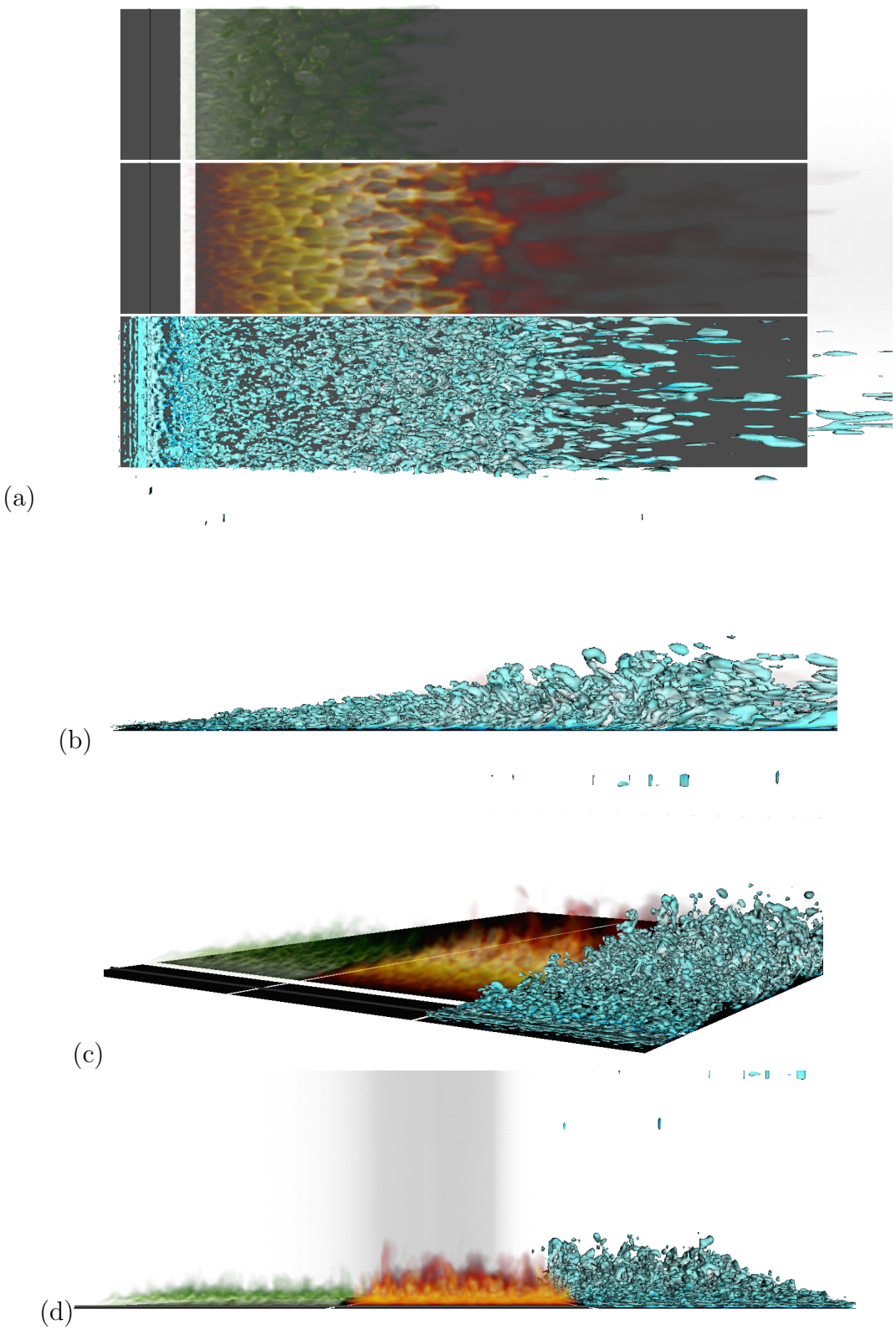

Figure 4.9: Instantaneous flame, plume and flow structure for the $U_\infty = 3$ m/s case at $t = 30$ s. See Figure 4.4 caption for additional details.

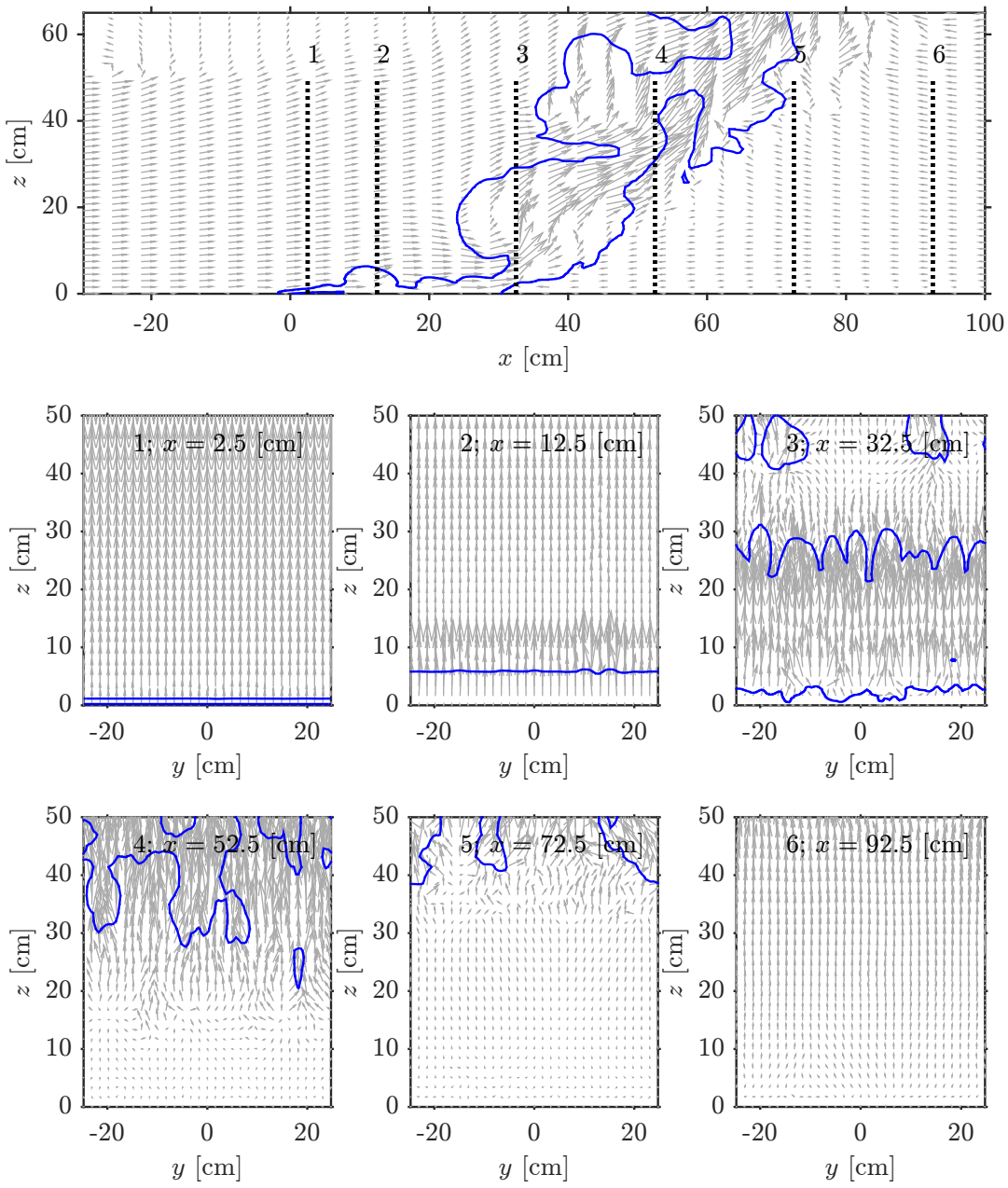

Figure 4.10: Spatial variations of the vector (u, w) at the $y = 0$ plane (first row) and of the vector (v, w) at six x planes (middle and bottom rows); for the $U_\infty = 0.75$ m/s case at $t = 30$ s. Solid lines are isolines of temperature (400 K) and are used for marking the flame and plume regions. The cross-flow is in the streamwise x-direction and gravity is in the negative vertical z-direction. The 50 cm high tunnel is placed at $x = -30$ cm and the burner starts (ends) at $x = 0$ (5) cm.

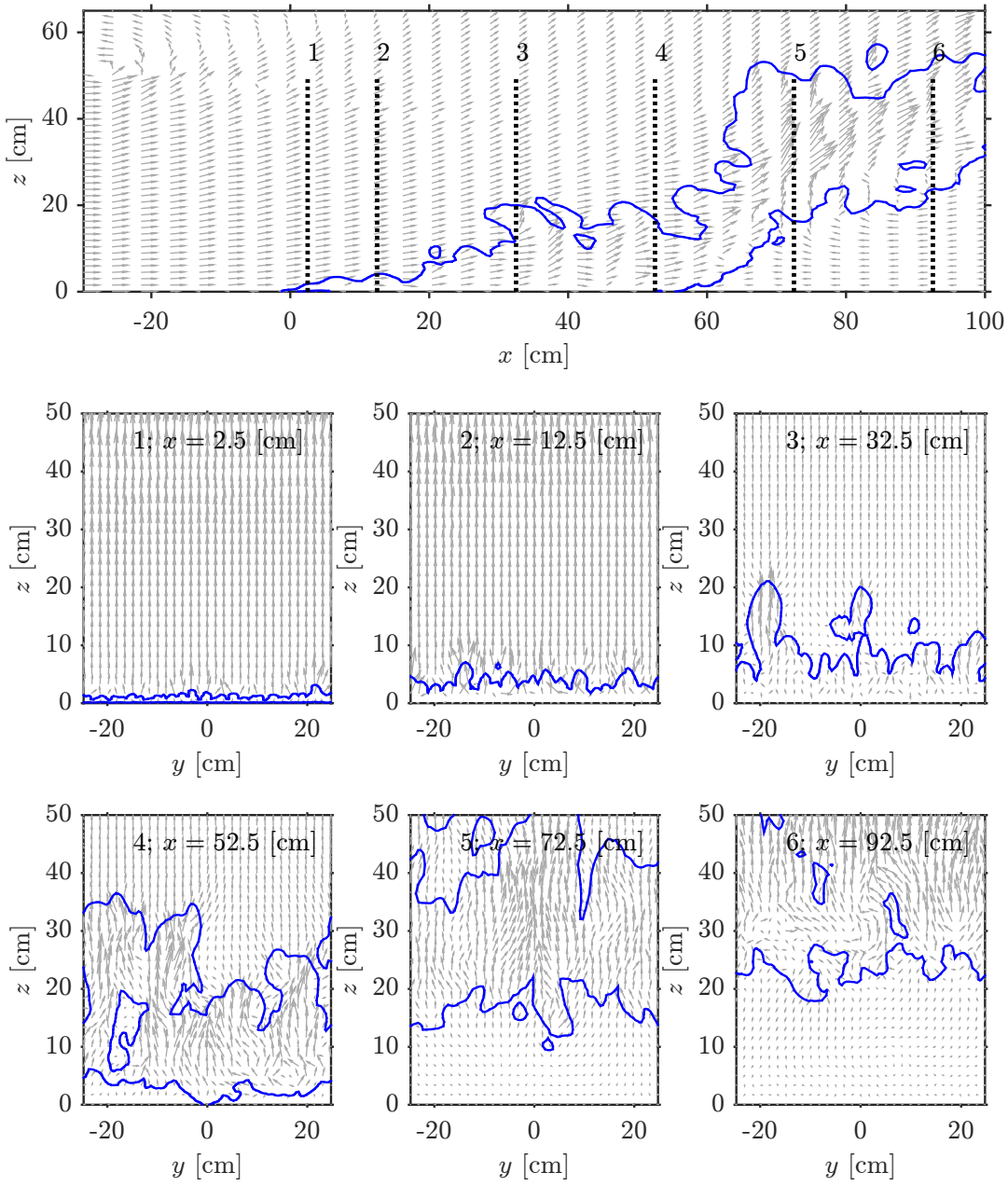

Figure 4.11: Instantaneous velocity vectors and temperature (400 K) isolines from the $U_\infty = 1.5$ m/s case at $t = 30$ s. See Figure 4.10 caption for additional details.

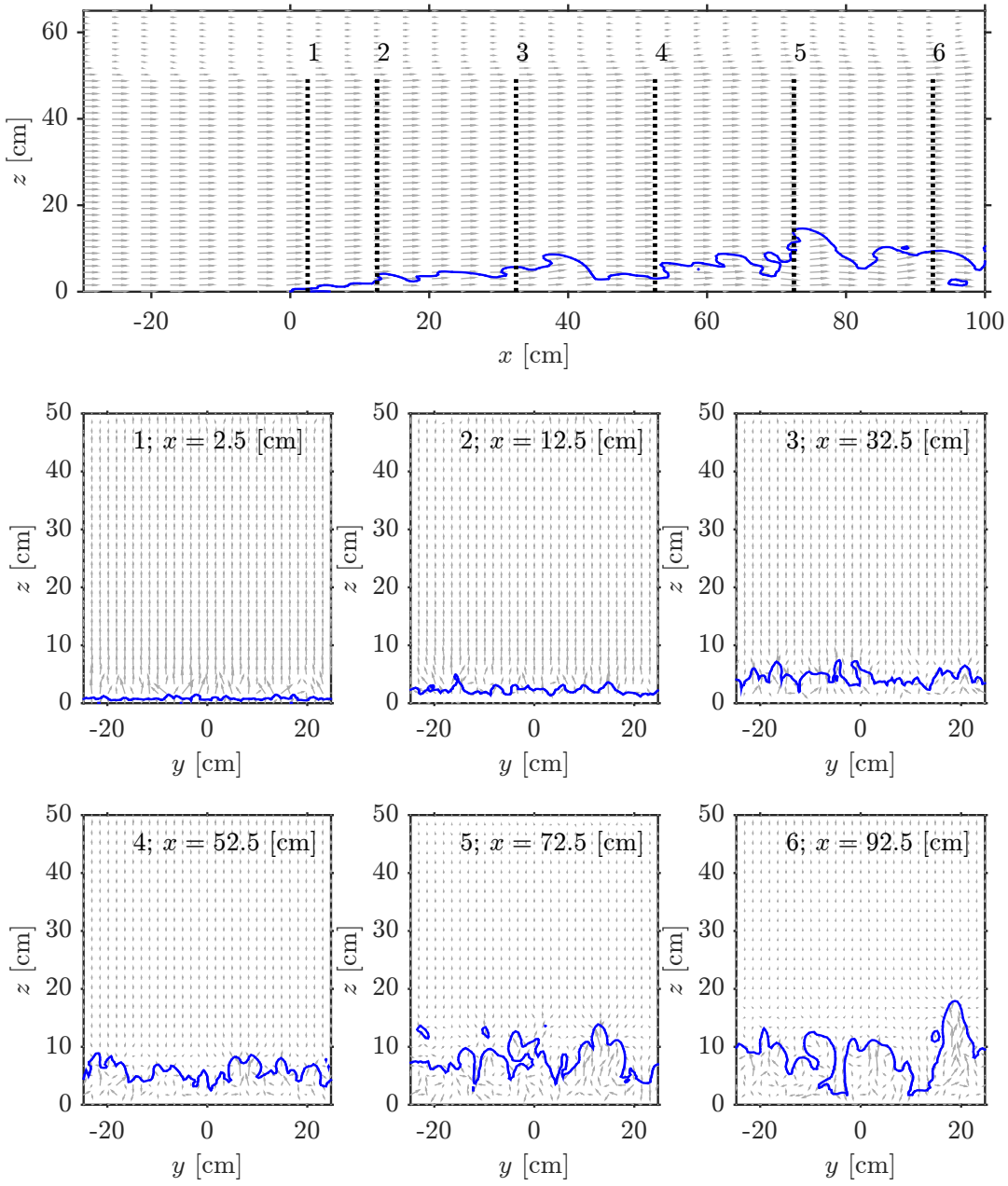

Figure 4.12: Instantaneous velocity vectors and temperature (400 K) isolines from the $U_\infty = 3$ m/s case at $t = 30$ s. See Figure 4.10 caption for additional details.

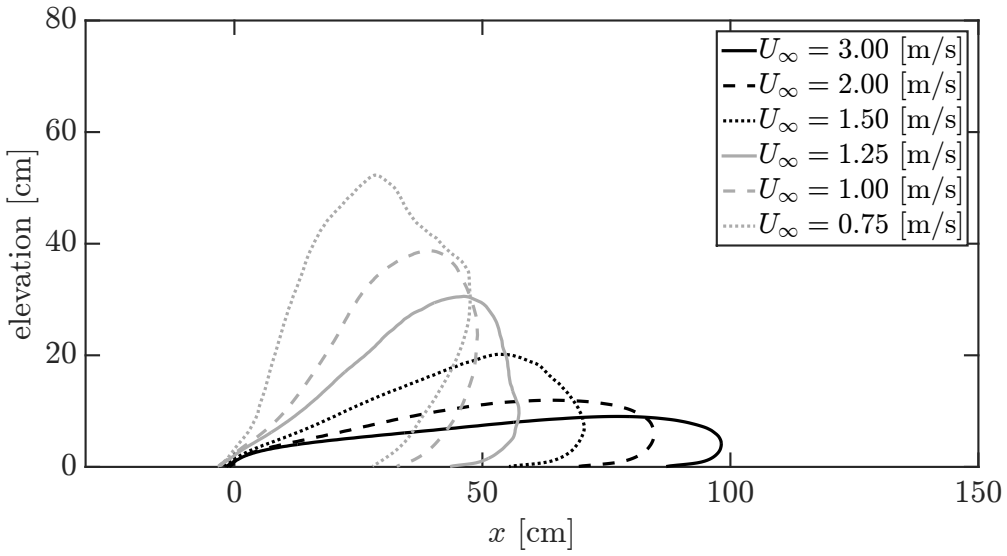

Figure 4.13: Mean flame shape visualized using a particular isoline of the time- and spanwise-averaged heat release rate per unit volume (50 kW/m^3).

kW/m^3 isocontours of time- and spanwise-averaged volumetric heat release rate. As U_∞ increases from 0.75 to 3 m/s, the flame transitions from a lifted (vertically tilted) flame to an attached (horizontal) flame. In the present configuration the transition from a vertical tilted flame to a horizontal flame is gradual. One interesting thing to note in this figure is that the 0.75 case does not show the two distinct regions (thin horizontal flame closer to the burner and a vertical flame further downstream, with an abrupt transition between the two regions) that were seen in the instantaneous view (see panel b in Figure 4.4), which shows that the flame geometry changes considerably in time.

Next, we consider the mean plume shape for the six different cases (Figure 4.14). The mean flame shape in this figure is marked by the 400 K isocontours of time- and spanwise-averaged temperature. With an increase in U_∞ from 0.75

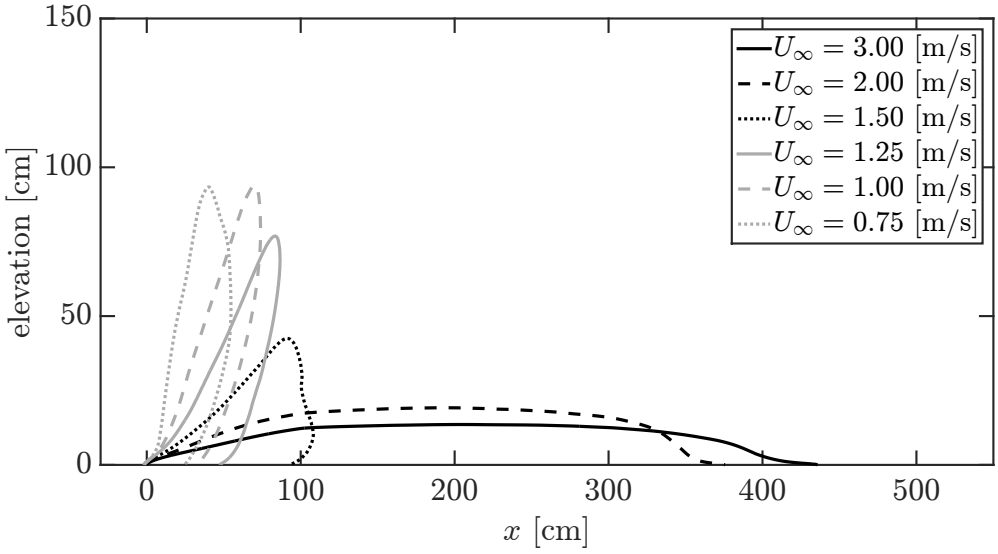

Figure 4.14: Mean plume shape visualized using a particular isoline of the time- and spanwise-averaged temperature (400 K).

to 3 m/s, the plume also transitions from a lifted (vertically tilted) plume to an attached (horizontal) plume. The plume, in contrast to the flame, transitions much more abruptly; for instance, the plume shape changes drastically (from vertically tilted to horizontal) when U_∞ is increased from 1.5 to 2 m/s. Again the two regions observed in the instantaneous view are not seen in this figure for the 0.75 m/s case.

Figure 4.15 adopts a quantitative perspective and shows the variations of flame and plume height, length and tilt angle with velocity. The definitions are shown in Figure 1.4. The height of the flame (plume) decreases from ≈50 (≈90) to ≈10 (≈10) cm. Flame length is nearly constant and is ≈50 cm, but the plume length first decreases and then increases significantly because of attachment to the downstream wall. The tilt angle decreases from ≈75 degrees to almost 0 degrees for both the flame and the plume.

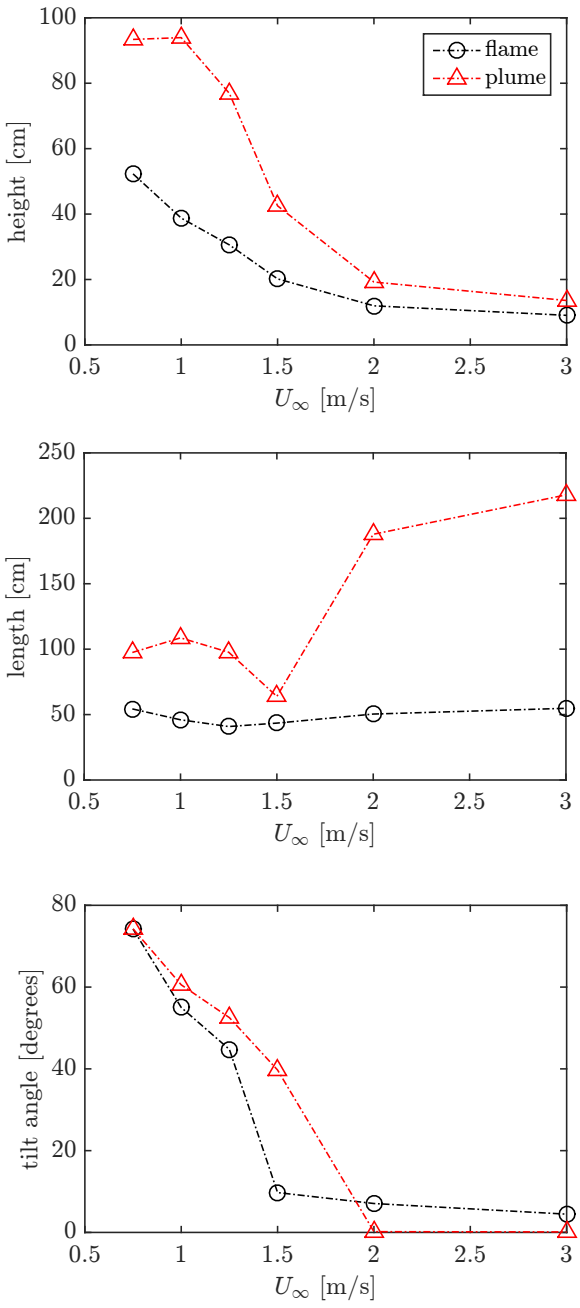

Figure 4.15: Flame and plume height, length and tilt angle based on the definitions presented in Figure 1.4; using the contours presented in Figures 4.13 and 4.14, respectively.

We now consider the spatial variations of mean velocity vector $(\overline{u}, \overline{w})$ for all the cases (Figure 4.16). In the cases with $U_\infty = 0.75$, 1 and 1.25 m/s, the cross-flow is strongly deflected upwards; in addition, a reversed flow is induced by the flame and plume on the downwind side leading to a two-sided entrainment similar to the flow structure in pool fires. In contrast, in the cases with $U_\infty = 2$ and 3 m/s, the cross-flow is only weakly affected by the presence of the flame and plume and entrainment is one-sided because both flame and plume are attached to the downstream surface. The case with $U_\infty = 1.5$ m/s is intermediate between the two configurations discussed above; in which the flame is unable to completely deflect the flow, but it ends up being deflected by the plume at a certain distance downstream of the flame zone.

4.4.3 Attachment length

In this section we focus on the attachment length, which is an important part of the wildland fire spread puzzle [37]. We first consider the following three (mean) attachment lengths in Figure 4.19:

- Plume attachment length; given by the x-distance downstream of the burner at which the 400 K temperature isoline intersects the bottom surface ($z = 0$), see Figure 4.14 (and Figure 4.17).

- Flame attachment length; given by the x-distance downstream of the burner at which the 50 kW/m^3 heat release rate isoline intersects the bottom surface ($z = 0$), see Figure 4.13.

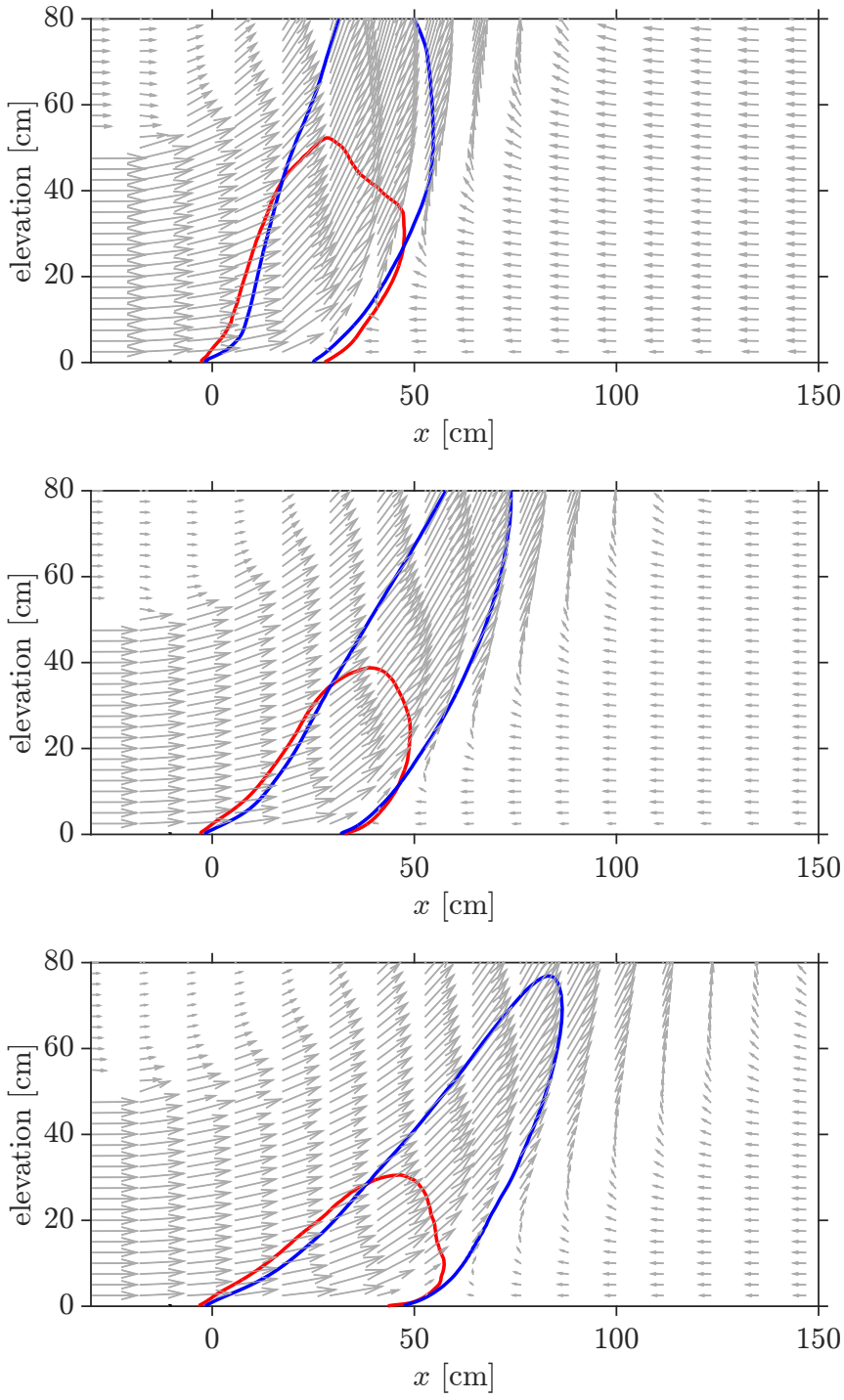

Figure 4.16: Spatial variations of the mean flow velocity vector $(\overline{u}, \overline{w})$: $U_\infty = 0.75$, 1, 1.25, 1.5, 2 and 3 m/s (top to bottom). Red (blue) lines are isolines of the mean heat release rate per unit volume (temperature), 50 kW/m^3 (400 K), and are used for marking the flame (plume) region.

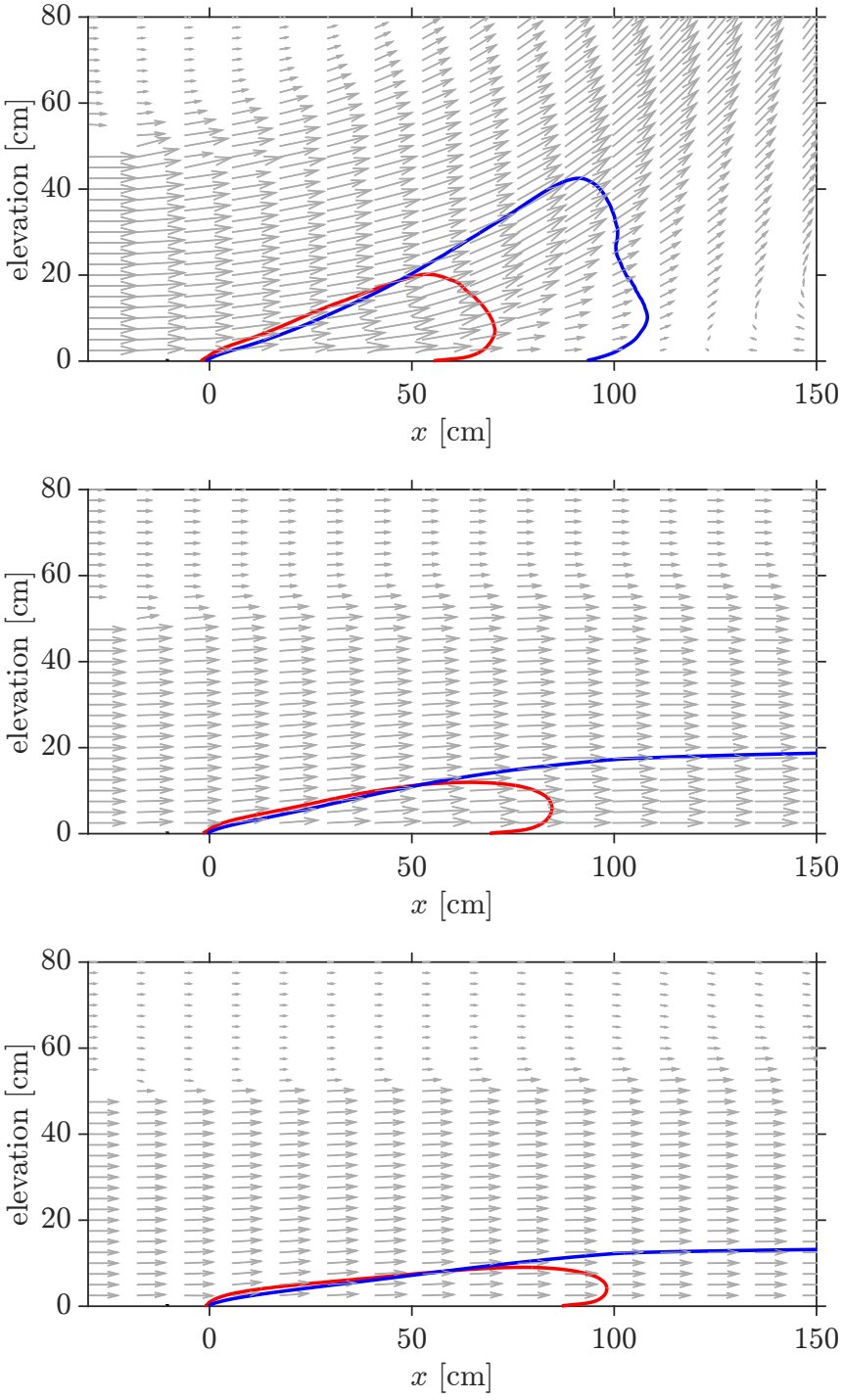

Figure 4.16: Continued.

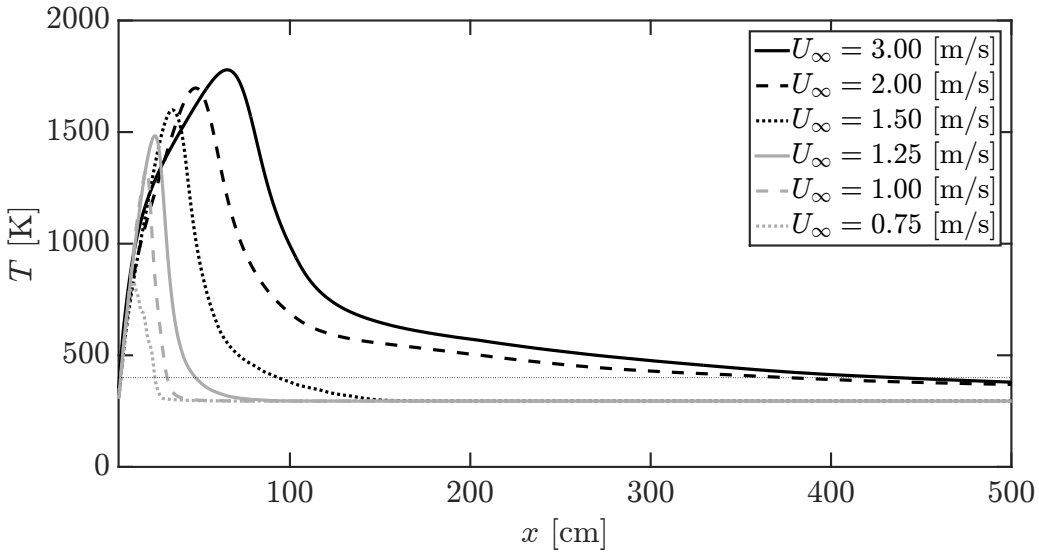

Figure 4.17: Streamwise variation of the time- and spanwise-averaged wall temperature, downstream of the burner. Thin dotted black horizontal line is drawn to visualize the condition $T = 400$ K.

- Flow attachment length, given by the x-distance downstream of the burner at which the wall shear stress τ_w changes sign or becomes 0 for the first time, see Figure 4.18.

For $U_\infty \leq 1.25$ m/s, the plume, flame and flow separate from the bottom surface at roughly the same x-location downstream of the burner. In this regime the heat transfer to the fresh fuel downstream of the flame zone is expected to be dominated by radiation. For $U_\infty = 1.5$ m/s the flame actually never separates, it just stops extending in the x-direction (as well as the z-direction) once all the fuel is consumed. The plume and flow both end up separating at a certain x-distance downstream of the flame zone. Over this distance (after the end of the flame zone and before the separation of the plume and flow) one can expect convective heat transfer

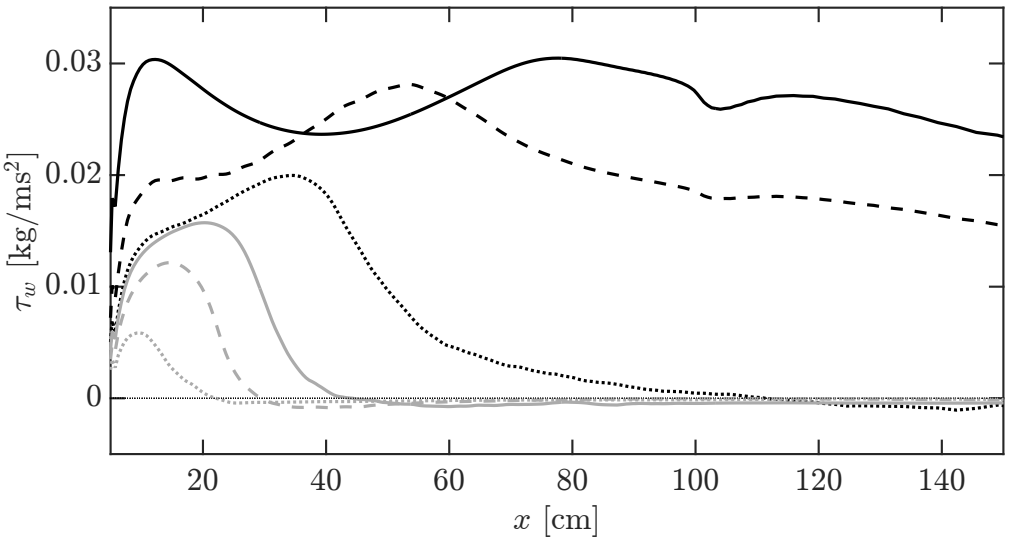

Figure 4.18: Streamwise variation of wall shear stress, τ_w, downstream of the burner. Thin dotted black horizontal line is drawn to visualize the condition $\tau_w = 0$. For legend see Figure 4.14. Note that τ_w becomes 0 for $x \geq 205$ cm (not shown) because of the slip wall (see Figure 4.1).

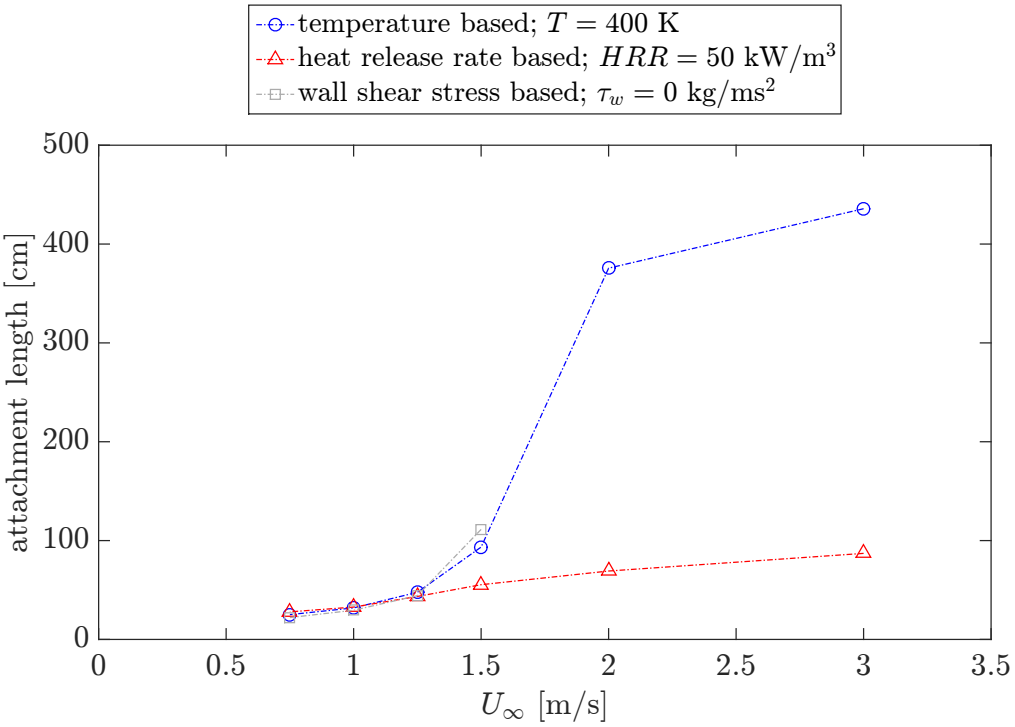

Figure 4.19: Change in plume (temperature based), flame (heat release rate based) and flow (wall shear stress based) attachment length with U_∞. For the cases with $U_\infty = 2$ and 3 m/s the flow remains attached throughout the computational domain, hence, these two points are omitted from the flow attachment length curve.

to play a significant role because of the transport of hot combustion products from the flame zone, by the flow, towards the fresh fuel. For the last two cases ($U_\infty = 2$ and 3 m/s), the flame, plume and flow never separate; the end of the flame is reached once the fuel is consumed and the the end of the plume is reached once enough mixing with the ambient wind has decreased the temperature to < 400 K. Again one can expect convective heat transfer to play a significant role in the region after the flame zone and before the end of the plume zone. Unfortunately, because of the adiabatic boundary condition used on the wall downstream of the burner, a heat transfer analysis can not be performed using the present simulations. Heat transfer will be studied in future work.

One important question, that an instrument like LES appears to be well-suited to answer, is: how far the attachment length can extend beyond its mean value? Due to this question, we now analyze the PDFs of the different attachment lengths. Shown in Figure 4.20 are the PDFs of the flame attachment length for all the cases. These PDFs are constructed by using heat release rate data from all the (100) cells along the span from 12 seconds of simulation, saved at every tenth time step. As can be seen, the PDFs shift to the right with an increase in U_∞ indicating an increase in the mean flame attachment length, which is expected. Additionally the PDFs get broader due to an increase in wind velocity, which indicates an increase in flame extension beyond the mean flame attachment length. Figure 4.21 provides normalized values of the minimum and maximum flame attachment lengths. Normalization in this figure is done using the attachment length that corresponds to the peak probability values in Figure 4.20. One can clearly see that the flame attachment length

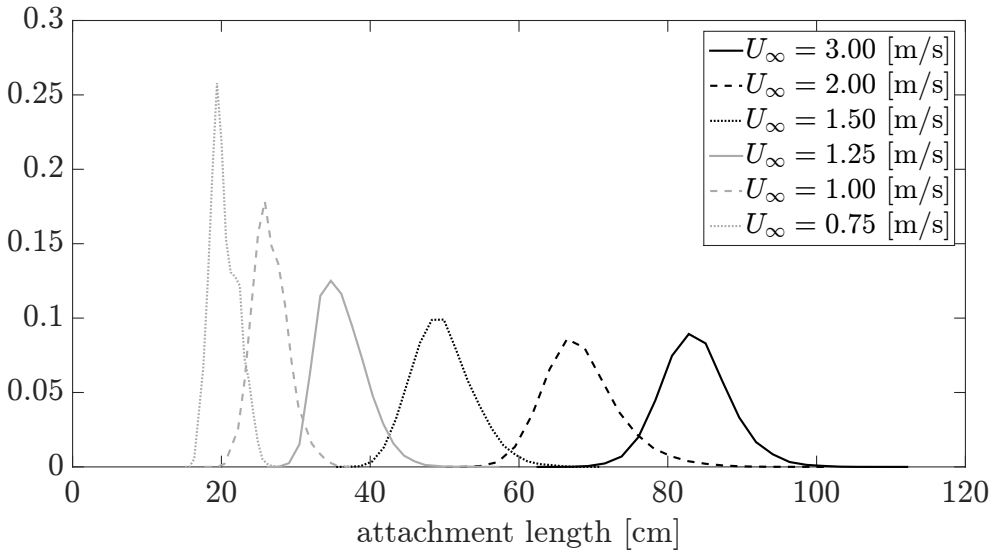

Figure 4.20: Probability Density Functions (PDFs) of flame attachment length; based on the 50 kW/m^3 isocontour.

varies significantly in time e.g., by almost 60% in the 1.25 m/s case. One interesting thing to note in Figure 4.21 is that the normalized minimum and maximum values are nearly constant; which could of significant value from a practical viewpoint.

Similarly, Figure 4.22 shows PDFs of plume attachment length based on 600 K isocontours of temperature and Figure 4.23 contains the normalized minimum and maximum values of the plume attachment length. A higher value of temperature (i.e., 600 K) is used here instead of 400 K because as seen in Figure 4.19 the plume attachment length based on 400 K reaches a value close to 400 cm for the 2 and 3 m/s cases; and at such high values of x the grid resolution is quite coarse in the current setup because of stretching (see top panel in Figure 4.2) which would not accurately capture plume attachment length changes over time. Similar to the flame attachment length PDFs, the plume attachment length PDFs also shift to the

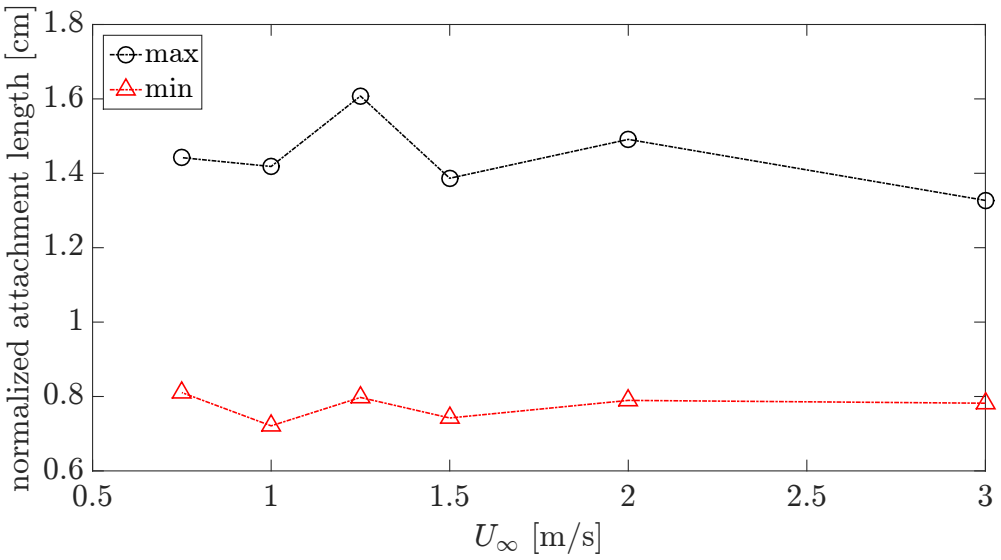

Figure 4.21: Maximum and minimum values of the normalized flame attachment length for all the cases. Normalization is done using the flame attachment length that has the maximum probability in Figure 4.20.

right with an increase in velocity; the PDFs also become broad with an increase in velocity. Figure 4.23 shows that the plume attachment length varies significantly over time e.g., by 80% in the 2 m/s case. Similar to the flame attachment length variation the plume attachment length also appears to be roughly constant with velocity, which again could be of significant interest from a practical perspective.

Overall, what is clear from the initial analysis presented in this section, is that flame dynamics deserves further study.

In the next section we will make detailed comparisons between data from LES and the integral model.

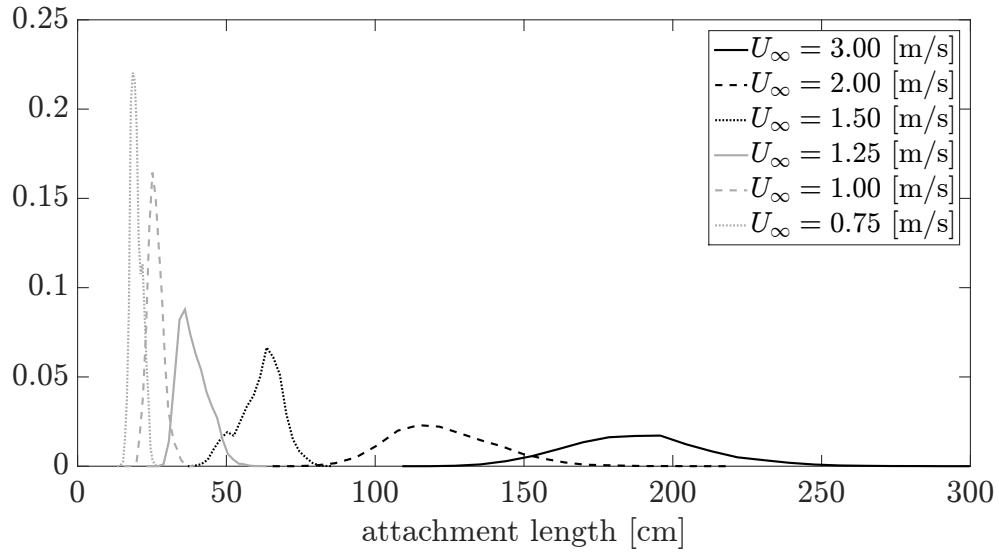

Figure 4.22: Probability Density Functions (PDFs) of flame attachment length; based on the 600 K isocontour.

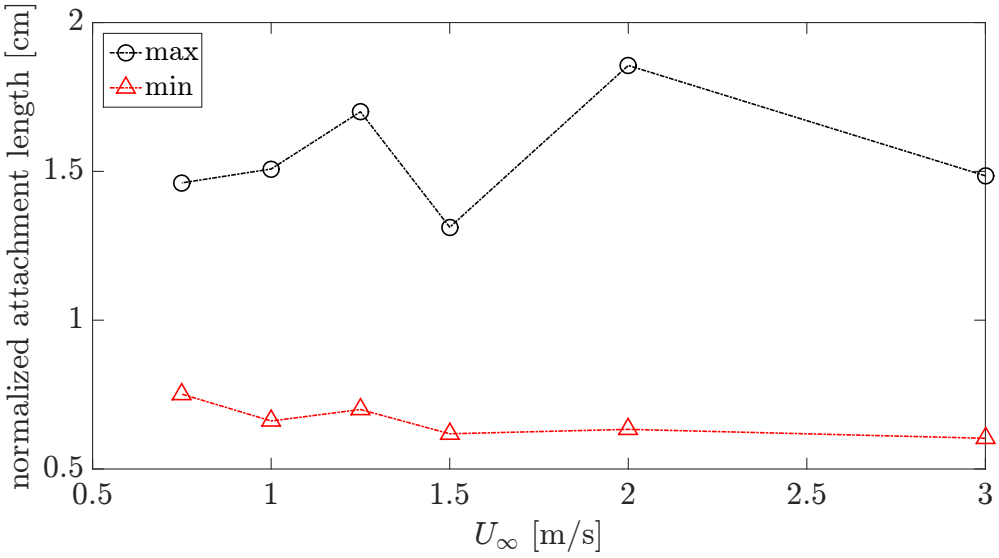

Figure 4.23: Maximum and minimum values of the normalized plume attachment length for all the cases. Normalization is done using the flame attachment length that has the maximum probability in Figure 4.22.

4.4.4 Comparison between LES and the integral model

This section shows comparisons between LES and the integral model. First we compare the flame and plumes shapes seen in LES with those seen in the integral model (see Figure 4.24). As can be seen the integral model predicts the flame shapes reasonably well for the cases with $U_\infty \leq 1.5$ m/s; for the other two cases the comparison is not as good; in particular a shorter flame is predicted by the integral model for the cases in the attached flame regime ($U_\infty \geq 2$ m/s or $N_C < 1$). This decrease in performance of the integral model in the attached flame regime is expected because in its current form the integral model does not have a sub-model that can account for the blockage of entrainment from one side due to the downstream wall. The plume shapes predicted by the model do not compare well with the LES plume shapes and are significantly short and wide in most cases; the model not only struggles in the attached flame regime but also in the detached flame regime. But it should be noted that in this figure the flame and plume shapes are determined in different manners in LES and the integral model. As discussed in one of the previous sections, in LES the flame shape is marked by the 50 kW/m^3 isocontour of heat release rate and the plume shape is marked by the 400 K isocontour of temperature. In the integral model, however, the coordinates of the upper (x_u, z_u) and lower (x_l, z_l) ends of both the flame and plume zones are determined as follows:

$$(x_u, z_u) = (x_c - b\,\sin(\theta), z_c + b\,\cos(\theta)) \tag{4.10}$$

$$(x_l, z_l) = (x_c + b\,\sin(\theta), z_c - b\,\cos(\theta)) \tag{4.11}$$

The flame in the integral model is considered to end along the flame/plume centerline when fuel mass fraction Y_F goes to 0 or at $s_{(Y_F=0)}$ and the plume is considered to end when T_p reaches a value of 400 K or at $s_{(T_p=400)}$. This difference in flame and plume shape definitions in LES and the integral model is expected to be behind some of the discrepancies seen in Figure 4.24 (discussed above).

There are two ways to tackle the aforementioned issue of different definitions in LES and the integral model: one is to consider the use of Gaussian profiles in the integral model [16, 86]; the other is to process the LES data in a way that is consistent with the integral model. We chose the second option; the results are discussed in the following.

First, we determine the flame/plume centerline from the LES data by smoothing the line connecting the points (on several temperature isocontours) that have the maximum distance from the burner center $(x = 2.5, z = 0)$ cm. See Figure 4.25 for visualization and additional details on the centerline extraction procedure adopted in this study.

The centerlines determined using the above procedure are compared with the centerlines given by the integral model in Figure 4.26. As expected from Figure 4.24 the centerlines for the 0.75, 1 and 1.25 m/s cases (both from LES and the integral model), first rise slowly and then much more rapidly. In these three cases the agreement between LES and the integral model is good up to $z_c \approx 30$ cm but

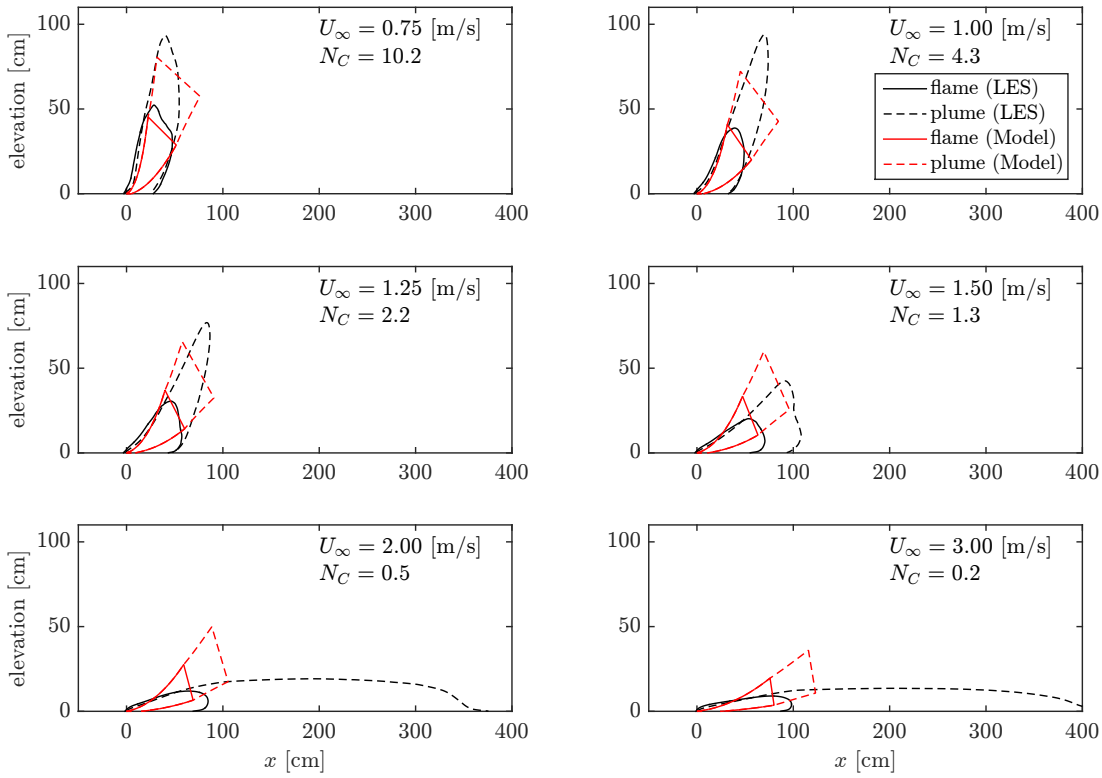

Figure 4.24: Comparison of flame and plume shapes, for the different cases, from LES and those from the integral model developed in this work.

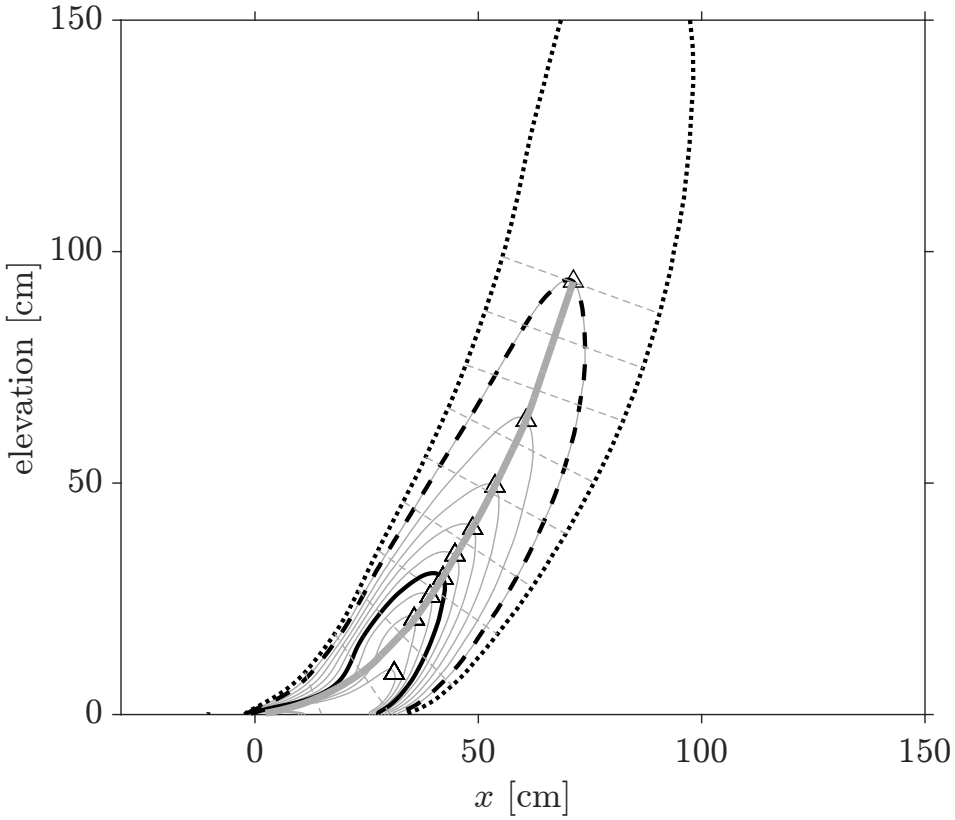

Figure 4.25: Visualization of the procedure used to extract the flame/plume centerline from LES data. This figure corresponds to the 1 m/s case. The black solid, dashed and dotted lines correspond to isocontours of 650, 400 and 350 K, respectively. The thin grey solid lines represent the temperature contours between 800 and 400 K, 50 K apart from each other. The black triangles denote the points on the different temperature isocontours that have the maximum distance from the burner center ($x = 2.5, z = 0$) cm. The thick grey solid line shows the flame/plume centerline which is generated by smoothing the line that results from connecting the black triangles. The thin grey dashed lines are local normals to the flame/plume centerline; these lines cover the local width of the 350 K isocontour.

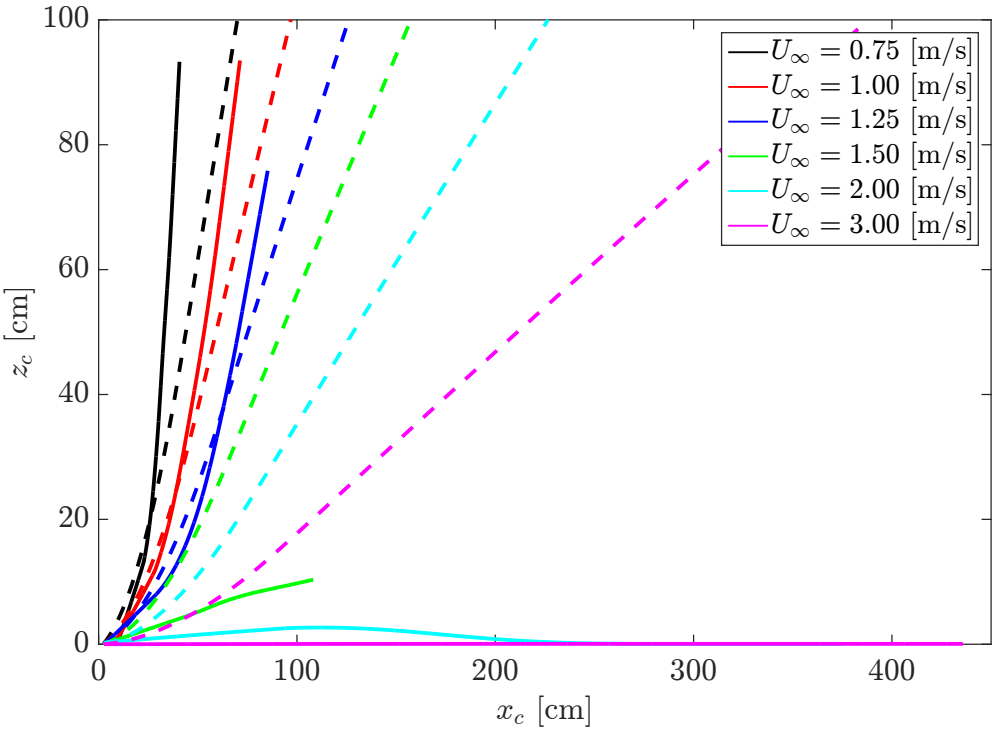

Figure 4.26: Flame/plume centerline for the different cases. Solid (dashed) lines correspond to LES (the integral model).

beyond that point the centerlines in LES rise relatively more rapidly. There are significant discrepancies between the LES and the integral model centerlines for the 1.5 m/s case. One of the reasons for the large discrepancies in this case is the lack of wall attachment model in the current version of the integral model. But another important reason is that the LES temperature isocontours in this case are not completely smooth (see Figure 4.24) and it appears that the centerline extraction procedure is not able to select the right point on the contour, which leads to a significantly different centerline in LES. For the 2 and 3 m/s cases the integral model fails to predict attachment of the centerline to the wall because of a lack of a wall attachment sub-model.

We now compare the angle made by the flame/plume centerlines with the horizontal plane in Figure 4.27. For the 0.75, 1 and 1.25 m/s cases there is an initial rapid increase both in LES and the integral model and then there is a plateau. The final values in LES are higher than the integral model (as expected from Figure 4.26). But the change in the final value of the angle with cross-wind velocity U_∞ in LES is captured well by the integral model: the angle decreases by $\approx$ 10 degrees when U_∞ is increased from 0.75 to 1 m/s; it decreases by roughly another 10 degrees when U_∞ is further increased to 1.25 m/s. For the rest of the cases (1.5, 2 and 3 m/s) the integral model disagrees with LES at almost every level for reasons already discussed above. It is worth mentioning here that the asymptotic value of the angle given by the integral model can be shown (after some approximations) to satisfy the following equation (which not surprisingly involves the Byram's convection number N_C):

$$(\tan(\theta))^2(\alpha\tan(\theta) + \beta) = \frac{N_C}{4} \tag{4.12}$$

Clearly, the above equation suggests that the angle θ is a function of the entrainment coefficients (α and β), which after some calibration can provide a better match between the angle seen in LES and the integral model. But we follow Mercer and Weber [16] and use $\alpha = 0.16$ and $\beta = 0.5$ in order to evaluate/show the performance of the model without any additional calibration.

In Figure 4.28 we compare the flame/plume width $2b$ from LES and the integral model. The model predicts a continuous increase in $2b$ with a similar rate throughout the flame/plume zones whereas the rate of increase changes significantly in LES

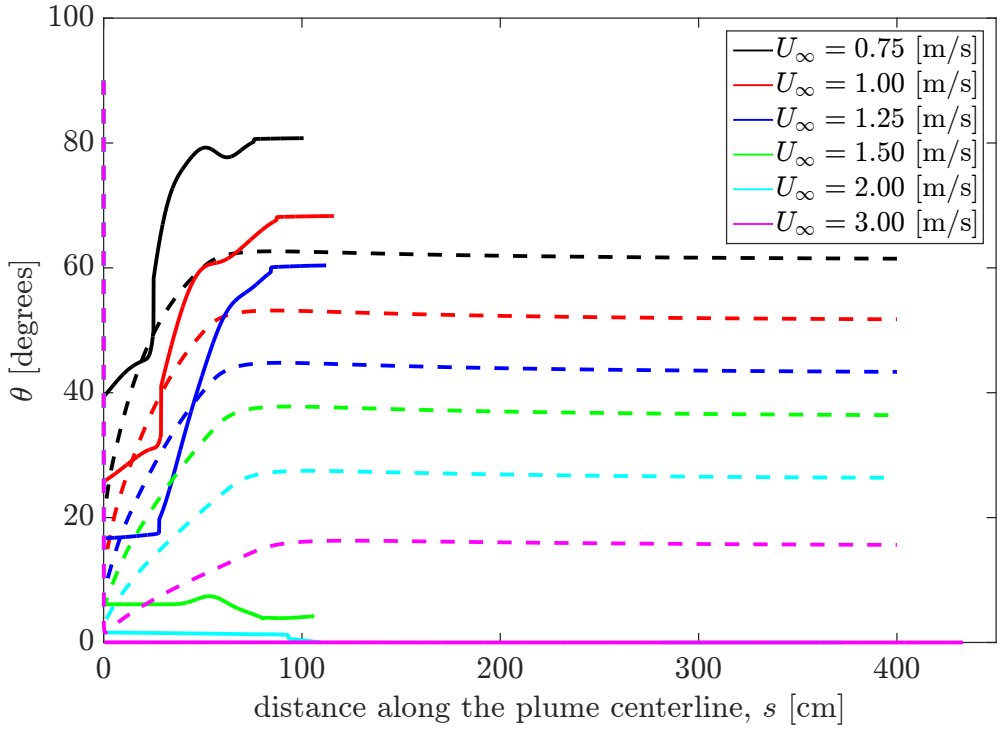

Figure 4.27: Angle made by the flame/plume centerline with the horizontal plane, for the different cases. Solid (dashed) lines correspond to LES (the integral model).

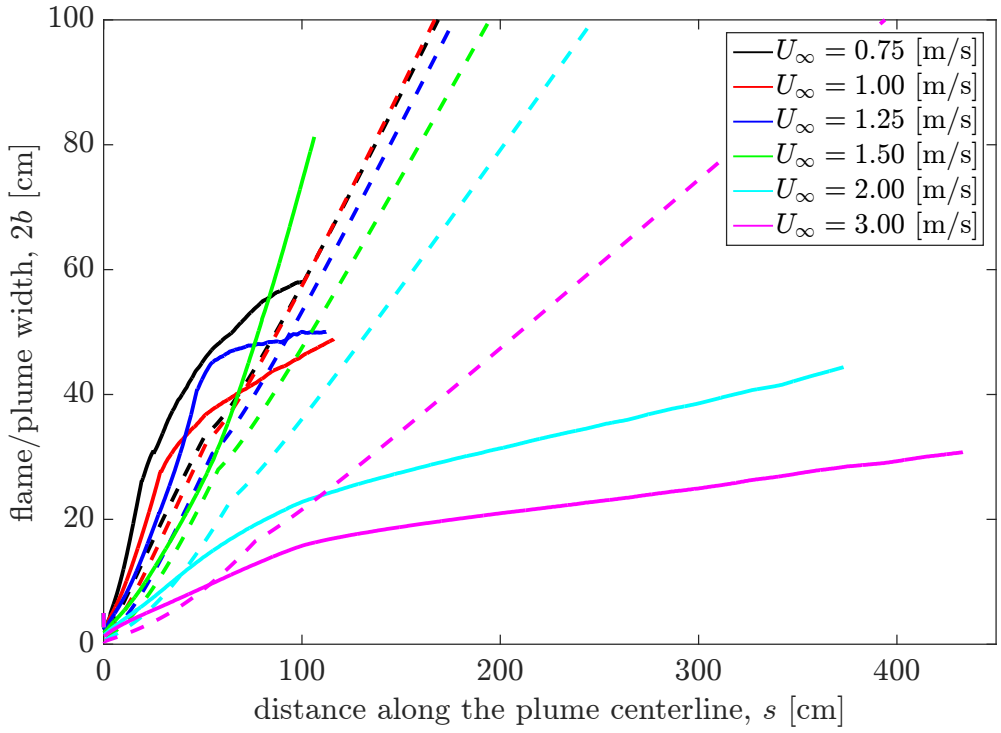

Figure 4.28: Variation of the flame/plume width with s, for the different cases. Solid (dashed) lines correspond to LES (the integral model).

curves, initially the rate is much higher than that during the later stages. This happens because in LES $2b$ is the local width of a particular (330 K) temperature isocontour (see Figure 4.25 for some sample isocontours of temperature in the 1 m/s case), which after a certain point stops changing significantly with s; it even starts shrinking beyond a certain point. Accordingly, only that region of the LES curves (in Figure 4.28) should be compared with the model in which the rate of increase of $2b$ with s is approximately constant. Overall, the agreement between LES and the integral model is reasonable for the cases with $U_\infty \leq 1.5$ m/s but the model struggles for the 2 and 3 m/s cases and predicts a consistently thicker plume because of lack of attachment.

After comparing the variables related to the flame/plume geometry from LES with those given by the integral model, we now compare the variation of temperature T_p along the flame/plume centerline in Figure 4.29. From LES T_p is extracted by spatially averaging, along the flame/plume width, the time- and spanwise-averaged value of grid-resolved temperature. All the curves have the same general shape: first a rapid increase then a slower decay. The integral model is able to predict the decay rate reasonably well for all the cases; albeit the actual values of T_p are significantly different in the 2 and 3 m/s cases which is probably because of a significant overprediction in the flame/plume width (see Figure 4.28). The model significantly underpredicts the peak temperature in all cases; this is expected to be because of the assumption of a global equivalence ratio (GER) of 0.1 in the integral model.

In summary, the integral model performs fairly well for cases with $U_\infty \leq 1.25$ m/s. The performance for the 1.5 m/s is not good mainly because the centerline extraction procedure is not able to extract the correct flame/plume centerline in this case. For the 2 and 3 m/s cases the performance is much worse because of a lack of wall attachment model.

4.5 Concluding remarks

Fine-grained LES are performed to bring fundamental insights into the effects of cross-wind velocity on the structure of a methane-air, buoyancy-driven, turbulent line flame (50 kW) stabilized on top of a horizontal floor surface. As the cross-flow velocity is increased, the flame transitions from a pool-like flame characterized

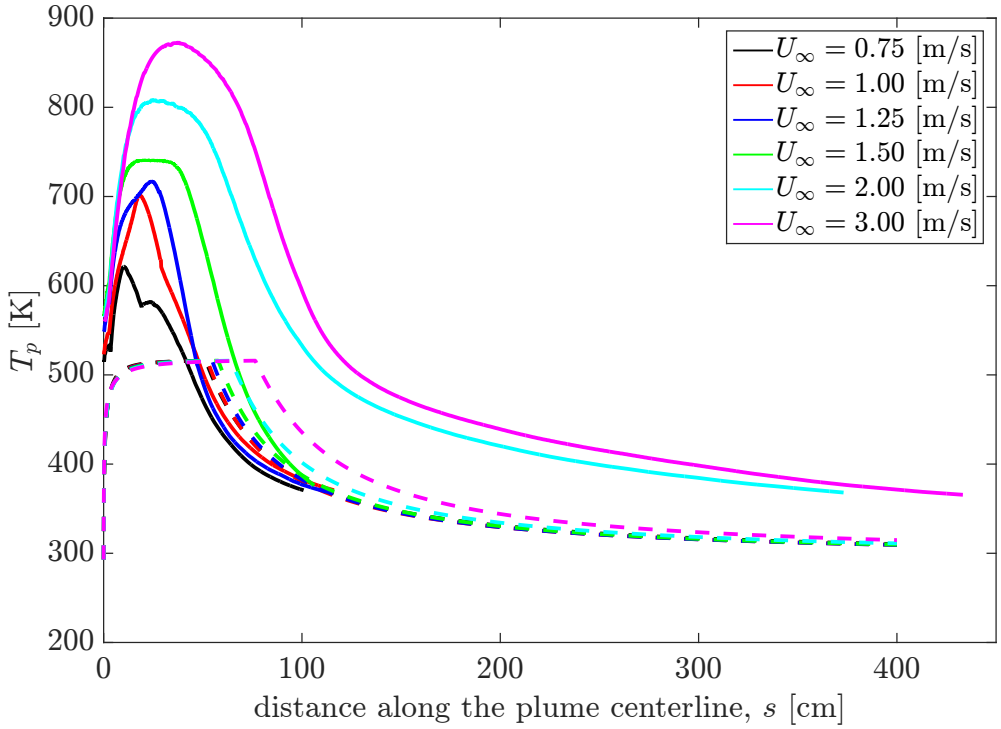

Figure 4.29: Variation of the flame/plume temperature T_p with s, for the different cases. Solid (dashed) lines correspond to LES (the integral model).

by a tilted vertical shape to a boundary layer flame characterized by a horizontal shape. The pool-like flame strongly deflects the incoming cross-flow upwards and features downwind flow separation and two- sided air entrainment into the flame. In contrast, the boundary layer flame does not significantly deflect the incoming cross-flow and features downwind flow attachment and one-sided air entrainment into the flame. The transition between the two regimes happens when the Byram's convection number $N_C \approx 1$. The flame, plume and flow attachment lengths are found to coincide in the buoyancy-dominated regime. The simulations suggest that the flame and plume attachment lengths fluctuate significantly in time.

An integral model is also developed that can describe the effects of cross-wind on the structure of a turbulent, buoyant line fire. The model, after some approximations, suggests that the plume tilt angle is controlled by N_C and the entrainment coefficients α and β. Detailed comparisons with LES are made which show that the model is capable of performing fairly well for cases with $U_\infty \leq 1.5$ m/s (or $N_C \gtrsim 1$); but is unable to describe the 2 and 3 m/s (or $N_C \lesssim 1$) cases due to the absence of a wall attachment sub-model.

5: Effects of slope on the structure of a turbulent line fire

5.1 Introduction

In this chapter we will study the effects of slope, using LES alone, on the structure of the same turbulent, buoyant, stationary, methane-fueled, line fire that was studied in the last two chapters. For doing so a few changes are made to the configuration discussed in the last chapter: first the wind tunnel is removed; second, the domain is made symmetric around the burner in the x-direction, this is done to allow simulations with inclination angles close to 0 degrees.

This chapter is organized as follows. The numerical configuration is presented in the next section. Then the results are presented and discussed. Some concluding remarks are made in the final section.

5.2 Numerical configuration

The numerical configuration is presented in Figure 5.1. The computational domain is 605-cm-long in the streamwise x-direction, 50-cm-wide in the spanwise y-direction and 250-cm-high in the vertical z-direction. The line burner face is 5-cm-long in the x-direction and 50-cm-wide in the y-direction; and the spanwise center of its leading edge is placed at the origin $(x, y, z) = (0, 0, 0)$. The burner

is flush-mounted on a 50-cm-wide horizontal solid plate that starts at $x = (-300)$ cm and ends at $x = 305$ cm. A 5-mm-long, 50-cm-wide and 5-mm-high trip wire is placed at $x = (-10.5)$ cm in order to perturb the entrained flow and promote laminar-to-turbulent transition.

The computational grid is a rectangular Cartesian mesh. Grid spacing in the streamwise x-direction is uniform and is equal to 5 mm for $(-50) \leq x \leq 55$ cm; beyond $x = (-50)$ and $x = 55$ cm the x-grid is stretched with a stretch factor equal to 1.06 (see top panel in Figure 5.2). Grid spacing in the spanwise y-direction is uniform and is equal to 5 mm. This streamwise (spanwise) resolution corresponds to 10 (100) grid cells across the burner length (width). Grid spacing in the vertical z-direction is non-uniform: the z-grid spacing is 1.2 mm at $z = 0$ (i.e, the first cell center is 0.6 mm above the south boundary of the computational domain) and is 20 mm at $z = 50$ cm with a stretching factor of 1.04. For $z \geq 50$ cm, the z-grid is stretched with a stretch factor equal to 1.06 (see bottom panel in Figure 5.2). Note that with the present resolution, the trip wire is under-resolved and is described with 1 (4) grid cell(s) in the x- (z-) direction. The total number of cells is 3.43 million.

The methane mass flow rate is prescribed at the burner boundary. Similar to the simulations in Chapters 3 and 4, both convective and diffusive mass fluxes are taken into account at the burner boundary [42]. The horizontal solid plate and the trip wire are both treated as no-slip adiabatic solid walls. The side boundaries at $y = (-25)$ and 25 cm correspond to periodic conditions. Other boundaries are treated as boundaries with open flow conditions.

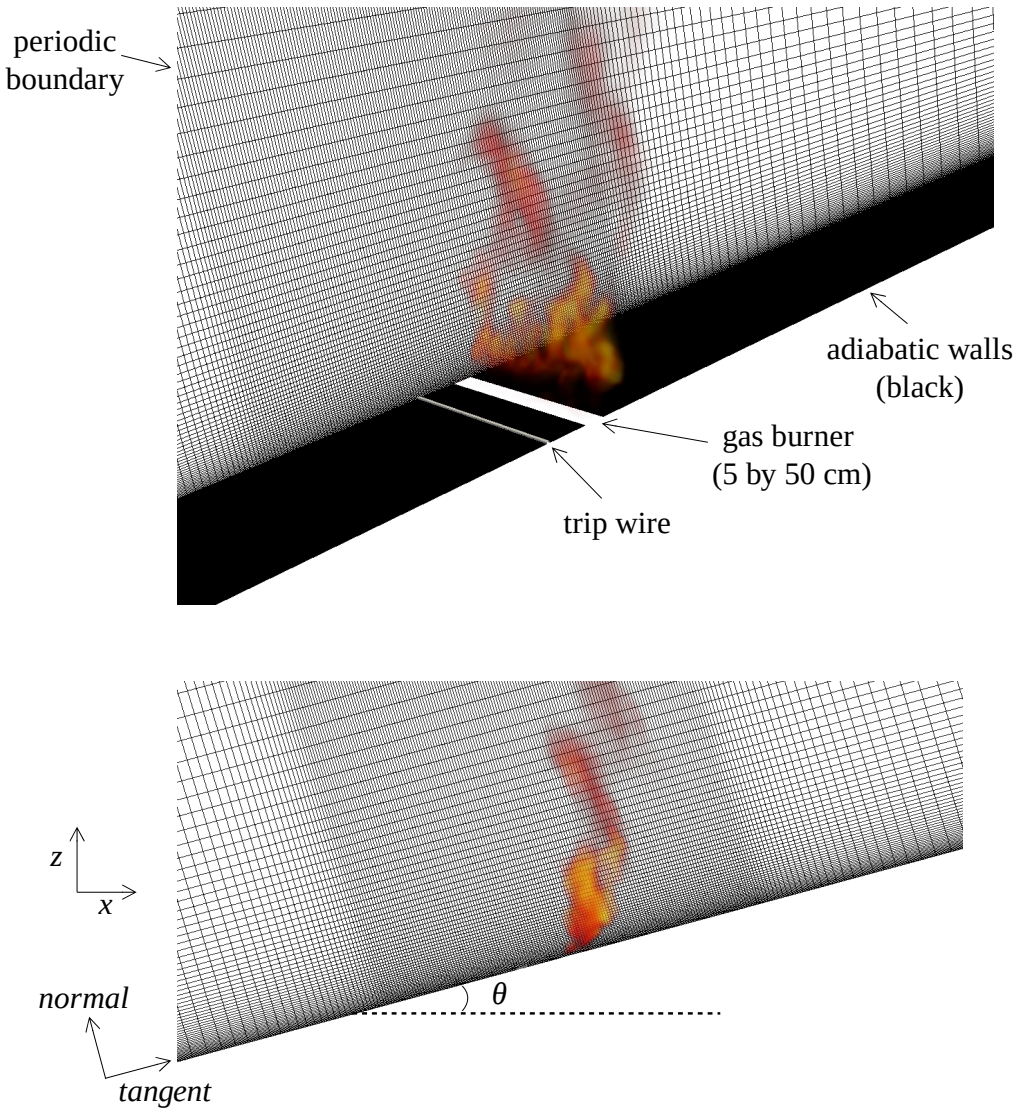

Figure 5.1: Numerical configuration used for studying the effects of slope on a turbulent line fire. Top panel presents a perspective view and bottom panel presents the side view. The Cartesian and normal-tangential coordinate systems are shown in the bottom panel; both of them are used in the following. As shown in the bottom panel, inclination angle (θ) in the present study is measured with respect to the horizontal plane. The 50 kW methane diffusion flame is visualized using volume rendering of temperature.

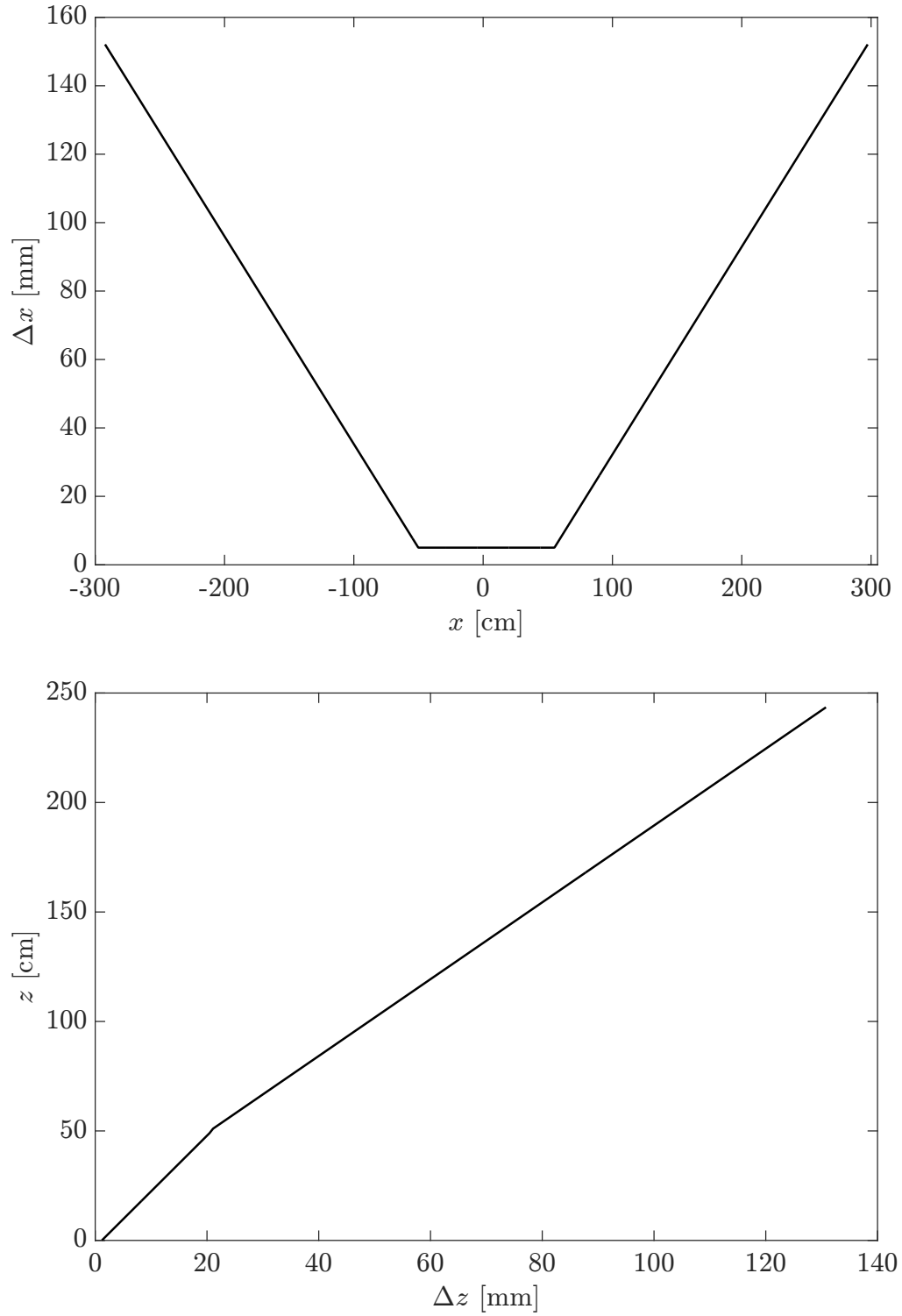

Figure 5.2: Horizontal variation of Δx (top) and vertical variation of Δz (bottom) for the case with $\theta = 0$ degrees.

The slopes for different cases are created by rotating the computational domain in the counter-clockwise direction, around the origin in the x-z plane.

All simulations are performed for a duration of 30 s. Turbulent statistics are collected for the final 15 s of each simulation, after the flow and flame become statistically stationary and long enough for the statistics to be converged (to improve convergence, statistics are computed using both temporal- and spanwise-averaging). The time step is controlled by a classical Courant-Friedrichs-Lewy (CFL) condition and is approximately equal to 0.35 ms. Each simulation is run using 200 processors on a large-scale Linux cluster with a typical simulation requiring 40,000 CPU-hours.

5.3 Results and discussion

5.3.1 Instantaneous flame, plume and flow structure

Similar to the horizontal configuration with wind (discussed in the previous chapter), we first study the instantaneous flame, plume and flow structure seen in our simulations with θ = 0, 8, 16, 24 and 32 degrees. Figures 5.3 to 5.7 present the flame, plume and flow structure in terms of volume rendering of heat release rate per unit volume, volume rendering of temperature and isocontour of Q-criterion colored with grid-resolved streamwise velocity u, for the five cases at t = 30 s. Four different views are provided in these figures. Note that these figures are created in the normal-tangential coordinate system.

The two regimes discussed in the literature and in Chapter 1 (detached and attached) can be clearly seen in Figures 5.3 to 5.7, specifically see panel b which

shows the side-view: cases with 0 and 8 degrees inclination belong to the former regime; the case with 32 degrees inclination belongs to the latter regime; the rest of the two cases (with 16 and 24 degrees inclination) are in the intermediate regime. So the transition, in terms of inclination angle, is gradual in the present simulations. Note that most of the literature [36, 37] suggests that the transition from one flame regime to the other happens around an inclination of 25 degrees; so the present simulations are consistent with the literature in this regard.

None of the five cases show any signs of puffing like the low velocity (or high N_C) cases in the last chapter and in the literature [18]. Also none of these cases show the two regions (one with the flame restricted to a relatively thin layer close to the wall and the other where the flame is almost normal to the bottom surface) seen in the low velocity cases in the last chapter.

As the flame transitions from the detached state to the attached state the maximum temperature encountered in the simulation rises (which is indicated by an increase in the semi-transparent white color in the temperature volume rendering presented in Figures 5.3 to 5.7). So, with an increase in inclination angle, flame spread is increased not only because of a smaller distance between the flame and the unburnt fuel but also because the flame is at a relatively higher temperature.

In all cases the flame transitions fairly rapidly (or within a short distance from the burner) from a laminar to a turbulent state. For the cases with the inclination of 16, 24 and 32 degrees, the Q criterion isocontours (see e.g., bottom plot in panel a in Figures 5.3 to 5.7) suggest that the perturbation wire plays an important role in the transition.

The flame structure in the intermediate regime (inclination of 16 and 24 degrees) in this configuration is significantly different from the flame structure in the intermediate regime in the cross-wind cases discussed in the previous chapter. For instance for the 16 degrees case the volume rendering of temperature in Figure 5.5 shows a few big randomly distributed structures, whereas the volume rendering of temperature in Figure 4.6 (for the 1.25 m/s case discussed in the last chapter) shows the presence of streaks close to the burner that increase in size with downstream distance. How exactly would the spread rate be affected by these differences in instantaneous structure is unclear and will be considered in future work.

In the next section we will consider the mean flame, plume and flow structure.

5.3.2 Mean flame, plume and flow structure

We first consider the mean flame shape for all five inclination angles, both in the Cartesian and normal-tangential coordinate systems (Figure 5.8). The mean flame shape in this figure is marked by the 50 kW/m^3 isocontours of time- and spanwise-averaged volumetric heat release rate. Overall, as θ increases from 0 to 32 degrees, the flame transitions from a detached to an attached flame; with the most significant change happening between θ = 16 and 32 degrees. Furthermore, an increase in the inclination angle from 0 to 16 degrees does not have a significant effect on the flame shape in the Cartesian coordinate system.

We then consider the mean plume shape for the five cases in the normal-tangential coordinate system (Figure 5.9). The mean plume shape in this figure is marked by the 400 K isocontours of time- and spanwise-averaged temperature.

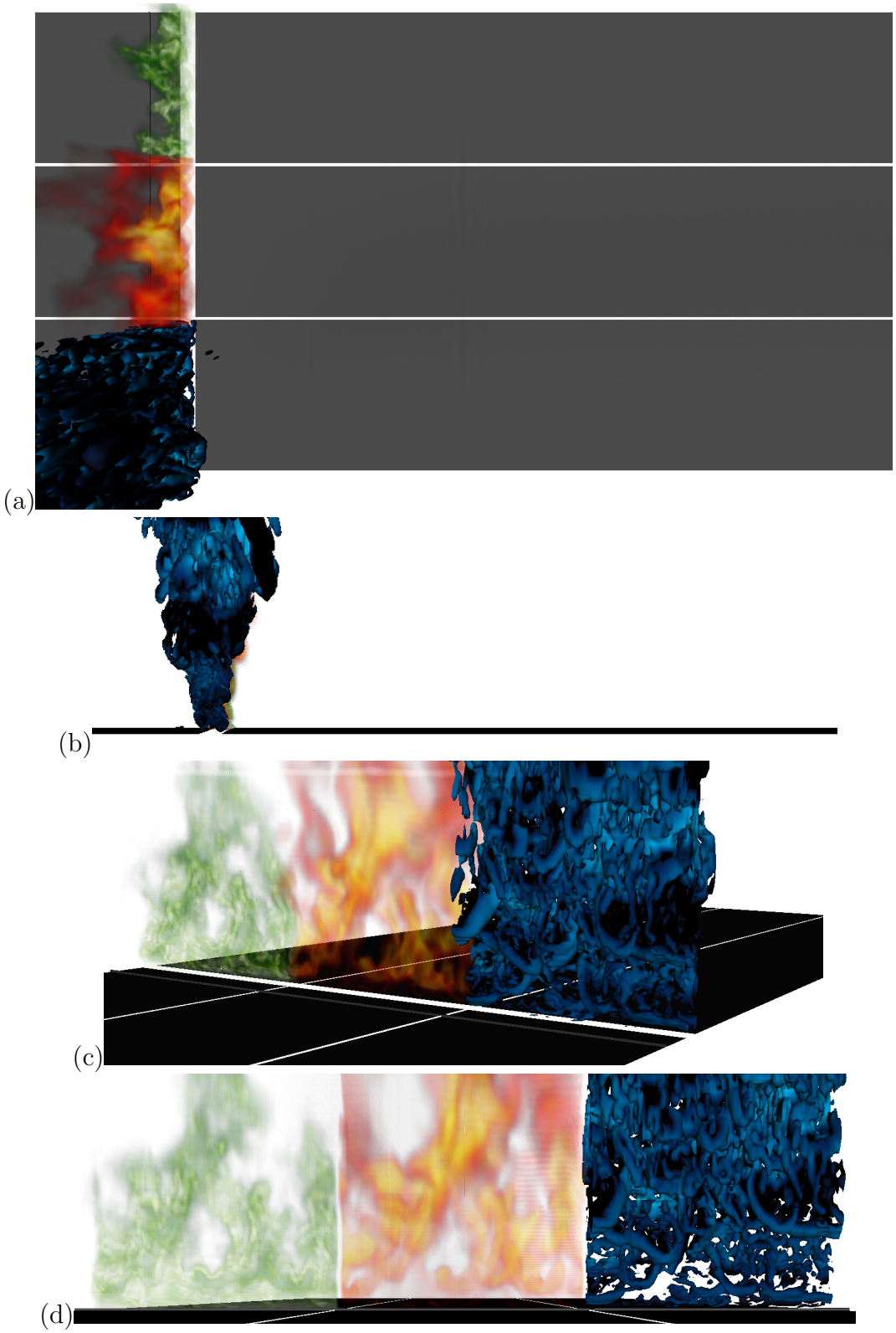

Figure 5.3: Instantaneous flame, plume and flow structure for the $\theta = 0$ degrees case at $t = 30$ s, in the normal-tangential coordinate system. See Figure 4.4 caption for additional details.

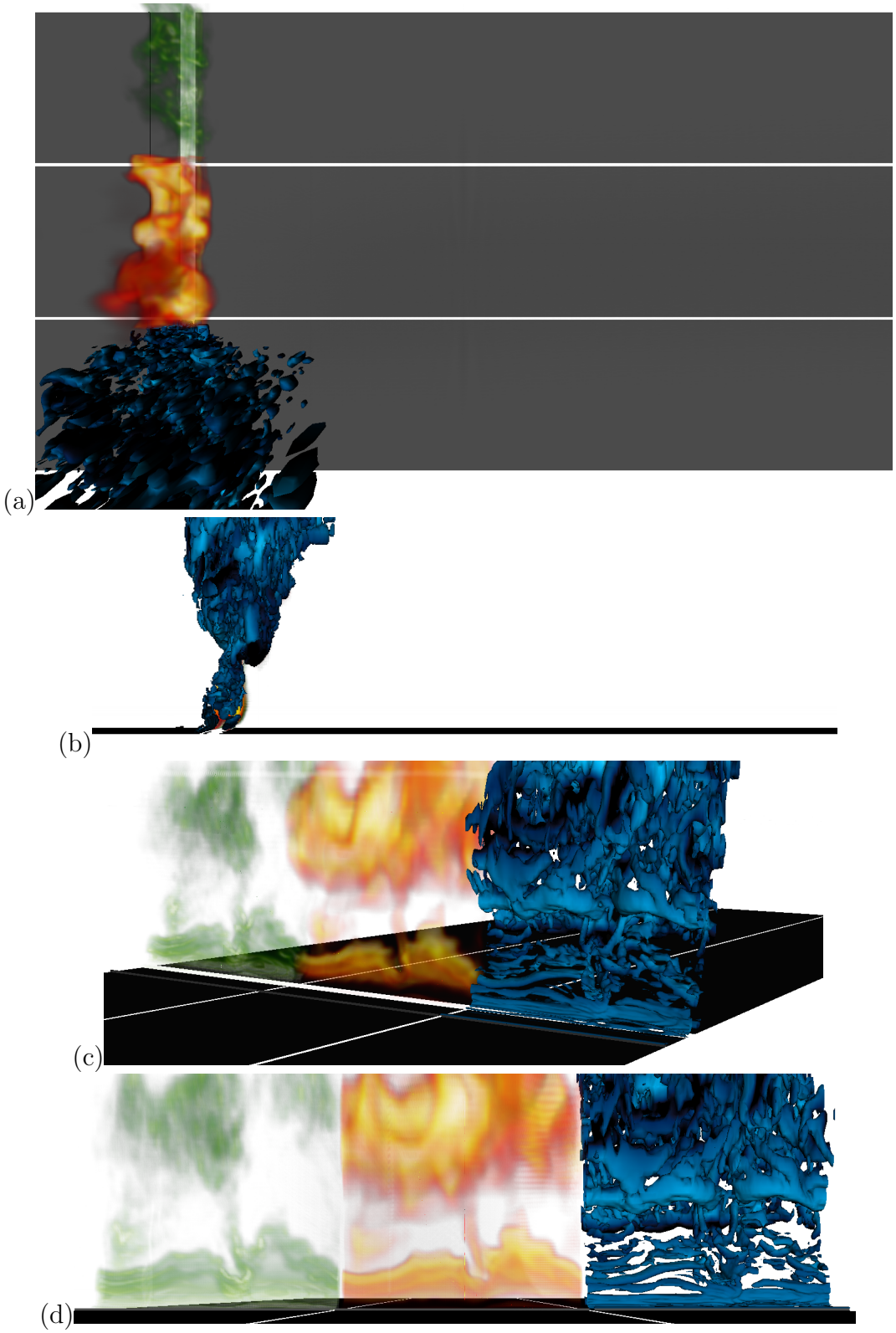

Figure 5.4: Instantaneous flame, plume and flow structure for the $\theta = 8$ degrees case at $t = 30$ s, in the normal-tangential coordinate system. See Figure 4.4 caption for additional details.

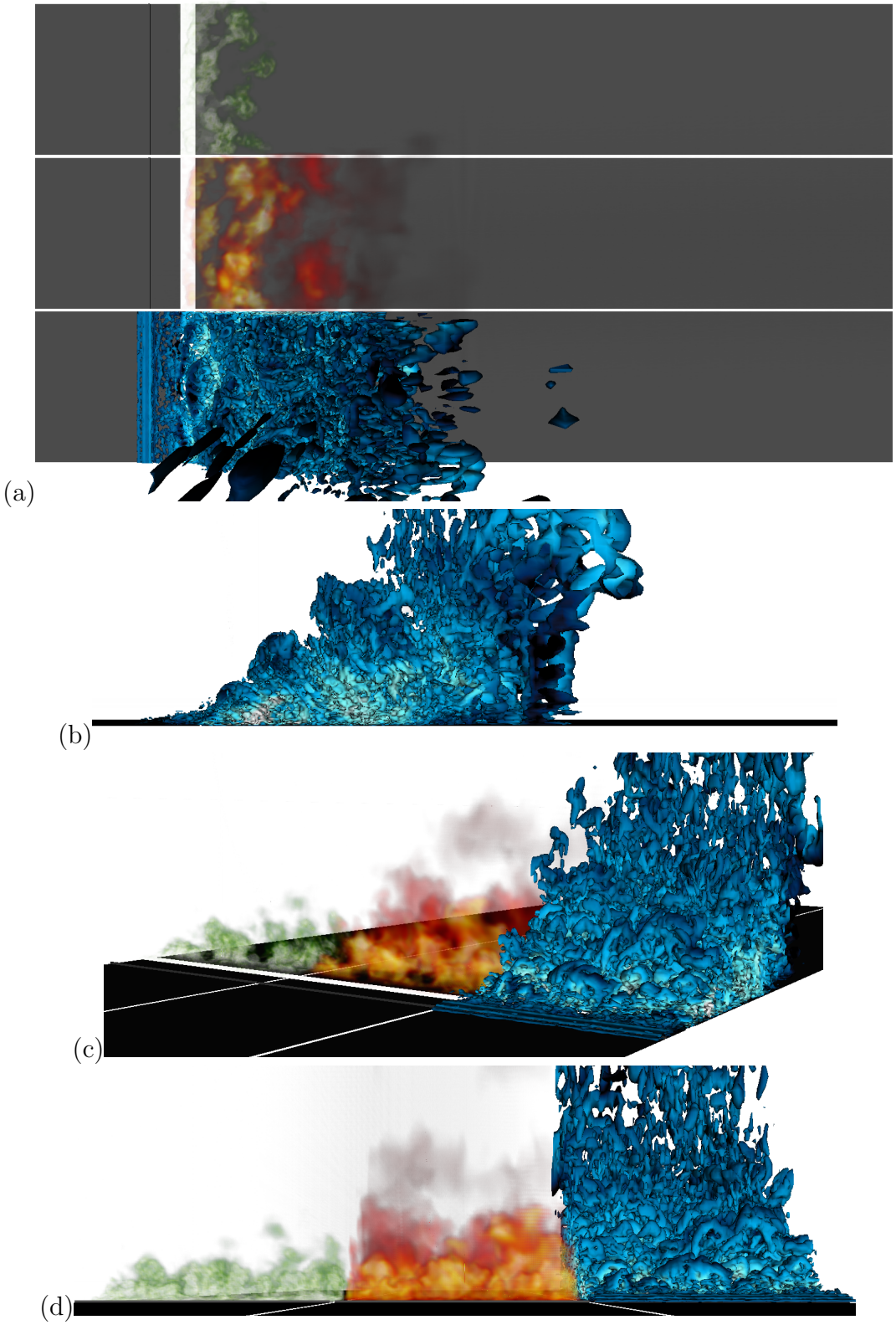

Figure 5.5: Instantaneous flame, plume and flow structure for the $\theta = 16$ degrees case at $t = 30$ s, in the normal-tangential coordinate system. See Figure 4.4 caption for additional details.

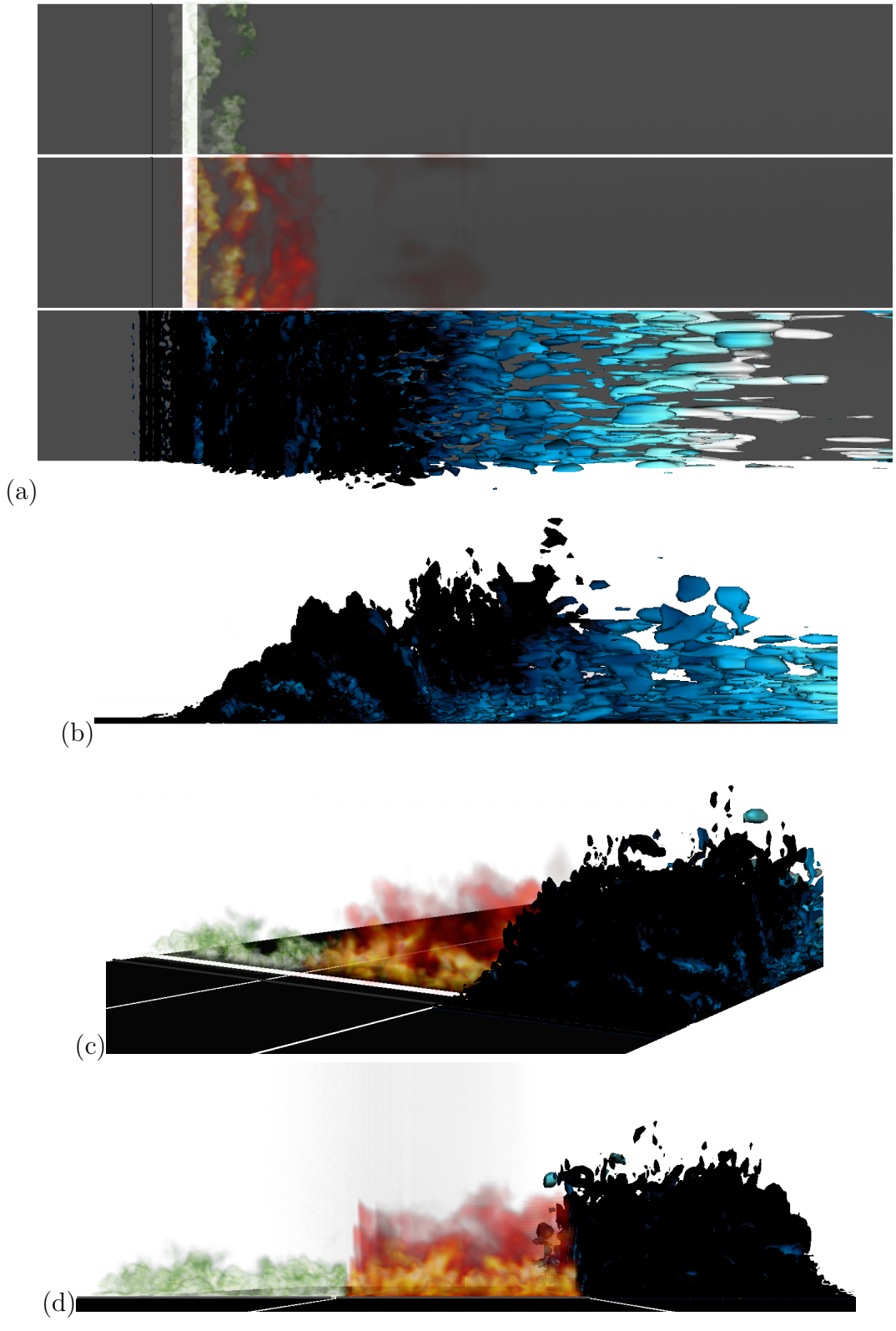

Figure 5.6: Instantaneous flame, plume and flow structure for the $\theta = 24$ degrees case at $t = 30$ s, in the normal-tangential coordinate system. See Figure 4.4 caption for additional details.

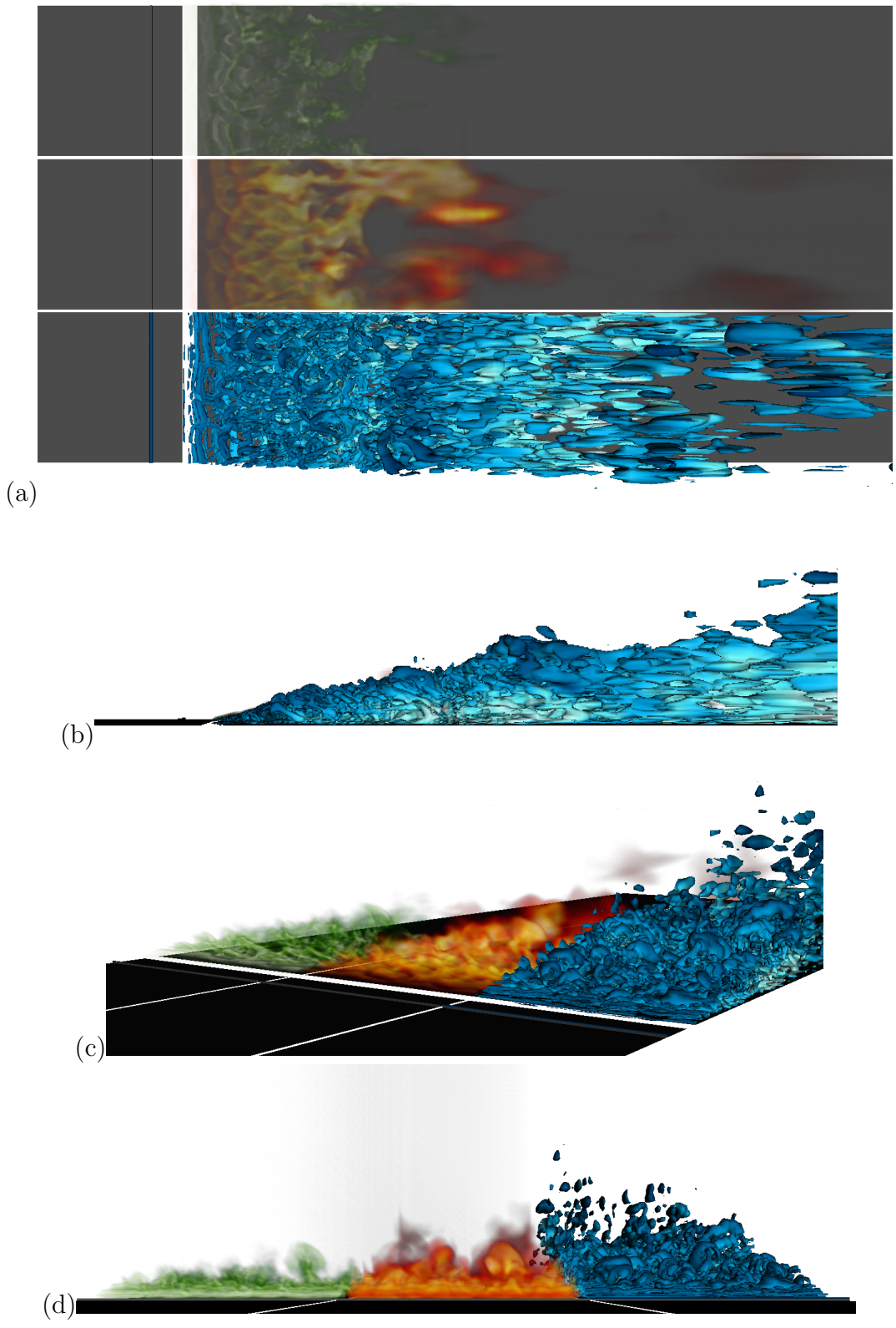

Figure 5.7: Instantaneous flame, plume and flow structure for the $\theta = 32$ degrees case at $t = 30$ s, in the normal-tangential coordinate system. See Figure 4.4 caption for additional details.

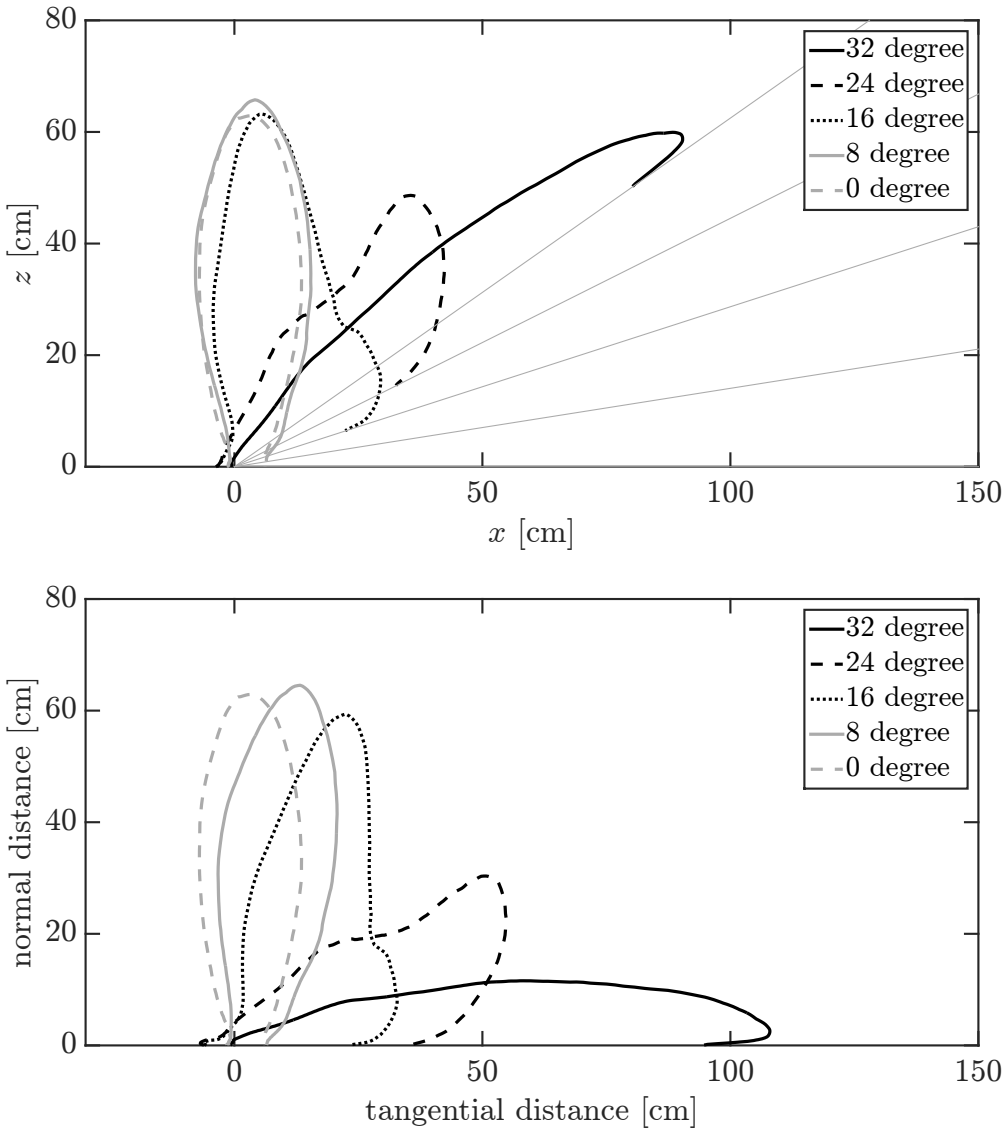

Figure 5.8: Mean flame shape visualized using a particular isoline of the mean heat release rate per unit volume (50 kW/m^3). Top (bottom) figure shows the flames in the Cartesian (normal-tangential) coordinate system. Thin grey lines in the top figure represent the inclined bottom plate.

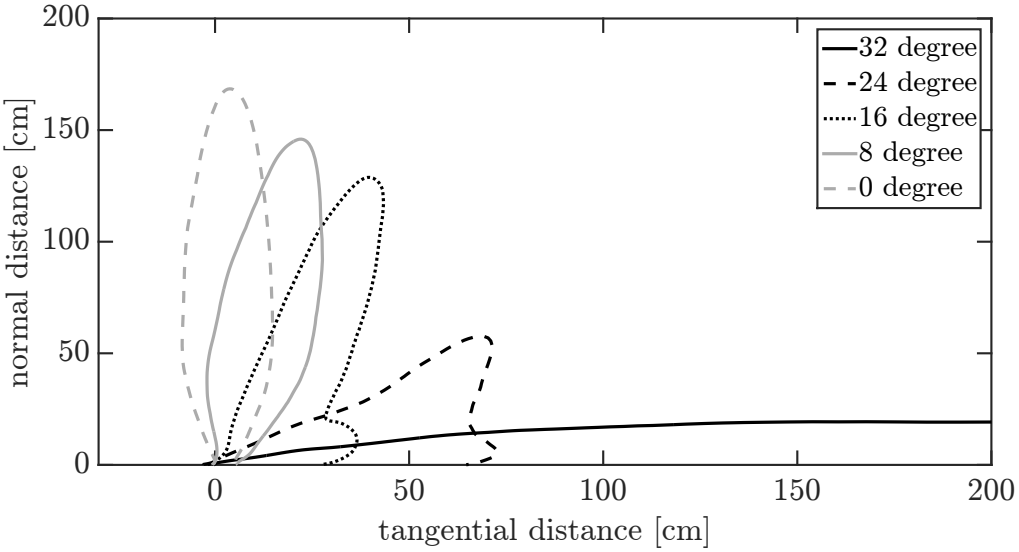

Figure 5.9: Mean plume shape visualized using a particular isoline of the mean temperature (400 K). Note that the present computational domain is not large enough to accommodate the entire plume in the 32 degrees case.

Overall, the response of the plume to an increase in θ is similar to that of the flame: as θ increases from 0 to 32 degrees, the plume transitions from a detached to an attached plume; with most of the change taking place between $\theta = 16$ and 32 degrees.

Figure 5.10 adopts a quantitative perspective and shows the variations of flame and plume height, length and tilt angle with inclination angle. The definitions are consistent with Figure 1.4. Note that the data is analyzed in the normal-tangential coordinate system here. Also note that the computational domain is unable to accommodate the entire plume in the 32 degrees case, so this data point is omitted from the plume based curves in Figure 5.10. As can be seen the flame height remains almost constant and ≈60 cm up to an inclination of 16 degrees, then it rapidly

decreases and goes down to a value of ≈10 cm for an inclination of 32 degrees. The plume height behaves in the same manner except it changes relatively more (from ≈ 170 to ≈ 130 cm) when the inclination is changed from 0 to 16 degrees. Interestingly, the flame length is nearly constant for all inclination angles and is ≈60 cm. The plume length on the other hand decreases with inclination angle, first relatively slowly from ≈ 170 to ≈ 130 cm when the inclination angle is changed from 0 to 16 degrees; then much more rapidly from ≈ 130 to ≈ 60 cm when the inclination is further increased from 16 to 24 degrees. Both the flame and plume tilt angles remain almost constant and ≈ 80 degrees when the inclination angle is increased from 0 to 16 degrees; then both these angles decrease rapidly with a further increase in the inclination angle.

Now we consider the spatial variations of time- and spanwise-averaged velocity vector $(\overline{u_t}, \overline{u_n})$ for all the cases (Figure 5.11), with u_t (u_n) representing the velocity tangent (normal) to the surface. In the cases with $\theta \leq 16$ degrees, the entrainment is two-sided, similar to pool fires, because of the flame and plume being mostly in a detached state. On the other hand, in the cases with $\theta \geq 24$ degrees the entrainment is one-sided due the flame and plume being mostly attached to the downstream surface. The tangential velocity, close to the bottom surface, in the region downstream of the flame changes drastically (from a small negative value to a fairly high positive value) when θ is increased from 16 to 32 degrees (see e.g., Figure 5.12). This sudden change in the flow state would lead to a drastic change in the fire spread rate (if there is fresh fuel downstream of the fire). This sudden increase in the spread rate of the fire has been observed in many accidents over the

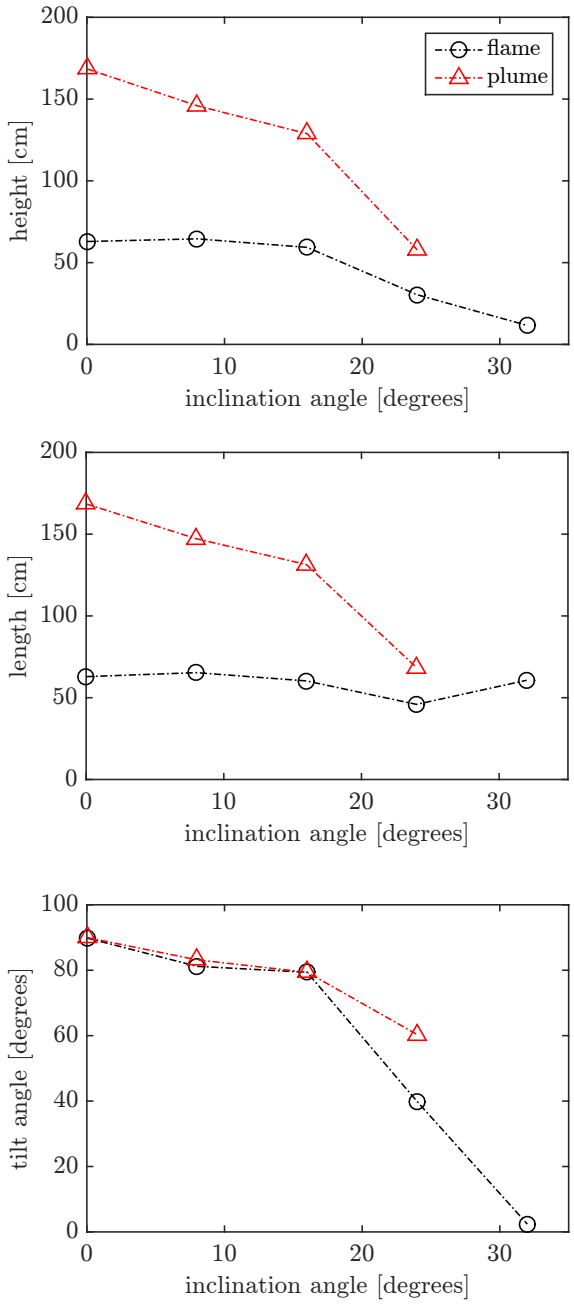

Figure 5.10: Flame and plume height, length and tilt angle based on the definitions presented in Figure 1.4; using the contours presented in Figures 5.8 and 5.9, respectively. Note that the current computational domain can not accommodate the entire plume for the 32 degrees case; thus this data point is omitted from the plume related curves in the figures above.

past several decades [31, 32, 34].

5.3.3 Attachment length

This section discusses the attachment length. Figure 5.13 provides the three attachment lengths discussed earlier in Section 4.4.3. They are defined slightly differently for the present configuration:

- Plume attachment length is defined as the tangential-distance downstream of the burner at which the 400 K temperature isoline intersects the bottom surface, see Figure 5.9 (see also Figure 5.14, which provides tangential variation of the time- and spanwise-averaged wall temperature downstream of the burner).

- Flame attachment length is defined as the tangential-distance downstream of the burner at which the 50 kW/m^3 heat release rate isoline intersects the bottom surface, see bottom panel in Figure 5.8.

- Flow attachment length is defined as the tangential-distance downstream of the burner at which the wall shear stress τ_w changes sign or becomes 0 for the first time, see Figure 5.15.

For $\theta \leq 8$ degrees all three attachment lengths are quite similar, which is expected based on Figure 5.11. In this regime one should expect radiative heat transfer to dominate downstream of the flame zone. For the 16 degrees inclination case the flow attachment length is significantly larger than the flame and plume attachment lengths, which at first sight seems inconsistent with Figure 5.11. But these two figures can be consistent if there is a thin and elongated recirculation

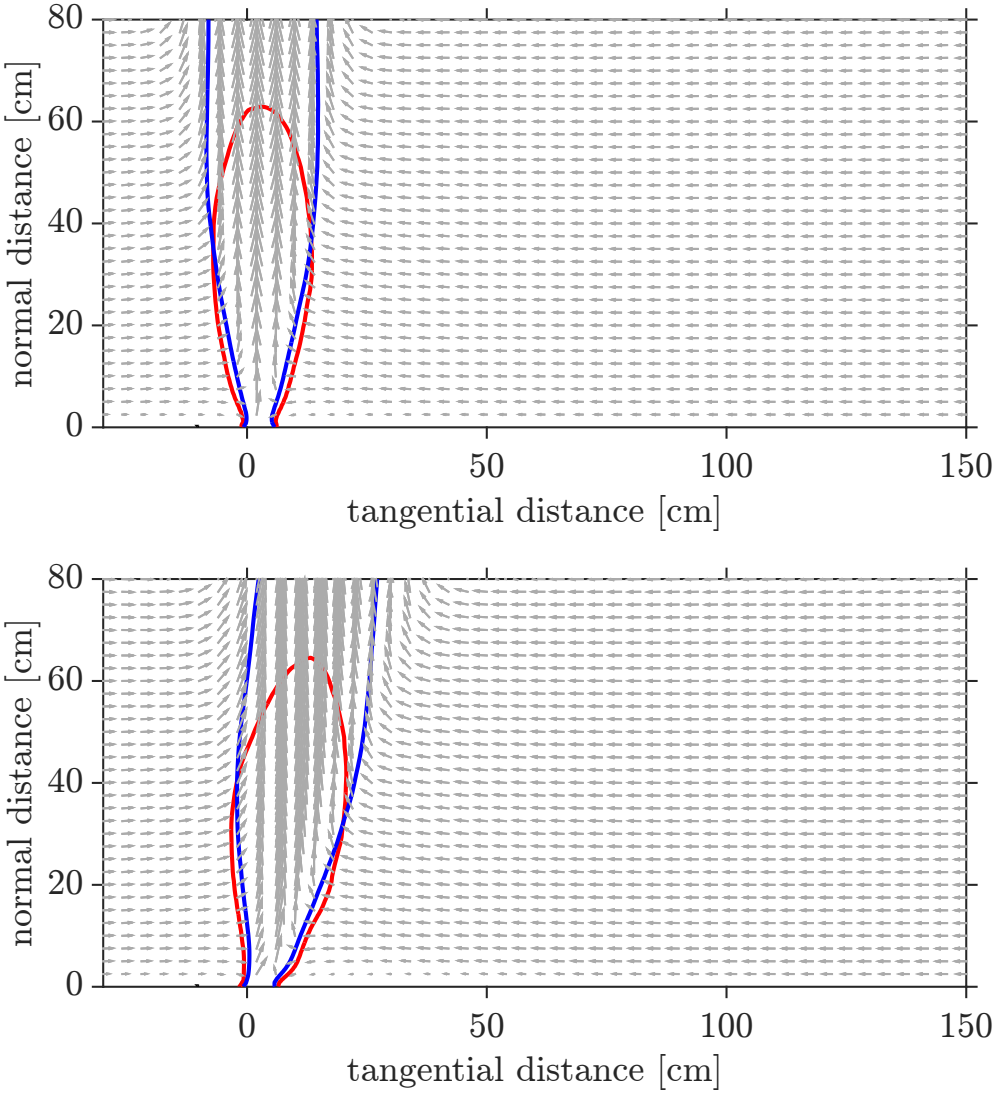

Figure 5.11: Spatial variations of the time- and spanwise-averaged flow velocity vector $(\overline{u_t}, \overline{u_n})$: $\theta = 0$, 8, 16, 24 and 32 degrees (top to bottom). Here u_t (u_n) represents the velocity tangential (normal) to the bottom surface. Red (blue) lines are isolines of the mean heat release rate per unit volume (temperature), 50 kW/m^3 (400 K), and are used for marking the flame (plume) region.

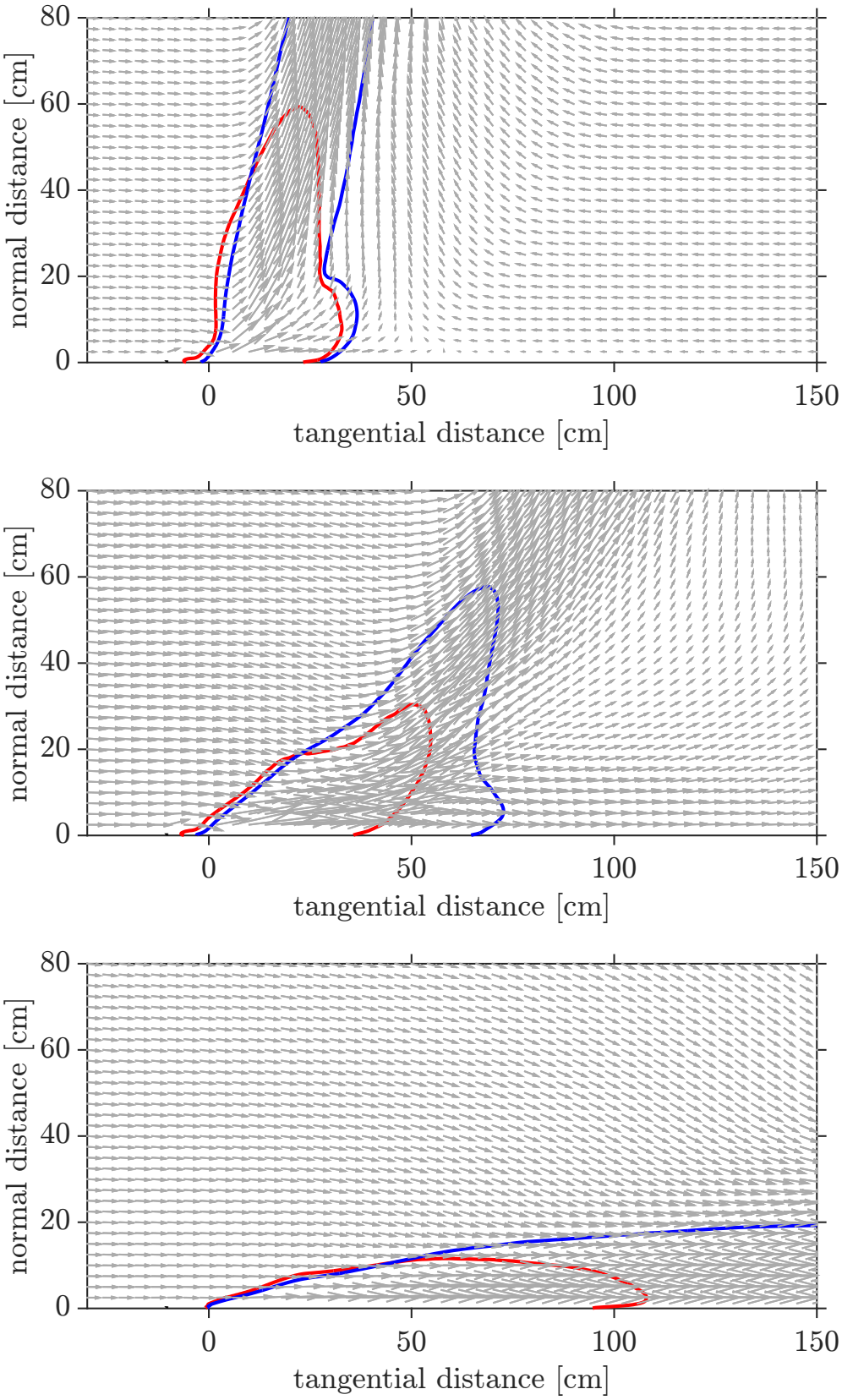

Figure 5.11: Continued.

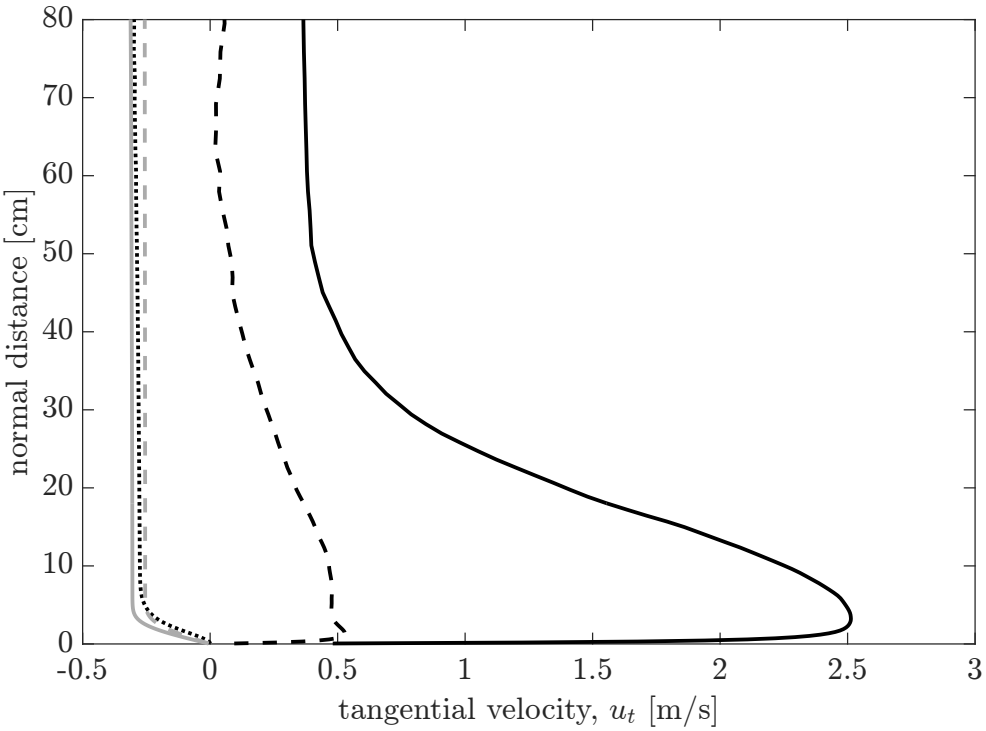

Figure 5.12: Wall normal variation of time- and spanwise-averaged tangential velocity, $\overline{u_t}$, at a tangential distance of 130 cm downstream of the burner leading edge. For legend see Figure 5.9.

bubble that is not visible in Figure 5.11. Nevertheless, Figure 5.11 suggests that in the 16 degrees cases as well radiative heat transfer is expected to dominate downstream of the flame zone. In the case with $\theta = 24$ the flame is mostly attached but the plume and flow separate some distance downstream of the flame, accordingly, this case is similar to the 1.5 m/s case discussed in the previous chapter. For the case with $\theta = 32$ degrees; the flame, plume and flow never separate, so this case is similar in terms of attachment lengths to the $U_\infty = 2$ and 3 m/s cases discussed in the previous chapter.

We now analyze the PDFs of the flame attachment length (Figure 5.16). Similar to the PDFs reported in the last chapter, these PDFs are also constructed by using heat release rate data from all the (100) cells along the span from 12 seconds of simulation, saved at every tenth time step. As expected the PDFs for the 0 and 8 degree cases remain close to downstream burner edge which is at a tangential distance of 5 cm. As the angle is increased the PDFs move to the right and become broader indicating that the flame attachment length increases with inclination angle and varies more in time. Interestingly the PDFs for the 16 and 24 degree cases almost overlap each other at a tangential distance of ≈ 30 cm, which seems inconsistent with Figure 5.13 but it should be noted that a smaller amount of data has been used to generate the PDFs; in addition for the PDFs the attachment length is defined as the maximum tangential distance at which a value of 50 kW/m^3 for the volumetric heat release rate is seen. Accordingly, if there are frequent flame bursts in a case then the PDFs will shift towards the right and will not be consistent with the mean value of the attachment length. Figure 5.17 provides normalized values of

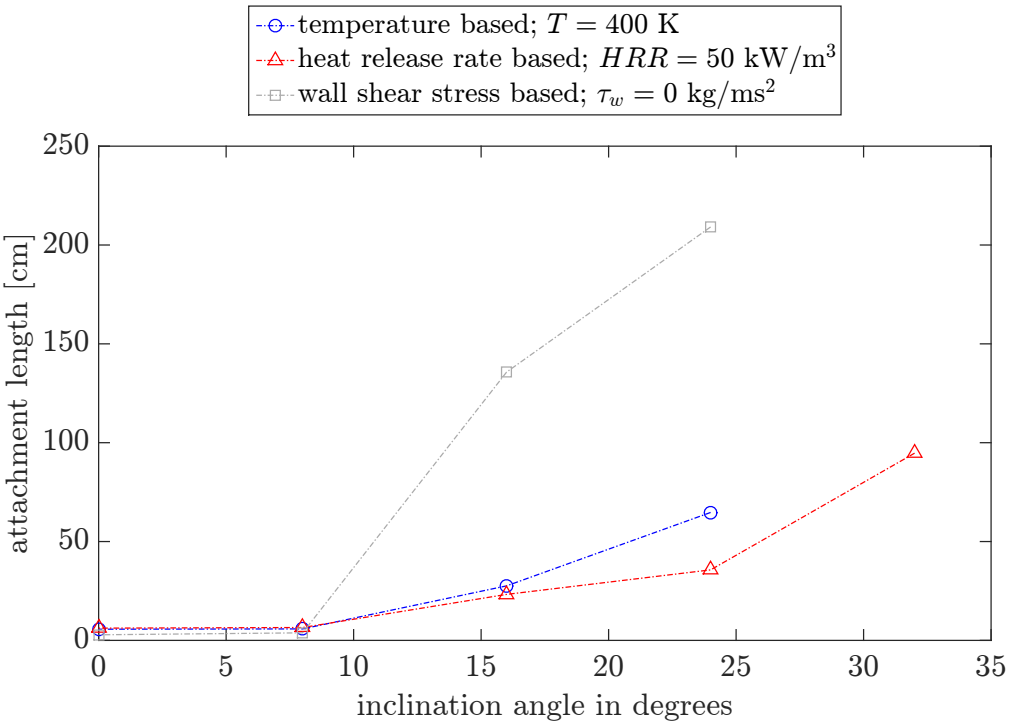

Figure 5.13: Change in plume (temperature based), flame (heat release rate based) and flow (wall shear stress based) attachment length with the inclination angle (θ). For the $\theta = 32$ degrees case the flow remains attached throughout the computational domain, hence, this point is omitted from the flow attachment length curve. Also, the computational domain is not large enough to accommodate the entire plume in this case, thus, this point is also not included in the plume attachment length curve.

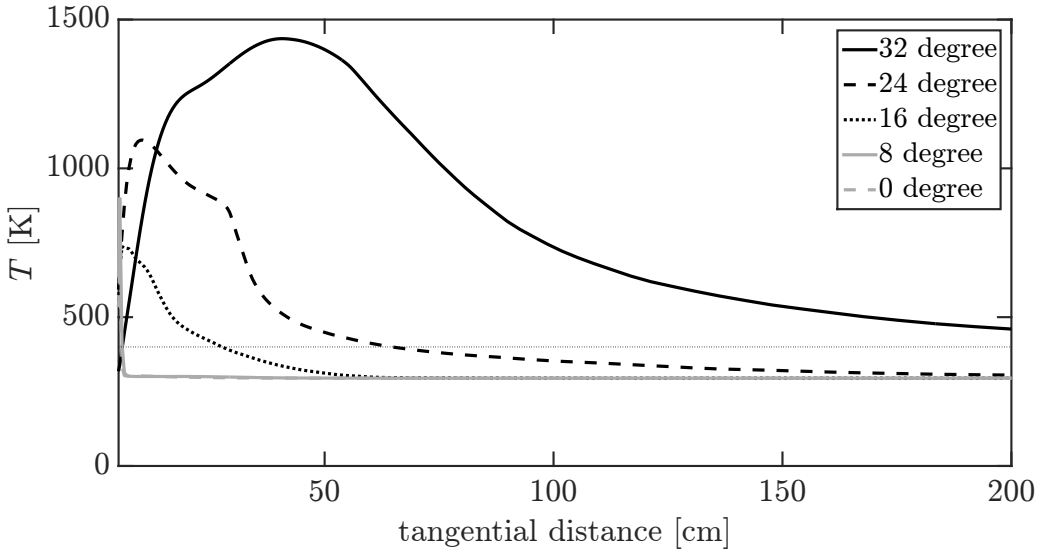

Figure 5.14: Tangential variation of the time- and spanwise-averaged wall temperature, downstream of the burner. Thin dotted black horizontal line is drawn to visualize the condition $T = 400$ K.

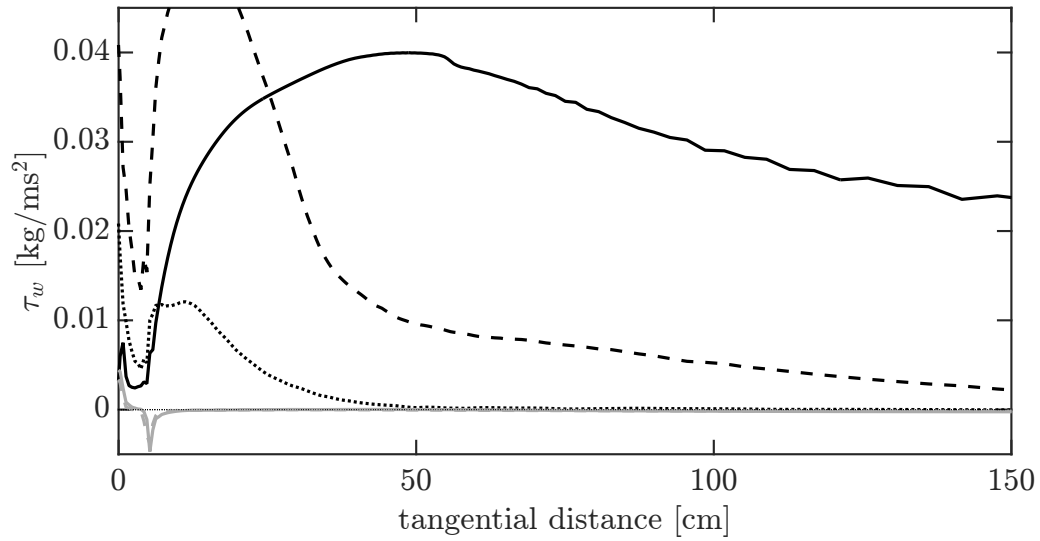

Figure 5.15: Tangential variation of mean wall shear stress, τ_w, downstream of the burner leading edge. Thin dotted black horizontal line is drawn to visualize the condition $\tau_w = 0$. For legend see Figure 5.14.

the minimum and maximum flame attachment lengths. Normalization in this figure is done using the attachment length that corresponds to the peak probability values in Figure 5.16. The 0 and 8 degree cases in this figure can be ignored because in these cases the flame is not attached and the attachment length looses meaning. The rest of the cases support the analysis in the previous chapter; and suggest that the minimum and maximum values of the normalized attachment length are independent of the inclination angle. Furthermore, Figure 5.16 shows that the attachment length varies significantly in time e.g., by almost 90% in the 24 degrees case.

5.4 Concluding remarks

Fine-grained LES are performed to bring fundamental insight into the effects of slope on the structure of a methane-air, buoyancy-driven, turbulent line flame (50 kW) stabilized on top of a flat surface. As the slope is increased, the flame and plume transition from a pool state to a boundary layer state, with most of the change happening between slopes of 16 and 32 degrees. The pool flame and plume feature two-sided air entrainment into the flame and plume zones. In contrast, the boundary layer flame and plume feature downwind flow attachment and one-sided air entrainment into the flame and plume zones. The tangential velocity upslope of the flame zone is found to change dramatically, from a relatively small negative value (≈ -0.3 m/s) to a relatively large positive value (≈ 2.5 m/s), when the slope is changed from 16 to 32 degrees. The flame attachment length is found to fluctuate significantly in time and when it is normalized with the value that has the maximum probability, its minimum and maximum value is found to be independent

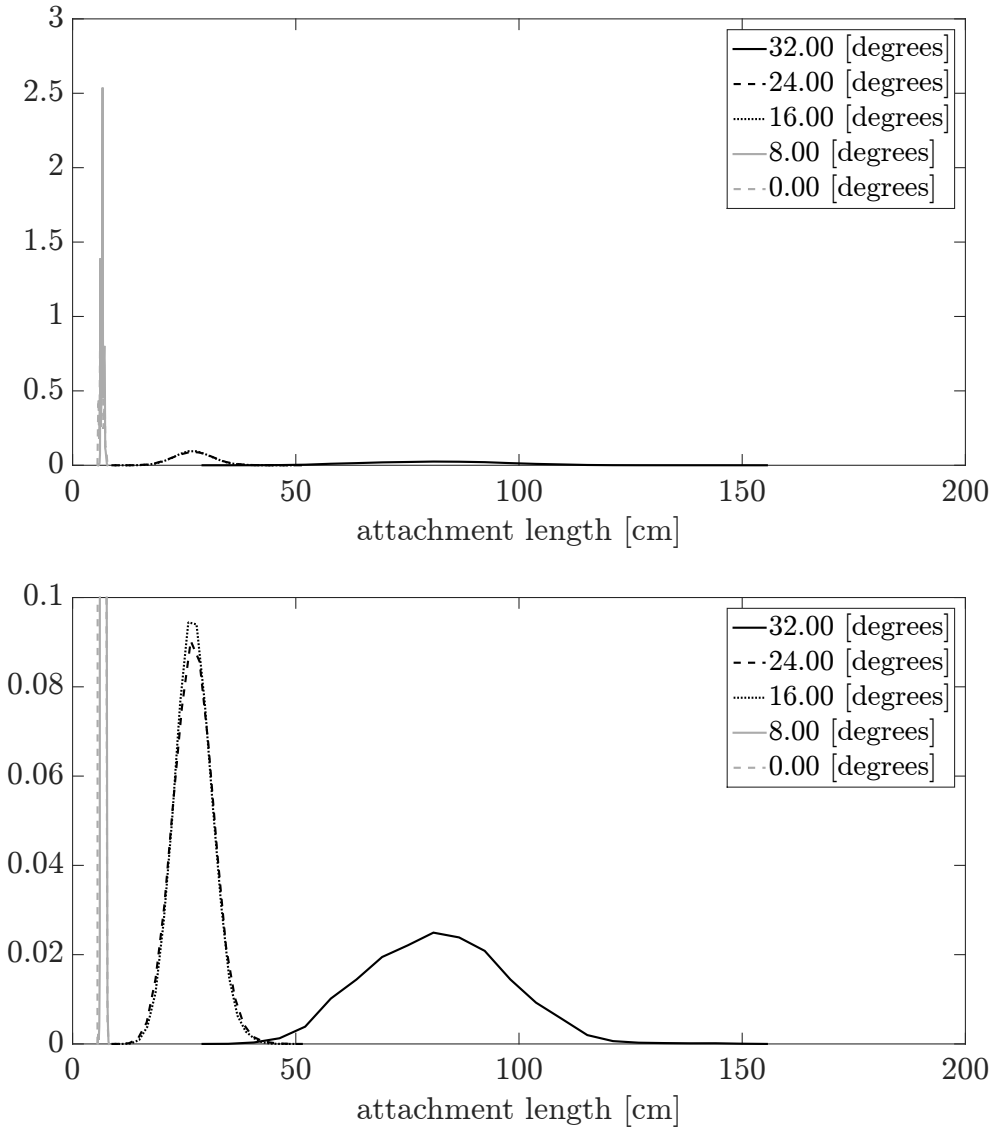

Figure 5.16: Probability Density Functions (PDFs) of flame attachment length; based on the 50 kW/m^3 isocontour. The bottom figure is identical to the top figure but focuses on the lower probability values.

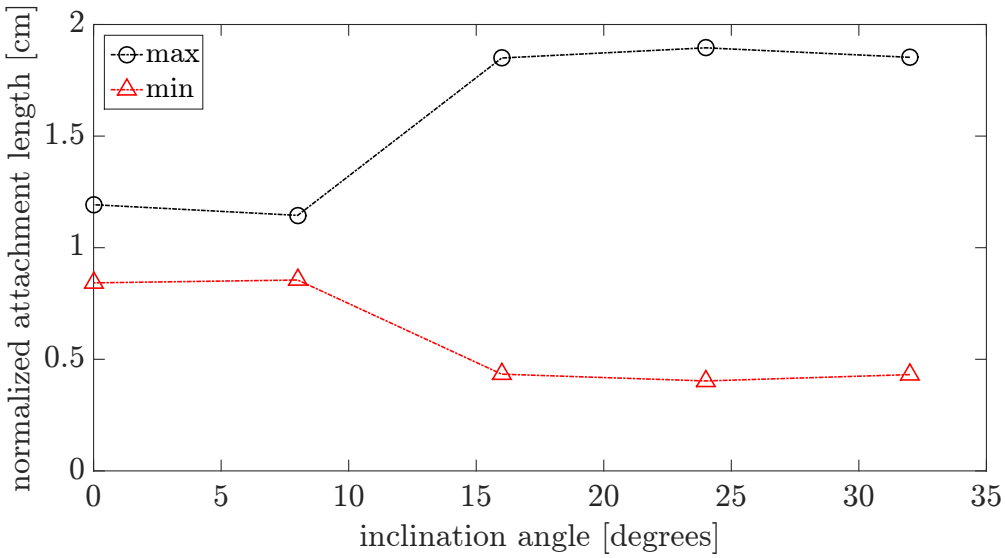

Figure 5.17: Maximum and minimum values of the normalized flame attachment length for all the cases. Normalization is done using the flame attachment length that has the maximum probability in Figure 5.16.

of the inclination angle, for the cases that feature some amount of flame attachment (or have inclination $\geq$ 16 degrees).

6: Summary and future work

Wind and slope have a leading-order impact on wildland fire spread rate, because, among other things, they tilt the flame and plume towards the unburnt fuel, which significantly increases the convective heat transfer and hence the spread rate. This study was primarily aimed at enhancing our fundamental understanding of the effects of wind and slope on the structure of turbulent, buoyant line fires.

6.1 Summary

In Chapter 2 the focus was on increasing our understanding of the numerical framework (the OpenFOAM CFD library, on which FireFOAM is based). In particular we aimed at a better description and assessment of some of the most popular convection and time integration schemes. Key findings from this effort are as follows:

- The *linearUpwind* scheme was found to correspond to the FROMM scheme instead of the Second Order Upwind (SOU) scheme, as has been incorrectly alluded to in the OpenFOAM documentation [58].

- The implementation of the *Gamma* scheme was found to be bugged; the implemented version does not satisfy the Convection Boundedness Criterion (CBC)

- The description of the *limitedLinear* scheme on the NVD diagram was found to be incorrect in the OpenFOAM documentation [58].

- By comparing with the *Gamma* scheme on the NVD diagram [63] it was found that the factor k for the *limitedLinear* scheme should not be set to values smaller than 0.2, because doing so is expected to induce the so-called "switching" instability [59]. In addition, for the same value of k the *limitedLinear* scheme is expected to be more accurate and less stable than the *Gamma* scheme because of a faster switch from the *upwind* to the *linear* (central difference) scheme.

- The *filteredLinear2* scheme was found to have a larger computational molecule or stencil than most of the other schemes in OpenFOAM and could not be described on the NVD diagram.

- The *limitedLinear* and the *dbGamma* schemes with $k = 0.2$ were found to have the best performance in terms of accuracy and boundedness in a representative test case. Here *dbGamma* represents the debugged version of the *Gamma* scheme.

- For the time integration schemes the *CrankNicolson* scheme with the factor ψ close to 1 had the best performance in a representative test case. The OpenFOAM's *CrankNicolson* scheme is a blend between backward Euler and the Crank-Nicolson schemes; with $\psi = 1$ (0) giving the pure Crank-Nicolson (backward Euler) scheme.

In Chapter 3 the primary goal was to perform a higher order validation of the numerical methodology (well-resolved LES) by simulating a co-flow stabilized, turbulent,

buoyant, methane-fueled, stationary, line fire in the absence of cross-wind and slope. The main findings of this effort are as follows:

- The spatial profiles of mean and *rms* temperature compare favorably with the measured profiles.
- The integral time scales along the burner centerline from the simulations compared well with those extracted from the experimental data. The values of the integral time scales were found not to change significantly with elevation and were ≈30 ms in the flame zone.
- The temperature Probability Density Functions (PDFs) from the simulation were found to compare well with the measured PDFs above the mean flame height; even the comparisons within the flame zone were found to be reasonable. Both experimental and simulated PDFs are broad and bi-modal at low elevations in the flame region, indicating intermittent occurrence of relatively cold gas due to ambient air entrainment and hot gas due to combustion; whereas the PDFs are narrow and mono-modal at high elevations in the plume region.

After the fairly successful higher order validation in Chapter 3, Chapter 4 focused on the effects of cross-wind on the same line fire that was used in Chapter 3 (but without co-flow). In addition to exploiting well- and wall-resolved LES, an integral model, capable of describing the effects of cross-wind on the structure of a turbulent, buoyant, line fire, was also developed in this chapter. Key results in Chapter 4 are as follows:

- The two flame regimes described in the literature (buoyancy-dominated and wind-dominated) were seen in the LES simulations and the transition was found to occur for a value of Byram's convection number $N_C \approx 1$.

- The simulations suggest that the attachment length fluctuates significantly in time. Furthermore, the minimum and maximum attachment length values, when normalized with the attachment length with the highest probability, were found to be approximately independent of the cross-wind velocity.

- The integral model after some simplifications suggests that the tilt angle θ satisfies the following relation: $(\tan(\theta))^2(\alpha\tan(\theta) + \beta) = N_C/4$. This provides additional theoretical support to the Byram's convection number N_C.

- The integral model was found to compare reasonably well to LES, in terms of flame and plume shapes, for the cases with $U_\infty \leq 1.5$ m/s (or $N_C \geq 1.3$). For the other two cases with $U_\infty \geq 2$ m/s, there are significant discrepancies between the model and LES, mainly because of a lack of wall blockage sub-model.

Chapter 5 considered the effects of slope on the same turbulent, buoyant, stationary, line fire that was considered in Chapter 4. The summary of this chapter is as follows:

- The two flame regimes discussed in the literature (detached and attached) were captured in the LES simulations and the transition was found to occur between $\theta = 16$ and 32 degrees.

- The velocity tangent to the bottom surface, in the region upslope of the flame,

is found to change from a relatively small negative value (≈ -0.3 m/s) to a relatively large positive value (≈ 2.5 m/s) when the inclination angle is changed from 16 to 32 degrees.

- The simulations show that the attachment length fluctuates significantly in time. Further, the minimum and maximum attachment length values, when normalized with the attachment length with the highest probability, are found to be approximately independent of the inclination angle; for the cases with a significant portion of the flame attached to the downstream wall (with $\theta \geq 16$ degrees).

6.2 Future work

Some recommendations for future work are as follows:

- Effects of gradient limiters on the performance of the *linearUpwind* and $LUST$ schemes could be checked; maybe these two schemes will outperform the rest of the schemes with an appropriate limiter.

- Effects of various parameters (fire heat release rate, burner length in the x-direction etc.) on the attachment length PDFs could be studied because of the importance of the attachment length to the wildland fire spread problem.

- A wall attachment sub-model could be developed and incorporated inside the integral model presented in Chapter 4. This would enable the integral model to predict flame and plume attachment lengths for different conditions.

- The integral model could be enhanced to handle the effects of slope as well.

Appendix A: Assessment of the vertical grid resolution at the wall for the wind-driven cases

This appendix presents an assessment of the vertical grid resolution at the wall, Δz_w, chosen in Chapter 4. Because of the grid sensitivity study performed in Chapter 3 (for the no wind scenario) one can expect the grid resolution of 5 mm chosen in Chapter 4 (for the wind-driven cases) to be sufficient in the x and y directions; but it is unclear if $\Delta z_w = 0.6$ mm, chosen in Chapter 4, is enough or not for wall-resolved LES (or for capturing the velocity gradients at the bottom wall, downwind of the burner). This issue is addressed in Figure A.1, which shows that $\Delta z_w = 0.6$ mm corresponds to a Δz_w^+ of $\lesssim 1$ throughout most of the flame zone for all the wind-driven cases; indicating that a $\Delta z_w = 0.6$ mm is quite sufficient for wall-resolved LES. Note that in the cases presented in Chapter 4, the gradients of temperature at the wall do not need to be considered because of the application of the zero gradient (or adiabatic) boundary condition (Figure 4.1).

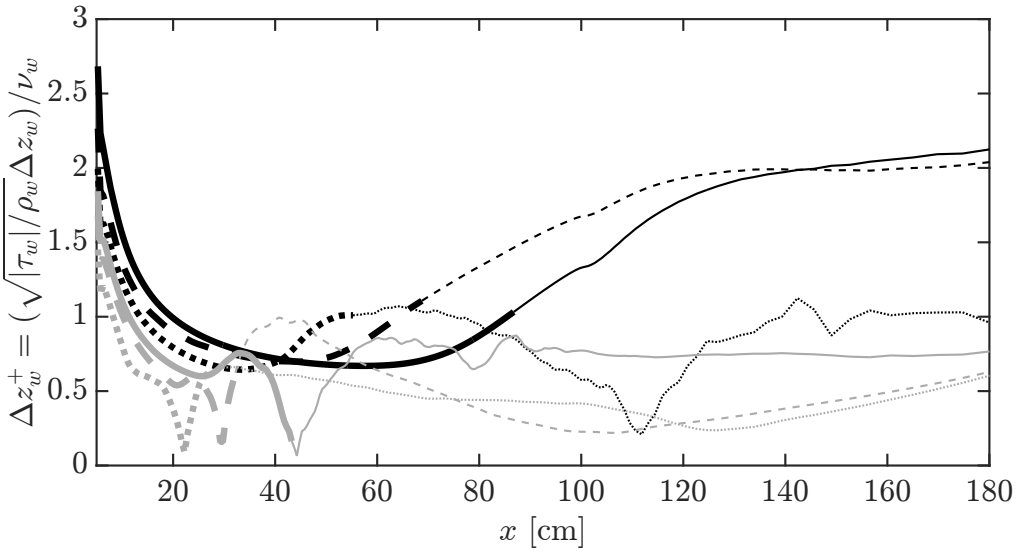

Figure A.1: Variation of Δz_w^+ with x. For legend see Figure 4.13; the thick portion of the lines represents data inside the flame zone. Note that Δz_w^+ in this figure is based on the cell center height and not the cell height (see the nomenclature for the definition of Δz_w). In addition magnitude of τ_w, $|\tau_w|$, is used for calculating $u_\tau = \sqrt{|\tau_w|/\rho_w}$ because of the presence of reversed flow in some of the cases. It is also worth noting that for $x > 205$ cm $\Delta z_w^+ = 0$ because of the application of the slip boundary condition at the bottom wall (see Figure 4.1).

Bibliography

[1] J. Towns, T. Cockerill, M. Dahan, I. Foster, K. Gaither, A. Grimshaw, V. Hazlewood, S. Lathrop, D. Lifka, G. Peterson, R. Roskies, J. Scott, and N. Wilkins-Diehr. XSEDE: Accelerating Scientific Discovery. *Computing in Science & Engineering*, 16(5):62–74, 2014.

[2] Y. Liu, J. Stanturf, and S. Goodrick. Trends in global wildfire potential in a changing climate. *Forest Ecology and Management*, 259(4):685–697, 2010.

[3] M. Flannigan, M. Krawchuk, W. de Groot, B. Wotton, and L. Gowman. Implications of changing climate for global wildland fire. *International Journal of Wildland Fire*, 18(5):483–507, 2009.

[4] M. Finney, J. Cohen, S. McAllister, and W. Jolly. On the need for a theory of wildland fire spread. *International Journal of Wildland Fire*, 22(1):25–36, 2013.

[5] E. Pastor, L. Zárate, E. Planas, and J. Arnaldos. Mathematical models and calculation systems for the study of wildland fire behaviour. *Progress in Energy and Combustion Science*, 29(2):139–153, 2003.

[6] M. Finney. FARSITE: Fire Area Simulator–Model Development and Evaluation. *Res. Pap. RMRS-RP-4, Revised 2004. Ogden, UT: US Department of Agriculture, Forest Service, Rocky Mountain Research Station. 47 p.*, 4, 1998.

[7] R. Linn, J. Winterkamp, C. Edminster, J. Colman, and W. Smith. Coupled influences of topography and wind on wildland fire behaviour. *International Journal of Wildland Fire*, 16(2):183–195, 2007.

[8] R. Nelson. An effective wind speed for models of fire spread. *International Journal of Wildland Fire*, 11(2):153–161, 2002.

[9] T. Beer. The interaction of wind and fire. *Boundary-Layer Meteorology*, 54(3):287–308, 1991.

[10] http://blogs.ubc.ca/firemodel/discussion/.

[11] W. Tang, C. Miller, and M. Gollner. Local flame attachment and heat fluxes in wind-driven line fires. *Proceedings of the Combustion Institute*, 36(2):3253–3261, 2017.

[12] X. Huang and M. Gollner. Correlations for evaluation of flame spread over an inclined fuel surface. *Fire Safety Science*, 11:222–233, 2014.

[13] D. Hoult, J. Fay, and L. Forney. A theory of plume rise compared with field observations. *Journal of the Air Pollution Control Association*, 19(8):585–590, 1969.

[14] M. Escudier. Aerodynamics of a burning turbulent gas jet in a crossflow. *Combustion Science and Technology*, 4(1):293–301, 1971.

[15] F. Albini. A model for the wind-blown flame from a line fire. *Combustion and Flame*, 43:155–174, 1981.

[16] G. Mercer and R. Weber. Plumes above line fires in a cross-wind. *International Journal of Wildland Fire*, 4(4):201–207, 1994.

[17] B. Porterie, J. Loraud, D. Morvan, and M. Larini. A numerical study of buoyant plumes in cross-flow conditions. *International Journal of Wildland Fire*, 9(2):101–108, 1999.

[18] D. Morvan, B. Porterie, M. Larini, and J. Loraud. Numerical simulation of turbulent diffusion flame in cross flow. *Combustion Science and Technology*, 140(1-6):93–122, 1998.

[19] B. Porterie, D. Morvan, J. Loraud, and M. Larini. Firespread through fuel beds: Modeling of wind-aided fires and induced hydrodynamics. *Physics of Fluids*, 12(7):1762–1782, 2000.

[20] F. Nmira, J. Consalvi, P. Boulet, and B. Porterie. Numerical study of wind effects on the characteristics of flames from non-propagating vegetation fires. *Fire Safety Journal*, 45(2):129–141, 2010.

[21] C. Lam and E. Weckman. Wind-blown pool fire, Part II: Comparison of measured flame geometry with semi-empirical correlations. *Fire Safety Journal*, 78:130–141, 2015.

[22] W. Tang, D. Gorham, M. Finney, S. Mcallister, J. Cohen, J. Forthofer, and M. Gollner. An experimental study on the intermittent extension of flames in wind-driven fires. *Fire Safety Journal*, 91:742–748, 2017.

[23] R. Nelson, B. Butler, and D. Weise. Entrainment regimes and flame characteristics of wildland fires. *International Journal of Wildland Fire*, 21(2):127–140, 2012.

[24] N. Frangieh, D. Morvan, S. Meradji, G. Accary, and O. Bessonov. Numerical simulation of grassland fires behavior using an implicit physical multiphase model. *Fire Safety Journal*, 102:37–47, 2018.

[25] F. Ricou and D. Spalding. Measurements of entrainment by axisymmetrical turbulent jets. *Journal of Fluid Mechanics*, 11(1):21–32, 1961.

[26] H. Nielsen and L. Tao. The fire plume above a large free-burning fire. In *Symposium (International) on Combustion*, volume 10, pages 965–972. Elsevier, 1965.

[27] A. Putnam. A model study of wind-blown free-burning fires. In *Symposium (International) on Combustion*, volume 10, pages 1039–1046. Elsevier, 1965.

[28] B. Magnussen and B. Hjertager. On mathematical modeling of turbulent combustion with special emphasis on soot formation and combustion. *Proceedings of the Combustion Institute*, 16(1):719–729, 1977.

[29] J. Mendes-Lopes, J. Ventura, and J. Amaral. Rate of spread and flame characteristics in a bed of pine needles. In *Proceedings of the III International Conference on Forest Fire Research–14th Conference on Fire and Forest Meteorology*, pages 16–20, 1998.

[30] E. Zukoski. Properties of Fire Plumes. In *Combustion Fundamentals of Fire*, pages 101–219. Academic Press, 1995.

[31] S. Simcox, N. Wilkes, and I. Jones. Computer simulation of the flows of hot gases from the fire at King's Cross underground station. *Fire Safety Journal*, 18(1):49–73, 1992.

[32] D. Drysdale, A. Macmillan, and D. Shilitto. The King's Cross fire: Experimental verification of the 'Trench effect'. *Fire Safety Journal*, 18(1):75–82, 1992.

[33] K. Moodie and S. Jagger. The King's Cross fire: Results and analysis from the scale model tests. *Fire Safety Journal*, 18(1):83–103, 1992.

[34] J. Sharples, A. Gill, and J. Dold. The trench effect and eruptive wildfires: lessons from the King's Cross underground disaster. In *Proceedings of Australian Fire and Emergency Service Authorities Council 2010 Conference*, pages 8–10, 2010.

[35] J. Dold and A. Zinoviev. Fire eruption through intensity and spread rate interaction mediated by flow attachment. *Combustion Theory and Modelling*, 13(5):763–793, 2009.

[36] Y. Wu, H. Xing, and G. Atkinson. Interaction of fire plume with inclined surface. *Fire Safety Journal*, 35(4):391–403, 2000.

[37] F. Morandini, X. Silvani, J. Dupuy, and A. Susset. Fire spread across a sloping fuel bed: Flame dynamics and heat transfers. *Combustion and Flame*, 190:158–170, 2018.

[38] P. Woodburn and D. Drysdale. Fires in inclined trenches: the dependence of the critical angle on the trench and burner geometry. *Fire Safety Journal*, 31(2):143–164, 1998.

[39] D. Drysdale and A. Macmillan. Flame spread on inclined surfaces. *Fire Safety Journal*, 18(3):245–254, 1992.

[40] Y. Xin, J. Gore, K. McGrattan, R. Rehm, and H. Baum. Fire dynamics simulation of a turbulent buoyant flame using a mixture-fraction-based combustion model. *Combustion and Flame*, 141(4):329–335, 2005.

[41] Y. Xin, S. Filatyev, K. Biswas, J. Gore, R. Rehm, and H. Baum. Fire dynamics simulations of a one-meter diameter methane fire. *Combustion and Flame*, 153(4):499–509, 2008.

[42] Y. Wang, P. Chatterjee, and J. de Ris. Large eddy simulation of fire plumes. *Proceedings of the Combustion Institute*, 33(2):2473–2480, 2011.

[43] S. Vilfayeau, J. White, P. Sunderland, A. Marshall, and A. Trouvé. Large eddy simulation of flame extinction in a turbulent line fire exposed to air-nitrogen co-flow. *Fire Safety Journal*, 86:16–31, 2016.

[44] V. Vuorinen, J. Keskinen, C. Duwig, and B. Boersma. On the implementation of low-dissipative Runge–Kutta projection methods for time dependent flows using OpenFOAM®. *Computers & Fluids*, 93:153–163, 2014.

[45] S. Deshpande, L. Anumolu, and M. Trujillo. Evaluating the performance of the two-phase flow solver interfoam. *Computational Science & Discovery*, 5(1):014016, 2012.

[46] F. Moukalled, L. Mangani, and M. Darwish. *The Finite Volume Method in Computational Fluid Dynamics: An advanced introduction with OpenFOAM and MATLAB*. Springer International Publishing, Switzerland, 2015.

[47] FireFOAM. FM Global, 2018. https://github.com/fireFoam-dev.

[48] OpenFOAM. OpenFOAM Foundation, 2018. www.openfoam.org.

[49] H. Weller, G. Tabor, H. Jasak, and C. Fureby. A tensorial approach to computational continuum mechanics using object-oriented techniques. *Computers in Physics*, 12(6):620–631, 1998.

[50] T. Poinsot and D. Veynante. *Theoretical and Numerical Combustion*. RT Edwards, Inc., 2005.

[51] Y. Wang, P. Chatterjee, and J. de Ris. Large eddy simulation of fire plumes. *Proceedings of the Combustion Institute*, 33:2473–2480, 2011.

[52] M. Chaos, M. Khan, and S. Dorofeev. Pyrolysis of corrugated cardboard in inert and oxidative environments. *Proceedings of the Combustion Institute*, 34:2583–2590, 2013.

[53] P. Chatterjee, J. de Ris, Y. Wang, and S. Dorofeev. A model for soot radiation in buoyant diffusion flames. *Proceedings of the Combustion Institute*, 33:2665–2671, 2011.

[54] K. Meredith, J. de Vries, Y. Wang, and Y. Xin. A comprehensive model for simulating the interaction of water with solid surfaces in fire suppression environments. *Proceedings of the Combustion Institute*, 34(2):2719–2726, 2013.

[55] H. Jasak. *Error Analysis and Estimation for the Finite Volume Method with Applications to Fluid Flows*. PhD thesis, Imperial College, London, UK, 1996.

[56] E. Robertson, V. Choudhury, S. Bhushan, and D. Walters. Validation of OpenFOAM numerical methods and turbulence models for incompressible bluff body flows. *Computers & Fluids*, 123:122–145, 2015.

[57] Y. Cao and T. Tamura. Large-eddy simulations of flow past a square cylinder using structured and unstructured grids. *Computers & Fluids*, 137:36–54, 2016.

[58] OpenFOAM Documentation. https://www.openfoam.com/documentation/.

[59] H. Jasak, H. Weller, and A. Gosman. High resolution NVD differencing scheme for arbitrarily unstructured meshes. *International Journal for Numerical Methods in Fluids*, 31(2):431–449, 1999.

[60] N. Ren, Y. Wang, S. Vilfayeau, and A. Trouvé. Large eddy simulation of turbulent vertical wall fires supplied with gaseous fuel through porous burners. *Combustion and Flame*, 169:194–208, 2016.

[61] S. Vilfayeau, T. Myers, A. Marshall, and A. Trouvé. Large eddy simulation of suppression of turbulent line fires by base-injected water mist. *Proceedings of the Combustion Institute*, 36(2):3287–3295, 2017.

[62] K. Rege and B. Hjertager. Application of foam-extend on turbulent fluid-structure interaction. In *IOP Conference Series: Materials Science and Engineering*, volume 276, page 012031. IOP Publishing, 2017.

[63] B. Leonard. Simple high-accuracy resolution program for convective modelling of discontinuities. *International Journal for Numerical Methods in Fluids*, 8(10):1291–1318, 1988.

[64] P. Gaskell and A. Lau. Curvature-compensated convective transport: SMART, a new boundedness-preserving transport algorithm. *International Journal for Numerical Methods in Fluids*, 8(6):617–641, 1988.

[65] H. Weller. Controlling the computational modes of the arbitrarily structured C grid. *Monthly Weather Review*, 140(10):3220–3234, 2012.

[66] J. Martínez, F. Piscaglia, A. Montorfano, A. Onorati, and S. Aithal. Influence of spatial discretization schemes on accuracy of explicit LES: Canonical problems to engine-like geometries. *Computers & Fluids*, 117:62–78, 2015.

[67] T. Mukha, S. Rezaeiravesh, and M. Liefvendahl. A library for Wall-Modelled Large-Eddy Simulation based on OpenFOAM technology. *arXiv preprint arXiv:1807.11786*, 2018.

[68] D. Lysenko, I. Ertesvåg, and K. Rian. Large-eddy simulation of the flow over a circular cylinder at Reynolds number 2×10^4. *Flow, Turbulence and Combustion*, 92(3):673–698, 2014.

[69] S. Verma, A. Trouve, C. Cadou, and J. Ruf. Assessment of OpenFOAM CFD library for numerical simulations of Shock Turbulence Interactions (STI). In *Thermal & Fluids Analysis Workshop*. NASA Goddard, 2015.

[70] N. Waterson and H. Deconinck. Design principles for bounded higher-order convection schemes–a unified approach. *Journal of Computational Physics*, 224(1):182–207, 2007.

[71] C. Greenshields, H. Weller, L. Gasparini, and J. Reese. Implementation of semi-discrete, non-staggered central schemes in a colocated, polyhedral, finite volume framework, for high-speed viscous flows. *International Journal for Numerical Methods in Fluids*, 63(1):1–21, 2010.

[72] C. Fureby, G. Tabor, H. Weller, and A. Gosman. A comparative study of subgrid scale models in homogeneous isotropic turbulence. *Physics of Fluids*, 9(5):1416–1429, 1997.

[73] F. Nicoud and F. Ducros. Subgrid-scale stress modelling based on the square of the velocity gradient tensor. *Flow, Turbulence and Combustion*, 62(3):183–200, 1999.

[74] R. Viskanta and M. Mengüç. Radiation heat transfer in combustion systems. *Progress in Energy and Combustion Science*, 13(2):97–160, 1987.

[75] J. White. *Measurement and Simulation of Suppression Effects in a Buoyant Turbulent Line Fire*. PhD thesis, University of Maryland, College Park, 2016.

[76] J. White, S. Verma, E. Keller, A. Hao, A. Trouvé, and A. Marshall. Water mist suppression of a turbulent line fire. *Fire Safety Journal*, 91:705–713, 2017.

[77] J. White, E. Link, A. Trouvé, P. Sunderland, A. Marshall, J. Sheffel, M. Corn, M. Colket, M. Chaos, and H. Yu. Radiative emissions measurements from a buoyant, turbulent line flame under oxidizer-dilution quenching conditions. *Fire Safety Journal*, 76:74–84, 2015.

[78] J. White, E. Link, A. Trouvé, P. Sunderland, and A. Marshall. A general calorimetry framework for measurement of combustion efficiency in a suppressed turbulent line fire. *Fire Safety Journal*, 92:164–176, 2017.

[79] L. Yuan and G. Cox. An experimental study of some line fires. *Fire Safety Journal*, 27(2):123–139, 1996.

[80] P. O'neill, D. Nicolaides, D. Honnery, and J. Soria. Autocorrelation functions and the determination of integral length with reference to experimental and numerical data. In *15th Australasian Fluid Mechanics Conference*. The University of Sydney, 2004.

[81] S. Verma. Understanding flame structure in wildfires using large eddy simulations. Master's thesis, University of Maryland, College Park, 2014.

[82] V. Le, A. Marchand, S. Verma, J. White, A. Marshall, T. Rogaume, F. Richard, J. Luche, and A. Trouvé. Simulations of a turbulent line fire with a steady flamelet combustion model and non-gray gas radiation models. In *Journal of Physics: Conference Series*, volume 1107, page 042009. IOP Publishing, 2018.

[83] C. Miller, W. Tang, M. Finney, S. McAllister, J. Forthofer, and M. Gollner. An investigation of coherent structures in laminar boundary layer flames. *Combustion and Flame*, 181:123–135, 2017.

[84] A. Trouvé and S. Verma. *A study of the structure of a turbulent line fire subjected to cross-flow using large eddy simulations*, pages 325–333. Imprensa da Universidade de Coimbra, Coimbra, 2018.

[85] J. Woods, B. Fleck, and L. Kostiuk. Effects of transverse air flow on burning rates of rectangular methanol pool fires. *Combustion and Flame*, 146(1-2):379–390, 2006.

[86] G. Davidson. Gaussian versus top-hat profile assumptions in integral plume models. *Atmospheric Environment (1967)*, 20(3):471–478, 1986.